

UNCLASSIFIED

AD NUMBER	
AD355562	
CLASSIFICATION CHANGES	
TO:	unclassified
FROM:	confidential
LIMITATION CHANGES	
TO:	Approved for public release, distribution unlimited
FROM:	Distribution authorized to U.S. Gov't. agencies and their contractors; Administrative/Operational Use; JUL 1958. Other requests shall be referred to Defense Atomic Support Agency, Washington, DC.
AUTHORITY	
DNA ltr, 7 Nov 1980; DNA ltr, 7 Nov 1980	

THIS PAGE IS UNCLASSIFIED

CONFIDENTIAL

P. Ransick

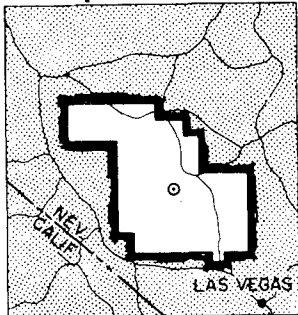
WT-1433

This document consists of 186 pages.

No. 95 of 165 copies, Series A

OPERATION PLUMBBOB

Ad 355562



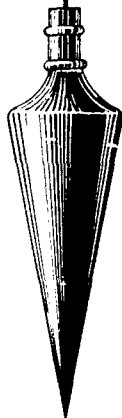
NEVADA TEST SITE
MAY-OCTOBER 1957

Project 5.4

IN-FLIGHT STRUCTURAL RESPONSE
OF THE MODEL A4D-1 AIRCRAFT
TO A NUCLEAR EXPLOSION (U)

Issuance Date: March 31, 1960

HEADQUARTERS FIELD COMMAND
DEFENSE ATOMIC SUPPORT AGENCY
SANDIA BASE, ALBUQUERQUE, NEW MEXICO



20070226113

This material contains information affecting the national defense of the United States within the meaning of the espionage laws Title 18, U. S. C., Secs. 793 and 794, the transmission or revelation of which in any manner to an unauthorized person is prohibited by law.

CONFIDENTIAL

Postal Registry No. *224250*

JUL - 8 1974

Postal Registry No. 14390 APR 21 1960

125948
21

Inquiries relative to this report may be made to

Chief, Defense Atomic Support Agency
Washington 25, D. C.

When no longer required, this document may be
destroyed in accordance with applicable security
regulations.

DO NOT RETURN THIS DOCUMENT

CONFIDENTIAL

WT-1433

Operation Plumbbob—Project 5.4

*IN-FLIGHT STRUCTURAL RESPONSE
OF THE MODEL A4D-1 AIRCRAFT
TO A NUCLEAR EXPLOSION (U)*

J. H. Walls, AD-42, Project Officer
And the Staff of
Douglas Aircraft Company, Inc.

Airframe Design Division
Bureau of Aeronautics
Department of the Navy

And

Advanced Design Section
Douglas Aircraft Company, Inc.
El Segundo Division
El Segundo, California

July 1958

This material contains information affecting the national defense of the United States within the meaning of the espionage laws Title 18, U. S. C., Secs. 793 and 794, the transmission or revelation of which in any manner to an unauthorized person is prohibited by law.

CONFIDENTIAL

FOREWORD

This report presents the final results of one of the 46 projects comprising the military-effect program of Operation Plumbbob, which included 24 test detonations at the Nevada Test Site in 1957.

For overall Plumbbob military-effects information, the reader is referred to the "Summary Report of the Director, DOD Test Group (Programs 1-9)," ITR-1445, which includes: (1) a description of each detonation, including yield, zero-point location and environment, type of device, ambient atmospheric conditions, etc.; (2) a discussion of project results; (3) a summary of the objectives and results of each project; and (4) a listing of project reports for the military-effect program.

ABSTRACT

This report presents the results of the participation of two A4D-1 aircraft in Operation Plumbob as Project 5.4.

The objectives of this project were to: (1) measure thermal and blast gust response of the A4D-1 aircraft to nuclear explosion effects, (2) obtain data to improve the methods of predicting blast gust response of aircraft with wings of triangular planform, and (3) correlate experimental response data for the A4D-1 with analytical methods for use in determining its nuclear weapon delivery capability.

The A4D-1 aircraft is a single engine, modified delta wing, carrier-based attack aircraft with capability for delivery of special weapons covering a wide range of weapon yields.

The A4D-1 aircraft, as Project 5.4, participated in seven shots: Boltzmann (11.5 kt), Priscilla (36.6 kt), Hood (74.1 kt), Diablo (18.7 kt), Shasta (16.8 kt), Doppler (10.7 kt), and Smoky (43.71 kt).

Since improvement of analytical methods of calculating gust response was the primary objective, instrumentation emphasis was placed on measuring wing pressure distributions, wing shears, moments, torques, and airplane accelerations. Instrumentation was also installed to measure thermal energy received at the aircraft and the temperature response in the thin skin panels on the lower surface of the aircraft. Additional instrumentation was installed to measure and record time of shock arrival, overpressure, and the effect of the shock wave on engine performance.

The gust response results of the tests are presented as wing chord-wise and span-wise pressure distributions versus time, span-wise plots of wing section lift coefficient, average pressure, and center of pressure versus time, airplane center of gravity and tail acceleration versus time, airplane pitching motion versus time, wing shear, torque, and bending moment versus time, and tail load versus time. Other results of the tests are presented as irradiance and radiant exposure versus time, temperature in thin skin areas versus time, maximum temperature rise at each thermocouple location, peak overpressure, and time of shock arrival.

Calculated weapon effects and aircraft responses are compared with the measured results to show the adequacy of the analytical methods. For gust responses, the calculated aircraft response used for comparison with the measured results reflects refinements in the analytical methods not included in pretest prediction of gust response. Primarily, the refinements needed to improve the gust response prediction methods were the inclusion of mass coupling effects in the analysis of wing vibration and a change in time duration of the shock diffraction loading. The resulting method of dynamic structural analysis provided analytical solutions which compared favorably with the experimental results.

The prediction methods presented in this report for the thermal effects gave fair agreement with the measured results for the radiant exposure and maximum temperature rise. From comparison of calculated and measured temperature rise using the measured radiant

exposure, it is shown that the temperature rise in critical skin panels can be calculated with reasonable accuracy. The principal improvement of the maximum temperature rise calculation appears to be in increasing the accuracy of estimating the radiant exposure.

Excellent agreement was obtained between the measured and calculated peak overpressure and time of shock arrival.

CONTENTS

FOREWORD	4
ABSTRACT	5
CHAPTER 1 INTRODUCTION	17
1.1 Objectives	17
1.2 Background	17
1.3 Theory	17
1.3.1 Thermal Radiation	17
1.3.2 Nuclear Radiation	18
1.3.3 Shock-Wave Effects	19
CHAPTER 2 PROCEDURE	21
2.1 Operation	21
2.1.1 Description of the A4D-1 Aircraft	21
2.1.2 Shot Participation	22
2.1.3 Criteria for Selecting Desired Aircraft Positions	22
2.1.4 Positioning of Aircraft for Test	22
2.1.5 Positioning System	23
2.2 Instrumentation	23
2.2.1 Installation	23
2.2.2 Scope of Instrumentation	23
2.2.3 Data Recorded on Oscillographs	24
2.2.4 Data Recorded on Photo Recorder	24
2.2.5 Calibration	24
2.2.6 Method of Instrumentation Operation	25
CHAPTER 3 SHOT PARTICIPATION, AIRCRAFT POSITIONS, AND FLIGHT ENVIRONMENTAL DATA	26
3.1 Shot Participation	26
3.2 Aircraft Positions and Flight Environmental Data	26
CHAPTER 4 THERMAL INPUT DATA	30
4.1 Scattered Radiation	30
4.2 Discussion of Radiometer and Calorimeter Measurements	30
4.3 Correlation of Measured and Calculated Radiant Exposure	32
CHAPTER 5 STRUCTURAL TEMPERATURE MEASUREMENTS AND CORRELATION WITH CALCULATED VALUES	42
5.1 Structural Temperature Measurements	42
5.2 Correlation of Measured and Calculated Maximum Temperature Rise	42
5.3 Quartz-Covered Thermocouples	44

CHAPTER 6	NUCLEAR RADIATION DATA	61
CHAPTER 7	ENGINE RESPONSE DATA	63
CHAPTER 8	SHOCK WAVE EFFECTS	65
8.1	Overpressure	65
8.2	Time of Shock Arrival	65
8.3	Aircraft Response to Blast Loading	65
8.3.1	Structural Loads	67
8.3.2	Wing Pressure Measurements	70
CHAPTER 9	DELIVERY CAPABILITY OF THE A4D-1 AIRCRAFT	145
CHAPTER 10	CONCLUSIONS	146
CHAPTER 11	RECOMMENDATIONS	148
APPENDIX A	INSTRUMENTATION	149
A.1	Recording Instrumentation	149
A.2	Instrumentation for Thermal Measurements	149
A.3	Measurement of Thermal Radiation Received by the Aircraft	149
A.4	Camera Locations	149
A.5	Overpressure Measurements	151
A.6	Wing Pressure Distribution Measurements	151
A.7	Structural Response Instrumentation	154
A.8	Engine Instrumentation	156
A.9	Flight Environmental and Special Instrumentation	156
APPENDIX B	METHOD OF SCALING SHOCK WAVE EFFECTS	157
APPENDIX C	DYNAMIC STRUCTURAL ANALYSIS	158
C.1	Introduction	158
C.2	Method of Analysis	158
C.2.1	Assumptions	158
C.2.2	Equations of Motion	158
C.2.3	Solution of the Equations of Motion	159
C.2.4	Scaling the Solutions	160
C.3	Determination of Critical Wing Response	161
APPENDIX D	THE ROSSETTE METHOD	164
APPENDIX E	WING PRESSURE TIME HISTORIES	166
REFERENCES	184
TABLES		
3.1	Summary of Test Event Information	26
3.2	Aircraft Positions at Time of Explosion	27
3.3	Aircraft Positions at Time of Shock Arrival	28
3.4	Flight and Environmental Parameters at Time of Explosion	29
3.5	Flight and Environmental Parameters at Time of Shock Arrival	29
4.1	Maximum Measured Irradiance and Radiant Exposure	31
5.1	Maximum Temperature Rise	43
5.2	Density and Specific Heat of Paint	44
5.3	Thermal Capacity of Aileron and Flap	44
6.1	Nuclear Radiation Data	62
7.1	Engine Response to Shock Wave	64
8.1	Measured and Calculated Peak Overpressure	66
8.2	Measured and Calculated Time of Shock Arrival	66
8.3	Comparison of Maximum Wing Bending Moments	66

8.4	Types of Wing and Tail Structural Response Data Obtained	68
A.1	Detailed Thermocouple Locations	151
A.2	Thermal Instruments	152
A.3	Detailed Wing Pressure Transducer Locations	154
D.1	Basic Coefficients	164
D.2	Correction Factors for Basic Coefficients	165

FIGURES

3.1	Definition of distances locating aircraft position	27
4.1	Thermal irradiance as a function of time, Shot Boltzmann	32
4.2	Thermal irradiance as a function of time, Shot Priscilla	33
4.3	Thermal irradiance as a function of time, Shot Hood	33
4.4	Thermal irradiance as a function of time, Shot Diablo	34
4.5	Thermal irradiance as a function of time, Shot Shasta	34
4.6	Thermal irradiance as a function of time, Shot Doppler, Airplane No. 137827	35
4.7	Thermal irradiance as a function of time, Shot Doppler, Airplane No. 137831	35
4.8	Thermal irradiance as a function of time, Shot Smoky	36
4.9	Radiant exposure as a function of time, Shot Boltzmann	36
4.10	Radiant exposure as a function of time, Shot Priscilla	37
4.11	Radiant exposure as a function of time, Shot Hood	37
4.12	Radiant exposure as a function of time, Shot Diablo	38
4.13	Radiant exposure as a function of time, Shot Shasta	38
4.14	Radiant exposure as a function of time, Shot Doppler, Airplane No. 137827	39
4.15	Radiant exposure as a function of time, Shot Doppler, Airplane No. 137831	39
4.16	Radiant exposure as a function of time, Shot Smoky	40
4.17	Correlation of measured and calculated radiant exposure, scattering included	40
4.18	Correlation of measured and calculated radiant exposure, scattering omitted	41
4.19	Correlation of measured and calculated radiant exposure, scattering omitted, $K_1 = 1.0$	41
5.1	Temperature time history of aileron skin, Shot Boltzmann	45
5.2	Temperature time history of aileron skin, Shot Priscilla	45
5.3	Temperature time history of flap skin, Shot Priscilla	46
5.4	Temperature time history of quartz-covered thermocouples compared to adjacent uncovered thermocouples, Shot Priscilla	46
5.5	Temperature time history of aileron skin, Shot Hood	47
5.6	Temperature time history of flap skin, Shot Hood	47
5.7	Temperature time history of quartz-covered thermocouples compared to adjacent uncovered thermocouples, Shot Hood	48
5.8	Temperature time history of aileron skin, Shot Diablo	48
5.9	Temperature time history of flap skin, Shot Diablo	49
5.10	Temperature time history of quartz-covered thermocouples compared to adjacent uncovered thermocouples, Shot Diablo	49
5.11	Temperature time history of aileron skin, Shot Shasta	50
5.12	Temperature time history of flap skin, Shot Shasta	50
5.13	Temperature time history of quartz-covered thermocouples compared to adjacent uncovered thermocouples, Shot Shasta	51
5.14	Temperature time history of fuselage skin, Shot Shasta	51
5.15	Temperature time history of elevator skin, Shot Shasta	52
5.16	Temperature time history of aileron skin, Shot Doppler, Airplane No. 137827	52

5.17	Temperature time history of flap skin, Shot Doppler, Airplane No. 137827	53
5.18	Temperature time history of quartz-covered thermocouples compared to adjacent uncovered thermocouples, Shot Doppler, Airplane No. 137827.	53
5.19	Temperature time history of aileron skin, Shot Doppler, Airplane No. 137831	54
5.20	Temperature time history of flap skin, Shot Doppler, Airplane No. 137831	54
5.21	Temperature time history of quartz-covered thermocouples compared to adjacent uncovered thermocouples, Shot Doppler, Airplane No. 137831.	55
5.22	Temperature time history of fuselage skin, Shot Doppler, Airplane No. 137831	55
5.23	Temperature time history of elevator skin, Shot Doppler, Airplane No. 137831	56
5.24	Temperature time history of aileron skin, Shot Smoky	56
5.25	Temperature time history of flap skin, Shot Smoky	57
5.26	Temperature time history of quartz-covered thermocouples compared to adjacent uncovered thermocouples, Shot Smoky	57
5.27	Temperature time history of fuselage skin, Shot Smoky	58
5.28	Temperature time history of elevator skin, Shot Smoky	58
5.29	Correlation of measured and calculated temperature rise, scattering included	59
5.30	Correlation of measured and calculated temperature rise, scattering omitted	59
5.31	Correlation of measured temperature rise and temperature rise calculated from measured radiant exposure	60
5.32	Correlation of measured temperature rise and temperature rise calculated from measured radiant exposure, combined thermal capacity of paint and aluminum skin.	60
8.1	Time history of nose boom overpressure, Shot Diablo	72
8.2	Overpressure data reduced to 1 kt at homogeneous, sea-level atmosphere	72
8.3	Time of shock arrival data reduced to 1 kt at homogeneous sea-level atmosphere	73
8.4	Comparison of wing shear measurements at Station 36.5, obtained by the matrix and rosette methods, Shot Diablo	73
8.5	Comparison of wing torque about fuselage Station 283, obtained by the matrix and rosette methods at Station 36.5, Shot Diablo	74
8.6	Wing shear at Station 36.5 from matrix measurements, Shot Boltzmann	74
8.7	Wing shear at Station 36.5 from matrix measurements, Shot Priscilla	75
8.8	Wing shear at Station 36.5 from matrix measurements, Shot Hood	75
8.9	Wing shear at Station 36.5 from matrix measurements, Shot Diablo	76
8.10	Wing torque about fuselage Station 283 from matrix measurements at Station 36.5, Shot Boltzmann	76
8.11	Wing torque about fuselage Station 283 from matrix measurements at Station 36.5, Shot Priscilla	77
8.12	Wing torque about fuselage Station 283 from matrix measurements at Station 36.5, Shot Hood.	77
8.13	Wing torque about fuselage Station 283 from matrix measurements at Station 36.5, Shot Diablo	78

8.14	Wing torque about fuselage Station 283 from matrix measurements at Station 36.5, Shot Doppler, Airplane No. 827	78
8.15	Comparison of calculated and measured wing bending moments at Station 36.5, rosette measurements, Shot Boltzmann	79
8.16	Comparison of calculated and measured wing bending moments at Station 36.5, rosette measurements, Shot Priscilla	79
8.17	Comparison of calculated and measured wing bending moments at Station 36.5, rosette measurements, Shot Hood	80
8.18	Comparison of calculated and measured wing bending moments at Station 36.5, rosette measurements, Shot Diablo	80
8.19	Comparison of calculated and measured wing bending moments at Station 36.5, rosette measurements, Shot Shasta	81
8.20	Comparison of calculated and measured wing bending moments at Station 36.5, rosette measurements, Shot Doppler, Airplane No. 827	81
8.21	Comparison of calculated and measured wing bending moments at Station 36.5, rosette measurements, Shot Doppler, Airplane No. 831	82
8.22	Comparison of calculated and measured wing bending moments at Station 36.5, rosette measurements, Shot Smoky	82
8.23	Comparison of calculated and measured wing bending moments at Station 36.5, matrix measurements, Shot Boltzmann	83
8.24	Comparison of calculated and measured wing bending moments at Station 36.5, matrix measurements, Shot Priscilla	83
8.25	Comparison of calculated and measured wing bending moments at Station 36.5, matrix measurements, Shot Hood.	84
8.26	Comparison of calculated and measured wing bending moments at Station 36.5, matrix measurements, Shot Diablo	84
8.27	Comparison of calculated and measured wing bending moments at Station 36.5, matrix measurements, Shot Doppler, Airplane No. 827	85
8.28	Comparison of calculated and measured wing bending moments at Station 36.5, pressure measurements, Shot Priscilla	85
8.29	Comparison of calculated and measured wing bending moments at Station 36.5, pressure measurements, Shot Diablo	86
8.30	Comparison of calculated and measured wing bending moments at Station 36.5, pressure measurements, Shot Doppler, Airplane No. 827	86
8.31	Wing bending moment at Station 72 from rosette measurements, Shot Boltzmann	87
8.32	Wing bending moment at Station 72 from rosette measurements, Shot Priscilla	87
8.33	Wing bending moment at Station 72 from rosette measurements, Shot Hood.	88
8.34	Wing bending moment at Station 72 from rosette measurements, Shot Diablo	88
8.35	Wing bending moment at Station 72 from rosette measurements, Shot Doppler, Airplane No. 827	89
8.36	Wing bending moment at Station 113 from rosette measurements, Shot Boltzmann	89
8.37	Wing bending moment at Station 113 from rosette measurements, Shot Priscilla	90
8.38	Wing bending moment at Station 113 from rosette measurements, Shot Diablo	90
8.39	Wing bending moment at Station 113 from rosette measurements, Shot Doppler, Airplane No. 827	91
8.40	Wing bending moment at Station 113 from rosette measurements, Shot Smoky	91

8.41	Wing bending moment at Station 36.5, matrix measurement, extended time plot, Shot Diablo	92
8.42	Wing shear at Station 36.5, matrix measurement, extended time plot, Shot Diablo	92
8.43	Wing torque about fuselage Station 283, matrix measurement, at Station 36.5, extended time plot, Shot Diablo	93
8.44	Horizontal stabilizer load, matrix method, Shot Diablo	93
8.45	Horizontal stabilizer load computed from actuator and lug reactions, Shot Shasta	94
8.46	Horizontal stabilizer load, matrix method, Shot Doppler, Airplane No. 827	94
8.47	Horizontal stabilizer load computed from actuator and lug reactions, Shot Doppler, Airplane No. 831	95
8.48	Horizontal stabilizer load computed from actuator and lug reactions, Shot Smoky	95
8.49	Horizontal stabilizer torque about fuselage Station 437.6, matrix method, Shot Diablo	96
8.50	Horizontal stabilizer torque about fuselage Station 437.6, matrix method, Shot Doppler, Airplane No. 827	96
8.51	Horizontal stabilizer bending moment, matrix method, Shot Diablo	97
8.52	Horizontal stabilizer load, matrix method, extended time plot, Shot Diablo	97
8.53	Horizontal stabilizer torque about fuselage Station 437.6, matrix method, extended time plot, Shot Diablo	98
8.54	Horizontal stabilizer bending moment, matrix method, extended time plot, Shot Diablo	98
8.55	Fuselage keel stresses, Shot Shasta	99
8.56	Fuselage keel stresses, Shot Doppler, Airplane No. 137831	99
8.57	Fuselage keel stresses, Shot Smoky	100
8.58	Measured tail acceleration versus time, Shot Boltzmann	100
8.59	Measured tail acceleration versus time, Shot Priscilla	101
8.60	Measured tail acceleration versus time, Shot Hood	101
8.61	Measured tail acceleration versus time, Shot Diablo	102
8.62	Measured tail acceleration versus time, Shot Doppler, Airplane No. 827	102
8.63	Comparison of measured and calculated center of gravity acceleration, Shot Boltzmann	103
8.64	Comparison of measured and calculated center of gravity acceleration, Shot Priscilla	103
8.65	Comparison of measured and calculated center of gravity acceleration, Shot Hood	104
8.66	Comparison of measured and calculated center of gravity acceleration, Shot Diablo	104
8.67	Comparison of measured and calculated center of gravity acceleration, Shot Shasta	105
8.68	Comparison of measured and calculated center of gravity acceleration, Shot Doppler, Airplane No. 827	105
8.69	Comparison of measured and calculated center of gravity acceleration, Shot Doppler, Airplane No. 831	106
8.70	Comparison of measured and calculated center of gravity acceleration, Shot Smoky	106
8.71	Incremental pitching acceleration versus time, Shot Boltzmann	107
8.72	Incremental pitching acceleration versus time, Shot Priscilla	107
8.73	Incremental pitching acceleration versus time, Shot Hood	108
8.74	Incremental pitching acceleration versus time, Shot Diablo	108

8.75	Incremental pitching acceleration versus time, Shot Doppler, Airplane No. 137827	109
8.76	Incremental pitching velocity versus time, Shot Boltzmann	109
8.77	Incremental pitching velocity versus time, Shot Priscilla	110
8.78	Incremental pitching velocity versus time, Shot Hood	110
8.79	Incremental pitching velocity versus time, Shot Diablo	111
8.80	Incremental pitching velocity versus time, Shot Doppler, Airplane No. 137827	111
8.81	Incremental pitch angle versus time, Shot Boltzmann	112
8.82	Incremental pitch angle versus time, Shot Priscilla	112
8.83	Incremental pitch angle versus time, Shot Hood	113
8.84	Incremental pitch angle versus time, Shot Diablo	113
8.85	Incremental pitch angle versus time, Shot Doppler, Airplane No. 137827	114
8.86	Center of gravity acceleration versus time, extended time plot, Shot Diablo	114
8.87	Incremental pitching acceleration, extended time plot, Shot Diablo	115
8.88	Incremental pitching velocity, extended time plot, Shot Diablo	115
8.89	Incremental pitch angle, extended time plot, Shot Diablo	116
8.90	Time-wise variation of chord-wise incremental pressure, Shot Priscilla	117
8.91	Time-wise variation of chord-wise incremental pressure, Shot Diablo	118
8.92	Time-wise variation of chord-wise incremental pressure, Shot Doppler, Airplane No. 137827	119
8.93	Time-wise variation of chord-wise incremental pressure, Shot Boltzmann	120
8.94	Time-wise variation of chord-wise incremental pressure, Shot Shasta	121
8.95	Time-wise variation of chord-wise incremental pressure, Shot Doppler. Airplane No. 137831	122
8.96	Time-wise variation of chord-wise incremental pressure, Shot Smoky	123
8.97	Time-wise variation of chord-wise incremental pressure, Shot Smoky	124
8.98	Time-wise variation of span-wise incremental pressure and chord-wise center of pressure locations, Shot Priscilla	125
8.99	Time-wise variation of span-wise incremental pressure and chord-wise center of pressure locations, Shot Diablo	126
8.100	Time-wise variation of span-wise incremental pressure and chord-wise center of pressure locations, Shot Doppler, Airplane No. 137827	127
8.101	Time-wise variation of span-wise section lift coefficients, Shot Priscilla	128
8.102	Time-wise variation of span-wise section lift coefficients, Shot Diablo	129
8.103	Time-wise variation of span-wise section lift coefficients, Shot Doppler, Airplane No. 137827	130
8.104	Time-wise variation of chord-wise center of pressure locations for three wing stations, Shot Priscilla	131
8.105	Time-wise variation of chord-wise center of pressure locations for three wing stations, Shot Diablo	131
8.106	Time-wise variation of chord-wise center of pressure locations for three wing stations, Shot Doppler, Airplane No. 137827	132
8.107	Time-wise variation of incremental section lift coefficients for three wing stations, Shot Priscilla	132

8.108	Time-wise variation of incremental section lift coefficients for three wing stations, Shot Diablo	133
8.109	Time-wise variation of incremental section lift coefficients for three wing stations, Shot Doppler, Airplane No. 137827	133
8.110	Time-wise variation of average incremental pressure for three wing stations, Shot Priscilla	134
8.111	Time-wise variation of average incremental pressure for three wing stations, Shot Diablo	134
8.112	Time-wise variation of average incremental pressure for three wing stations, Shot Doppler, Airplane No. 137827	135
8.113	Time-wise variation of average incremental pressure, Shot Boltzmann	135
8.114	Time-wise variation of average incremental pressure, Shot Shasta	136
8.115	Time-wise variation of average incremental pressure, Shot Doppler, Airplane No. 137827	137
8.116	Time-wise variation of average incremental pressure, Shot Smoky	137
8.117	Time-wise variation of average incremental pressure, Shot Smoky	138
8.118	Time-wise variation of incremental section lift coefficients, Shot Boltzmann	138
8.119	Time-wise variation of incremental section lift coefficients, Shot Shasta	139
8.120	Time-wise variation of incremental section lift coefficients, Shot Doppler, Airplane No. 137831	139
8.121	Time-wise variation of incremental section lift coefficients, Shot Smoky	140
8.122	Time-wise variation of incremental section lift coefficients, Shot Smoky	140
8.123	Time-wise variation of chord-wise center of pressure location, Shot Boltzmann	141
8.124	Time-wise variation of chord-wise center of pressure location, Shot Shasta	141
8.125	Time-wise variation of chord-wise center of pressure location, Shot Doppler, Airplane No. 137831	142
8.126	Time-wise variation of chord-wise center of pressure location, Shot Smoky	142
8.127	Time-wise variation of chord-wise center of pressure location, Shot Smoky	143
8.128	Time-wise variation of span-wise center of pressure location, Shot Priscilla	143
8.129	Time-wise variation of span-wise center of pressure location, Shot Diablo	144
8.130	Time-wise variation of span-wise center of pressure location, Shot Doppler, Airplane No. 137827	144
A.1	Thermocouple locations	150
A.2	Wing and fuselage pressure transducer locations	153
A.3	Strain gage locations	155
C.1	Assumed diffraction model shown shortly after the blast wave has begun enveloping the wing	162
C.2	Unit overpressure forcing function, f_0 , rigid body translation	162
C.3	Unit overpressure forcing function, f_1 , first bending mode	163
C.4	Unit overpressure forcing function, f_2 , first torsion mode	163
E.1	Local wing pressure time histories, Shot Diablo	167
E.2	Local wing pressure time history, Shot Diablo	168
E.3	Local wing pressure time histories, Shot Diablo	169
E.4	Local wing pressure time history, Shot Diablo	170

E.5	Local wing pressure time history, Shot Diablo.	171
E.6	Local wing pressure time history, Shot Diablo.	172
E.7	Local wing pressure time histories, Shot Diablo	173
E.8	Local wing pressure time histories, Shot Diablo	174
E.9	Local wing pressure time history, Shot Diablo.	175
E.10	Local wing pressure time history, Shot Diablo.	176
E.11	Local wing pressure time history, Shot Diablo.	177
E.12	Local wing pressure time histories, Shot Diablo	178
E.13	Local wing pressure time histories, Shot Diablo	179
E.14	Local wing pressure time histories, Shot Diablo	180
E.15	Local wing pressure time history, Shot Diablo.	181
E.16	Local wing pressure time history, Shot Diablo.	182
E.17	Local wing pressure time history, Shot Diablo.	183

CONFIDENTIAL

Chapter 1

INTRODUCTION

1.1 OBJECTIVES

The objectives of Project 5.4 of Operation Plumbbob were to: (1) measure thermal and blast gust response of the A4D-1 aircraft to nuclear explosion effects, (2) obtain data to improve the methods of predicting blast gust response of aircraft with wings of triangular planform, and (3) correlate experimental response data for the A4D-1 with analytical methods for use in determining its nuclear weapon delivery capability.

1.2 BACKGROUND

The A4D-1 is a carrier-based attack aircraft with an assigned delivery capability covering a wide range of nuclear weapons, including those with yields in the megaton range. Theoretical analysis (Reference 1) had indicated that the A4D-1 could safely deliver such weapons. Experimental data from actual field tests were important for substantiating analytical derivations of structural and thermal response characteristics for aircraft of the A4D-1 configuration.

The A4D-1 has a modified delta-wing planform. In planning the experiment, particular emphasis was placed on obtaining data on the effect of the shock wave and the associated material velocity on this wing geometry to extend the available analytical methods for predicting gust response. Since it was anticipated that the rigid A4D-1 wing would be responsive to diffraction loading, a system of pressure transducers was installed in the wing to provide pressure-time histories which included the diffraction process.

1.3 THEORY

Aircraft flying in the vicinity of a nuclear explosion are subjected to the effects of thermal radiation and blast loading; the crew is subjected to nuclear radiation. These effects are of primary significance in the design of aircraft and in the establishment of techniques and procedures for delivery of nuclear weapons. Methods for analytically predicting weapon effects have been derived by various investigators from basic theory and from empirical data obtained in previous tests.

The following sections give a general outline of the prediction methods used to plan positions and correlate the measured data of the two A4D-1 aircraft during Operation Plumbbob. For a complete description of the positioning methods, see Reference 2 and Appendix C.

1.3.1 Thermal Radiation. The radiant exposure at the aircraft location and the temperature rise in a horizontal aircraft skin were calculated from the following equations which

CONFIDENTIAL

include the effects of terrain reflection, fireball orientation, aerodynamic cooling, flyaway factor, and atmospheric attenuation and scattering.

$$Q = \frac{W_{th} \times 10^{12}}{4\pi d^2 \exp(kD)} \left[K_1 \sin \beta_E + \left(\frac{Q_{RN}}{Q_I} \right) \frac{A}{\exp(0.5kD)} + \frac{Q_S}{Q_I} \right] [(1-F)] \quad (1.1)$$

$$\Delta T = \frac{Q (1-FH)}{(1-F)} \left(\frac{a}{G} \right) \quad (1.2)$$

where

Q = radiant exposure, cal/cm²

ΔT = maximum temperature rise in the skin, °F

W_{th} = thermal yield, kt = 0.44 (W_{rc}) 0.94

W_{rc} = radiochemical yield, kt

k = attenuation coefficient

D = radial distance from explosion, thousands of feet

d = radial distance from explosion, cm

β_E = effective angle between slant range line and horizontal, degrees

A = albedo of terrain

$\frac{Q_{RN}}{Q_I}$ = terrain reflection factor

$\frac{Q_S}{Q_I}$ = scattering factor

(1-F) = flyaway factor

(1-FH) = combined flyaway and cooling factor

a = thermal absorptivity of aircraft skin

$G = \rho c_p s$ thermal capacity of aircraft skin, cal/cm²-°F

ρ = density of material, lbs/cm³

c_p = specific heat, cal/lb-°F

s = skin thickness, cm

K_1 = factor to account for fireball distortion and aircraft orientation to surface or near-surface bursts

$\exp(kD) = e^{kD}$

Values of linear attenuation, k , were obtained by assuming a value of 0.0142 at sea level and varying this value with altitude and burst height so that the attenuation obtained for the actual path was equal to that obtained through the same mass of air at sea level. The factor to account for fireball distortion and aircraft orientation, K_1 , was obtained from Reference 3. The reflection factor Q_{RN}/Q_I was obtained from Reference 4. A value of 0.44 was used for the albedo, A , of the terrain surface at the Nevada Test Site (NTS). The scattering ratio as defined by the Bureau of Aeronautics can be expressed as:

$$Q_S/Q_I = \frac{(SR-4667)}{1000} (0.01125) \quad (1.3)$$

where SR = slant range, feet.

The factors (1-FH) and (1-F) were obtained from Reference 5. The combined flyaway and cooling varied from 0.908 to 0.957 for the range of yields covered in the tests. The flyaway factor varied from 0.98 to 1.02. The values greater than 1.0 occur because the aircraft was flying toward the explosion at time zero.

1.3.2 Nuclear Radiation. The predicted nuclear radiation was calculated from data given in Reference 6, with the following modifications: for the first four shot participations in the test series, the combined gamma and neutron radiation was increased by a factor of 1.25, rather than 2.0 per Reference 6, to account for an airborne receiver. On the basis of a comparison of measured and predicted radiations for these first shots, the factor was reduced to

1.0 for Shot Shasta and subsequent events. One rem was added to the calculated nuclear radiation for all cases where the airplane was flying toward ground zero at a horizontal range of 1,000 feet or more at time zero. This was to provide for a radiation increase in approaching the rising cloud.

1.3.3 Shock-Wave Effects. Basic data for predicting overpressure, gust velocity, time of shock arrival, density in the shock wave, and length of the positive phase were obtained from Headquarters, Armed Forces Special Weapons Project (Reference 6). This data was in the form of curves for a 1 kt burst in a sea level, homogeneous atmosphere, and was scaled for other yields and altitudes by the modified Sachs scaling equations (Reference 7). A detailed description of these scaling equations is presented in Appendix B.

The location of the triple-point path was predicted from BuAer-supplied data (Reference 8). For aircraft positions beyond the triple-point path, where the direct and reflected shocks are fused, the effects were calculated using twice the yield. In Shots Diablo and Shasta, for which the scaled heights of burst were less than 175 feet, there was a possibility of a fused region directly above the burst. For these cases, 1.2 times the yield was used. Conservative estimates of the effects in the triple-point path were calculated using twice the Mach region overpressure and assuming a vertical gust. Late in the program the criteria for triple-point effects calculations were changed to use three times the yield and a radial gust.

The structural response of an aircraft struck by a blast wave is influenced by two distinct phenomena, each characteristic of traveling shock waves.

The first and usually most important of these phenomena is the moving velocity field or gust which travels immediately behind the shock wave and consists of high velocity air particles whose motion is directed normal to the shock front. This gust induces aircraft structural loads in a manner analogous to that of a conventional atmospheric gust.

The second shock wave phenomenon contributing to structural loading is the blast-wave overpressure which consists of a moving pressure field also traveling immediately behind the shock wave. The overpressure field reacts with the aircraft as a result of the diffractive distortion of the shock wave in its passage over the aircraft. The distortion of the wave subjects certain portions of the aircraft to the blast wave overpressure while others are experiencing only steady state pressures. This unbalance results in structural loads which must be considered in addition to the gust loading.

Since the blast wave envelopes the aircraft in a relatively short period of time, the diffraction loading lasts only briefly. For most aircraft structures, the characteristic structural response time (period of the lowest order natural mode of vibration) is sufficiently long to make the response to the diffraction impulse negligible. The extreme structural rigidity of the A4D-1 aircraft, however, results in a short characteristic response time. Consequently, the diffraction loading cannot be neglected.

The short characteristic response time of the A4D-1 aircraft introduces a further complication into the problem of predicting blast response, namely, the influence of lift build-up time because of the gust. For aircraft of conventional flexibility this factor is of little importance since the lift build-up even for atmospheric gusts occurs in a small fraction of the response time. The A4D-1 aircraft, however, has a response time which is actually smaller than the lift build-up time predicted by conventional gust theory, and thus its response is highly sensitive to the precise nature of this build-up. For the purpose of analytical prediction this factor is determined through the choice of a so-called gust indicial function. The choice of this function for the blast problem has long been the subject of debate, and to date no satisfactory solution has been found. Conventional gust theory would suggest the use of the Wagner function which gives the theoretical lift build-up for a two-dimensional wing experiencing an instantaneous increase in upwash. Another possible choice is the Kussner function which gives the lift build-up for a two-dimensional wing flying into a stationary sharp edged gust. Another indicial function suggested by the results of recent research on the problem of traveling gusts is the step function. Reference 9 presents theoretical indicial functions for both two- and three-dimensional wings penetrating gusts which closely resemble blast gusts. The results of

Reference 9 indicated that a step function might be well suited to the delta wing planform of the A4D-1 aircraft for the Mach number range encountered in Operation Plumbbob.

For the purposes of after-the-fact correlation with measured structural responses from Operation Plumbbob, the above-mentioned indicial functions were tried and the one which gave the best experimental agreement was selected. The function giving the best experimental agreement was the step function. It was found that even in this case the total response was unconservatively estimated. Consequently, the remainder of the response was attributed to diffraction loading. Several assumed models of the diffraction phenomenon were examined and the one which yielded the structural response sufficient to give good correlation with measurements was selected.

The method of analysis used was one of normal mode superposition as explained in Reference 10. The equations of motion together with pertinent assumptions and the method of scaling the unit solutions to obtain results for specific aircraft positions and gust overpressures are given in Appendix C.

Chapter 2

PROCEDURE

Two A4D-1 aircraft (Bureau Nos. 137827 and 137831) were instrumented. The second aircraft was provided primarily to serve as an alternate in the event that the first could not participate. Simultaneous participation of both aircraft in Shot Doppler was accomplished to obtain additional test data. The major portion of the instrumentation was designed to give data on structural stresses and gust responses to the blast. Instrumentation was also provided to obtain data for the effects of thermal radiation, aircraft thermal response, nuclear radiation, overpressure, and engine response.

2.1 OPERATION

For the low yield devices tested during Operation Plumbbob, nuclear radiation was the most critical effect limiting the choice of positions for the aircraft. Another limiting factor was the incomplete knowledge of the shock wave diffraction loading process. Therefore, test positions were selected to give the optimum thermal and blast response consistent with allowable nuclear radiation and aircraft structural limits. In most events, these positions were short of ground zero at time of detonation and directly over or slightly beyond ground zero at time of shock arrival.

2.1.1 Description of the A4D-1 Airplane. The Model A4D-1 airplane is a light weight, single place, single engine, modified delta wing, carrier-based attack aircraft with an intended capability for delivery of special weapons covering a wide range of weapon yields. Special weapons are carried externally on the fuselage centerline bomb rack. The power plant is a Wright J65-W-4 engine.

The A4D-1 aircraft has a limit load factor of 7 g at 12,500 pounds. For the weight at time of shock arrival, approximately 13,000 pounds, the allowable load factor is 6.75 g.

The thinner skin thicknesses on the lower surface of the airplane which are exposed to thermal radiation are listed below. All these skins were 7075 ST.

Surface	Skin Thickness (inches)
Landing flap	0.032
Aileron	0.020
Wing leading edge	0.032
Wing tip	0.032
Gun access door	0.025
Elevator	0.032
Rudder	0.020
After fuselage	0.025

The aircraft were painted white on the lower surfaces of the wing, horizontal stabilizer, and fuselage, and gull gray on the sides and top of the fuselage, sides of the vertical, and upper surfaces of the wing and horizontal stabilizer. After Shot Boltzmann the lower surface of the flap was changed to gray. The white areas were painted with insignia gloss white acrylic lacquer, Mil Spec MIL-L-19537; the gray areas with light gull gray acrylic lacquer, Mil Spec MIL-L-19538.

The leading edges of the wing and horizontal tail of production A4D-1 aircraft are coated with light gull gray Type 121 CORA-GARD. This material extends approximately 3 inches aft of the leading edge on both the upper and lower surfaces. Laboratory experiments had indicated that the surface erupts in small bubbles at approximately 370F. Further heat causes the paint to burn and separate from the surface. For the most severe case during Operation Plumbbob, the predicted temperature of the leading edge of the horizontal stabilizer was in excess of 370F. For this reason the gray CORA-GARD on the test aircraft was replaced with white CORA-GARD (Minnesota Mining and Manufacturing Company experimental X-649002) except for a small strip near the tip of the horizontal stabilizer which was left for assessment of damage to the gray CORA-GARD.

The large blue and red insignia on the lower surface of the right-hand wing was relocated so that it covered only 0.062 inch skin. If the insignia had not been relocated, excessive temperatures could have been experienced in areas where the dark paint covered 0.032 skin.

2.1.2 Shot Participation. The A4D-1 aircraft (Project 5.4) participated during seven shots: Boltzmann, Priscilla, Hood, Diablo, Shasta, Doppler, and Smoky. Participation was also scheduled for Shots Stokes and Kepler; however, radar jamming during Shot Kepler and radar malfunction during Shot Stokes resulted in aborted missions.

2.1.3 Criteria for Selecting Desired Aircraft Positions. The desired aircraft positions were selected so that if possible errors in aircraft positions and predicted weapon inputs accumulated, the effects would not exceed a 450F temperature rise, a nuclear radiation of 5 rem, an overpressure of 1.5 psi, and a wing root bending moment of 2.9×10^6 in.-lb.

2.1.4 Positioning of Aircraft for Test. For all tests the aircraft were piloted and flown on a straight and level course directly over ground zero.

Because of incomplete knowledge of the diffraction type loading expected, one A4D-1 was positioned for relatively low inputs during the first participation, Shot Boltzmann. The same angle of incidence planned for Shot Priscilla was chosen to provide an empirical basis for verifying the predicted response to the larger blast inputs desired in Shot Priscilla.

For Shot Priscilla, one aircraft was positioned over the top of the burst and slightly beyond ground zero at shock arrival. Although it had originally been planned for both aircraft to participate during Shot Priscilla, positioning radar was available for only one.

Shot Hood was the highest yield shot in which the A4D-1 participated. Both aircraft were scheduled to participate, but difficulties with the positioning radar resulted in the abort of the aircraft scheduled for low-angle thermal effects. The other was positioned to obtain gust response at a relatively low incidence angle.

For Shot Diablo, one A4D-1 was positioned to be directly over the burst at shock arrival to maximize diffraction and gust loading.

Shot Shasta was similar to Shot Diablo. BuNo. 137831 was positioned directly over the burst at shock arrival to compare data with that obtained by BuNo. 137827 in Shot Diablo under similar conditions.

Shot Doppler was detonated at a relatively high scaled height of burst. Therefore, the location of the triple-point path permitted positioning at an incidence angle of 45 degrees and inside the triple-point path at the time of shock arrival. Both aircraft were positioned in formation, using the one available radar, to obtain wing pressure data at this angle.

During Shot Smoky, the aircraft was positioned outside the triple-point path and received the gust at an angle of 31 degrees to the fuselage reference line.

2.1.5 Positioning System. The A4D-1 was positioned with a modified M-33 gun-tracking radar. This equipment utilized a plotting board with a pen recorder for tracking. The desired pattern was drawn to scale; a controller compared the actual position with the desired position and transmitted corrections to the pilot by UHF radio. A computer was designed for the M-33 radar which solved the positioning problem during the 5 minutes prior to time zero. The computer solution was presented to the controller as errors in time and aircraft velocity. An electric pen recorder system was installed to provide azimuth, range, and elevation for after-the-fact position data. This recording system included a time-zero signal from a blue box circuit and continuous 1-second timing marks. Time of shock arrival used to determine after-the-fact position was obtained from instrumentation in the aircraft. The accuracy of after-the-fact positions was determined to be approximately ± 200 feet.

The normal A4D-1 participation flight consisted of takeoff at H - 39 minutes, pattern entry at H - 31 minutes, two practice orbits around a race track pattern approximately 35 naut mi in length, a final run-in over ground zero from H - 5 minutes, and landing at H + 10 minutes.

2.2 INSTRUMENTATION

The instrumentation installed in the A4D-1 aircraft to record weapon effects and aircraft response is summarized in this section. A detailed description of the instrumentation is presented in Appendix A. The instrumentation was installed by the Douglas Aircraft Company prior to delivery of the aircraft to the Naval Air Special Weapons Facility (NASWF).

2.2.1 Installation. The small physical size of the A4D-1 aircraft imposed definite limitations as to the size, shape, and location of the extensive instrumentation required. To alleviate the critical internal space situation, it was necessary to install the majority of the data-recording equipment in a modified, external 300-gallon fuel tank which was carried on the centerline bomb rack station. The remaining instrumentation was divided between the nose compartment and the space normally occupied by the guns and ammunition boxes.

The basic recording equipment consisted of one 36- and one 50-channel oscillograph installed in the 300-gallon external fuel tank; an additional 18-channel oscillograph and a photo panel recorder system were installed in the aircraft nose section. The number of thermocouples, strain gages, pressure transducers, and other instruments exceeded the total number of available recording channels. Therefore, the instrumentation was designed to permit selection at the test site of the information to be recorded.

The electronic equipment normally installed in the nose section was deleted or moved to other locations. The APX-6 (IFF) installation was moved aft in the fuselage.

2.2.2 Scope of Instrumentation. The aircraft were instrumented with pressure transducers to measure the pressure distribution on the top and bottom of the wing during blast loading.

Instrumentation was installed to record the time history of the overpressure pulse, the primary instrument being a pressure transducer located in the nose boom. Two additional pressure transducers were mounted, one on each side of the fuselage just forward of and above the speed brakes.

Structural response to symmetrical gusts was measured by systems of electrical strain gages located on the wing, the horizontal stabilizer, and the fuselage keels. Other instruments installed for measurement of gust response were: (1) normal accelerometer at center of gravity, (2) normal accelerometer in tail, (3) aircraft attitude gyro, (4) pitch rate gyro, and (5) fuel quantity gages for determining airplane weight and center of gravity.

Thermocouples were installed to measure the temperature of various critical aircraft surfaces. The amount of aerodynamic cooling in thin skins of the aileron and flap was investigated by the comparison of the temperature readings of quartz-covered thermocouples with those of uncovered thermocouples at the same location.

For the purpose of evaluating thermal effects on the aircraft, two calorimeters and a radiometer were installed in the instrumentation store to measure the radiant exposure and

irradiance. Two calorimeters were also installed in the nose section to measure scattered radiation. The thermal instruments mounted in the instrumentation store were pointed vertically downward with respect to the centerline of the aircraft and therefore measured only the vertical component of the thermal radiation. All radiometers and calorimeters were supplied and calibrated by the Naval Radiological Defense Laboratory (NRDL). Furthermore, all data recorded by these thermal instruments was reduced by NRDL.

Two gun-sight-aiming-point (GSAP) cameras were installed in the forward portion of the instrumentation store to provide a view of the terrain and any cloud cover in the field of view of the vertical thermal instruments.

Theoretical analysis and the results of previous nuclear weapon tests indicated that no detrimental engine effects would be experienced during shot participations; however, a limited amount of instrumentation was installed on the engine for the purpose of confirming this.

Nuclear radiation was measured by Landsverk dosimeters and by film badges. Four film badges were located in the bottom portion of the nose section, and six in the cockpit map case. Dosimeters with various ranges were located in the nose wheel door and in the leg pocket of the pilot's flight suit.

Special instrumentation was installed to measure such items as time of explosion, control surface position, time, outside air temperature, airspeed, altitude, compass heading, pitch attitude, and reference static pressure for overpressure transducers.

2.2.3 Data Recorded on Oscillographs. The following data was recorded on three oscillographs; one 50-channel, one 36-channel, and one 18-channel. The paper traveled through the 50-channel and 36-channel oscillographs at a speed of 40 in./sec. The paper speed was 20 in./sec for the 18-channel oscillograph.

1. Time zero (t_0), determined by a photoelectric cell.
2. Skin and structural temperatures and temperature rise (ΔT), measured by copper-constantan thermocouples.
3. Thermal irradiance (I) and radiant exposure (Q), measured by radiometers and calorimeters.
4. Free stream overpressure (ΔP), measured by pressure pickups mounted on the nose boom and each side of the fuselage.
5. Normal acceleration of the center of gravity and tail, measured by accelerometers.
6. Structural strain, measured by strain gages.
7. Aircraft pitch rate and attitude, measured by aircraft gyros.
8. Engine temperatures and pressures, measured by thermocouples and pressure transducers.
9. Stabilizer, elevator, and rudder positions, measured by selsyn type instruments.

2.2.4 Data Recorded on Photo Recorder. The following data in the photo recorder was presented on visual indicating instruments and photographed by a 35 mm camera:

1. airspeed
2. altitude
3. outside air temperature
4. stabilizer, elevator, and rudder positions
5. engine speed
6. normal acceleration
7. pitch attitude

2.2.5 Calibration. Standard procedures were used for the calibration of the oscillograph traces and the instruments located in the photorecorder. NRDL calibrated the calorimeters and radiometers. Standard thermocouple calibration curves were used in reducing the thermocouple data.

Standard procedures were used to convert the keel and wing strain-gage trace deflections to stress in psi. Since the keel member at the instrumented station had a simple angle cross section and was designed to take only axial load, the converted strain-gage values were used directly to indicate stress in the member. The strain gages installed on the wing were located

to measure strains in all the principal load paths. These stresses were combined by analytical methods and compared with inflight calibrations to obtain wing bending moments and shear and torsion loads. The calibrations consisted of recording strain-gage and acceleration data in controlled, steady-state maneuvers for which wing loading was known. Preliminary data reduction of the wing strain gages made use of the in-flight calibrations. Data for analysis and presentation in this report was based on combined analytical methods and laboratory calibration of the wing strain gages.

The horizontal stabilizer was calibrated in the laboratory prior to delivery of the aircraft. Calibration consisted of installation of strain gages at numerous locations on the structure; pure bending moments, pure shear loads, and pure torsion loads were then applied to the structure, and strain-gage responses were recorded. Using high-speed computing equipment, these responses were analyzed in all possible combinations and sorted to provide three bridge circuits responsive to bending moment, shear loading, and torsion loading, respectively.

The attach points between the stabilizer and the fuselage formed a determinate system. These points were also instrumented and laboratory calibrated to give the total stabilizer load.

2.2.6 Method of Instrumentation Operation. All instruments were checked prior to each shot. For the actual test the instrumentation was started at the time count 5 seconds prior to time zero. Data was continuously recorded until approximately 50 seconds after shock arrival. The oscillographs were calibrated when the instrumentation was turned on and off by introducing known resistances and voltages into the circuit of all the channels.

Chapter 3

SHOT PARTICIPATION, AIRCRAFT POSITIONS, AND FLIGHT ENVIRONMENTAL DATA

The results of the tests of Project 5.4 are presented in this and the following chapters. The chapters are organized to include data for a particular effect from representative shots. Because of the interdependence of the various parts of the data, such as the thermal input and temperature time history, the discussion of each phase immediately follows the presentation of results. This is done to maintain a logical progression and understanding of the interdependent factors.

3.1 SHOT PARTICIPATION

Table 3.1 is a summary of the test events in which the A4D-1 aircraft participated. All test detonations were conducted at the NTS.

3.2 AIRCRAFT POSITIONS AND FLIGHT ENVIRONMENTAL DATA

In understanding the level of the data obtained in these tests it must be appreciated that several factors can reduce the magnitude of the effects received. Test aircraft positions for a

TABLE 3.1 SUMMARY OF TEST EVENT INFORMATION

Shot	Yield*	Type	Burst Height	
			Above Terrain	Above Mean Sea Level
	kilotons		feet	feet
Boltzmann	11.5	Tower	500	4,743
Priscilla	36.6	Balloon	700	3,776
Hood	74.1	Balloon	1500	5,714
Diablo	18.7	Tower	500	4,969
Shasta	16.8	Tower	500	4,882
Doppler	10.7	Balloon	1500	5,686
Smoky	43.7	Tower	700	5,179

*Naval Air Special Weapons Facility Secret Restricted
Data letter A9, Serial 0042 dated 26 February 1958.

desired response level must be selected for a detonation of magnitude equal to the positioning yield, a magnitude that represents the highest probable yield of an experimental device. In addition, the test position must consider the maximum positioning errors possible. In actual test the yield variations and positioning errors may so combine, that the effects magnitudes are low indeed.

Tables 3.2 and 3.3 present the aircraft positions at time of explosion and shock arrival. The distances used in presenting the positions are defined in Figure 3.1. The flight and environmental parameters which are significant for the data analysis of the time of explosion and shock arrival are presented in Tables 3.4 and 3.5. For all test participations, the surface visibility was officially reported as unrestricted at time zero. There were no clouds at time zero except for Shot Boltzman for which official reports stated $\frac{4}{10}$ altocumulus and $\frac{1}{10}$ cirrus clouds.

TABLE 3.2 AIRCRAFT POSITIONS* AT TIME OF EXPLOSION

Shot Airplane Number	Boltzmann 137827	Priscilla 137827	Hood 137827	Diablo 137827	Shasta 137831	Doppler 137827	Doppler 137831	Smoky 137831
Slant range	13,620	12,189	13,525	10,840	10,191	9,750	9,863	11,858
Horizontal range	5,736	4,774	2,453	5,370	5,032	1,633	1,717	5,156
Altitude above burst	12,353	11,215	13,300	9,416	8,862	9,612	9,712	10,678
Altitude above terrain	12,853	11,915	14,800	9,916	9,362	11,112	11,212	11,378
Altitude above mean sea level	17,096	14,995	19,038	14,401	13,757	15,290	15,394	15,857
X distance	-5,733	-4,735	-2,285	-5,370	-5,030	1,632	1,717	†
Y distance	-198	-616	892	-22	-99	-59	-9	†

* All distances are in feet

† Data not available

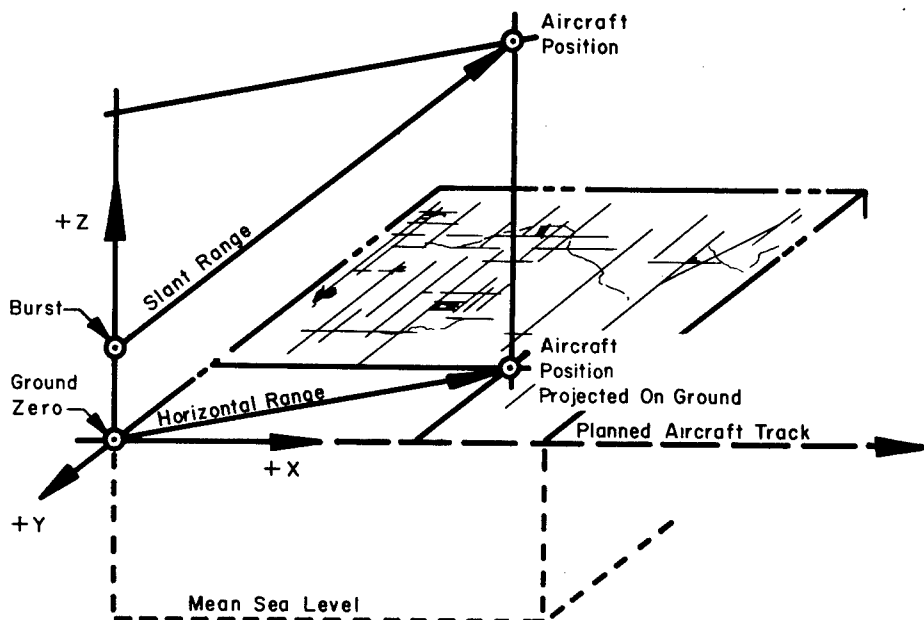


Figure 3.1 Definition of distances locating aircraft positions.

TABLE 3.3 AIRCRAFT POSITIONS* AT TIMES OF SHOCK ARRIVAL

Shot	Boltzmann	Priscilla	Hood	Diablo	Shasta	Doppler	Doppler	Smoky
Airplane Number	137827	137827	137827	137827	137831	137827	137831	137831
Time of first shock wave (seconds)	10.13	8.52	10.53	6.68	6.48	10.26	10.50	15.70
Slant range	12,499	11,442	14,330	9,275	9,094	13,202	13,575	20,386
Horizontal range	2,062	1,813	5,015	530	258	9,043	9,478	17,404
Altitude above burst	12,328	11,297	13,424	9,260	9,090	9,618	9,718	10,615
Altitude above terrain	12,828	11,997	14,924	9,760	9,590	11,118	11,218	11,315
Altitude above mean sea level	17,071	15,077	19,162	14,245	13,985	15,300	15,400	15,784
X distance	1,930	1,698	4,922	-523	-255	9,043	9,477	†
Y distance	-720	636	959	88	37	56	116	†
Time of second shock wave (seconds)	11.78	10.76	12.86	8.62	8.35	13.77	14.01	
Slant range	12,655	11,949	14,951	9,100	9,047	15,277	15,397	†
Horizontal range	3,072	3,533	6,522	962	850	11,974	12,048	
Altitude above burst	12,276	11,415	13,454	9,049	9,007	9,487	9,587	
Altitude above terrain	12,776	12,115	14,954	9,549	9,507	10,987	11,087	
Altitude above mean sea level	17,019	15,195	19,192	14,034	13,902	15,169	15,269	
X distance	3,030	3,453	6,483	962	826	11,973	12,045	
Y distance	-520	747	709	-21	201	199	249	
Time of third shock wave (seconds)								
Slant range			13.98					
Horizontal range			15,183					
Altitude above burst			7,109					
Altitude above terrain			13,416					
Altitude above mean sea level			14,916					
X distance			19,154					
Y distance			7,081					
			623					

*All distances are in feet

† Data not available

‡ Airplane beyond triple point path

TABLE 3.4 FLIGHT AND ENVIRONMENTAL PARAMETERS AT TIME OF EXPLOSION

Shot Airplane Number	Boltzmann 137827	Priscilla 137827	Hood 137827	Diablo 137827	Shasta 137831	Doppler 137827	Doppler 137831	Smoky 137831
Pressure alt. (ft)	16,780	*	18,340	13,740	13,090	14,350	14,350	15,410
Ambient air temp. (°R)	474	*	486	503	508	494	494	482
True airspeed (knots)	433	*	385	418	395	414	414	420
True airspeed (ft/sec)	731	*	650	706	667	700	700	709
Mach number	0.684	*	0.602	0.641	0.603	0.641	0.641	0.659
Ambient pressure (psf)	1,110	*	1,041	1,255	1,290	1,229	1,229	1,175
Ambient speed of sound (ft/sec)	1,063	*	1,080	1,100	1,102	1,090	1,090	1,075
Wind speed (knots)	25	6	15	8	12	7	7	11
Wind direction (deg.)	140	220	180	210	140	150	150	290
Ground speed (ft/sec)	748	*	674	718	682	707	707	703
Airplane weight (lb)	12,625	12,885	13,000	12,975	12,990	12,900	12,900	12,300
Fuel in wing (lb)	625	883	1,000	975	1,090	900	1,000	360
Fuel in fuselage (lb)	1,500	1,500	1,500	1,500	1,400	1,500	1,400	1,430
Center of gravity (% Mac)	19.75	20.25	20.15	20.45	20.48	20.3	20.3	19.1

* No data obtained because of photo recorder failure.

TABLE 3.5 FLIGHT AND ENVIRONMENTAL PARAMETERS AT TIME OF SHOCK ARRIVAL*

Shot Airplane Number	Boltzmann 137827	Priscilla 137827	Hood 137827	Diablo 137827	Shasta 137831	Doppler 137827	Doppler 137831	Smoky 137831
Pressure alt. (ft)	16,800	†	18,300	13,650	13,100	14,250	14,300	15,400
Ambient air temp. (°R)	474	†	486	503	508	494	494	482
True airspeed (knots)	436	†	387	421	392	416	417	421
True airspeed (ft/sec)	739	†	655	712	661	702	705	711
Mach number	0.692	†	0.605	0.647	0.600	0.644	0.647	0.661
Ambient pressure (psf)	1,110	†	1,041	1,260	1,290	1,230	1,230	1,175
Ambient speed of sound (ft/sec)	1,063	†	1,080	1,100	1,102	1,090	1,090	1,075
Ambient air	1.365	†	1.249	1.460	1.480	1.452	1.452	1.421
Density (slugs/ft ³)	$\times 10^{-3}$		$\times 10^{-3}$	$\times 10^{-3}$	$\times 10^{-3}$	$\times 10^{-3}$	$\times 10^{-3}$	$\times 10^{-3}$
Airplane weight (lb)	12,625	12,885	13,000	12,975	12,990	12,900	12,900	12,300

* Data apply to arrival of first, second, and third shock wave. After first shock wave pressure sensitive instruments are unreliable.

† No data obtained because of photo recorder failure.

Chapter 4

THERMAL INPUT DATA

The results of the thermal quantities as measured by the radiometers and calorimeters are presented in this section. The radiometers measured the rate of energy received as a function of time (irradiance) and the calorimeters measured the total thermal energy (radiant exposure) received with time.

In all cases, two calorimeters and one radiometer were pointed vertically downward so that they measured the vertical component of the total radiation. In addition, two calorimeters were mounted in the nose boom to measure any scattered radiation. One was pointed forward and up, and the other was aimed in a horizontal direction to the left of the airplane. Table 4.1 presents the maximum values of irradiance, radiant exposure, and the time to the second maximum irradiance for each shot.

4.1 SCATTERED RADIATION

The maximum value of scattered radiation recorded by the nose-boom mounted calorimeters for each shot participation is presented in Table 4.1. The scattered thermal radiation measured by the instrument directed overhead was less than 1 percent of the direct radiation. The values obtained by the instrument directed to the side varied from 1 to 4 percent of the vertical component of the direct radiation. The higher values obtained by the side-directed instrument could be caused by reflected energy from the terrain surface, as the field of view of this instrument would include some of the ground surface to the side of the airplane.

In these tests the aircraft were flying in clear cloudless sky during the release of the thermal energy. Therefore, although these data indicated that the amount of scattered radiation was negligible, it cannot be assumed that all atmospheres were zero scattering.

4.2 DISCUSSION OF RADIOMETER AND CALORIMETER MEASUREMENTS

The basic thermal input data is presented as irradiance versus time from radiometer measurements and radiant exposure versus time from the calorimeter measurements.

A pulse calculated from the normalized thermal pulse of Figure 2, Reference 5, is shown on each measured pulse to compare the irradiance versus time relationship. The normalized thermal pulse is in the form of I/I_{\max} versus t/t_{\max} and to use it for comparative purposes the I_{\max} and t_{\max} values must be defined. The t_{\max} was taken from the generally accepted equation of $t_{\max} = 0.032W^{1/2}$, where W is the total radio chemical yield. There is no generally accepted theory or expression for defining I_{\max} , so for the purpose of this comparison the calculated I_{\max} was taken as equal to the measured I_{\max} . Therefore, the peak irradiance values were the same for both the measured and calculated pulse, and a time dependent comparison was possible.

TABLE 4.1 MAXIMUM MEASURED IRRADIANCE AND RADIANT EXPOSURE

Shot Aircraft Number	Time to Maximum Irradiance	Maximum* Irradiance	Radiant* Exposure	Scattered Radiant Exposure	
				Up	Side
	sec	cal/cm ² -sec	cal/cm ²	cal/cm ²	
Boltzmann					
137827	0.19	3.92	2.65	<0.009	<0.07
Priscilla					
137827	0.23	14.50	10.13	<0.04	<0.14
Hood					
137827	0.29	14.07	12.85	<0.07	<0.16
Diablo					
137827	0.25	3.12	3.73	0	<0.07
Shasta					
137831	0.25	4.07	3.86	0	<0.13
Doppler					
137827	0.12	12.28	3.60	†	†
Doppler					
137831	0.12	11.43	3.72	<0.007	<0.07
Smoky					
137831	0.27	11.29	10.52	<0.03	<0.13

*Instruments pointed vertically downward.

† Instruments not installed.

For Shots Priscilla, Hood, and Doppler (Figures 4.2, 4.3, 4.6, and 4.7), it can be seen that the measured pulse agreed fairly well with the pulse calculated from the normalized curve, both in time to peak and general shape of the curve. However, for Shots Boltzmann, Diablo, Shasta, and Smoky (Figures 4.1, 4.4, 4.5, and 4.8), the pulses did not agree. The times to peak were much longer than would be expected, and the irradiance after the peak value was much higher than calculated. Shot Diablo had a particularly odd shaped pulse at times prior to the maximum irradiance. Although no definite reasons for the difference in pulse shape can be given, it is interesting to note that the pulses that did not agree with the normalized pulse were from tests in which it is believed the device was shielded. However, any definite conclusion of the effect of the shielding on the thermal pulse is beyond the scope of this project.

The measured radiant exposure versus time is presented for each shot in Figures 4.9 to 4.16. The values obtained by the nose calorimeters measuring the scattering radiation were so low that a complete time history was meaningless. So, only the maximum values are tabulated in Table 4.1. Also shown on the calorimeter data is the integration of the irradiance versus time pulse for each shot. Since the radiometer records rate-of-energy release, the integration with time should give the same values as recorded by the calorimeter. For Shots Priscilla, Shasta, and Doppler (Figures 4.10, 4.13, 4.14, and 4.15), the agreement of the integrated radiometer and the calorimeter was acceptable. However, Shots for Boltzmann, Diablo, and Smoky (Figures 4.9, 4.12, and 4.16), the integrated radiometer showed much less radiant exposure than recorded by the calorimeters. For Shot Hood the agreement was acceptable until approximately 3½ seconds. After this time the integrated radiometer reached a near constant value, but the measured radiant exposure continued to increase. The increase in the measured radiant exposure after this time was unusual, and no apparent reason can be found. In the radiant exposure and temperature correlation discussion, Shot Hood had the greatest discrepancy. These are the same shots where the measured thermal pulse was at the greatest variation from the normalized pulse. The reason for this discrepancy is not apparent; although, as pointed out in the discussion of the radiometer data, the shielding of the device may have affected the release of the thermal energy.

4.3 CORRELATION OF MEASURED AND CALCULATED RADIANT EXPOSURE

In computing the effect of the thermal energy on the temperature rise in the aircraft structure, one of the most important quantities was the total radiant exposure at the aircraft location. Although the rate of energy release as a function of time does affect the amount of cooling experienced by the surface, this effect is minor for relatively low-yield weapons.

The correlation of the calculated and measured radiant exposure is shown in Figure 4.17 for the methods of calculation presented in Section 1.3.1. It can be seen that the calculated value is consistently greater than the measured. Since the scattered radiation was found in all cases to be small, or negligible, the radiant exposure was calculated omitting the scattering term. This correlation is shown in Figure 4.18. The agreement is somewhat improved, although there is still some scatter between shots. An analysis of the calculations indicated that the factor for fireball distortion and orientation (K_1 factor) could be causing this scatter. Therefore, an additional check was made using the K_1 factor as 1.0. This comparison is shown in Figure 4.19. From this it can be seen that the agreement between shots is improved, particularly for Shots Doppler, Diablo, and Shasta, although in some cases the calculated value is now unconservative. The above suggestion of eliminating the fireball distortion and orientation angle correction factor to improve the correlation cannot be sufficiently justified at this time. However, it is a possibility that can be further checked from the results of Operation Hardtack, when the low orientation angle data will provide a larger range of this variable.

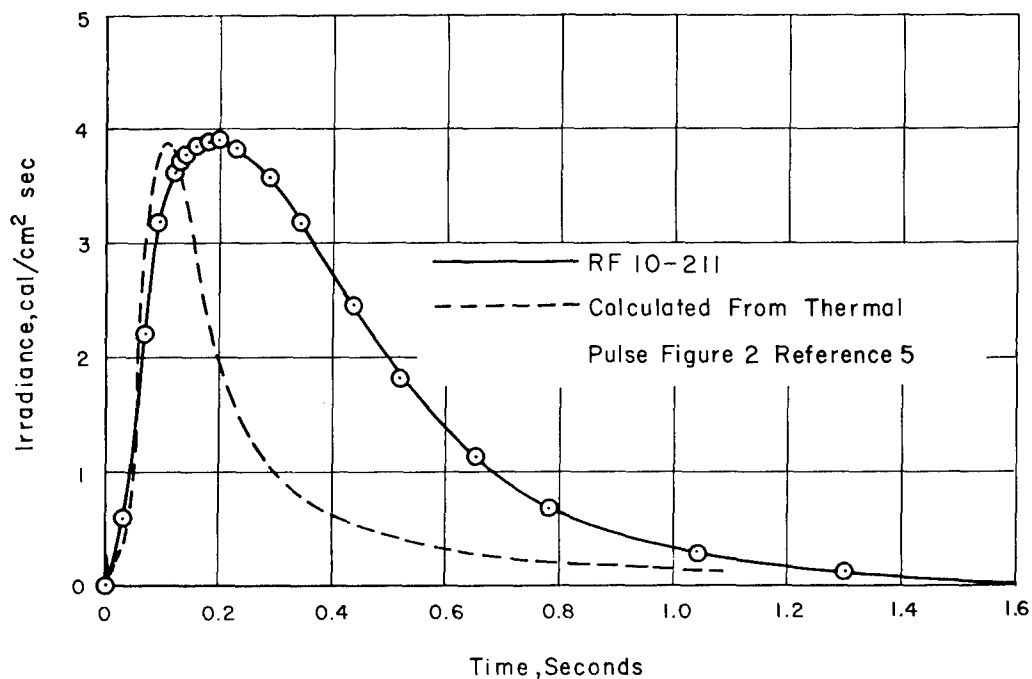


Figure 4.1 Thermal irradiance as a function of time, Shot Boltzmann.

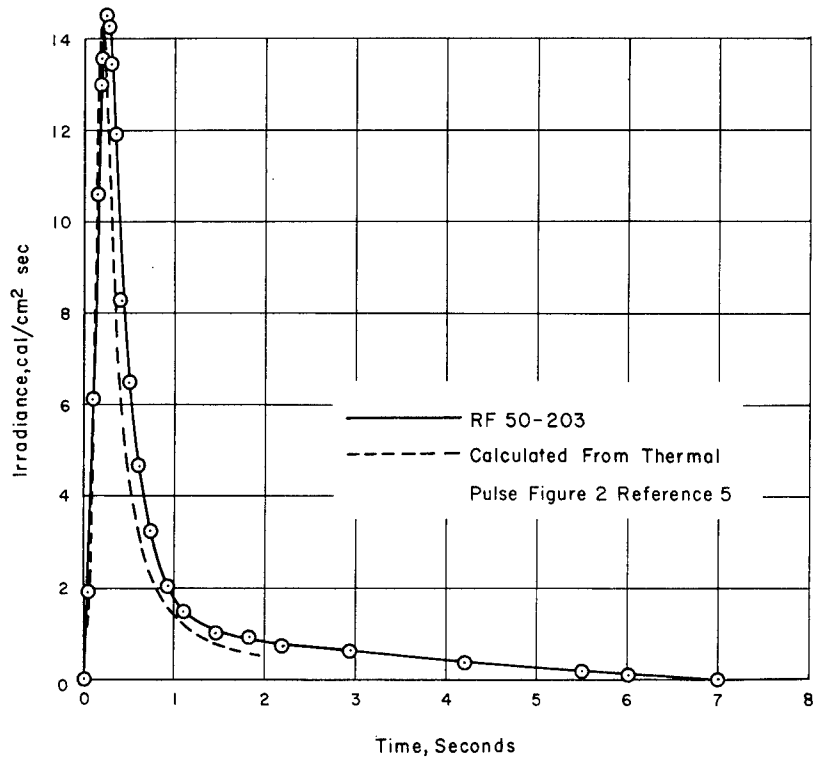


Figure 4.2 Thermal irradiance as a function of time, Shot Priscilla.

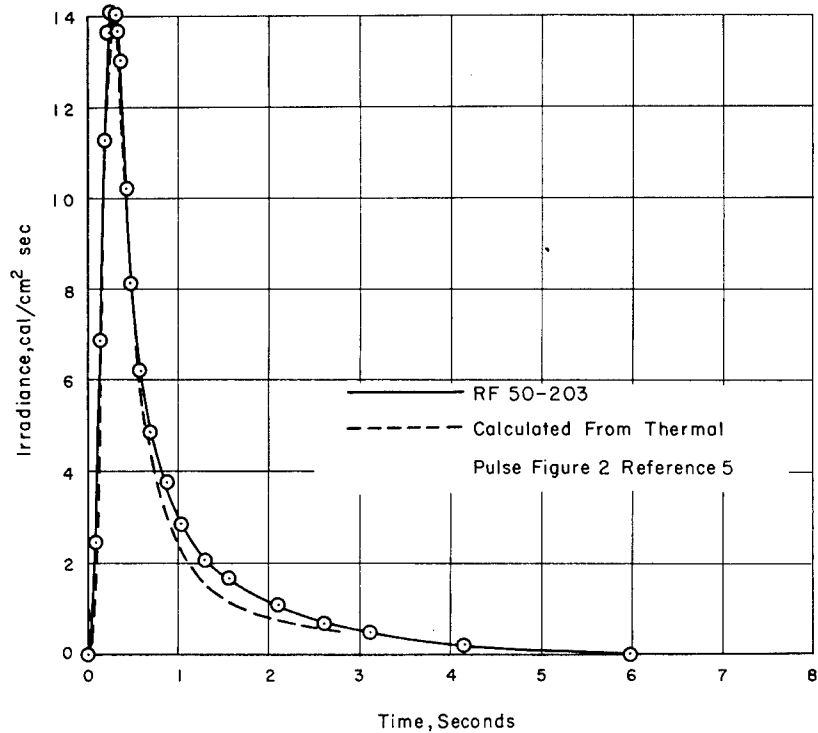


Figure 4.3 Thermal irradiance as a function of time, Shot Hood.

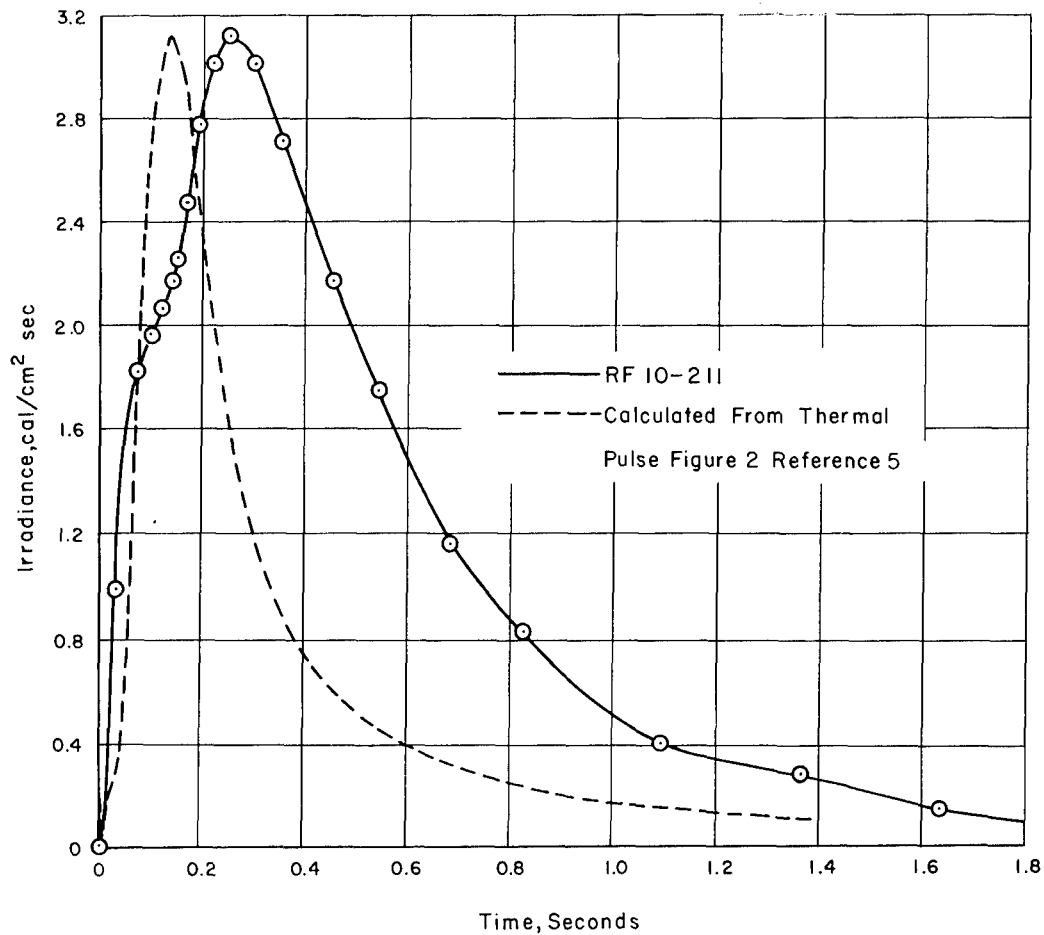


Figure 4.4 Thermal irradiance as a function of time, Shot Diablo.

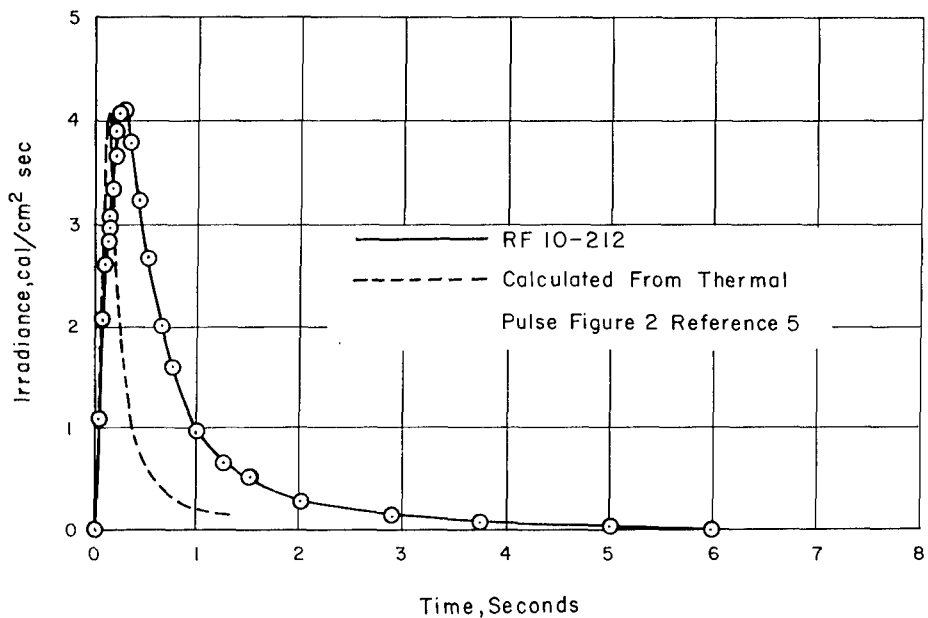


Figure 4.5 Thermal irradiance as a function of time, Shot Shasta.

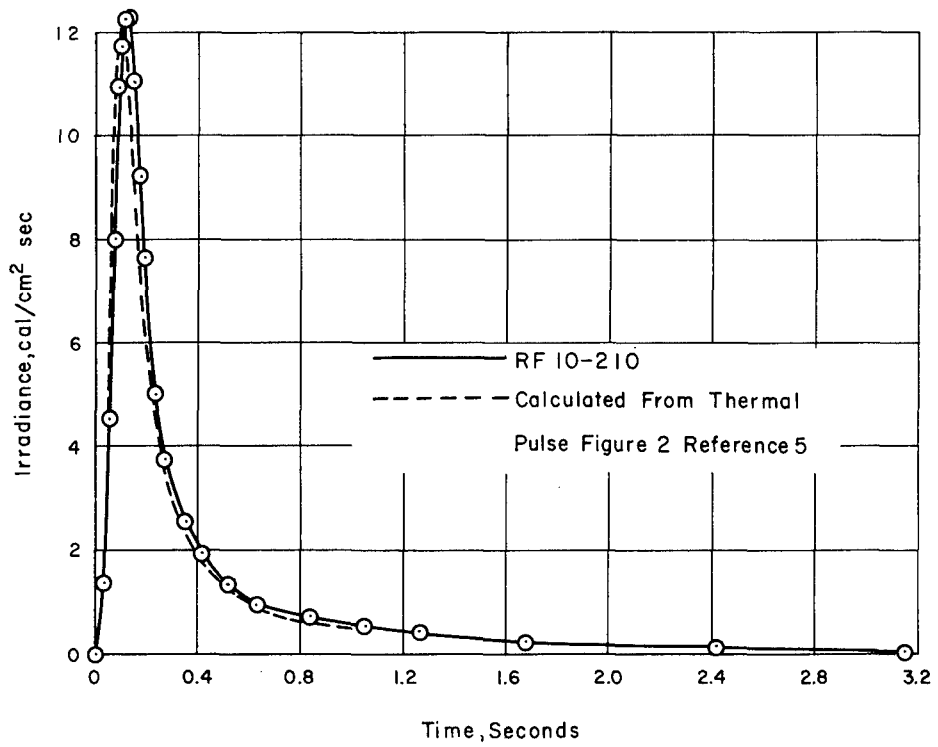


Figure 4.6 Thermal irradiance as a function of time, Shot Doppler, Airplane No. 137827.

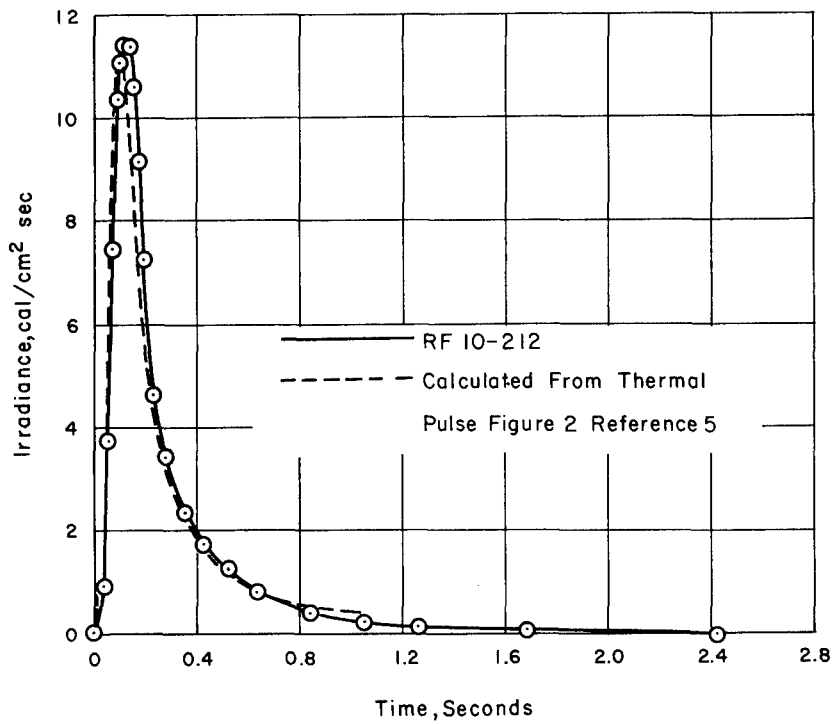


Figure 4.7 Thermal irradiance as a function of time, Shot Doppler, Airplane No. 137831.

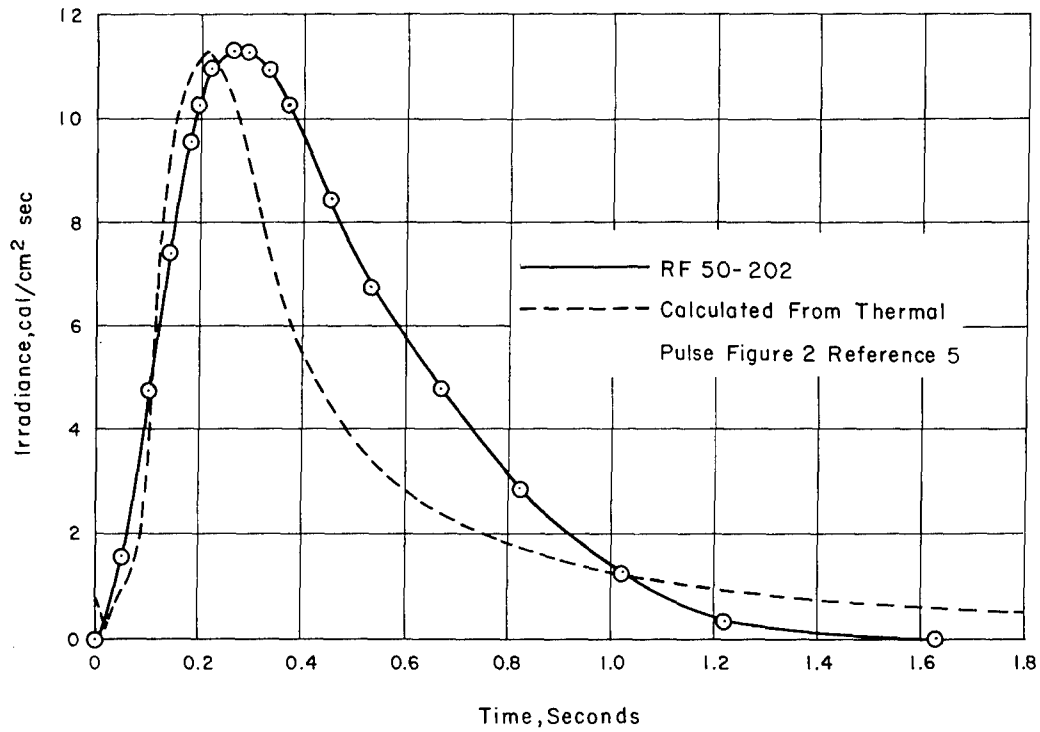


Figure 4.8 Thermal irradiance as a function of time, Shot Smoky.

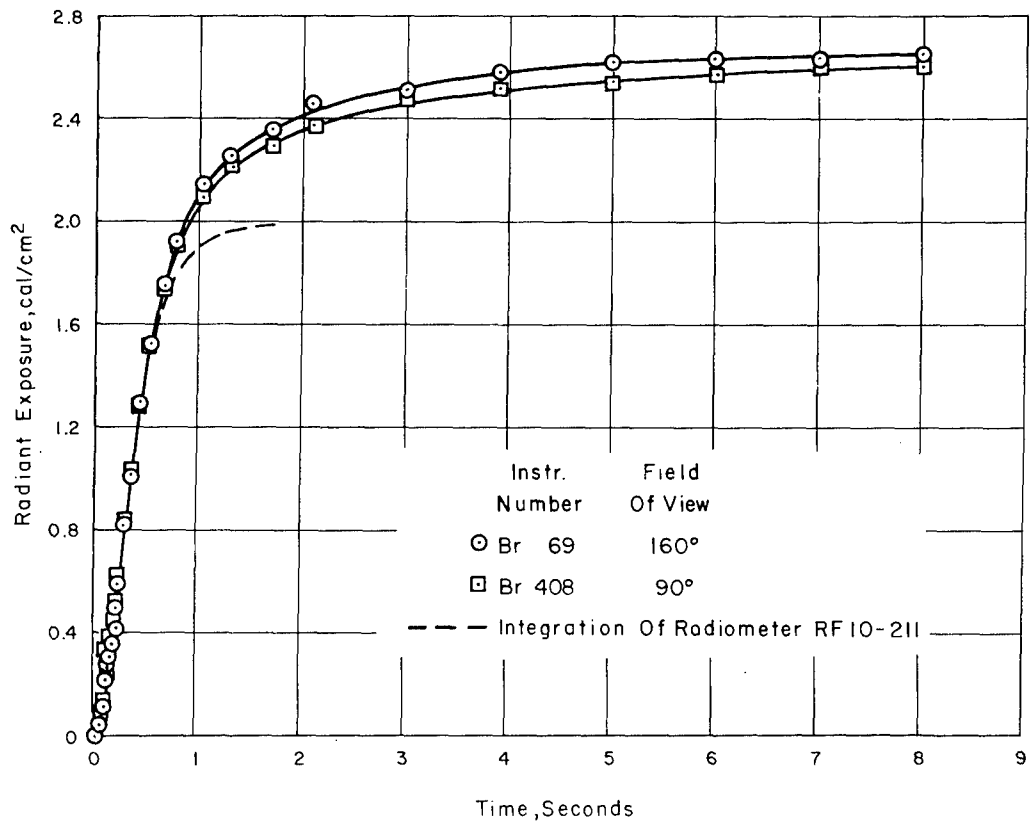


Figure 4.9 Radiant exposure as a function of time, Shot Boltzmann.

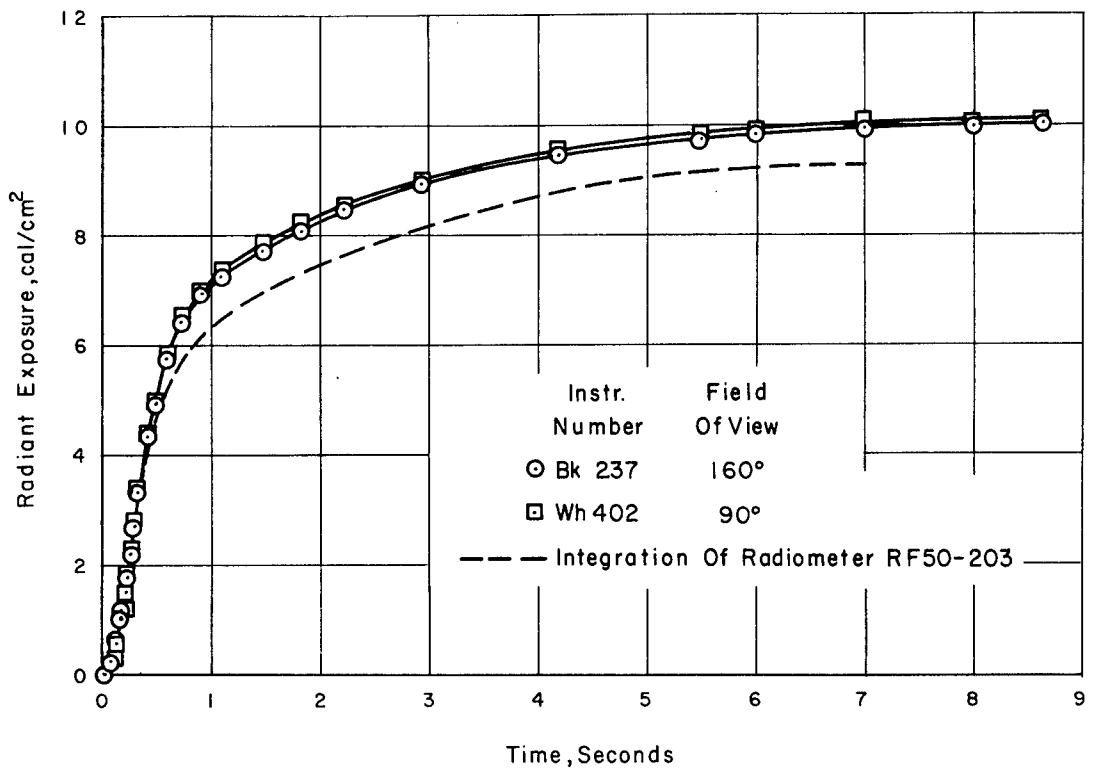


Figure 4.10 Radiant exposure as a function of time, Shot Priscilla.

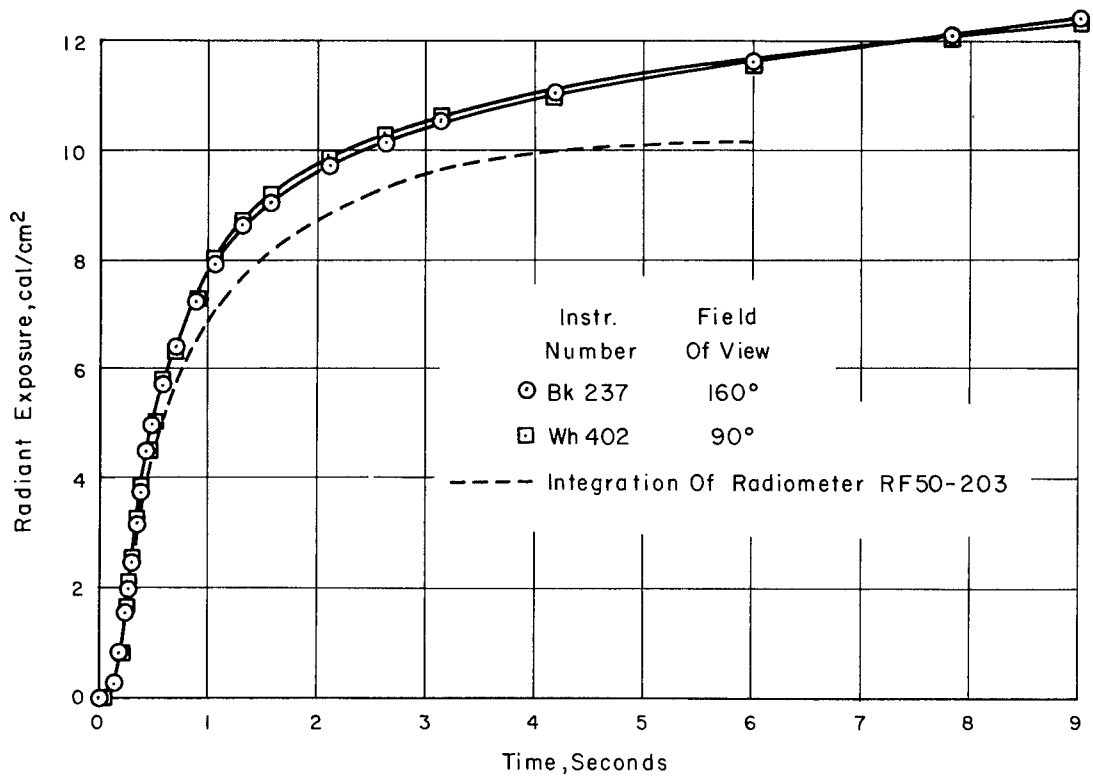


Figure 4.11 Radiant exposure as a function of time, Shot Hood.

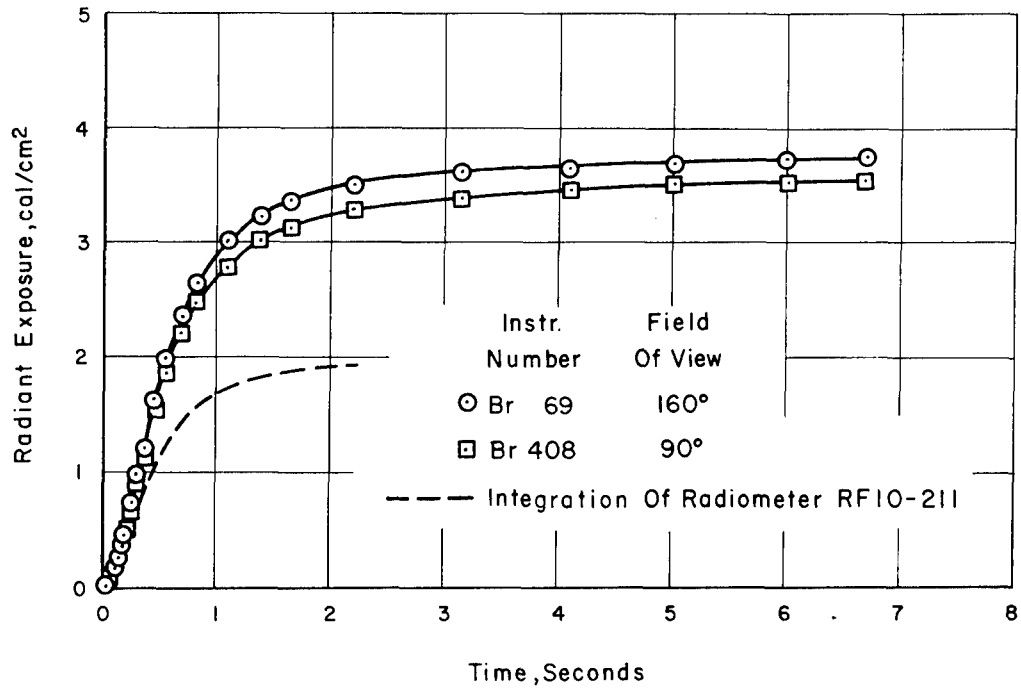


Figure 4.12 Radiant exposure as a function of time, Shot Diablo.

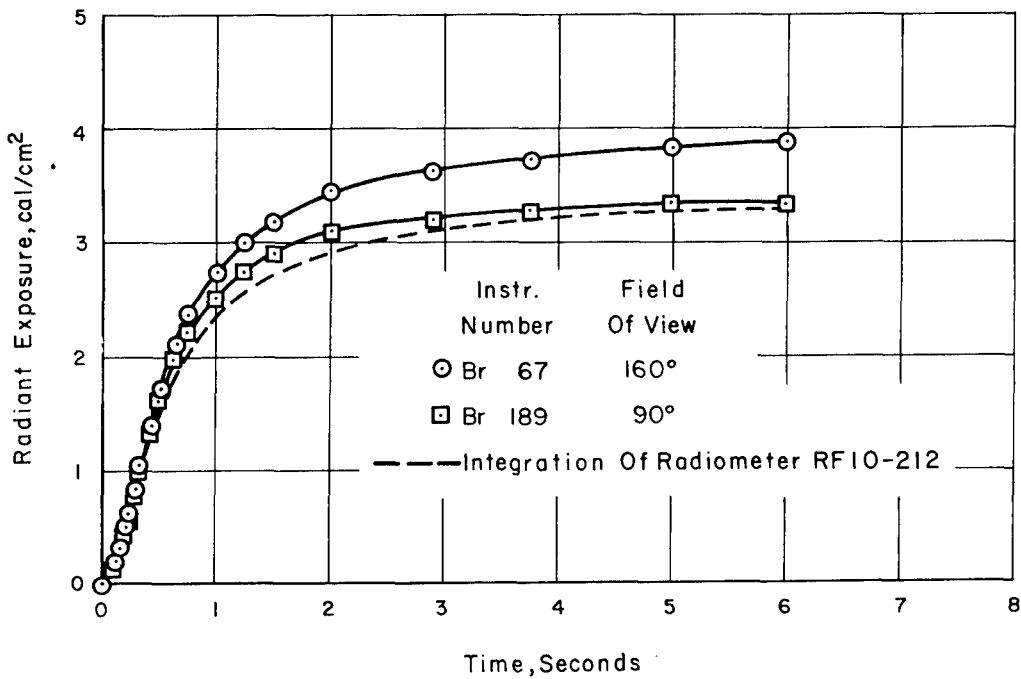


Figure 4.13 Radiant exposure as a function of time, Shot Shasta.

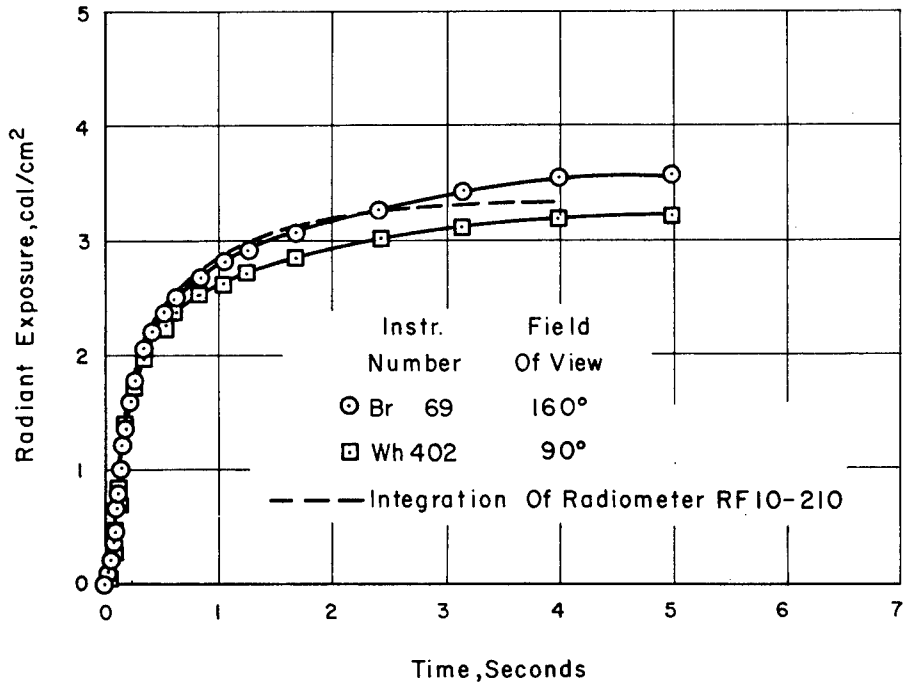


Figure 4.14 Radiant exposure as a function of time, Shot Doppler, Airplane No. 137827.

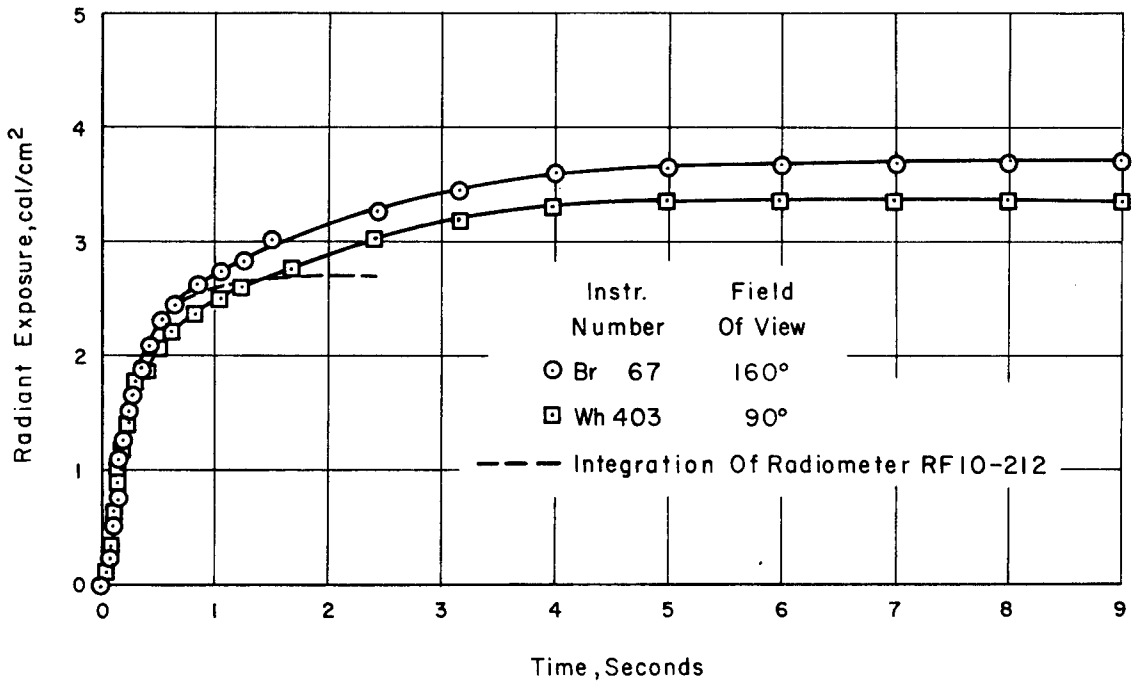


Figure 4.15 Radiant exposure as a function of time, Shot Doppler, Airplane No. 137831.

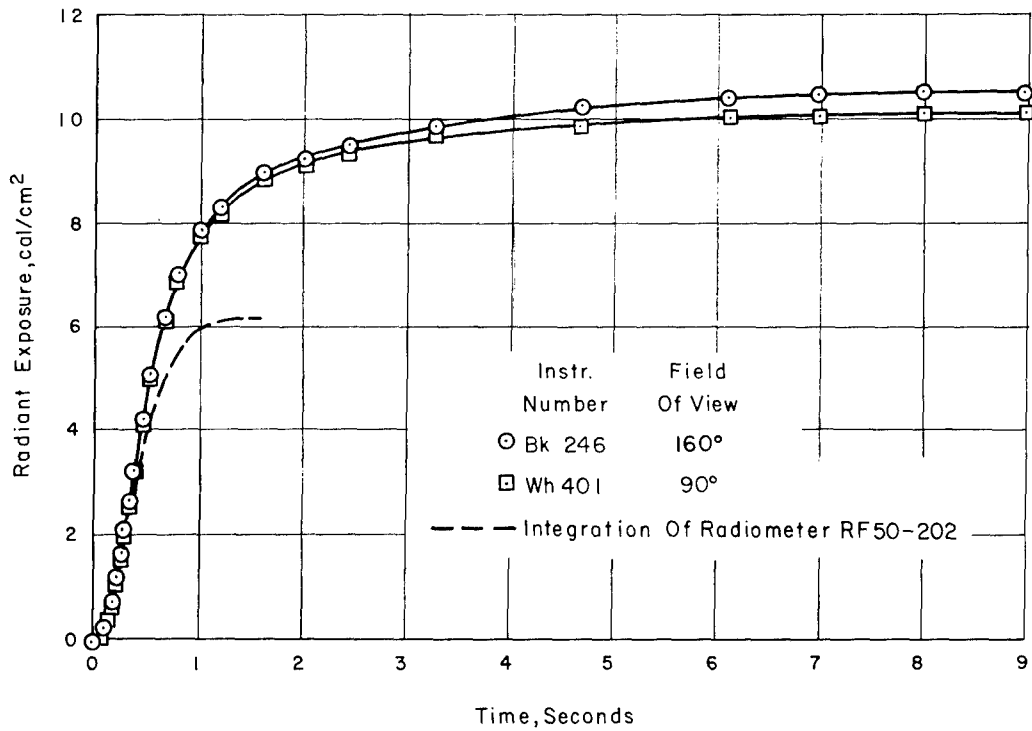


Figure 4.16 Radiant exposure as a function of time, Shot Smoky.

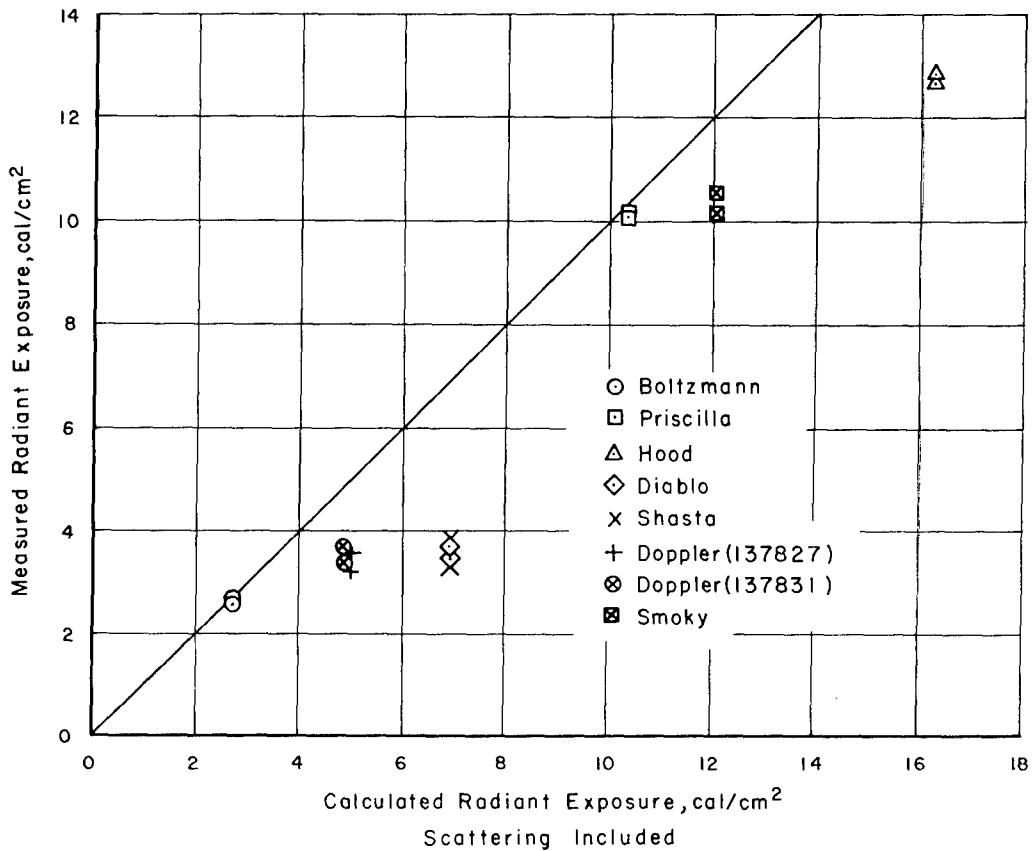


Figure 4.17 Correlation of measured and calculated radiant exposure, scattering included.

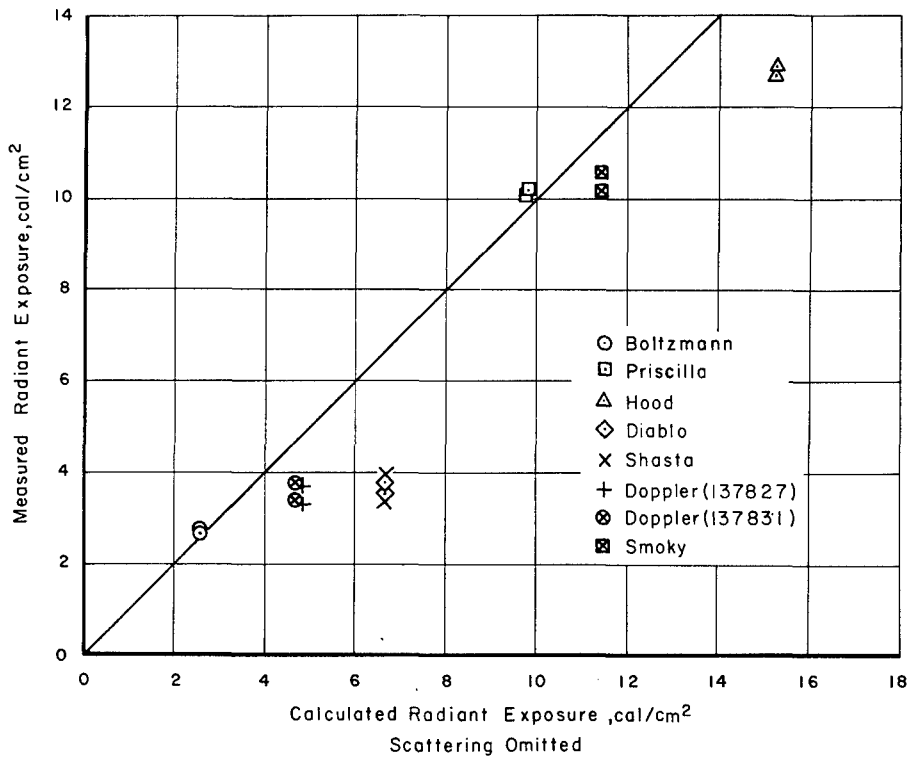


Figure 4.18 Correlation of measured and calculated radiant exposure, scattering omitted.

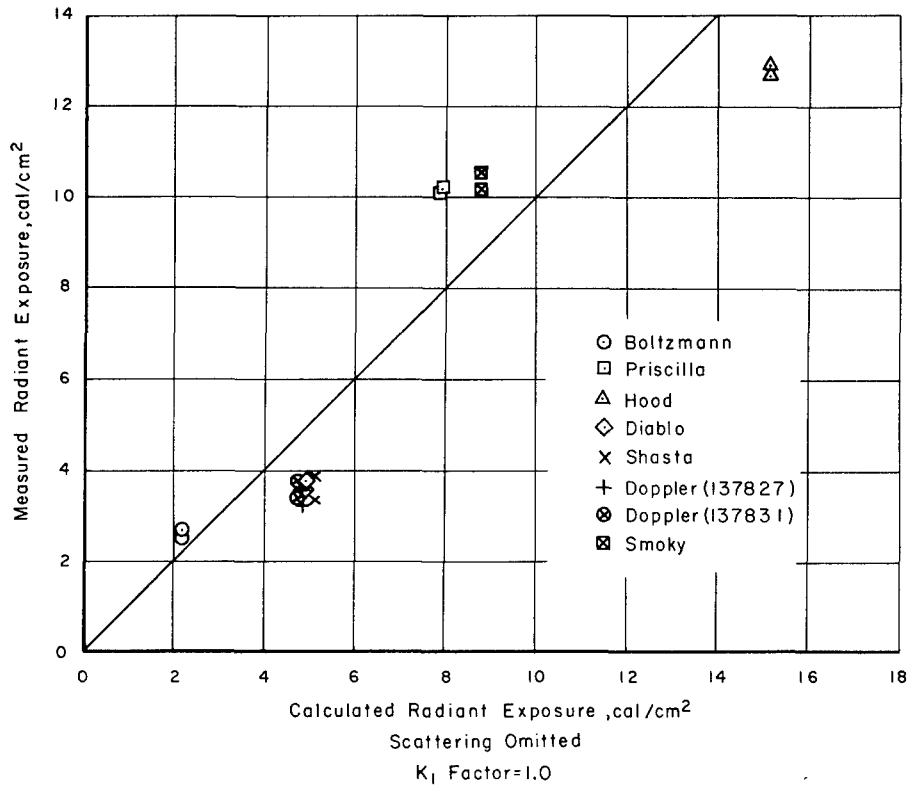


Figure 4.19 Correlation of measured and calculated radiant exposure, scattering omitted, K₁ = 1.0.

Chapter 5

STRUCTURAL TEMPERATURE MEASUREMENTS AND CORRELATION WITH CALCULATED VALUES

5.1 STRUCTURAL TEMPERATURE MEASUREMENTS

The temperature rises recorded at the various locations on the lower surface of the airplane are summarized in Table 5.1. The thermocouple locations and skin thickness at each position are shown in Figure A.1.

Table 5.1 presents only the maximum temperature rise at each thermocouple location. The measured temperature-time histories are shown in Figures 5.1 to 5.28, inclusive.

5.2 CORRELATION OF MEASURED AND CALCULATED MAXIMUM TEMPERATURE RISE

The correlation of the measured maximum temperature rise and the value calculated by Equation 1.2 is shown in Figure 5.29. It will be noted that the calculated temperature rise is consistently greater than the measured value. Since the scattered radiation was always negligible, one of the obvious means of improving the correlation was to eliminate the scattering term (Q_S/Q_I). As shown in Figure 5.30, this gave better correlation, but the calculated values were still conservative.

There were two components to consider in the calculation of temperature rises in the aircraft structure. One was computing the thermal input, or radiant exposure, and the other was converting the thermal energy into temperature in the skin. The agreement of the calculated and measured radiant exposure is discussed in Section 4.3. The calculated values are usually greater than measured. This would give a greater calculated temperature rise. To check the other phase of the calculation, the temperature rise has been computed from the measured radiant exposure. This correlation is shown in Figure 5.31 and indicates that the calculated values are usually conservative, with the agreement being much better than with the calculated radiant exposure. The correlation of Shot Hood is poor, but this is due to the uncertainty of the Shot Hood radiant exposure measurement. The calculation of the temperature rise from the measured radiant exposure was made from the following equation:

$$\Delta T = Q_M (1-H) a/G \quad (5.1)$$

where ΔT = temperature rise, °F
 Q_M = measured radiant exposure, cal/cm²
(1-H) = cooling factor
 a = absorptivity of surface
 G = thermal capacity of material, cal/cm²-°F

The cooling factor was taken from Reference 5 as the value with no flyaway correction. This was used since the measured radiant exposure included the effect of the moving aircraft.

TABLE 5.1 MAXIMUM TEMPERATURE RISE

Number	Thermocouple Location	Boltzmann 137827	Priscilla 137827	Hood 137827	Diablo 137827	Shasta 137831	Doppler 137827	Doppler 137831	Smoky 137831
1	LH gun access door	*							
2	RH wing, lower skin								
3	RH wing, lower skin								
4	RH aileron, lower	30.5	132.4		43.7	42.9	60.0	43.6	117.5
5	RH aileron, lower†		113.0	111.4	36.7	57.6	42.5		145.7
6	RH aileron, lower	27.7	126.5	133.8	42.9	85.4	55.5		
7	RH aileron, lower	7.4	120.2	126.1	44.1		50.1		122.7
8	RH flap, lower skin†		206.9	232.4	76.2	80.6	72.3	77.4	212.9
9	RH flap, lower skin		172.8	183.8	63.5	64.7	60.2	58.0	179.6
10	RH flap, lower skin		173.8	193.3	73.2	64.6	67.5	62.3	184.3
11	RH flap, lower skin		168.5	190.6	69.0		63.2		
12	Aft fuselage								
13	Aft fuselage					34.9		38.3	100.4
14	RH elevator, lower					30.3		29.7	84.9
15	RH elevator, lower								
16	RH elevator, lower					30.4		35.1	86.4
17	Rudder, RH side								
18	Rudder, LH side								

*Spaces left blank indicate data not measured.

†Quartz covered.

Examination of Equation 5.1 shows that the calculated temperature rise would be decreased if the thermal capacity of the material were increased. An increase does, in fact, exist because the mass and thermal capacity of the paint should be added to the mass and thermal capacity of the metal.

The total thermal capacity is given by the expression:

$$G = \rho_m CP_m t_m + \rho_p CP_p t_p$$

where G = total thermal capacity of metal and paint, cal/cm²-°F

ρ = density of material, gm/cm³

CP = specific heat, cal/gm-°F

t = thickness of material, cm

subscripts m = metal

p = paint

Laboratory tests were conducted to determine the characteristics of the paint and the results are reported in Reference 16. The pertinent quantities from this report are summarized in Table 5.2.

When the above values for the metal and paint are used, and the proper unit conversions are made, the expression for thermal capacity becomes:

for white paint, $G = 0.885 t_m + 0.720 t_p$, cal/cm²-°F

for gray paint, $G = 0.885 t_m + 0.725 t_p$, cal/cm²-°F

where t = skin or paint thickness, inches

The specification thickness for the paint is 0.002 inch; hence, the values of G were computed and are shown in Table 5.3 for the appropriate skin thickness and paint. The correlation of calculated and measured temperature rise using the measured radiant exposure and the combined thermal capacity of the aluminum skin and paint is shown in Figure 5.32. The agreement for these conditions is good with none of the shots deviating far from the line of complete agreement.

TABLE 5.2 DENSITY AND SPECIFIC HEAT OF PAINT

Paint	Density	Specific Heat
	lb/ft ³	Btu/lb-°F
MIL-L-19537 acrylic white lacquer	96.9	0.33
MIL-L-19538 acrylic Navy gray lacquer	100.5	0.32

TABLE 5.3 THERMAL CAPACITY OF AILERON AND FLAP

Surface	Skin Thickness	Thermal Capacity, cal/cm ² -°F	
		Neglecting Paint	Including Paint
	inches		
Aileron	0.020	1.77×10^{-2}	1.91×10^{-2}
Flap	0.032	2.83×10^{-2}	2.977×10^{-2}

From the above comparison, it appears that if the radiant exposure received by the airplane is known, the resulting temperature rise in the thin skin panels can be calculated with reasonable accuracy. Therefore, the main reason for the discrepancy between calculated and measured temperature rise is the inaccuracy in predicting the radiant exposure.

To summarize the results as indicated by the tests, it appeared that the assumed absorptivity of the paint was satisfactory, the thermal capacity of the paint should be included with that of the metal skin, and the cooling factor of Reference 5 gave a satisfactory correlation. The principal improvement of the maximum temperature rise calculation would be in increasing the accuracy of estimating the radiant exposure. Possible methods of accomplishing this have been discussed previously in Section 4.3, and the comments would also apply for the calculation of the maximum temperature rise.

5.3 QUARTZ-COVERED THERMOCOUPLES

An attempt was made to obtain the reduction in temperature because of aerodynamic cooling by comparing a quartz-covered insulated skin section with the adjacent uncovered skin. The ratio of the uncovered skin to the quartz-covered skin specimen would then give the cooling factor.

The accuracy of this method proved to be insufficient for any conclusion to be reached. During the tests the ratios of the temperature rises of the measured uncovered and quartz-covered skin samples varied from 0.749 to 0.844. The cooling factors estimated from Reference 5 varied from 0.908 to 0.957. This would seem to indicate that the estimated cooling factors of Reference 5 were too conservative. However, this discrepancy only represented a temperature difference of from 9 to 27F. Considering the possibility of accumulative reading errors for two thermocouples at both ambient and at maximum temperature rise conditions this discrepancy was within the accuracy of the data.

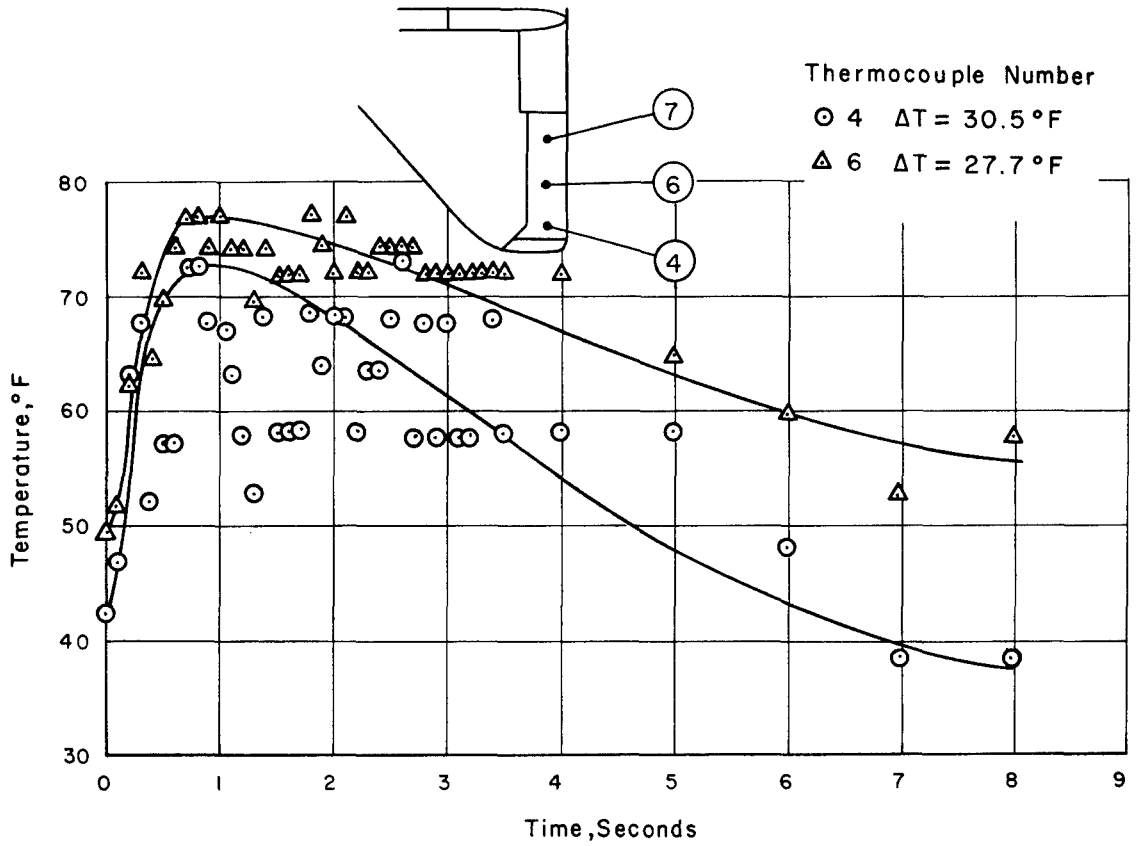


Figure 5.1 Temperature time history of aileron skin, Shot Boltzmann.

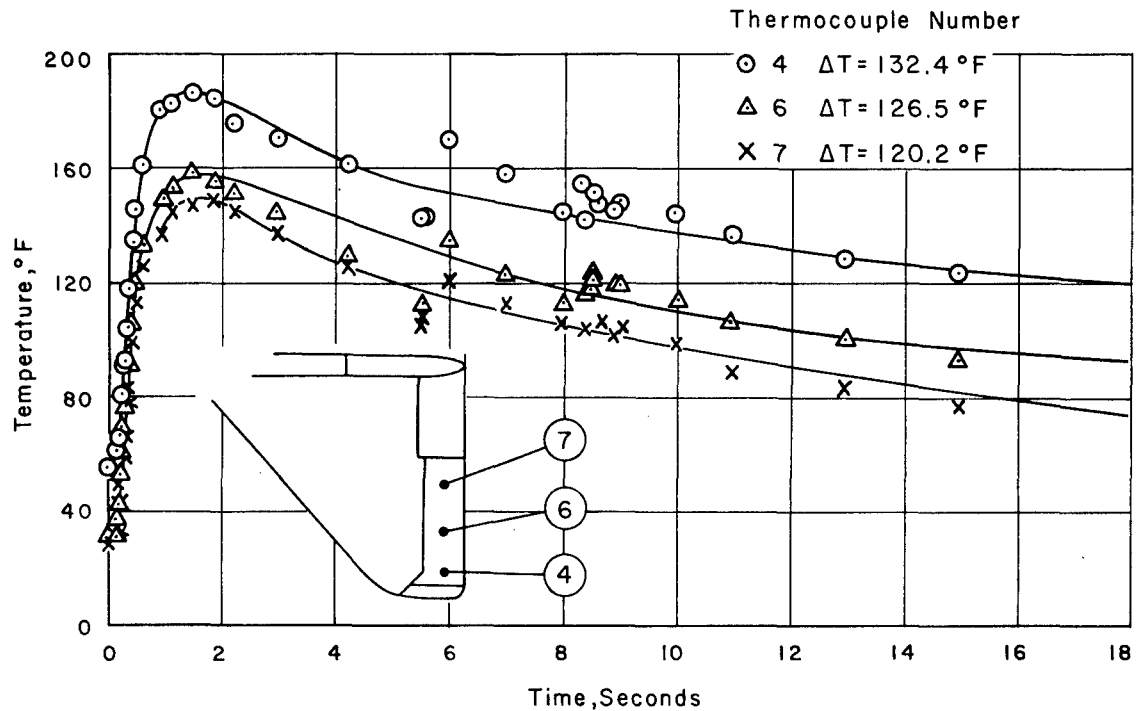


Figure 5.2 Temperature time history of aileron skin, Shot Priscilla.

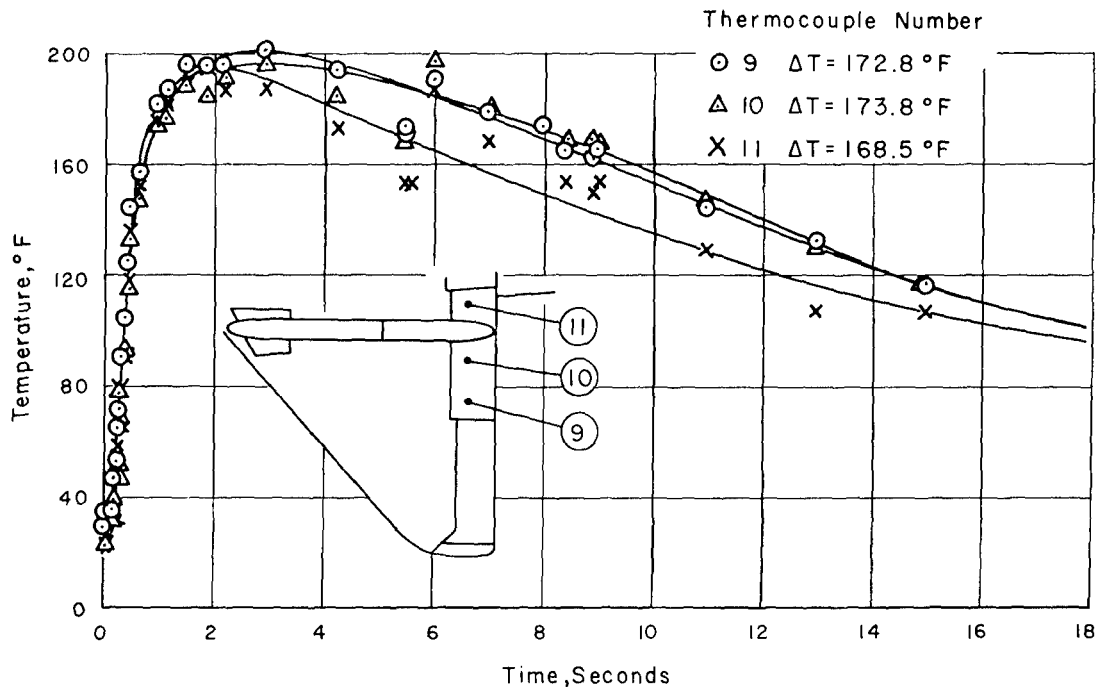


Figure 5.3 Temperature time history of flap skin, Shot Priscilla.

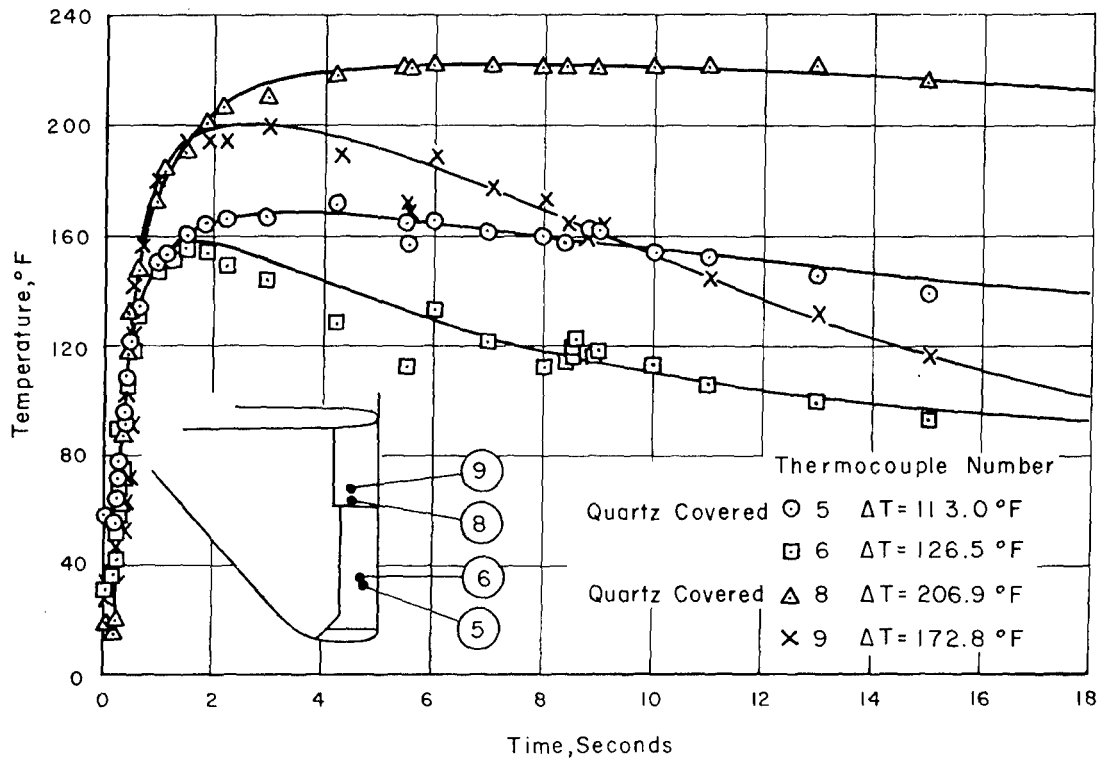


Figure 5.4 Temperature time history of quartz-covered thermocouples compared to adjacent uncovered thermocouples, Shot Priscilla.

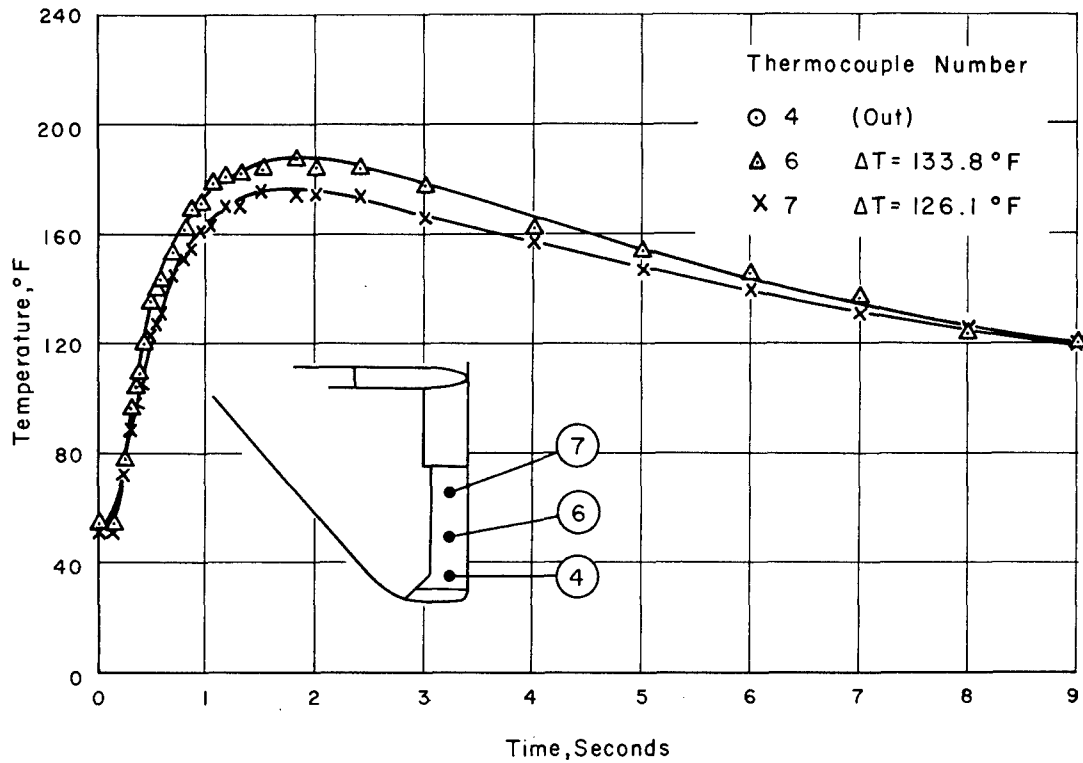


Figure 5.5 Temperature time history of aileron skin, Shot Hood.

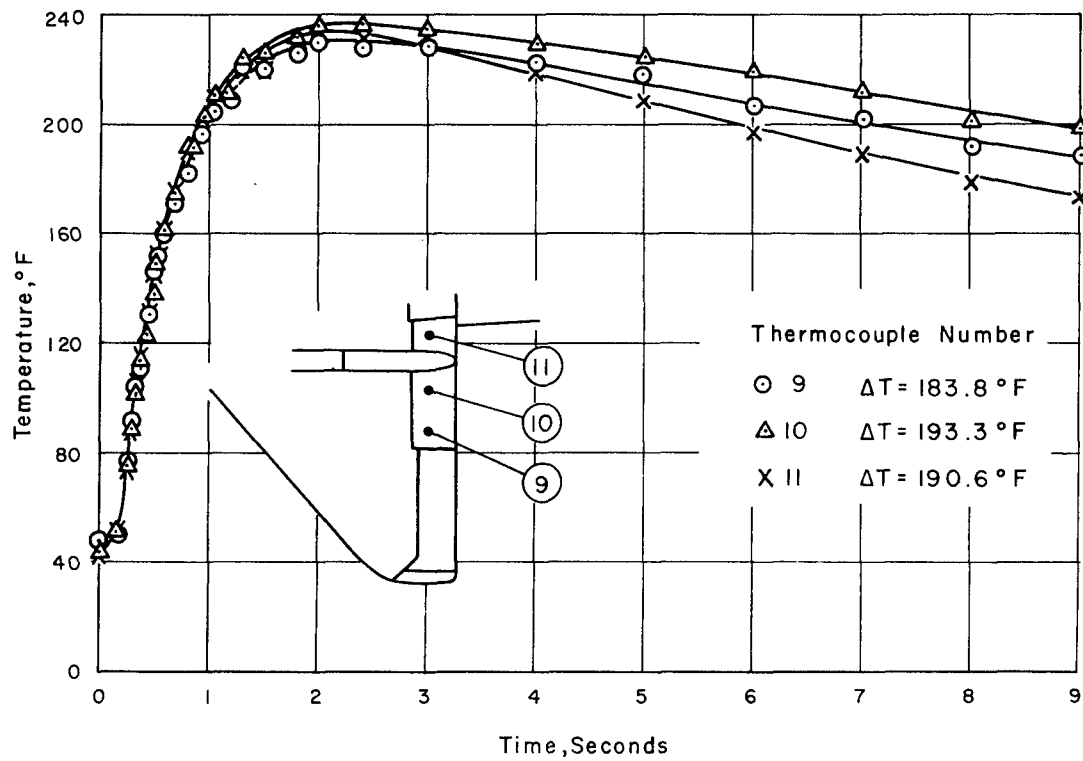


Figure 5.6 Temperature time history of flap skin, Shot Hood.

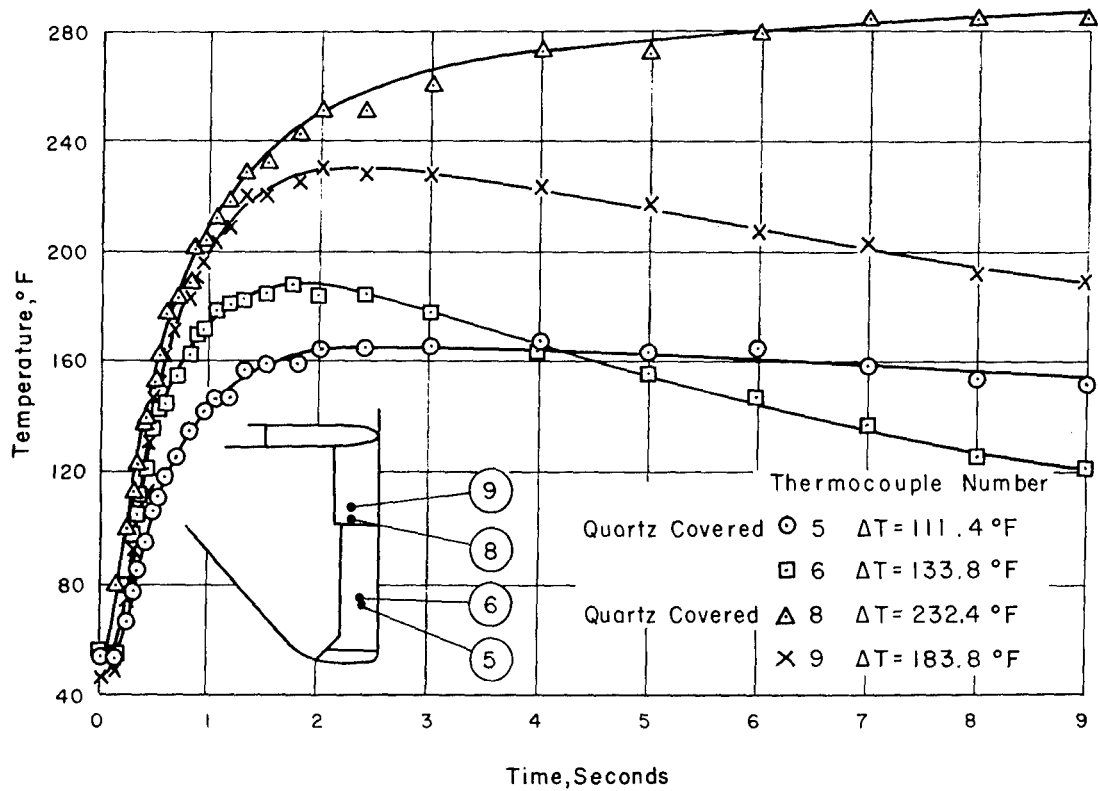


Figure 5.7 Temperature time history of quartz-covered thermocouples compared to adjacent uncovered thermocouples, Shot Hood.

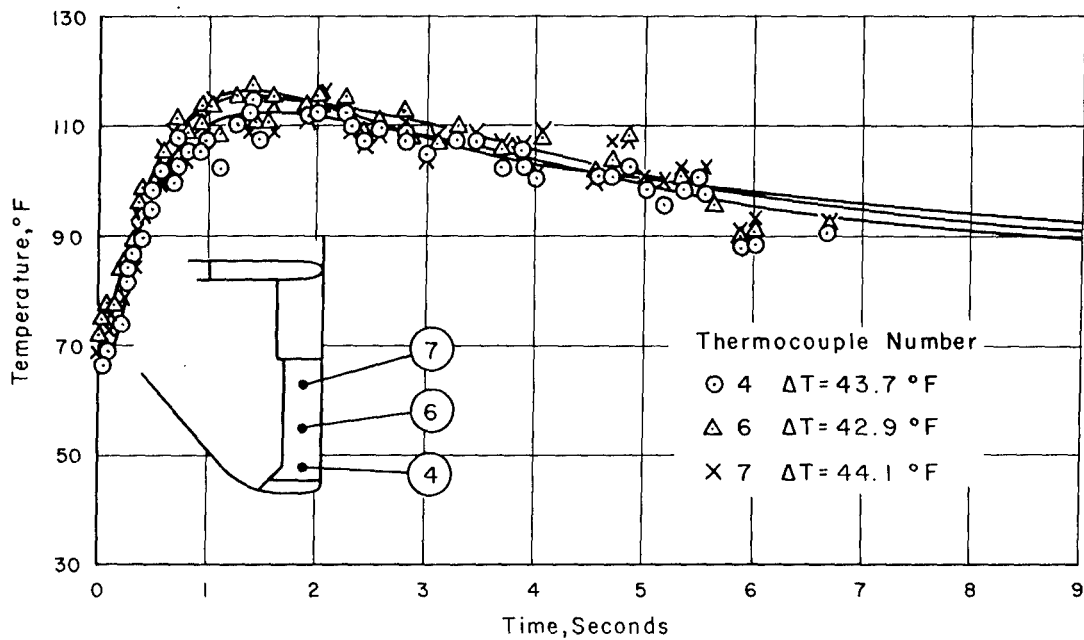


Figure 5.8 Temperature time history of aileron skin, Shot Diablo.

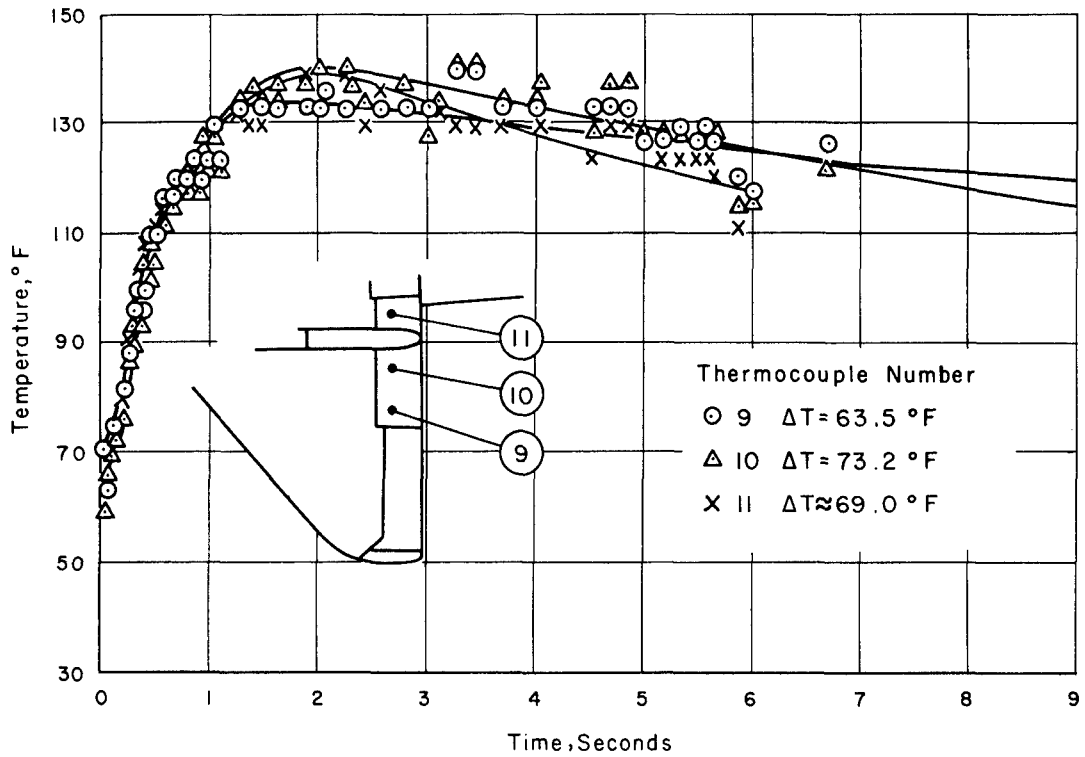


Figure 5.9 Temperature time history of flap skin, Shot Diablo.

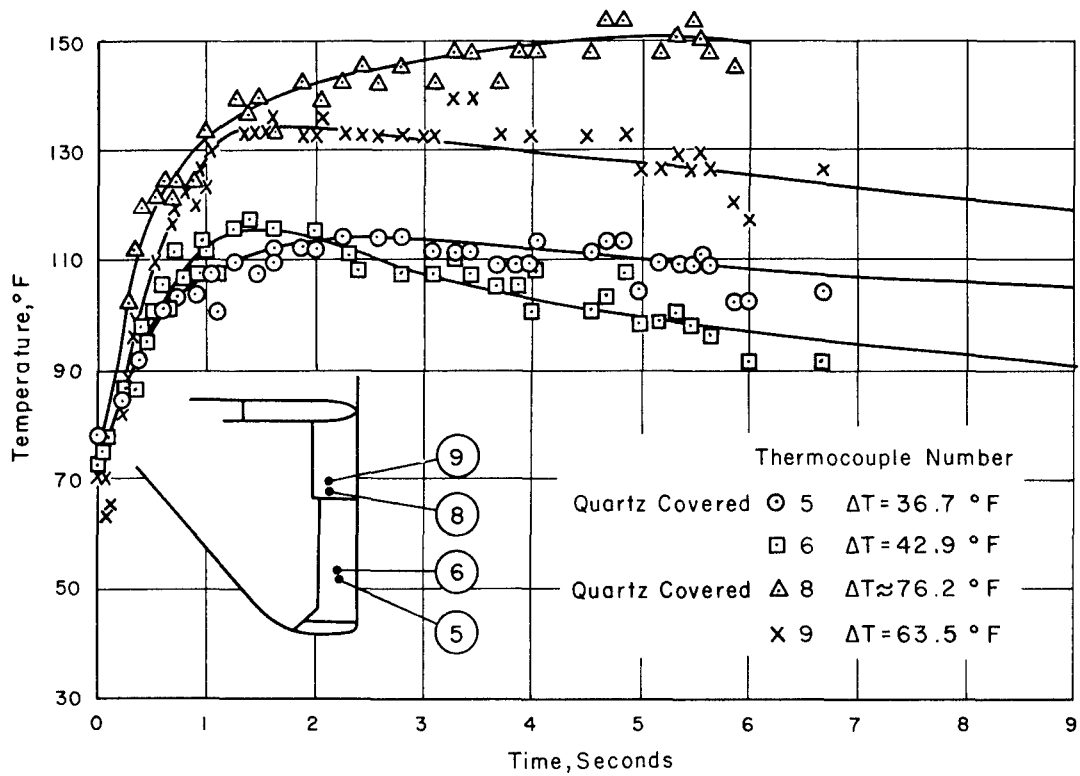


Figure 5.10 Temperature time history of quartz-covered thermocouples compared to adjacent uncovered thermocouples, Shot Diablo.

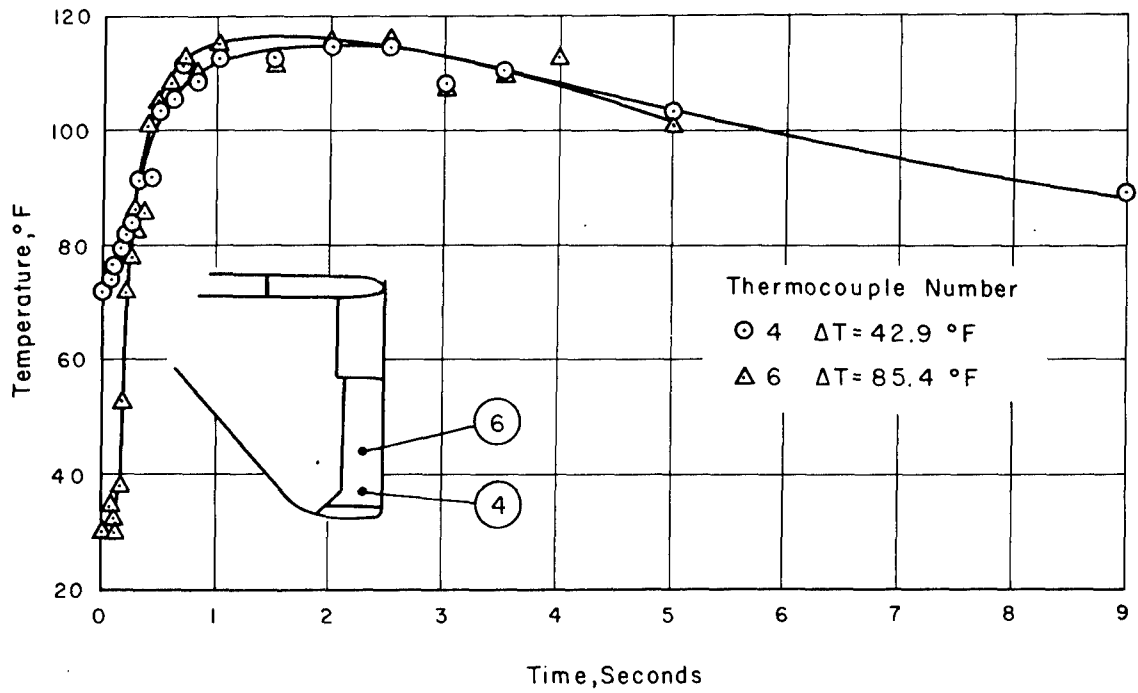


Figure 5.11 Temperature time history of aileron skin, Shot Shasta.

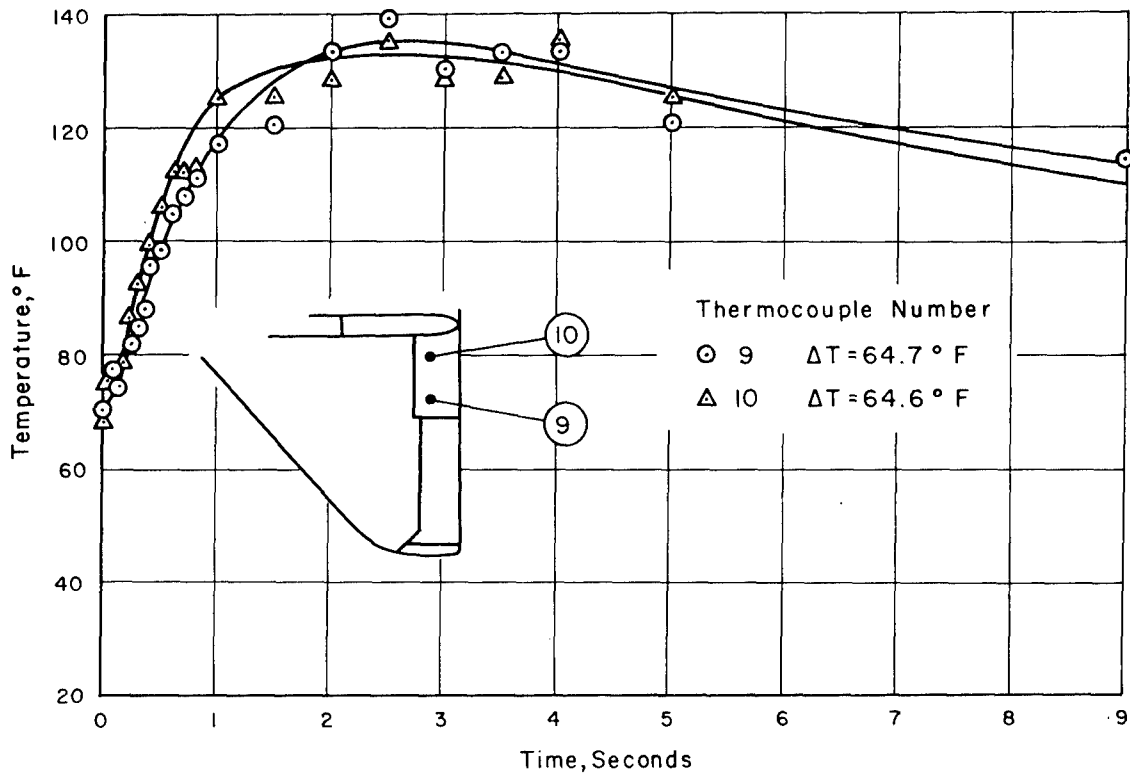


Figure 5.12 Temperature time history of flap skin, Shot Shasta.

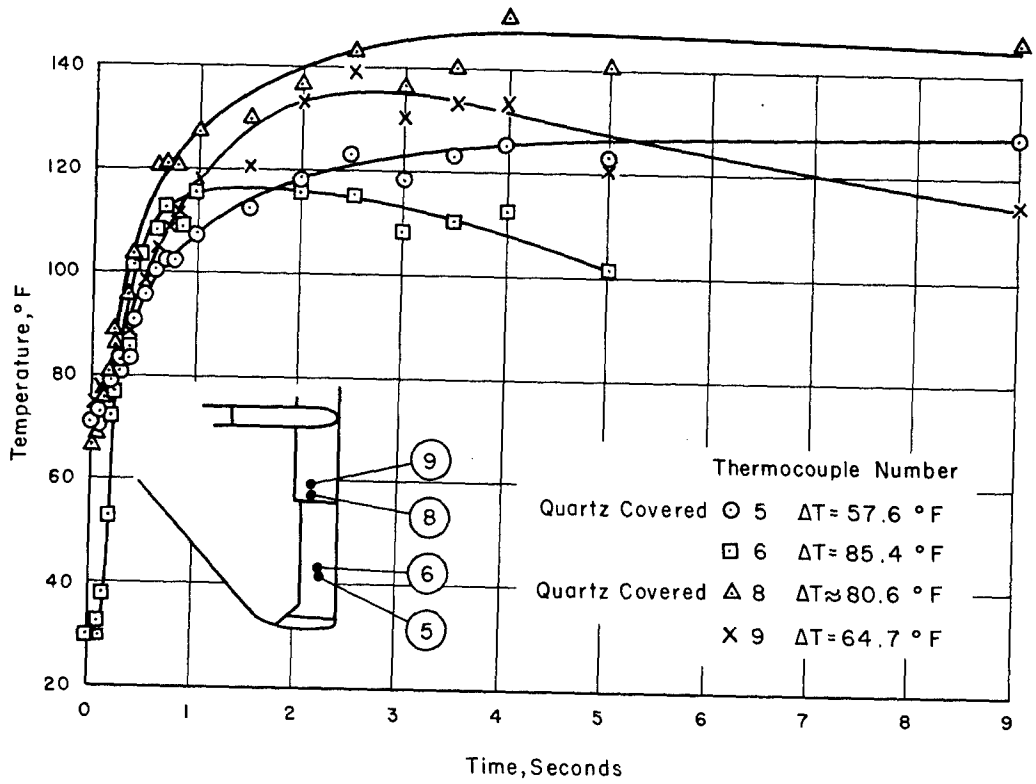


Figure 5.13 Temperature time history of quartz-covered thermocouples compared to adjacent uncovered thermocouples, Shot Shasta.

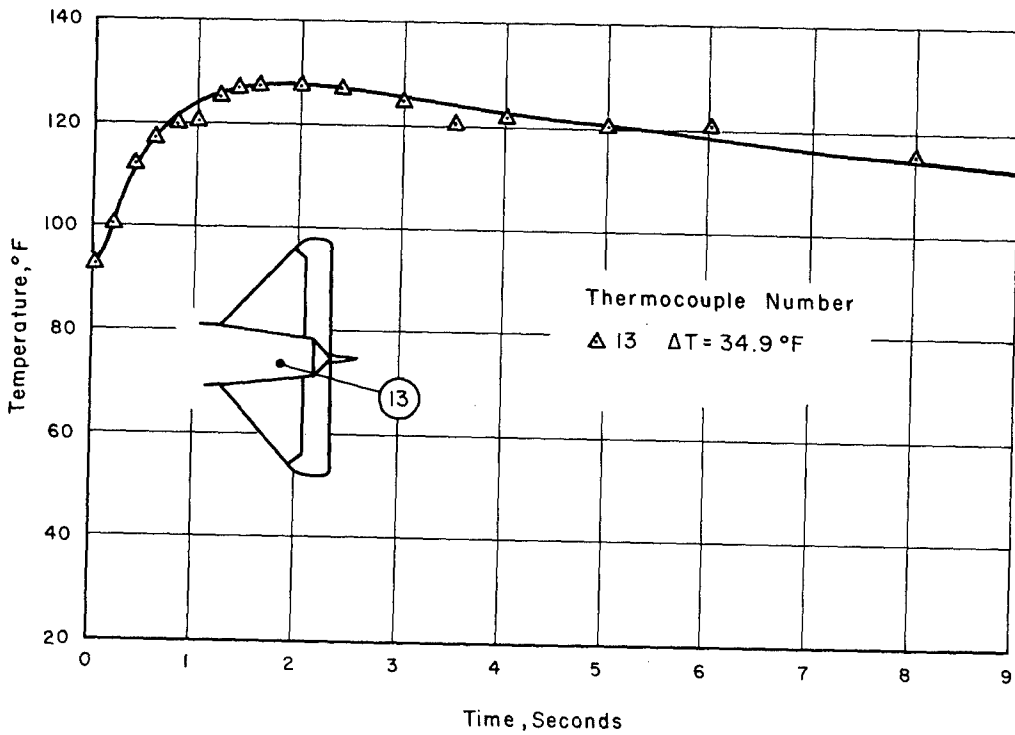


Figure 5.14 Temperature time history of fuselage skin, Shot Shasta.

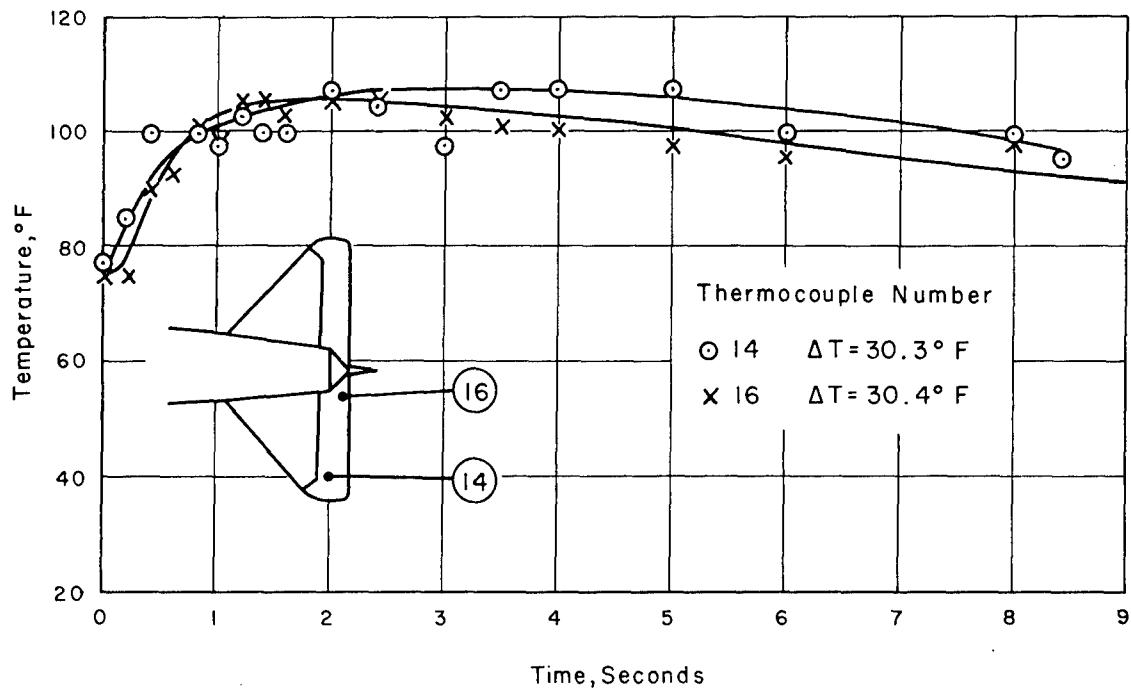


Figure 5.15 Temperature time history of elevator skin, Shot Shasta.

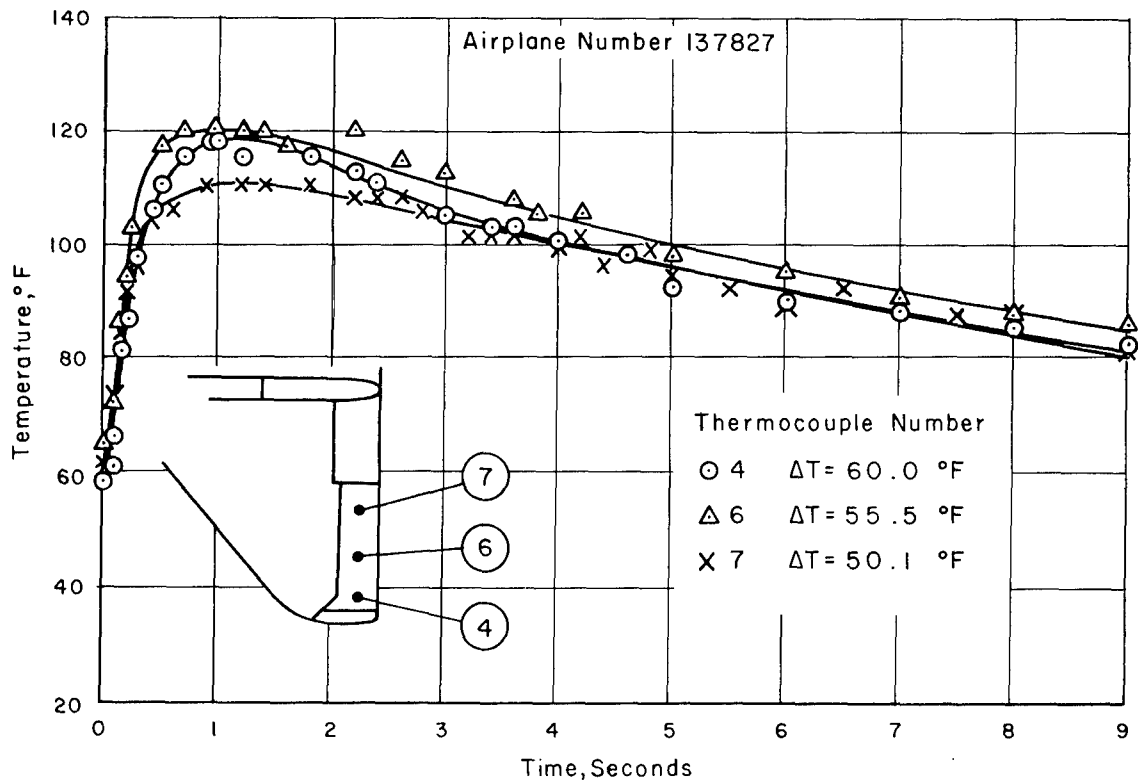


Figure 5.16 Temperature time history of aileron skin, Shot Doppler, Airplane No. 137827.

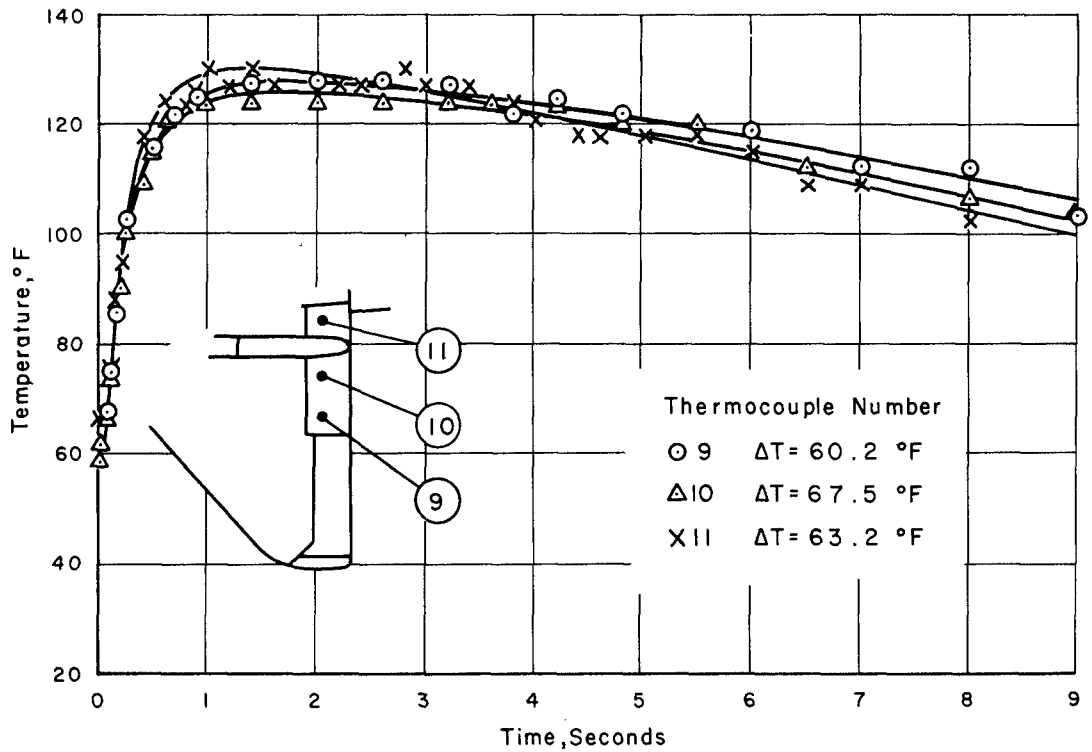


Figure 5.17 Temperature time history of flap skin, Shot Doppler, Airplane No. 137827.

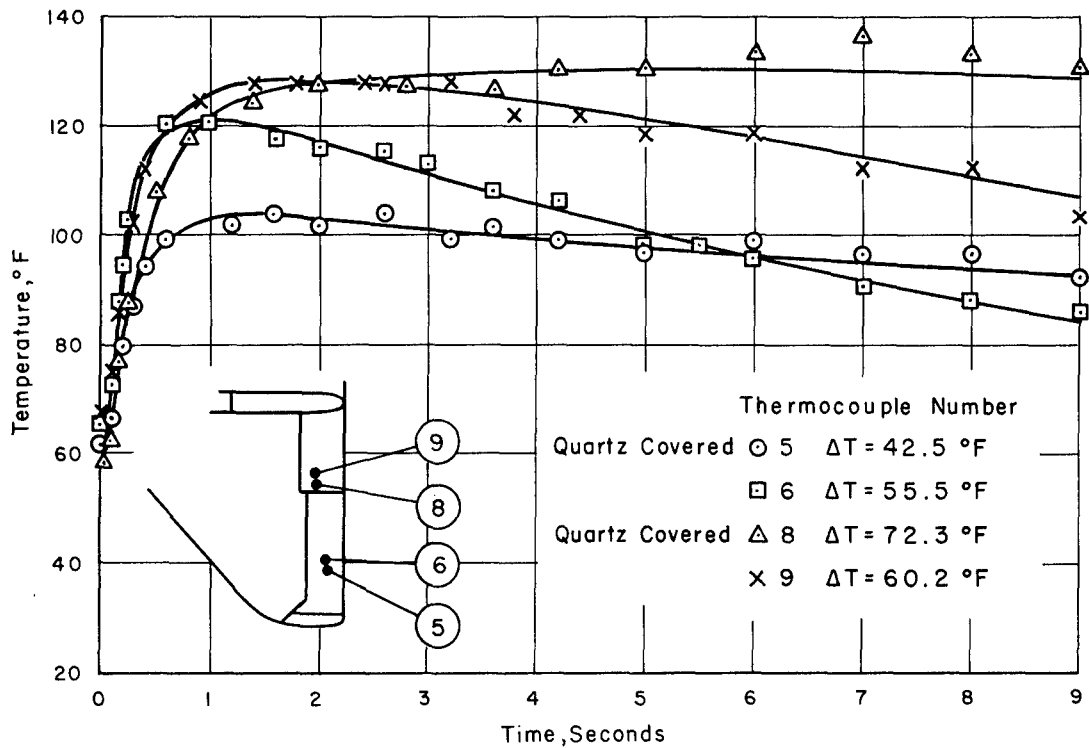


Figure 5.18 Temperature time history of quartz-covered thermocouples compared to adjacent uncovered thermocouples, Shot Doppler, Airplane No. 137827.

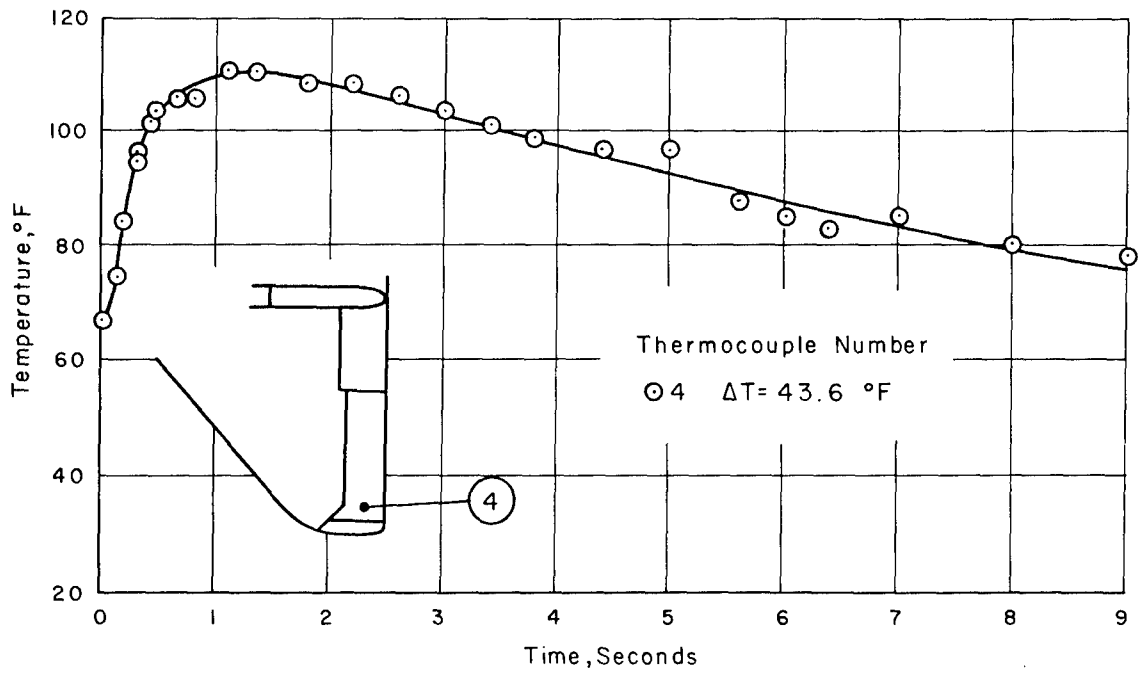


Figure 5.19 Temperature time history of aileron skin, Shot Doppler, Airplane No. 137831.

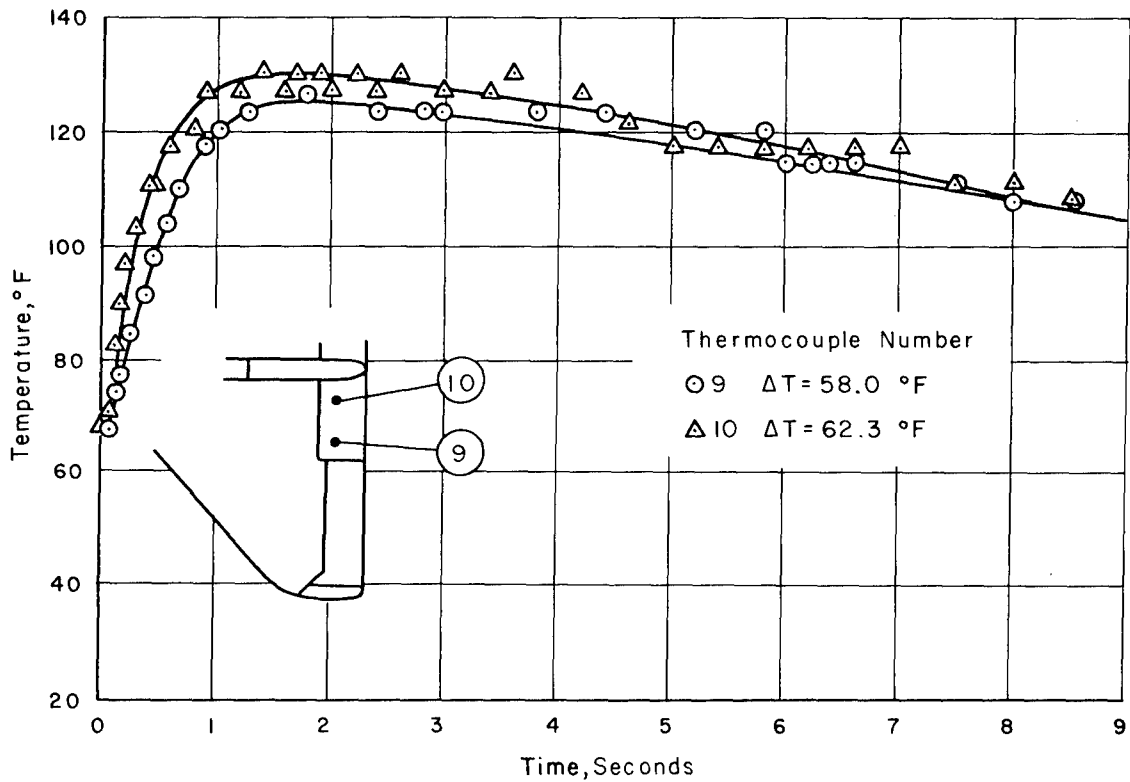


Figure 5.20 Temperature time history of flap skin, Shot Doppler, Airplane No. 137831.

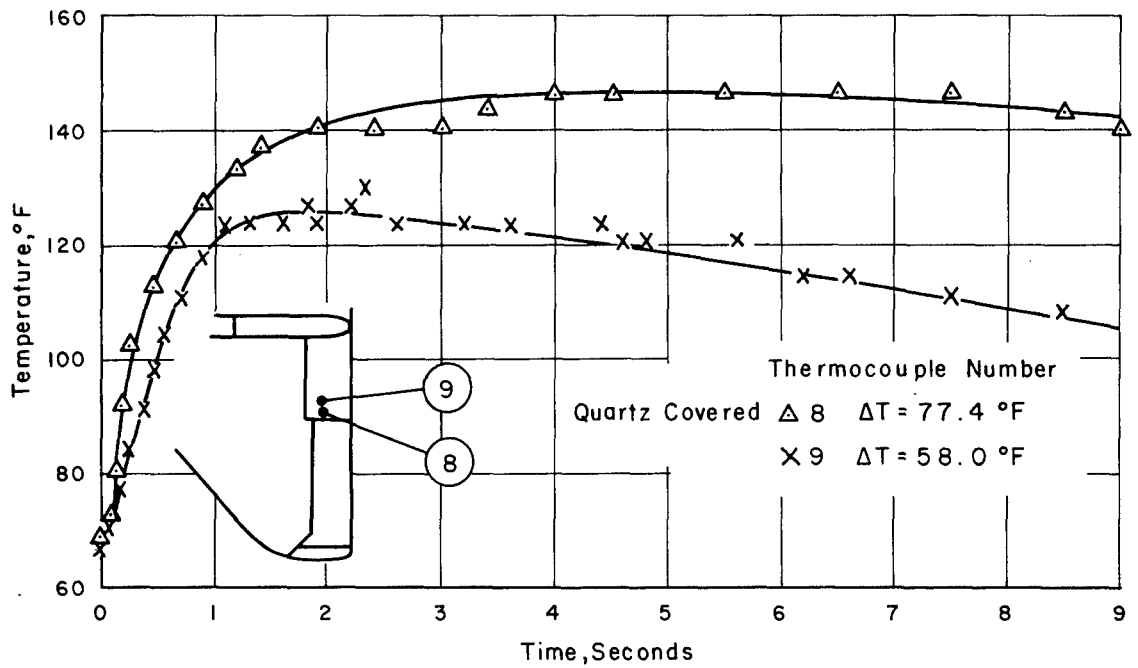


Figure 5.21 Temperature time history of quartz-covered thermocouples compared to adjacent uncovered thermocouples, Shot Doppler, Airplane No. 137831.

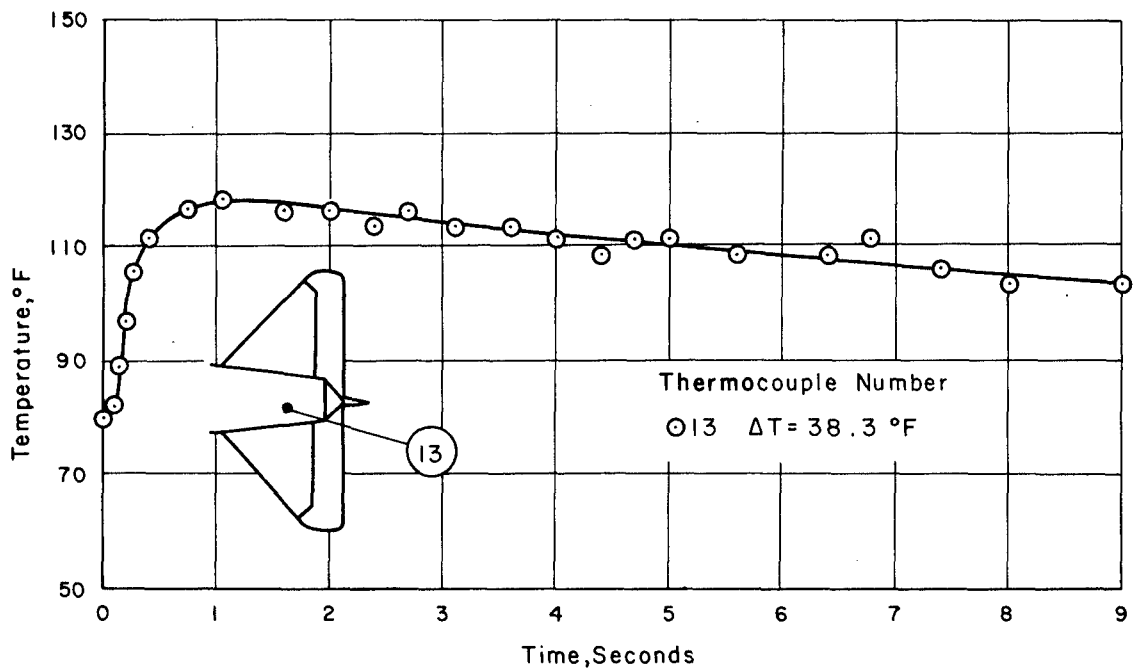


Figure 5.22 Temperature time history of fuselage skin, Shot Doppler, Airplane No. 137831.

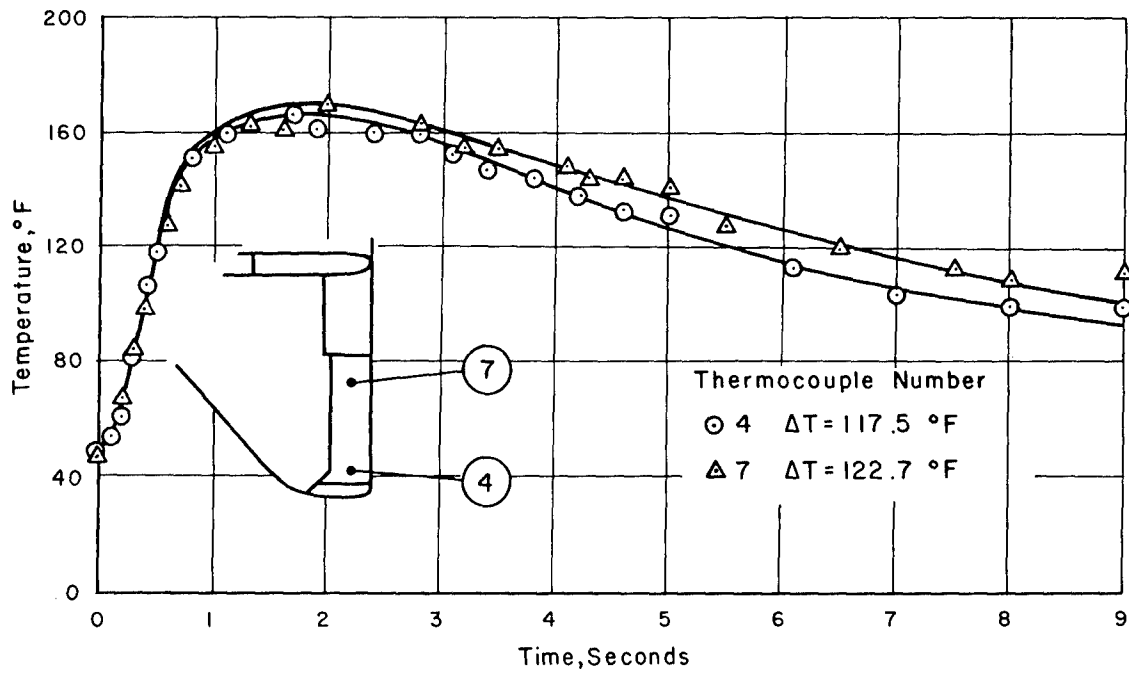


Figure 5.23 Temperature time history of elevator skin, Shot Doppler, Airplane No. 137831.

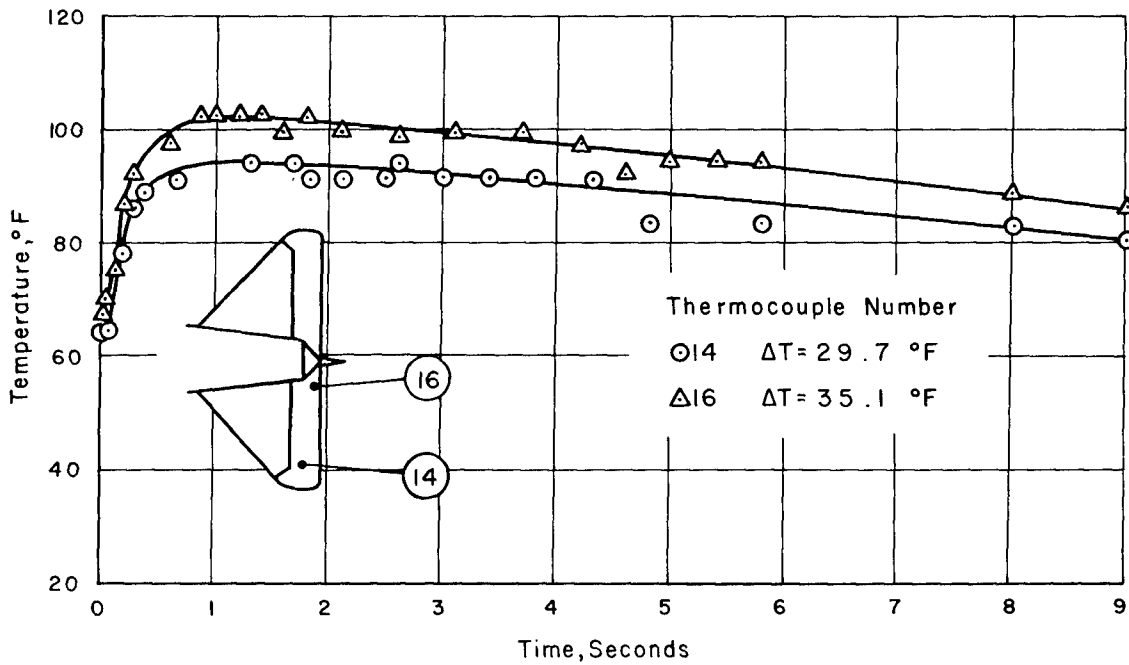


Figure 5.24 Temperature time history of aileron skin, Shot Smoky.

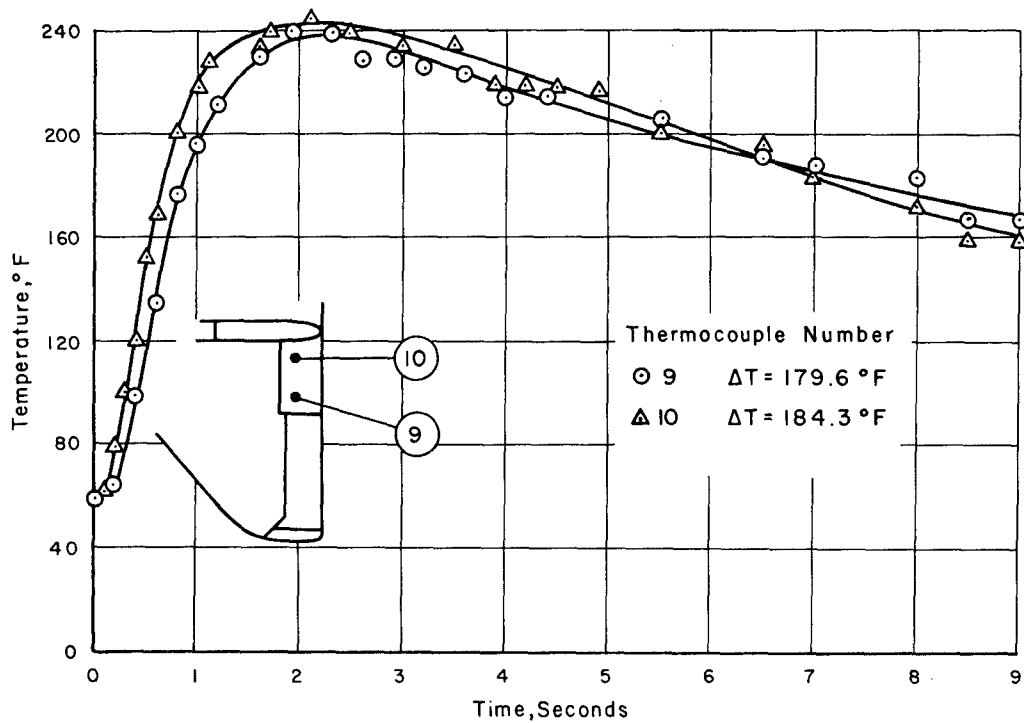


Figure 5.25 Temperature time history of flap skin, Shot Smoky.

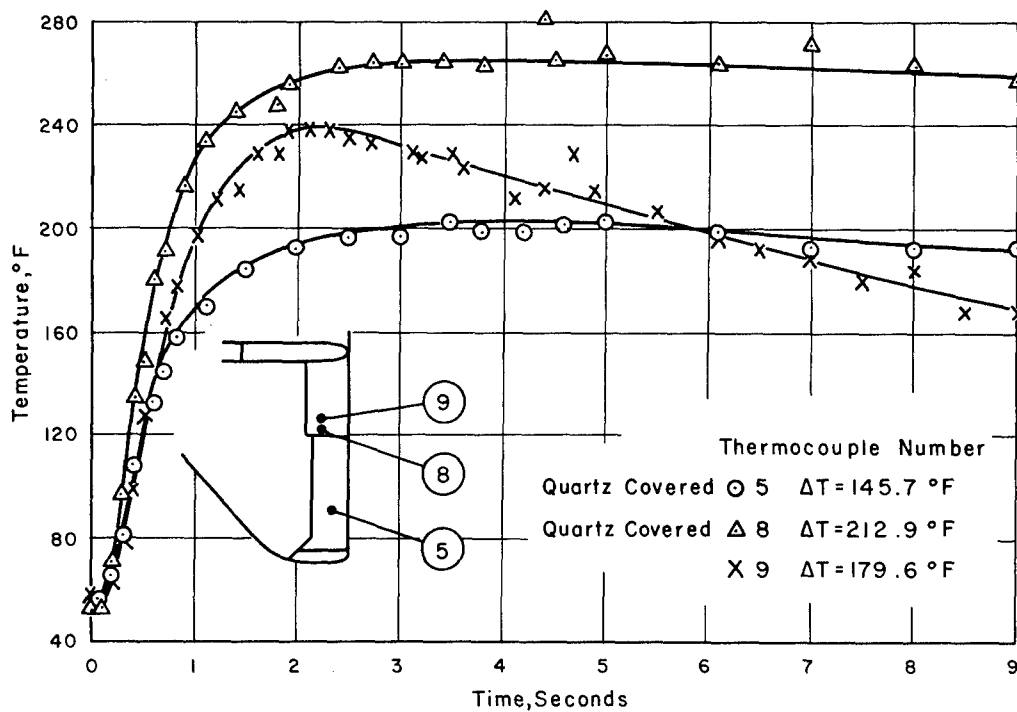


Figure 5.26 Temperature time history of quartz-covered thermocouples compared to adjacent uncovered thermocouples, Shot Smoky.

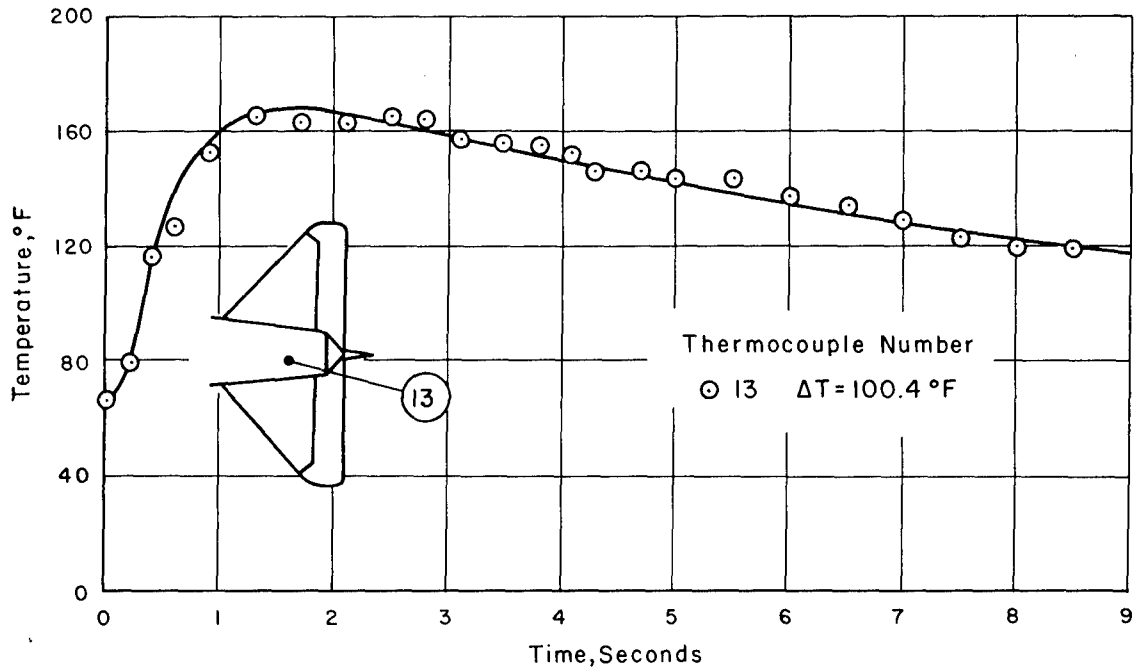


Figure 5.27 Temperature time history of fuselage skin, Shot Smoky.

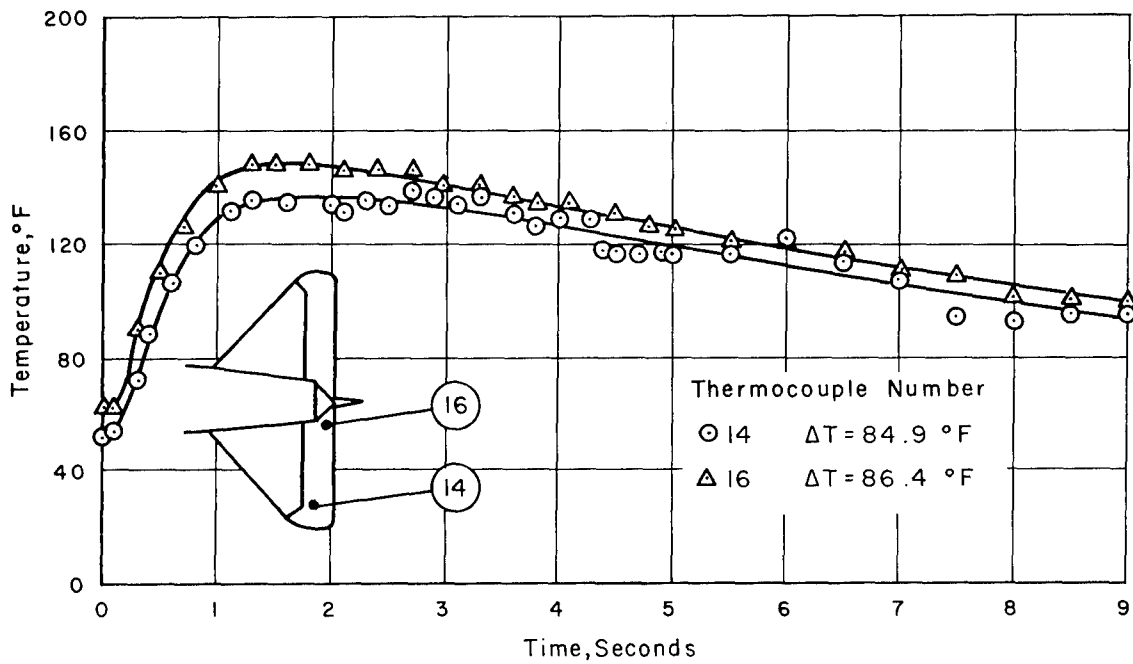


Figure 5.28 Temperature time history of elevator skin, Shot Smoky.

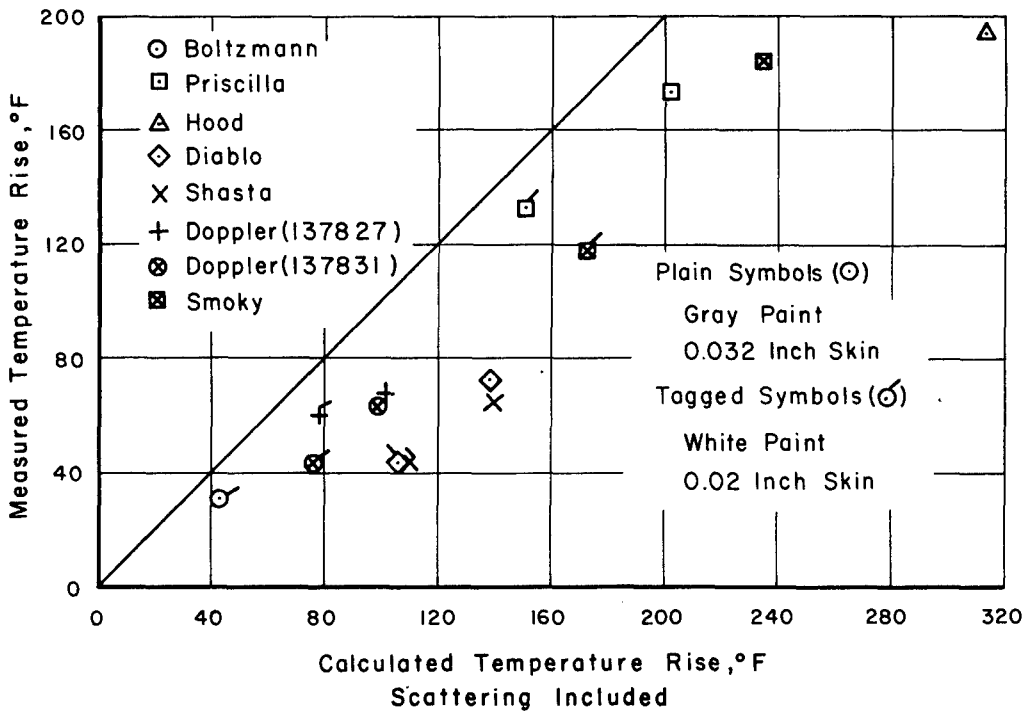


Figure 5.29 Correlation of measured and calculated temperature rise, scattering included.

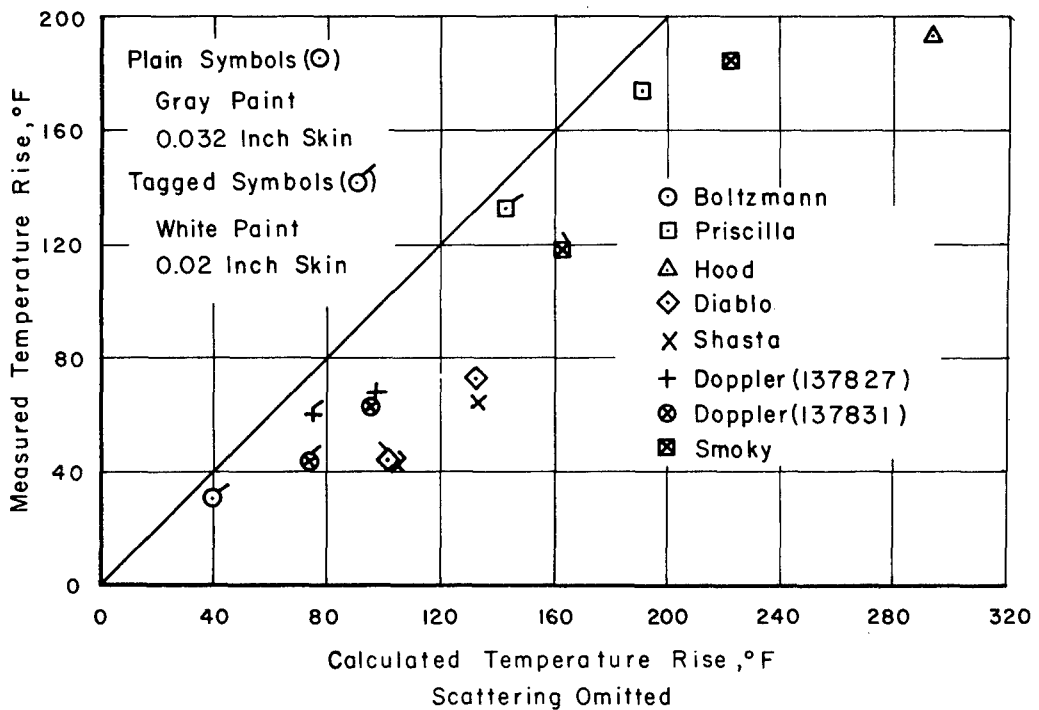


Figure 5.30 Correlation of measured and calculated temperature rise, scattering omitted.

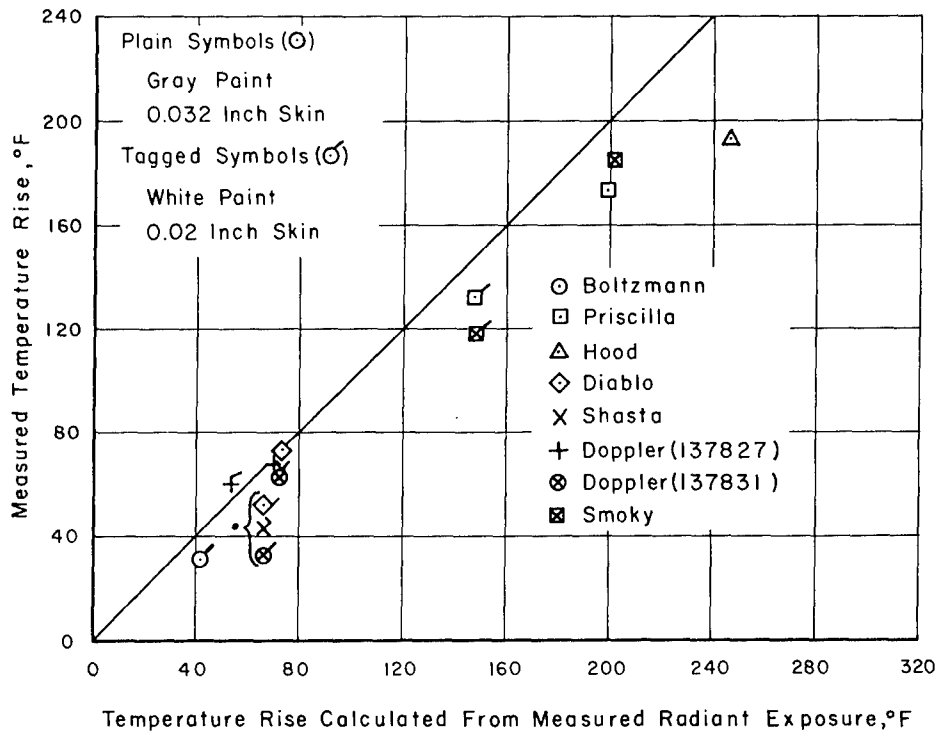


Figure 5.31 Correlation of measured temperature rise and temperature rise calculated from measured radiant exposure.

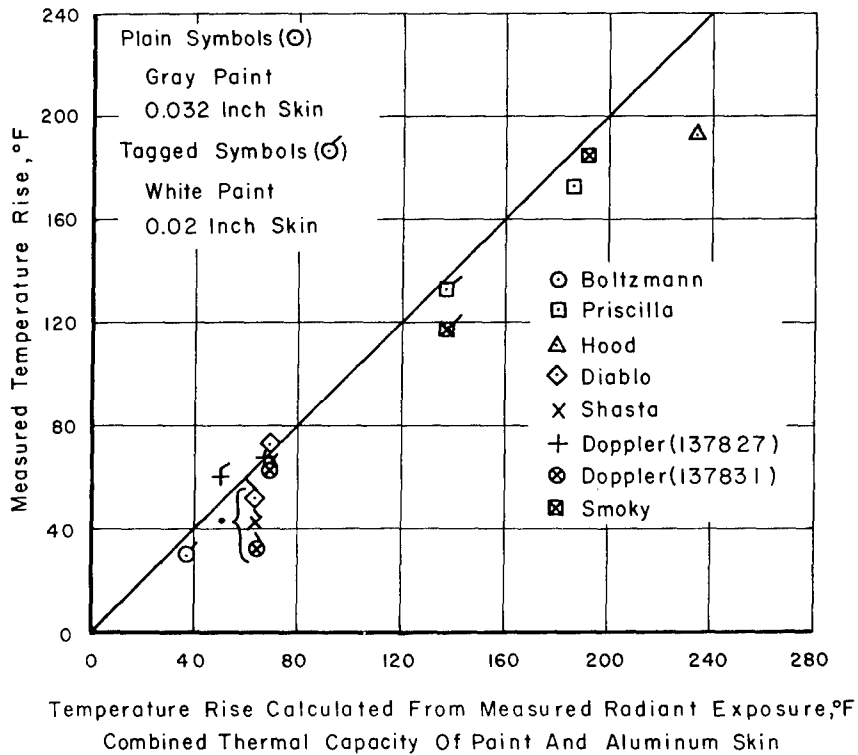


Figure 5.32 Correlation of measured temperature rise and temperature rise calculated from measured radiant exposure, combined thermal capacity of paint and aluminum skin.

Chapter 6

NUCLEAR RADIATION DATA

Values of nuclear radiation recorded by the various nuclear radiation instruments are presented in Table 6.1. Also presented is the value calculated from data given in Reference 6 with no increase included to account for an airborne receiver. However, one rem was included in the calculated dose value of those participations where the horizontal range was greater than 1,000 feet and the aircraft was flying toward ground zero at time zero. This was done to provide for the dose increase because of the decreasing slant range between the aircraft and the nuclear cloud.

The results of the dosimeter and film-badge measured nuclear radiation are inconsistent when compared between various locations and various events with the calculated radiation. The inconsistency is such that no discussion is possible. However, in general, for a specific location in the airplane, the several indicators agreed well.

TABLE 6.1 NUCLEAR RADIATION DATA

Shot Airplane Number	Boltzmann 137827	Priscilla 137827	Hood 137827	Diablo 137827	Shasta 137831	Doppler 137827	Doppler 137831	Smoky 137831
Nuclear radiation, rem								
Cockpit dosimeters:								
1	OS*	OS	OS	OS	OS	OS	OS	†
2	OS	OS	OS	OS	OS	OS	OS	
3	0.3	1.6	1.8	1.4	1.65	2.8	3.2	1.5
4	0.2	1.4	1.3	1.1	1.2	NA‡	2.4	1.1
5	1.0	1.5	1.7	0	2.0	NA	2.0	1.0
Airplane dosimeters								
6	OS	OS	OS	OS	OS	NA	OS	
7	NA	NA	NA	NA	NA	NA	NA	
8	0.35	2.5	2.0	1.8	2.2	NA	3.55	1.6
9	0.4	2.5	2.1	2.0	2.25	4.2	3.75	1.7
10	0.3	1.9	1.9	1.8	2.1	4.5	3.0	1.7
Cockpit film badges								
1	0.28	0.64	2.25	1.53	NA	NA	NA	NA
2	0.28	0.79	2.25	1.52	NA	NA	NA	NA
3	0.29	0.76	2.22	1.53	NA	NA	NA	NA
4	0.32	0.70	2.30	1.65	NA	NA	NA	NA
5	0.32	0.76	2.23	1.65	NA	NA	NA	NA
6	0.29	0.68	2.25	1.67	NA	NA	NA	NA
Airplane film badges								
7	NA	0.43	2.48	2.3	NA	NA	NA	NA
8	0.34	0.48	2.48	2.0	NA	NA	NA	NA
9	0.35	0.44	2.48	2.05	NA	NA	NA	NA
10	0.33	0.44	2.48	2.0	NA	NA	NA	NA
Calculated	1.10	2.38	2.99	2.76	3.42	2.89	2.57	2.85

*OS, off scale.

†Spaces left blank, data not measured.

‡NA, not available. Record of film badge data not retained.

Chapter 7

ENGINE RESPONSE DATA

Analysis of the engine data obtained during flight of the A4D-1 aircraft radially outbound from the test explosions at time of shock arrival indicated that there were no violent reactions of the engine because of the passage of the shock wave.

Although the engine response was at a low level, an attempt was made to determine whether the data indicated any tendency toward compressor stall or significant changes in thrust. Table 7.1 presents the before and after shock engine data for each event. Since no significant effects on engine operation were observed for the first three shots, part of the engine data was not obtained during the other participations.

The effect of the blast wave on the engine was considered in terms of its effect on air temperature, pressure, and velocity. It was concluded that the maximum overpressure pulse of the blast waves was too small to allow entry into the tailpipe. Therefore, no difficulty from interference with the discharge flow would have been expected, and indeed none was experienced. When considering engine inlet conditions, it is known that an overpressure to ambient pressure ratio ($\Delta P/P_{AM}$) of 0.6 is required to separate a turbulent boundary layer and since a maximum $\Delta P/P_{AM}$ of 0.11 was experienced, no inlet flow separation occurred nor would any have been expected.

The pressure and temperature effects were considered as follows: The temperature rise will produce a sudden reduction in compressor corrected rotational speed. This effect reduces the compressor pressure ratio and therefore tends to unload the compressor slightly. Temperature ratios in the engine are similarly reduced, but both pressure and temperature effects are offset by the rise in absolute values of entry pressure and temperature. Considering the small size of the pressure and temperature rises experienced and the compensating nature of the overall effects, it is reasonable to conclude that the weapon delivery capability of the A4D-1 aircraft is not limited by any adverse engine operational effects.

TABLE 7.1 ENGINE RESPONSE TO SHOCK WAVE

Shot Aircraft Number		Boltzmann 137827	Priscilla 137827	Hood 137827	Diablo 137827	Shasta 137831	Doppler 137827	Doppler 137831	Smoky 137831
Compressor									
inlet total pressure, psi	Before*	15.8	14.97	14.97	†				
	After‡	16.5	17.14	15.98					
Compressor									
inlet static pressure, psi	Before	14.63	14.52	14.10					
	After	15.28	15.60	14.93					
Compressor									
discharge static pres- sure, psi	Before	254	266	196					
	After	270	304	218					
Turbine dis- charge total temp., °F	Before					794		NA§	844
	After					777		NA	844
Fuel distri- bution mani- fold pressure, psi									
	Before	NA	171.7	106					
	After	NA	206.3	136					
Rotor speed, rpm	Before	NA	NA	NA	7,440	7,420	7,530	7,505	7,450
	After	NA	NA	NA	NA	7,400	7,480	7,520	7,450

*Before, value immediately before shock arrival.

†Space left blank, data not measured.

‡After, maximum value after shock arrival.

§NA, reduced data not available.

Chapter 8

SHOCK WAVE EFFECTS

Presented in this chapter are the results and discussion of overpressure, time of shock arrival, and blast gust response effects of the shock wave.

8.1 OVERPRESSURE

The peak values of the measured and calculated overpressure are presented in Table 8.1. A sample time history of nose-boom measured overpressure is presented in Figure 8.1, together with the method used to read the peak value.

Values of calculated overpressure are presented in Table 8.1 for comparative purposes. The methods of modified Sachs scaling as outlined in Appendix B were used with yield factors based on the aircraft location with respect to the triple-point path (see Section 1.3.3).

Figure 8.2 presents the nose-boom measured data reduced to correspond to a 1-kt burst at sea level by modified Sachs scaling compared with the basic curve used for predicting this effect. In general, the prediction curve produced conservative values of overpressure.

8.2 TIME OF SHOCK ARRIVAL

The time of shock arrival as actually measured and as calculated using the method of modified Sachs scaling as outlined in Appendix B is shown in Table 8.2. Calculations of the shock arrival time were made using the speed of sound at the aircraft altitude and yield factors based on the aircraft position with respect to the triple-point path. (See Section 1.3.3). Figure 8.3 shows the measured time of shock arrival for each shot reduced to correspond to a 1-kt burst at sea level by modified Sachs scaling compared with the basic curve used to predict shock arrival time. In general, very good correlation between measured and predicted values was obtained.

8.3 AIRCRAFT RESPONSE TO BLAST LOADING

The installed instrumentation provided two types of measurements of aircraft response to blast loading: the measurement of structural loads and the measurement of wing pressures. Each will be discussed separately.

Structural load measurements served the dual purpose of providing information for correlation with load prediction methods and of providing an index to positioning safety during the tests. The critical item of structural response was the wing root bending moment. A summary of the percentages of design limit bending moment experienced during the tests is given in Table 8.3, together with the calculated values for the same quantity.

TABLE 8.1 MEASURED AND CALCULATED PEAK OVERPRESSURE

Shot	Maximum Overpressure (psi)				
	Boom	Measured		Calculated	
		LH Fuselage	RH Fuselage	YF*	Pressure
Boltzmann	0.44	NA†	NA	1	0.459
Priscilla	0.80	0.78	0.88	1	NA
Hood	0.65	0.73	0.83	1	0.795
Diablo	0.98	0.96	1.04	1.2	0.952
Shasta	0.93	1.05	1.01	1.2	0.943
Doppler (137827)	0.39	0.37	0.43	1	0.445
Doppler (137831)	0.40	0.43	0.48	1	0.429
Smoky	0.56	0.49	0.57	2	0.595

*YF, yield factor based on aircraft location with respect to triple-point path (see Section 1.3.3).

†NA, not available because of instrumentation failure.

TABLE 8.2 MEASURED AND CALCULATED TIME OF SHOCK ARRIVAL

Shot	Time of Shock Arrival, (seconds)		
	Measured	Calculated	
		YF*	Time
Boltzmann	10.13	1	9.93
Priscilla	8.52	1	NA†
Hood	10.53	1	10.35
Diablo	6.68	1.2	6.55
Shasta	6.48	1.2	6.35
Doppler (137827)	10.26	1	10.40
Doppler (137831)	10.50	1	10.79
Smoky	15.70	2	15.50

*YF, yield factor based on aircraft location with respect to triple-point path (see Section 1.3.3).

†NA, not available because of instrumentation failure.

TABLE 8.3 COMPARISON OF MAXIMUM WING BENDING MOMENTS

Shot	Aircraft Number	Percent Design Limit Load	
		Measured	Calculated
Boltzmann	137827	37	36
Priscilla	137827	55	53
Hood	137827	49	41
Diablo	137827	63	57
Shasta	137831	53	55
Doppler	137827	26	26
Doppler	137831	26	26
Smoky	137831	25	27

The measured values shown in the table are based upon the maximum wing root bending moment obtained from either the matrix or rosette data reduction method, whichever was larger, while the calculated values are based upon the analytical method given in Appendix C using actual test conditions. It can be seen that the agreement between measurement and calculation is satisfactory.

8.3.1 Structural Loads. The results of structural load measurements for Operation Plumbbob consisted of recorded time histories of loads for the wing, the tail, and the fuselage keel, and time histories of aircraft motion. The headings of Table 8.4 indicate the types of response data obtained for each shot participation.

Wing Loads. Wing strain gages were installed to permit the measurement of wing shear, torque, and bending moment at Wing Station 36.5 and only the wing bending moment at Stations 72.0 and 113.0. Two different methods of converting strain gage readings to load were employed.

The first method was based upon the conversion of the gage data to elastic strain, computation of principal stresses, resolution of the stresses into loads through coefficients derived from the distribution of structural material area, and finally a computation of the resultant load at the station in question through a knowledge of the wing geometry. In this report, this method is called the rosette method since the majority of the gages used were strain rosettes. The coefficients used for the rosette method together with the modifications used to compensate for missing strain gage data are given in Appendix D.

The second method was the more conventional one of utilizing the results of laboratory calibration of the strain gage installation. In this report this method of reduction is called the matrix method, since the results of the calibration are given in the form of a matrix which is multiplied by combinations of gage readings. The matrices used and applicable gages for each matrix are given in Reference 11.

A third method of determining wing bending moment was employed for three of the test participations. This method did not depend upon the strain gage data but instead was based upon the measured wing pressures as described in Section 8.3.2 and thereby provided a means of checking the strain gage methods. In brief, the method consisted of determining from the wing pressure taps the variation in time and space of the applied wing air loads, computing from these (and a knowledge of the wing normal modes of vibration¹) the generalized forces corresponding to each normal mode, then solving the resulting differential equations for the wing bending moment. Table 8.4 shows the types of reduction procedures employed for each case. The rosette method was employed at all three wing stations to determine bending moment, except when gage malfunctions made this impossible. The matrix method was used to determine wing shear, torque, and bending moment at Wing Station 36.5 for all cases in which Aircraft No. 137827 participated. Since no laboratory calibration of the wing strain gage installation for Aircraft 137831 was conducted, the matrix method could not be employed for test participation of this aircraft.

The shear and torque at Station 36.5 was determined by the rosette method for Shot Diablo. Figures 8.4 and 8.5 show comparisons of the matrix and rosette methods used for the determination of shear and torque. It can be seen that the rosette method yielded results which were too small to be reasonable. Since the rosette shear and torque results were not satisfactory, no further attempt was made to determine these quantities by the rosette method. Thus, the usable shear and torque results given in this report were obtained by using the matrix method. The rosette method was employed only for the determination of bending moment. Shear and torque results for all test participations of Airplane No. 137827 are shown in Figures 8.6 through 8.14.

For all test participations, the wing bending moment at Station 36.5 was determined by the analytical method of Appendix C and is compared with the test results in the figures which follow.

¹As in the prediction method described in Appendix C, three normal modes were used, rigid body translation, first bending, and first torsion.

TABLE 8.4 TYPES OF WING AND TAIL STRUCTURAL RESPONSE DATA OBTAINED

Shot	Airplane Number	Bending Moment	Bending Moment	Bending Moment	Wing Shear	Wing Torque	Tail Incremental Bending Moment	Tail Incremental Shear	Tail Incremental Torque
		Station 36.5	Station 72	Station 113	Station 36.5	Station 36.5			
Boltzmann	137827	R* M†	R	R	M	M			
Priscilla	137827	R M P‡	R	R	M	M			
Hood	137827	R M	R		M	M			
Diablo	137827	R M P	R	R	R M	R M	M	M	M
Shasta	137831	R						L & A§	
Doppler	137827	R M P	R	R		M		M	M
Doppler	137831	R						L & A	
Smoky	137831	R		R				L & A	

*R, rosette strain gage reduction.

†M, matrix strain gage reduction.

‡P, bending moment calculated from measured wing pressure.

§L & A, tail load computed from lug and actuator loads.

Figures 8.15 through 8.22 show comparisons of calculated bending moment for Station 36.5 with the results of rosette data reduction. It can be seen that the agreement exhibited for rise time and for peak bending moment is good. For values of time greater than the rise time, analysis and measurement tend to diverge. This divergence might be explained by an incomplete knowledge of the aircraft normal modes. This point will be discussed at greater length in a succeeding paragraph.

Figures 8.23 through 8.27 show comparisons of calculated bending moment for Station 36.5 with the results of matrix data reduction. Four reduction matrices were available from the laboratory calibration of the wing strain gages. These matrices are referred to on the figures as matrices A, B, C, or D. It can be seen that in general the agreement with the calculations is similar to that exhibited by the rosette results. For all cases, with the exception of Shot Boltzmann, Figure 8.23, the matrix method shows a slightly higher bending moment than the rosette method. Particular attention is called to the results for Shot Priscilla, Figure 8.24, where a spurious peak bending moment was shown to result from the data reduction by different matrices. This result was apparently erroneous since it occurred nowhere else in the data reduction program and was believed due to an incorrect recording of the response for a strain gage common to certain of the reduction matrices.

Figures 8.28 through 8.30 show comparisons of calculated and measured bending moments at Station 36.5, where the measured values were obtained from the wing pressures as previously described. It can be seen that the peak value and rise time agreement was substantially the same as that shown for the matrix and rosette methods. The subsequent divergence of measurement and calculation shown by the preceding methods, however, was absent from the

pressure determined moments. It is felt that this adds weight to the argument that the divergence arises from inadequate knowledge of the aircraft modes since the same mode values are used for both the calculated and pressure measured methods.

Figures 8.31 through 8.40 show the time-wise variation of wing bending moment at Station 72.0 and 113.0 as obtained by the rosette method. The analytical method was not employed for the calculations of wing response at Station 72.0 and Station 113.0 since response at these points was not critical.

The time duration of plotted data was extended to 0.2 second for the bending moment, shear, and torque at Station 36.5 for Shot Diablo. This was done to illustrate the fact that the maximum response was attained well within the first 70 msec after shock arrival. The matrix method of data reduction was used for this purpose. These plots appear in Figures 8.41 through 8.43. The rate of response decay exhibited by Shot Diablo was typical for all the shots of Operation Plumbbob.

Tail Loads. The horizontal tail load recording instrumentation was utilized for only the last four test participations. A matrix type calibration was available for Aircraft No. 137827, but the tail load recording equipment for Aircraft No. 137831 was limited to the strain gages installed on the horizontal stabilizer supporting lugs and the stabilizer actuator. A summary of the type of data obtained is given in Table 8.4. Tail bending moment data for Shot Doppler (137827) was lost through the malfunction of a strain gage. The calibration matrix and significant gages are given in Reference 11. The results are shown in Figures 8.44 through 8.51.

To illustrate the decay of tail load with time, plots were made of tail shear, torque, and bending moment with the time scale extended to 0.4 second. These appear in Figures 8.52 through 8.54.

Fuselage Keel Stresses. Prior to participation in Operation Plumbbob it was anticipated that the fuselage keel at Station 145 would be the most critically loaded structural member. The fuselage keel stresses were later determined not to be critical since they were based upon the flight design weight distribution of Reference 12, which located a fictitious weight of 623 pounds in the airplane nose at Fuselage Station 64.0; a weight distribution prescribed to establish the extreme forward aircraft center of gravity for basic structural design. This loading can never be encountered in fleet operation of the A4D-1 airplane. Since the 623-pound weight was absent from the Operation Plumbbob test aircraft the observed fuselage keel stresses were well below the critical value of 55,000 psi.

Figures 8.55 through 8.57 show plots of fuselage keel stresses for the three test participations of Aircraft No. 137831. Inconsistencies were observed between the left- and right-hand keel readings obtained for Aircraft No. 137827, which cast considerable doubt on their validity. Consequently, keel stress data for Aircraft No. 137827 have been omitted from this report.

Aircraft Motion. Time histories of aircraft center of gravity acceleration were obtained from each A4D-1 test participation. Time histories of tail acceleration were obtained only from participation of Aircraft No. 137827. An accelerometer malfunction resulted in the loss of all tail acceleration data for Aircraft No. 137831. Plots of tail acceleration time histories are given in Figures 8.58 through 8.62. Calculations of center of gravity acceleration based on the analytical methods of Appendix C are shown superimposed upon the measured results in Figures 8.63 through 8.70.

In comparing the calculated and measured center of gravity accelerations it should be noted that galvanometers having a relatively low natural frequency were employed for the measurements. These galvanometers had a natural frequency of 100 cps and employed 64 percent critical damping which permitted flat frequency response up to only 60 cps. Since this relatively low frequency instrumentation did not permit faithful recording of the applied acceleration at the instant of shock arrival, agreement between the calculated and measured acceleration at time of shock arrival could hardly be expected. It is believed that the disagreement shown between the measured and calculated center of gravity acceleration following time of shock arrival resulted from both the response characteristics of the recording galvanometer and the high degree of idealization used in making the analytical comparisons. Notable among these idealizations were the absence from the analytical model of: (1) the pitching degree of

freedom, (2) several high frequency modes of airplane vibration, and (3) the effects of fuselage flexibility.

Pitch rate and attitude recording equipment was installed in the aircraft for all test participations. The data obtained from these instruments was obviously in error and is not presented in this report. It was felt, however, that an adequate estimate of airplane pitching motion could be obtained by integration of the center of gravity and tail acceleration data. Pitching acceleration, velocity and displacement were obtained from the following formulas:

$$\Delta\ddot{a} = \frac{(\Delta n_{C.G.} - \Delta n_T) g}{s} \quad (8.1)$$

$$\Delta\dot{a} = \int_0^t \Delta\ddot{a} dt \quad (8.2)$$

$$\Delta a = \int_0^t \Delta\dot{a} dt \quad (8.3)$$

where $\Delta\ddot{a}$ = incremental pitching acceleration (change from steady state)
 $\Delta\dot{a}$ = incremental pitching velocity
 Δa = incremental pitching angle
 $\Delta n_{C.G.}$ = center of gravity acceleration
 Δn_T = tail acceleration
 g = acceleration due to gravity
 s = distance between center of gravity and tail accelerometers (204 inches)

The results are shown in Figures 8.71 through 8.85. To illustrate typical response decay rates, plots of airplane motion in Shot Diablo with the time scale extended to 0.8 second are shown in Figures 8.86 through 8.89.

8.3.2 Wing Pressure Measurements. Pressure data were obtained from all but one test participation for the A4D-1 aircraft in Operation Plumbbob. The data obtained consisted of time histories of the local pressures experienced by each pressure gage installed on the wing. A diagram showing the pressure gage locations is shown in Figure A.2. Aircraft No. 137831 carried only the pressure instrumentation shown for Wing Station 61.125. Aircraft No. 137827 carried the full instrumentation shown, but oscillograph and pressure gage malfunctions resulted in the loss of data from the two outboard stations in Shot Boltzmann and in the loss of all pressure data from Shot Hood. Complete data were obtained from Aircraft No. 137827 participation in Shots Priscilla, Diablo, and Doppler. The pressure data obtained were reduced to various forms for convenient presentation but no attempt was made to reconcile the results with theoretical aerodynamic pressure distributions.

Information Obtained from Data. The measured data consisted of time histories of pressure for the various wing pressure taps. A typical set of these curves (for Shot Diablo) appears in Appendix E. The complete set of time histories obtained from Operation Plumbbob is published separately from this report in Reference 13. From these data the following information was obtained concerning the incremental (changes from steady state) pressures:

1. Chord-wise pressure distributions for various time intervals after shock arrival;
2. Span-wise distribution of the wing average pressure and chord-wise center of pressure locations for various time intervals after shock arrival;
3. Span-wise variation of section lift coefficients;
4. Time-wise variation of the average pressure for the three instrumented wing stations;
5. Time-wise variation of section lift coefficients for the three instrumented wing stations;
6. Time-wise variation of chord-wise center of pressure locations for the three instrumented wing stations; and
7. Time-wise variation of wing span-wise center of pressure.

Plots of the chord-wise pressure distributions for various time intervals after shock arrival are given in Figures 8.90 through 8.97. The chord-wise pressure distributions were ob-

tained from the pressure tap data for each of the three instrumented wing stations for Shots Priscilla, Diablo, and Doppler (137827). Chord-wise pressure distributions at Wing Station 61.12 only were obtained from Shots Boltzmann, Shasta, Doppler (137831), and Smoky. Extrapolations are shown with broken lines. Separate curves are shown for the upper and lower wing surfaces. The pressure difference between the upper and lower surfaces is indicated by the areas containing arrows. The arrowheads point to the pressure curve for the upper surface. It should be noted that a pressure difference representing lift occurs where the arrow points upward. The quantity plotted represents pressure change from steady state and for this reason is called incremental pressure.

Since space limitations prohibited the installation of pressure taps in the vicinity of the leading edge slats and in the thin trailing edge structure, it was necessary to extrapolate the pressure curves into these regions. The extrapolation of the curves to the wing trailing edge was accomplished by extending both the upper and lower surface curves so that each agreed at the trailing edge with the measured free stream overpressure as measured by the nose boom. The instrumentation at Wing Stations 88.56 and 131.87 did not provide pressure readings for areas forward of the 25 percent chord station. The measured results were extrapolated to the leading edge region of the wing by fairing a smooth curve forward from the last data point so that the pressure readings coincided with, or slightly exceeded the value measured at 3.5 percent chord at Wing Station 61.12. This method of extrapolation gave results which were in agreement with steady state wind tunnel measurements.

Span-wise distributions of wing average pressure and chord-wise center of pressure locations are presented in Figures 8.98 through 8.100. From the chord-wise pressure distributions described above it was possible in the cases for which data was obtained at three span-wise stations to determine span-wise distributions of wing pressure. For this purpose, the chord-wise pressure distributions were averaged over the local wing chords for the particular time intervals considered and plotted versus span. In addition, the chord-wise center of pressure was determined for each particular time interval and plotted versus span. The resulting curves were obtained by fairing a smooth curve through the three data points obtained from each span-wise station.

Curves of section lift coefficient (C_l) versus span for various time increments are shown in Figures 8.101 through 8.103. Section lift coefficients were determined from

$$C_l = \frac{\Delta p_{av}}{q} \quad (8.4)$$

where Δp_{av} = average pressure difference between the wing upper and lower surfaces, psf

$$q = \frac{1}{2} \rho V^2, \text{ psf}$$

ρ = free stream ambient density, slugs/ft³

V = airplane forward speed prior to shock arrival, ft/sec

The average incremental pressures, section lift coefficients, and chord-wise centers of pressure for the three instrumented span-wise stations are presented versus time in Figures 8.104 through 8.112.

The average incremental pressures, section lift coefficients, and chord-wise centers of pressure for the test participations in which data was obtained for Station 61.12 only, appear in Figures 8.113 through 8.127.

The wing span-wise center of pressure was located for the cases having three instrumented stations and plotted versus time. These plots appear in Figures 8.128 through 8.130.

Subsequent to the compilation of the pressure data described above, calculations were made to convert the measured pressures into forces. These were combined with the airplane generalized masses and flexibility characteristics to obtain calculated time histories of airplane response. Some of the results of these calculations are the bending moment curves described in section 8.3.1, but in addition to bending moment the airplane center of gravity acceleration was computed. Both the wing bending moments and the airplane acceleration determined by this method were found to agree well with the strain gage and accelerometer results. From this it was concluded that the pressure measurements gave a good estimate of the total force experienced by the wing as a result of blast gust encounter.

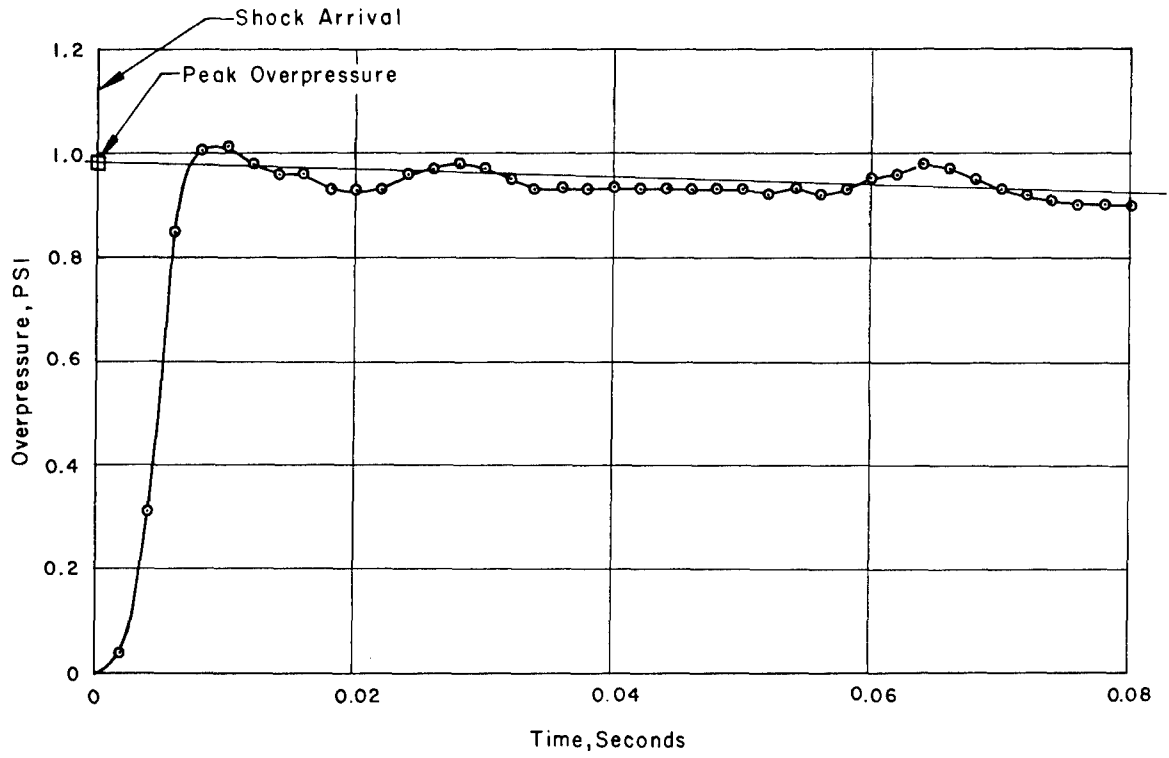


Figure 8.1 Time history of nose boom overpressure, Shot Diablo.

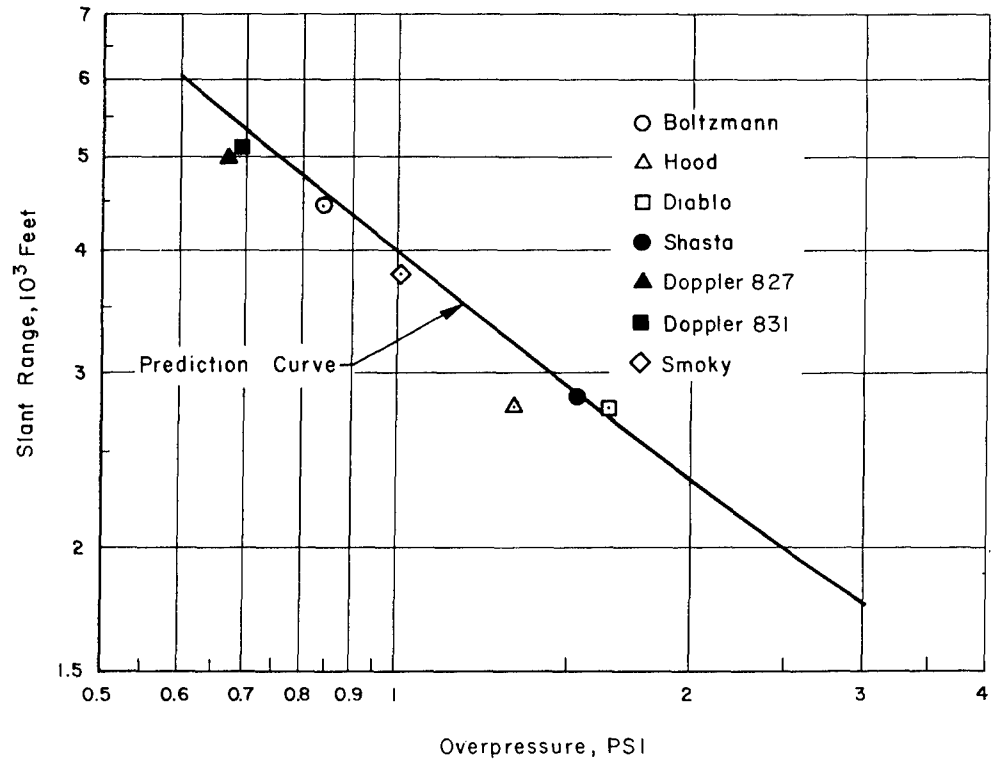


Figure 8.2 Overpressure data reduced to 1 kt at homogeneous, sea-level atmosphere.

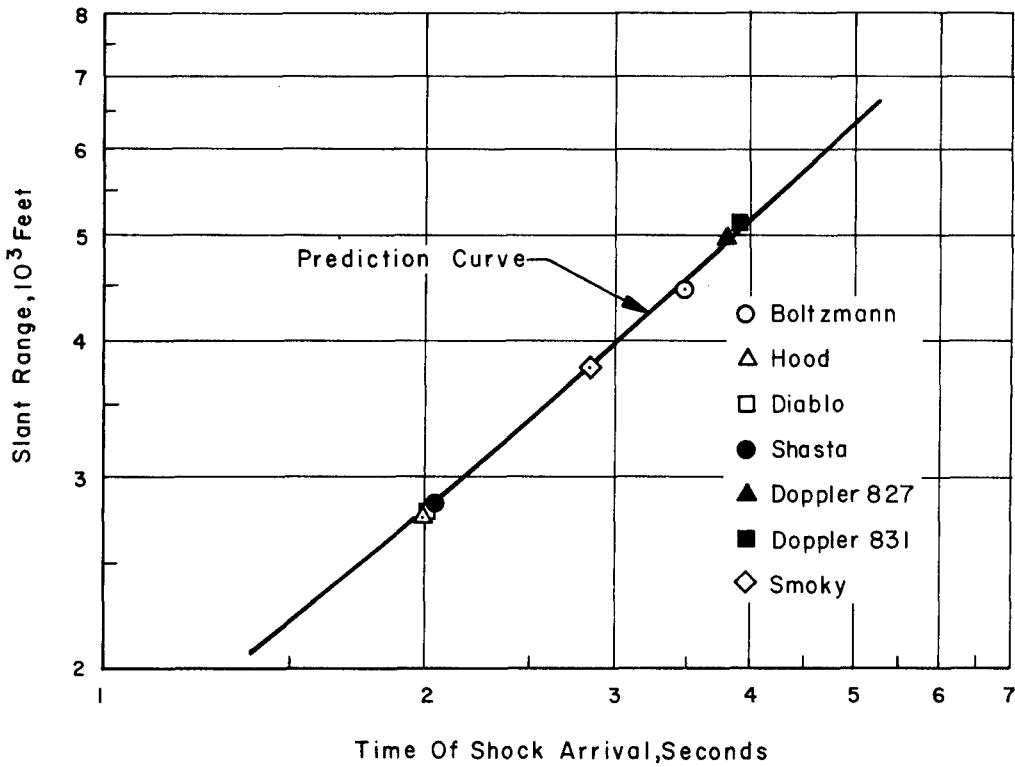


Figure 8.3 Time of shock arrival data reduced to 1 kt at homogeneous sea-level atmosphere.

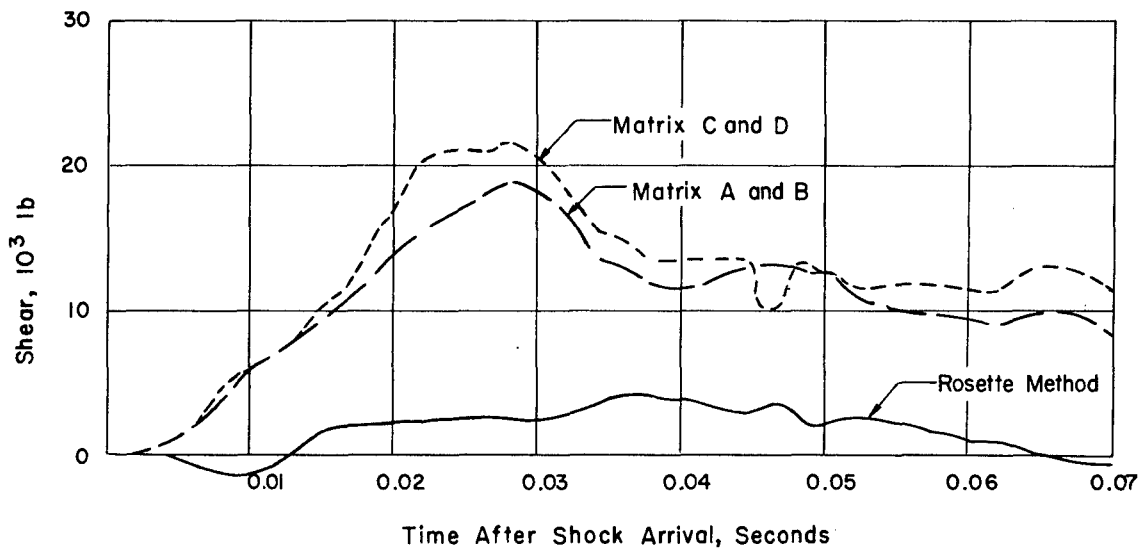


Figure 8.4 Comparison of wing shear measurements at Station 36.5, obtained by the matrix and rosette methods, Shot Diablo.

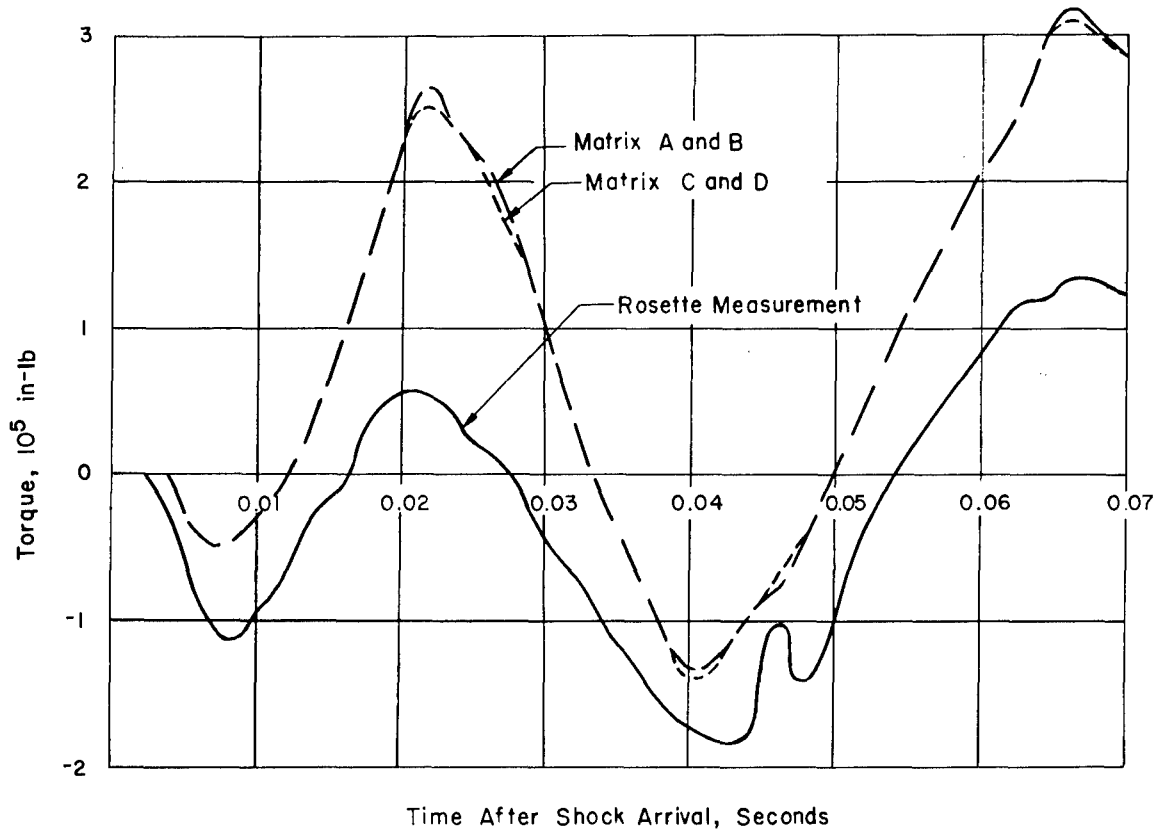


Figure 8.5 Comparison of wing torque about fuselage Station 283, obtained by the matrix and rosette methods at Station 36.5, Shot Diablo.

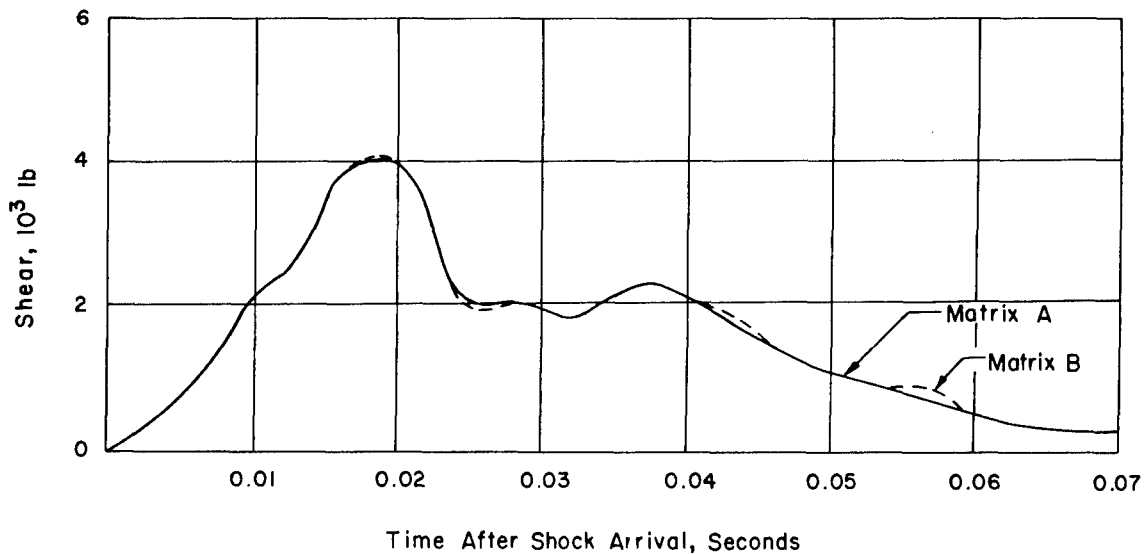


Figure 8.6 Wing shear at Station 36.5 from matrix measurements, Shot Boltzmann.

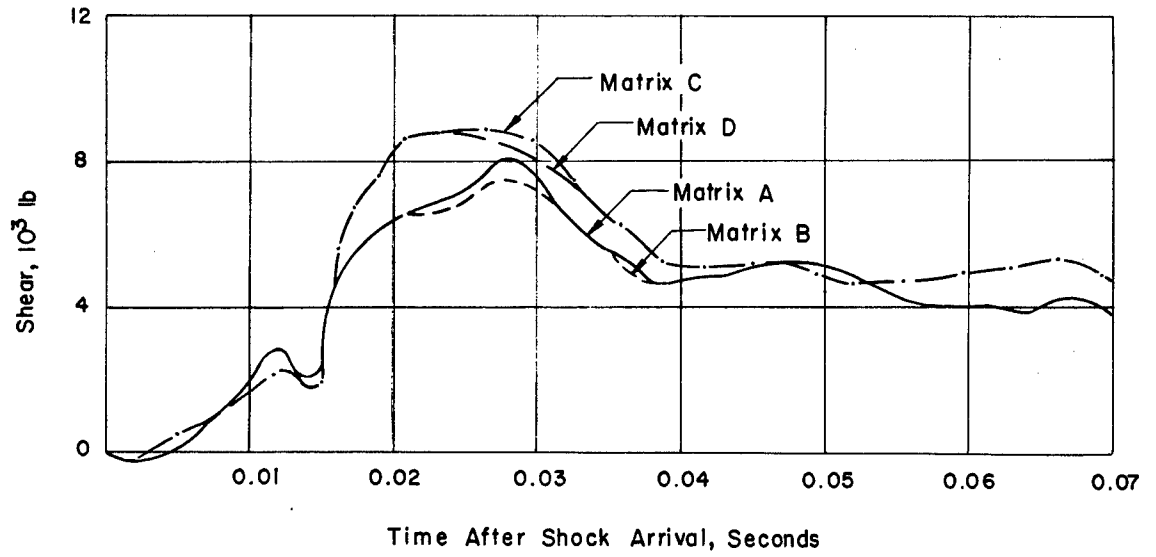


Figure 8.7 Wing shear at Station 36.5 from matrix measurements, Shot Priscilla.

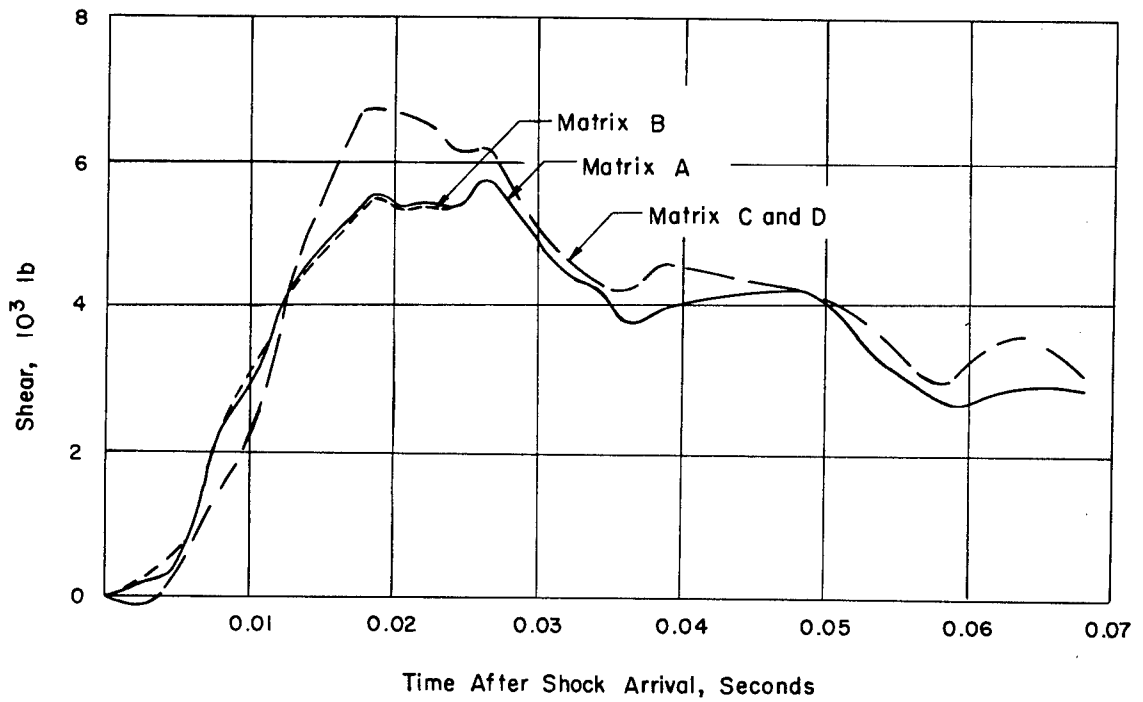


Figure 8.8 Wing shear at Station 36.5 from matrix measurements, Shot Hood.

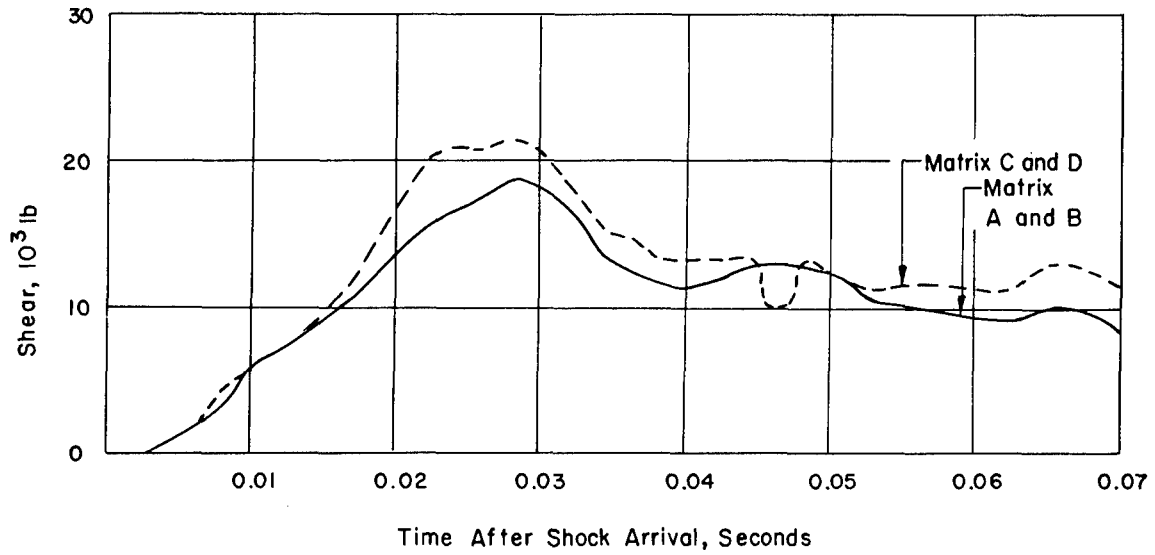


Figure 8.9 Wing shear at Station 36.5 from matrix measurements, Shot Diablo.

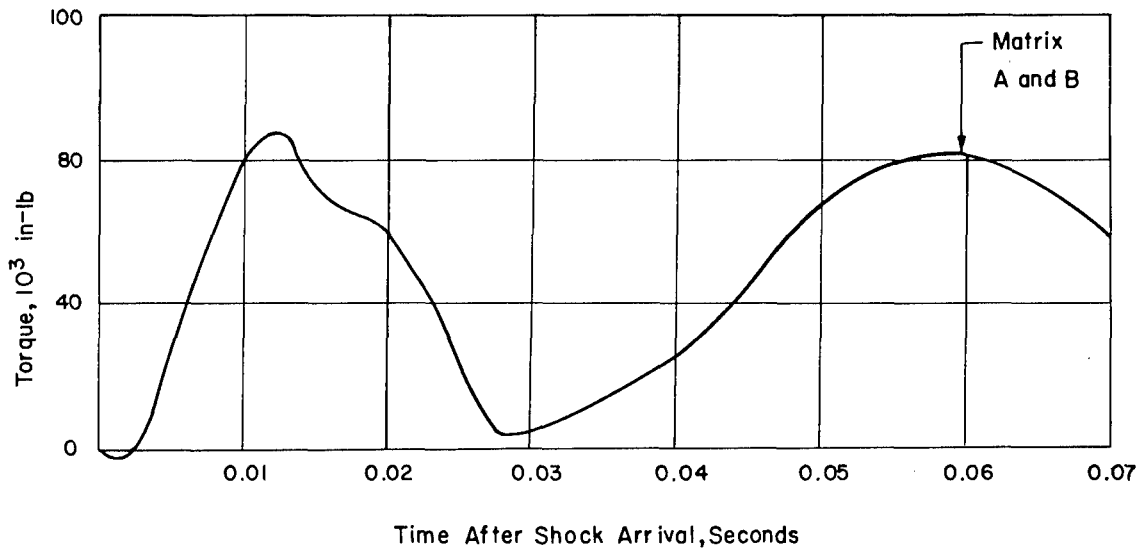


Figure 8.10 Wing torque about fuselage Station 283 from matrix measurements at Station 36.5, Shot Boltzmann.

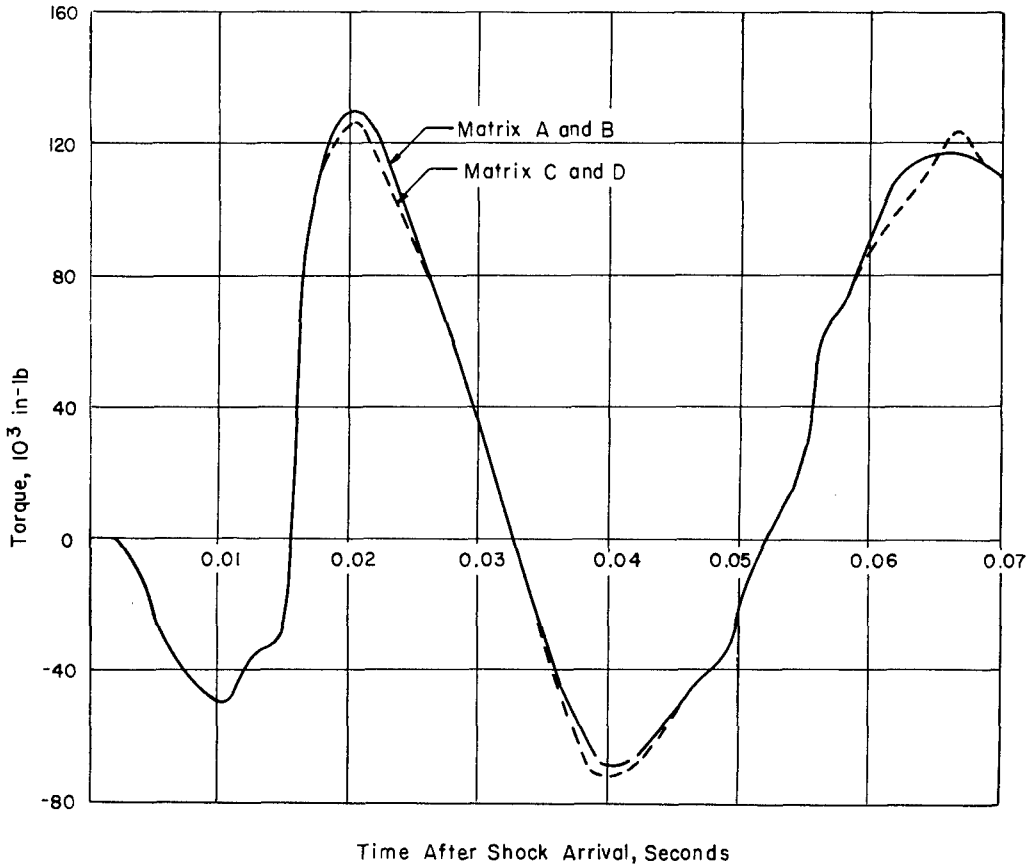


Figure 8.11 Wing torque about fuselage Station 283 from matrix measurements at Station 36.5, Shot Priscilla.

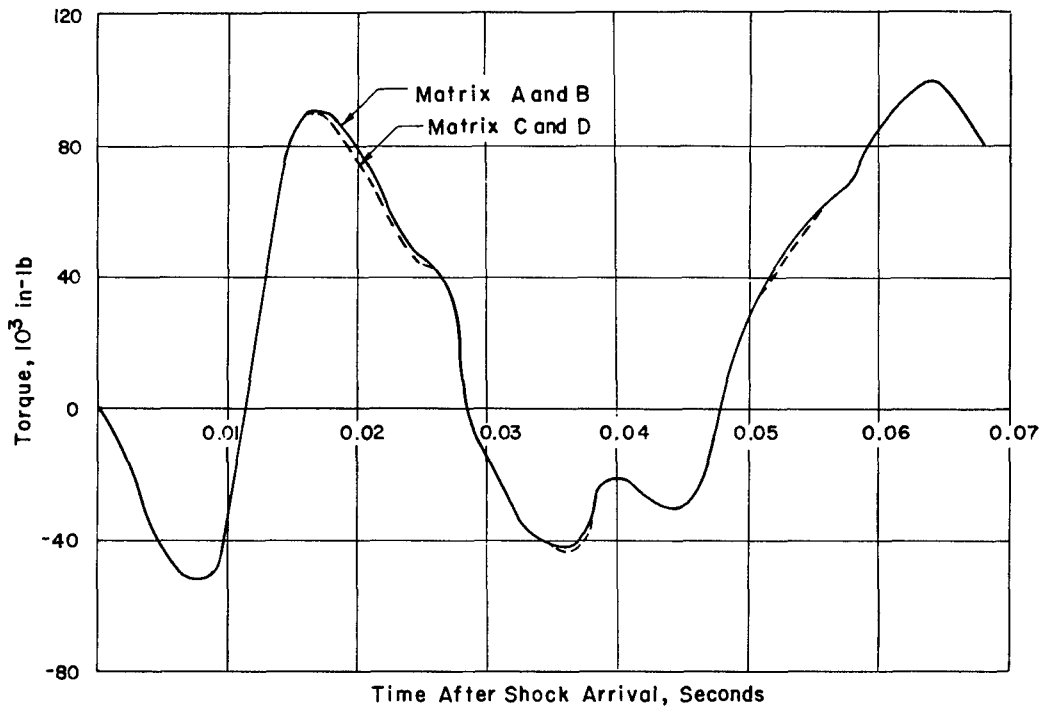


Figure 8.12 Wing torque about fuselage Station 283 from matrix measurements at Station 36.5, Shot Hood.

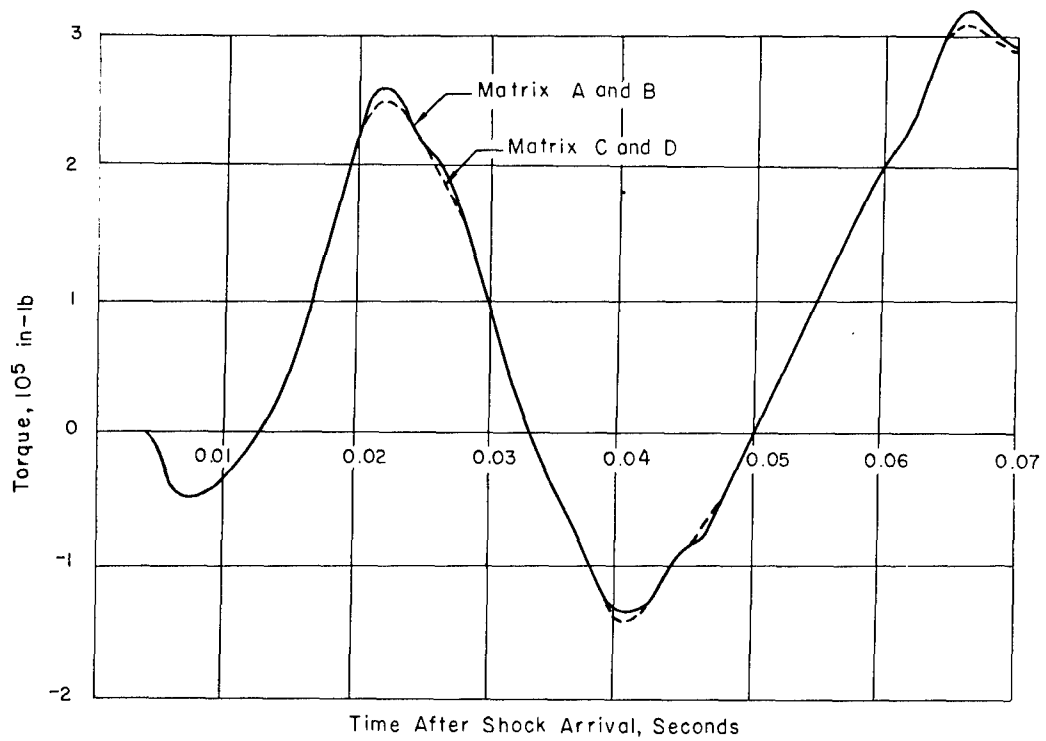


Figure 8.13 Wing torque about fuselage Station 283 from matrix measurements at Station 36.5, Shot Diablo.

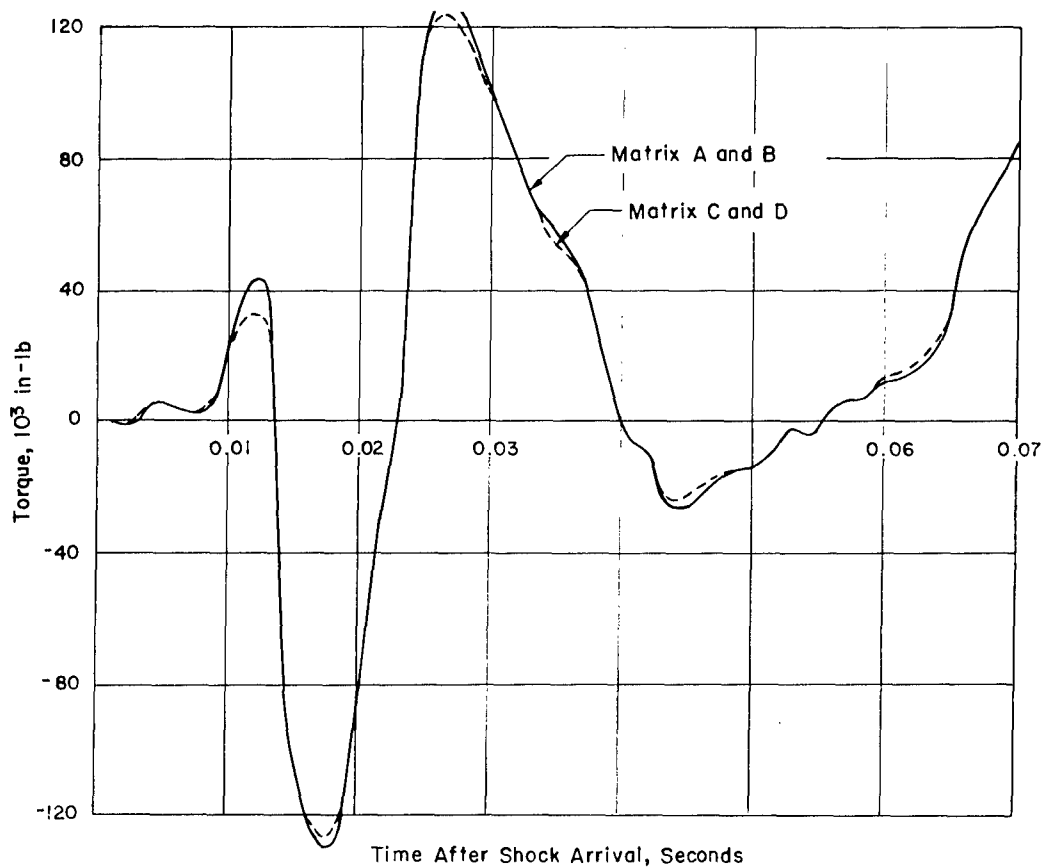


Figure 8.14 Wing torque about fuselage Station 283 from matrix measurements at Station 36.5, Shot Doppler, Airplane No. 827.

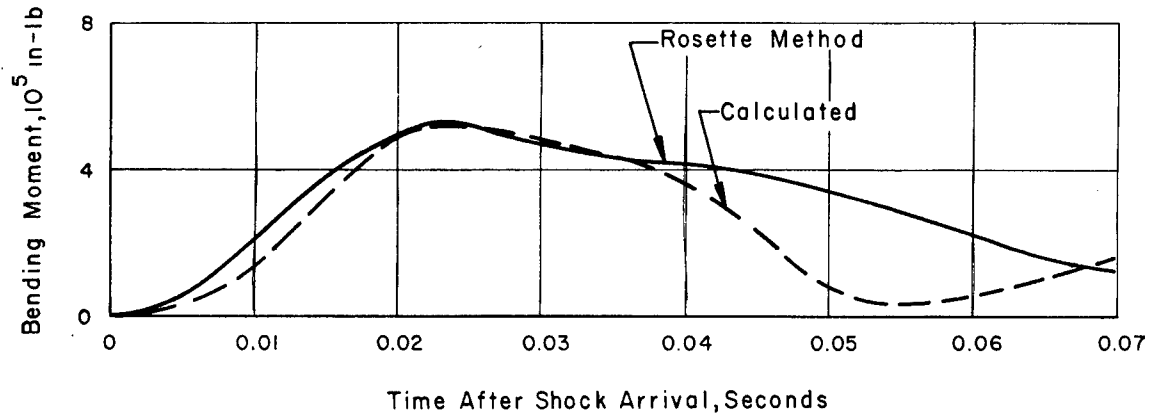


Figure 8.15 Comparison of calculated and measured wing bending moments at Station 36.5, rosette measurements, Shot Boltzmann.

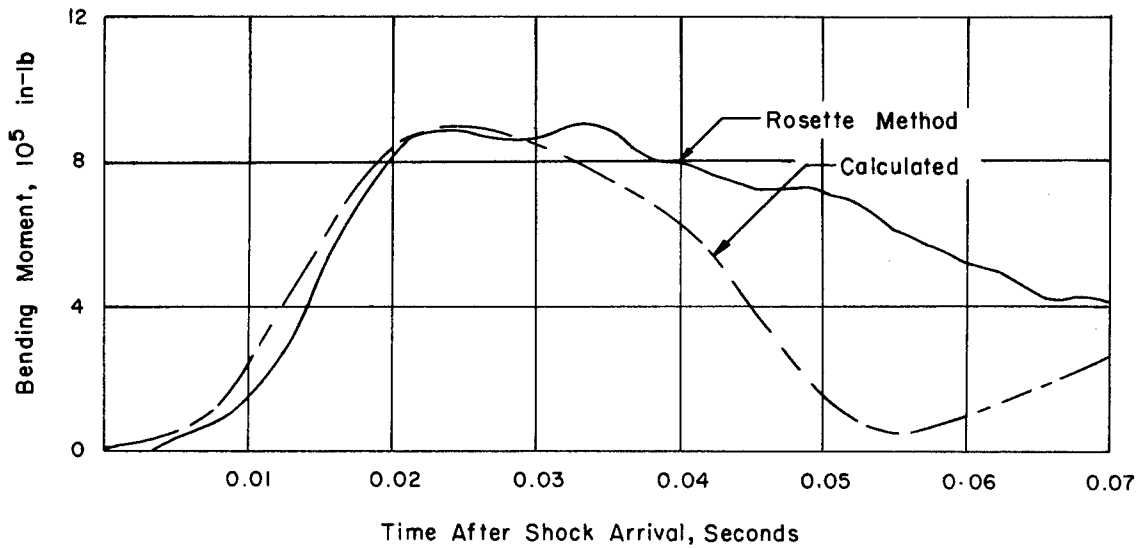


Figure 8.16 Comparison of calculated and measured wing bending moments at Station 36.5, rosette measurements, Shot Priscilla.

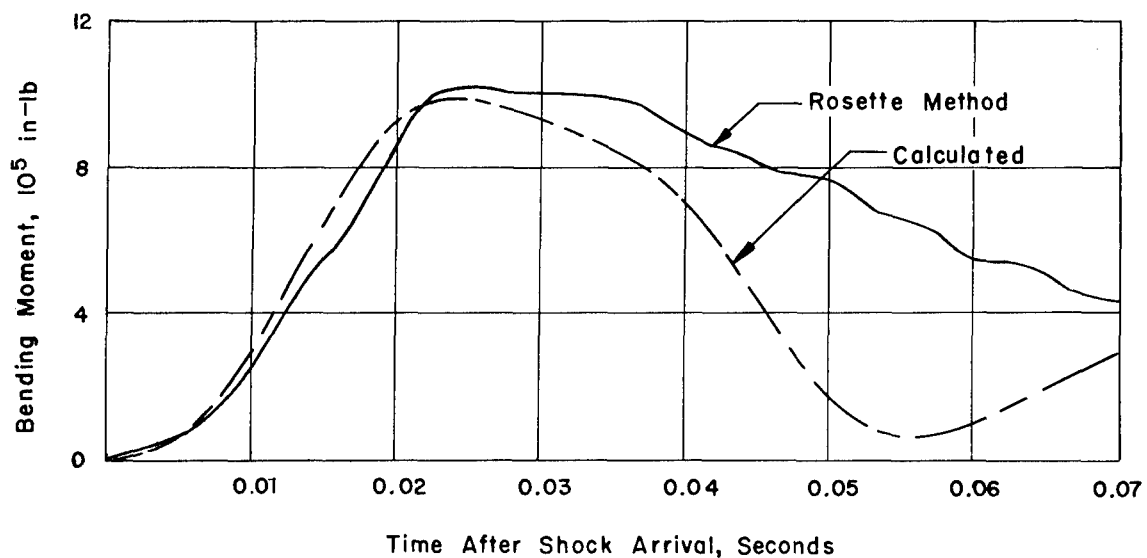


Figure 8.17 Comparison of calculated and measured wing bending moments at Station 36.5, rosette measurements, Shot Hood.

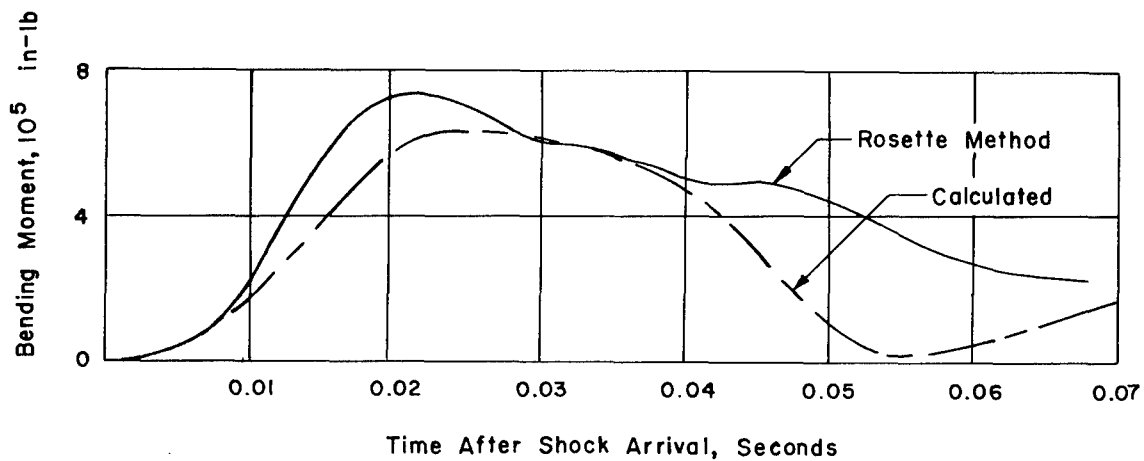


Figure 8.18 Comparison of calculated and measured wing bending moments at Station 36.5, rosette measurements, Shot Diablo.

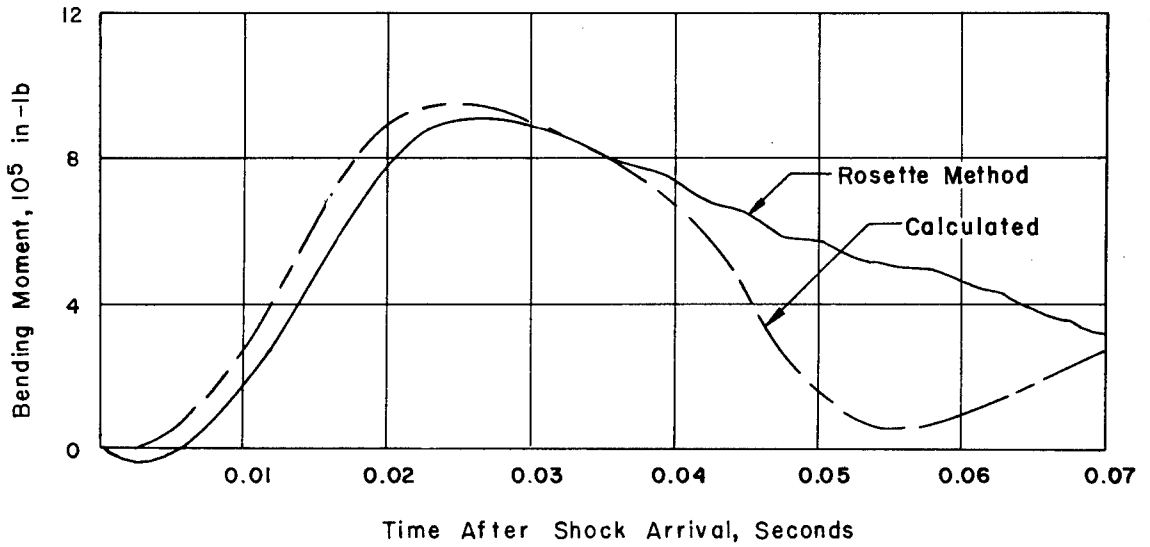


Figure 8.19 Comparison of calculated and measured wing bending moments at Station 36.5, rosette measurements, Shot Shasta.

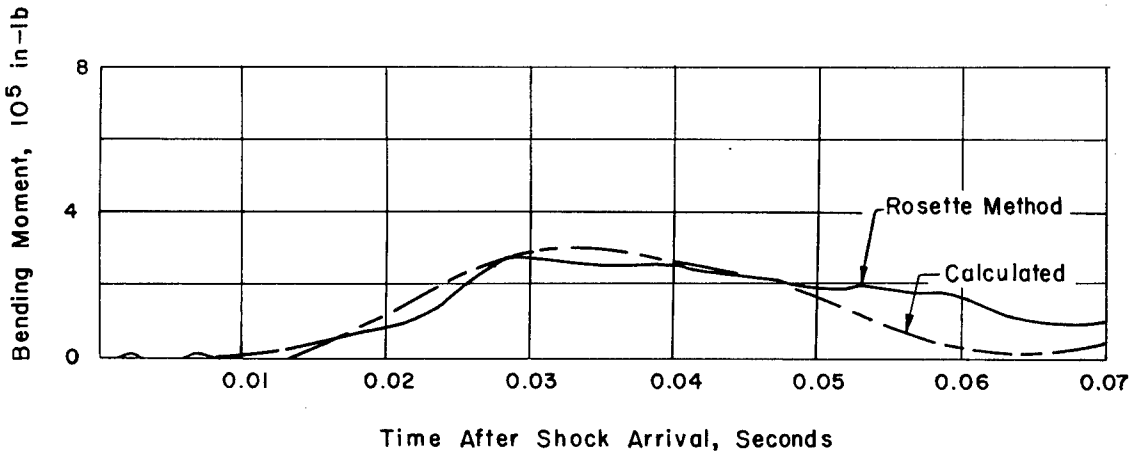


Figure 8.20 Comparison of calculated and measured wing bending moments at Station 36.5, rosette measurements, Shot Doppler, Airplane No. 827.

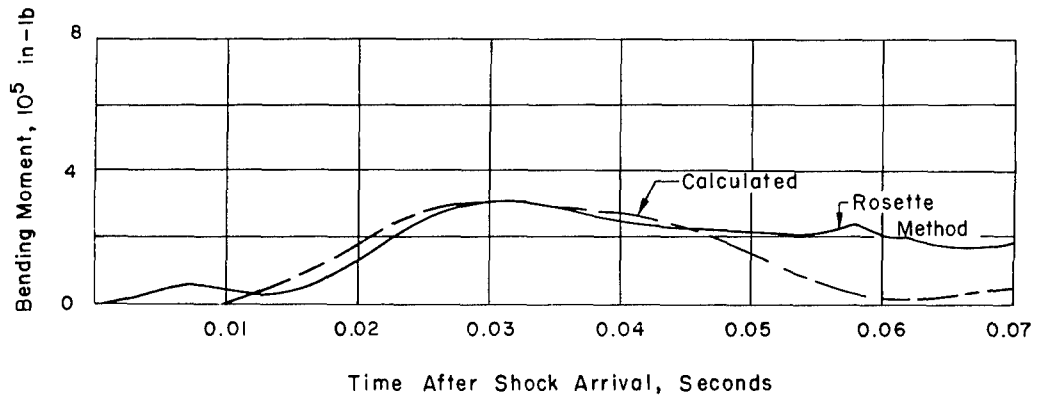


Figure 8.21 Comparison of calculated and measured wing bending moments at Station 36.5, rosette measurements, Shot Doppler, Airplane No. 831.

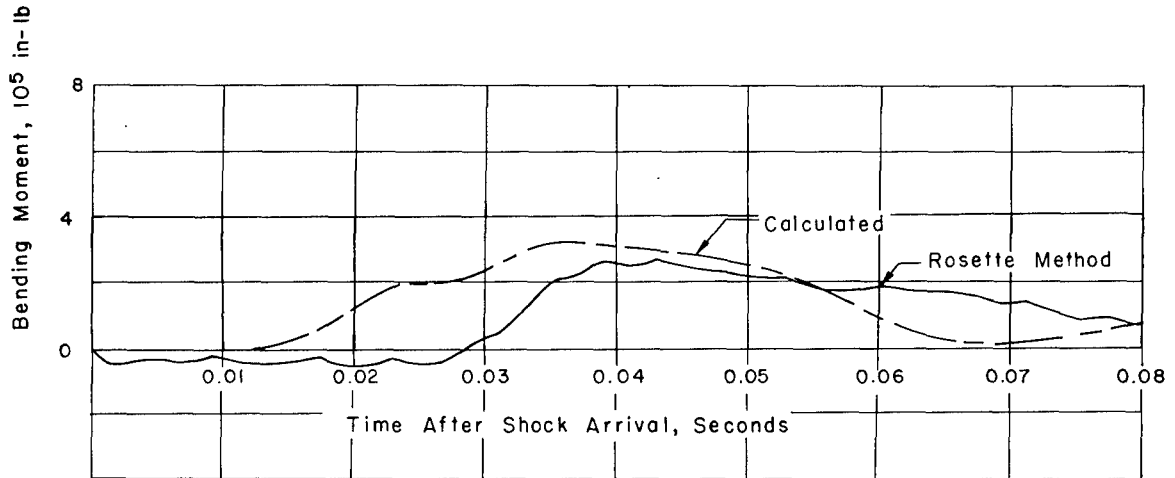


Figure 8.22 Comparison of calculated and measured wing bending moments at Station 36.5, rosette measurements, Shot Smoky.

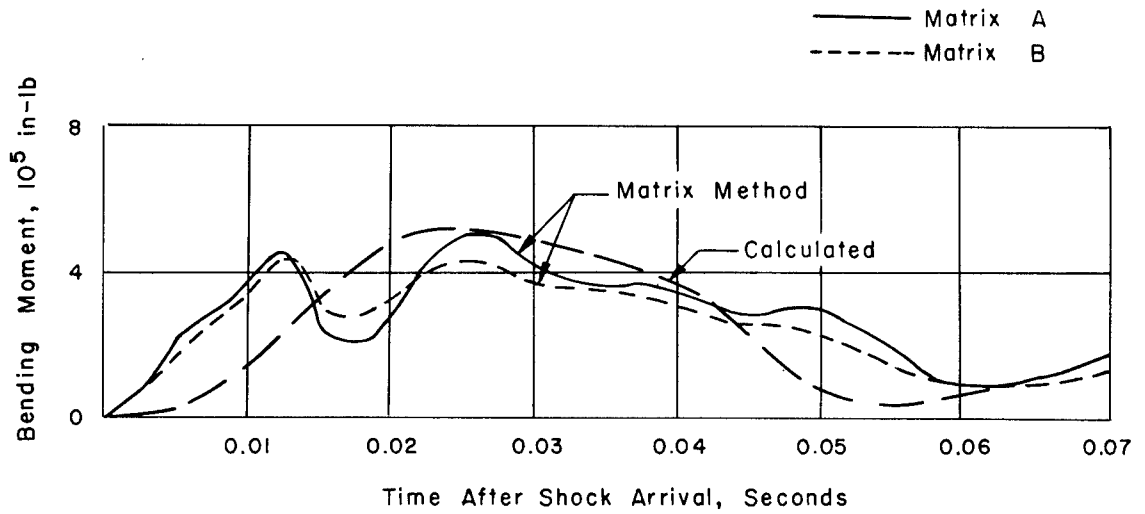


Figure 8.23 Comparison of calculated and measured wing bending moments at Station 36.5, matrix measurements, Shot Boltzmann.

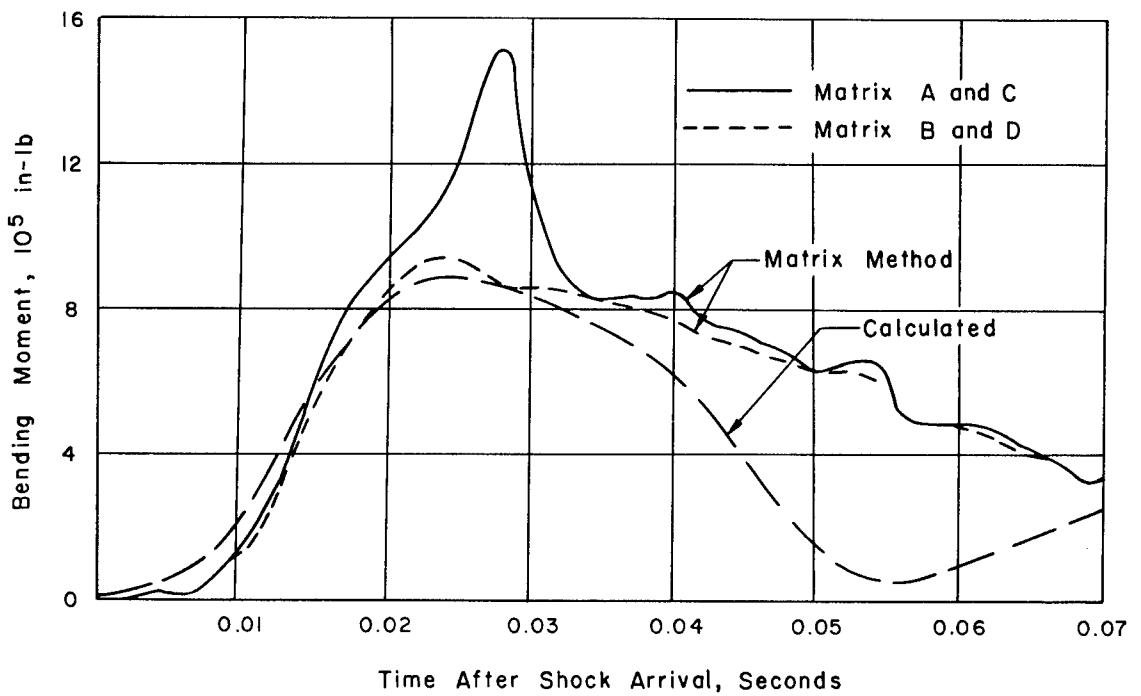


Figure 8.24 Comparison of calculated and measured wing bending moments at Station 36.5, matrix measurements, Shot Priscilla.

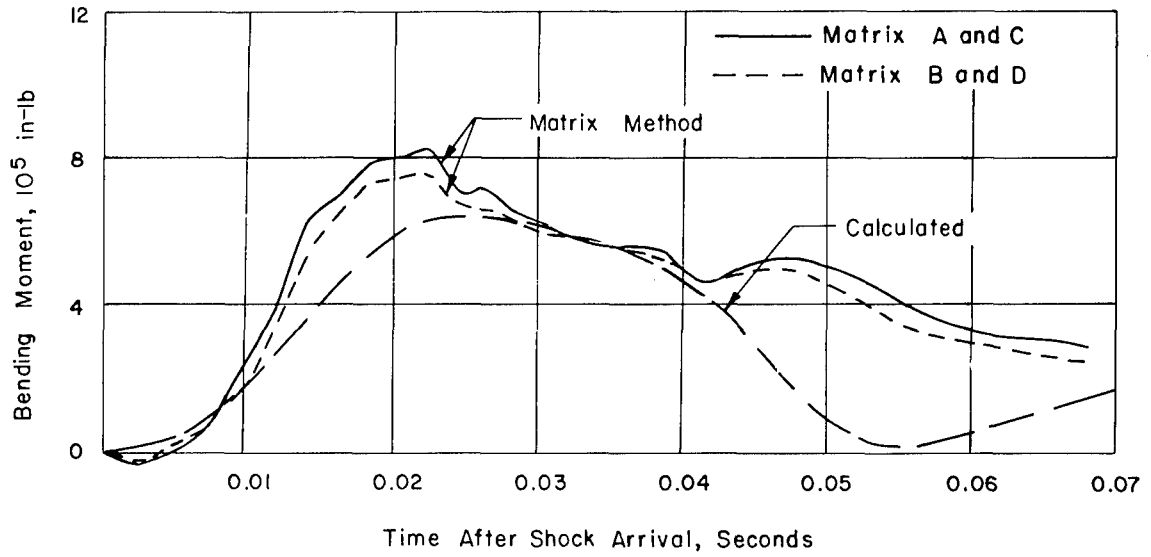


Figure 8.25 Comparison of calculated and measured wing bending moments at Station 36.5, matrix measurements, Shot Hood.

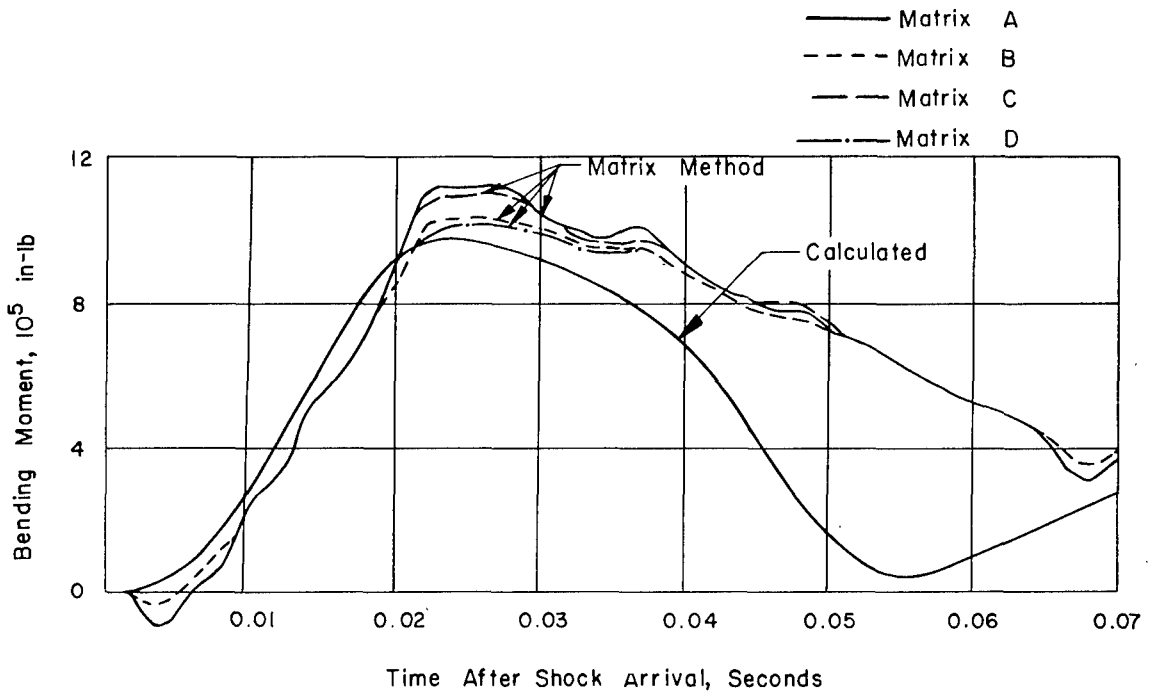


Figure 8.26 Comparison of calculated and measured wing bending moments at Station 36.5, matrix measurements, Shot Diablo.

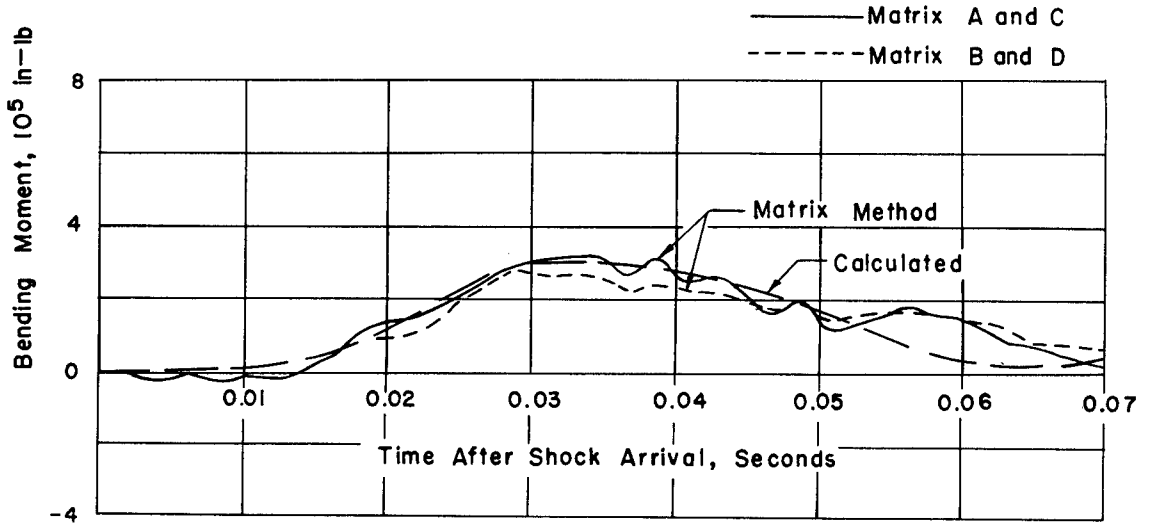


Figure 8.27 Comparison of calculated and measured wing bending moments at Station 36.5, matrix measurements, Shot Doppler, Airplane No. 827.

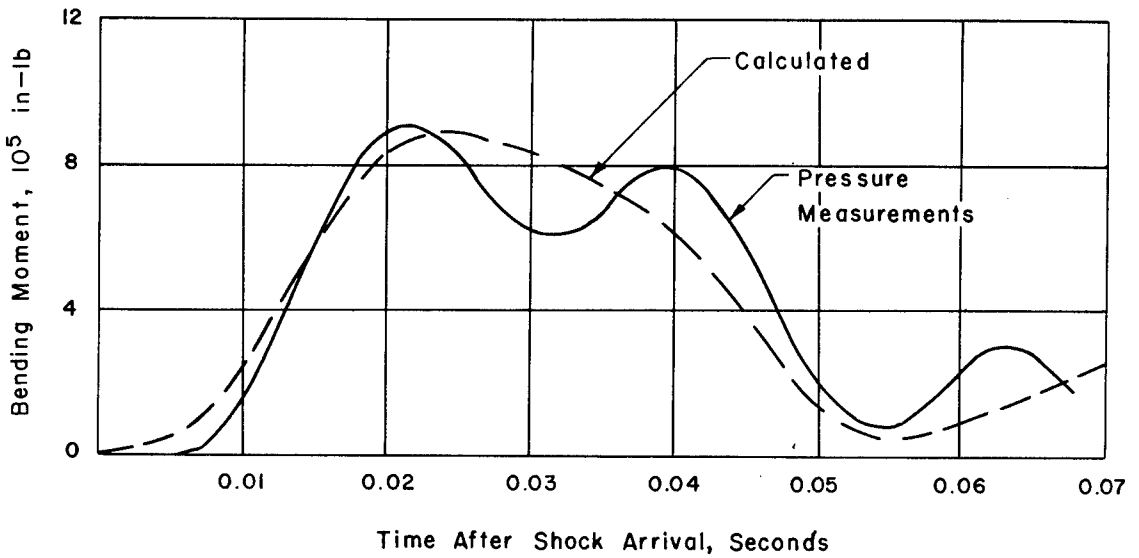


Figure 8.28 Comparison of calculated and measured wing bending moments at Station 36.5, pressure measurements, Shot Priscilla.

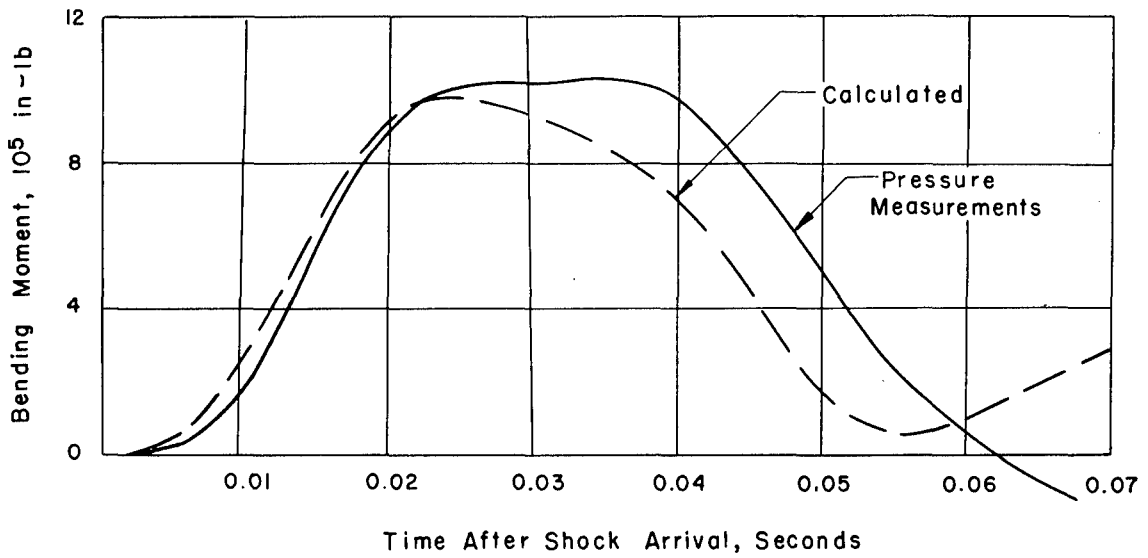


Figure 8.29 Comparison of calculated and measured wing bending moments at Station 36.5, pressure measurements, Shot Diablo.

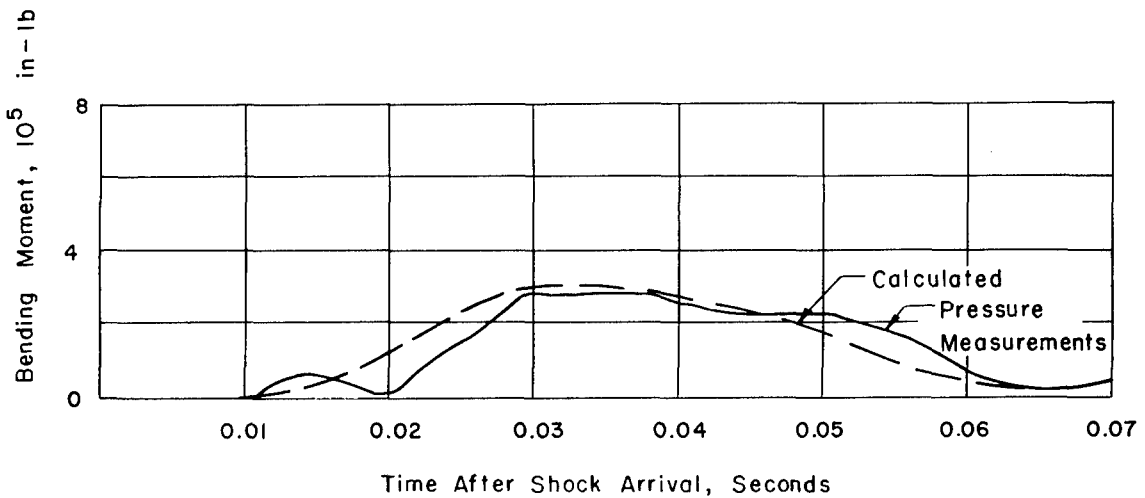


Figure 8.30 Comparison of calculated and measured wing bending moments at Station 36.5, pressure measurements, Shot Doppler, Airplane No. 827.

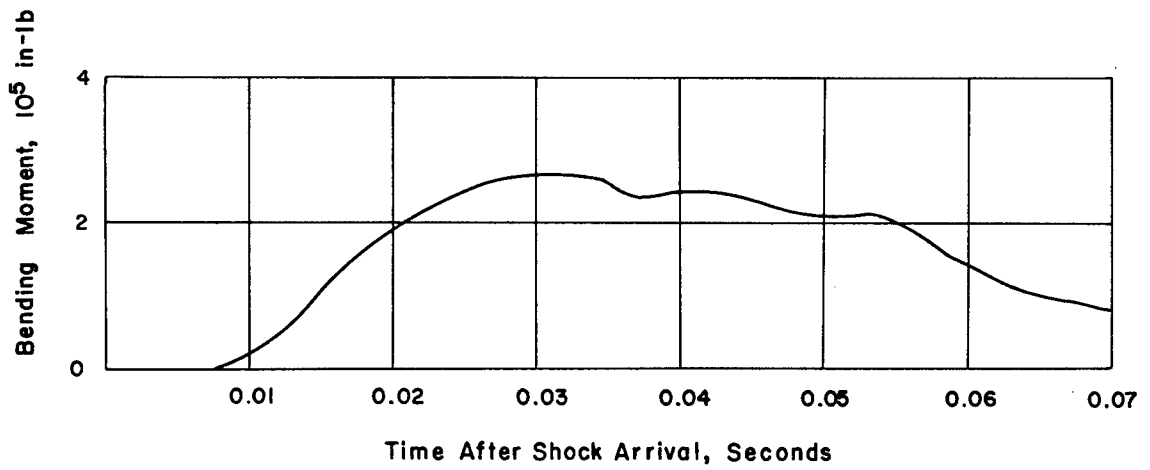


Figure 8.31 Wing bending moment at Station 72 from rosette measurements, Shot Boltzmann.

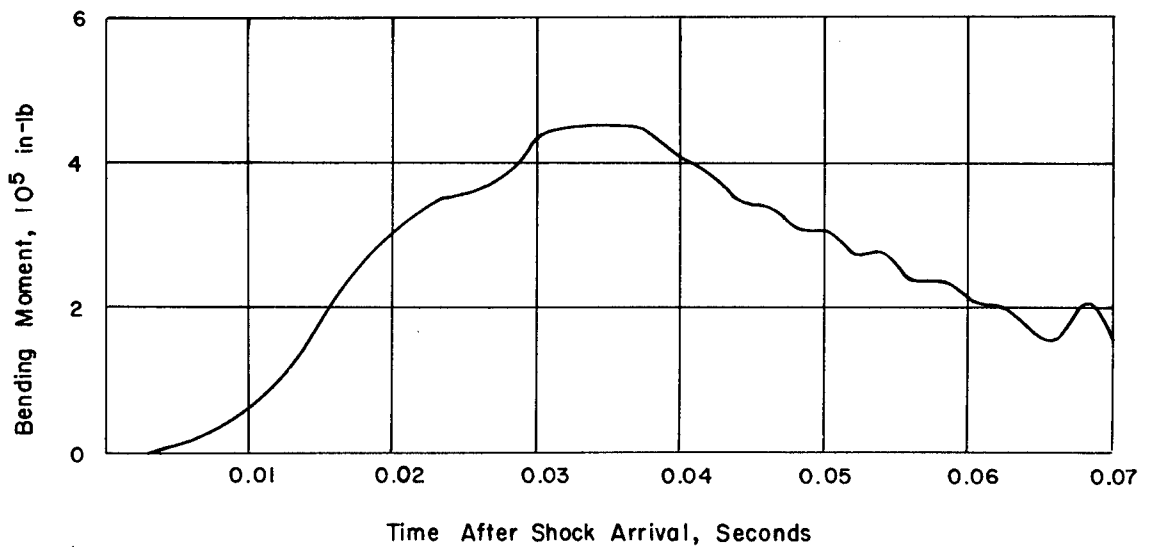


Figure 8.32 Wing bending moment at Station 72 from rosette measurements, Shot Priscilla.

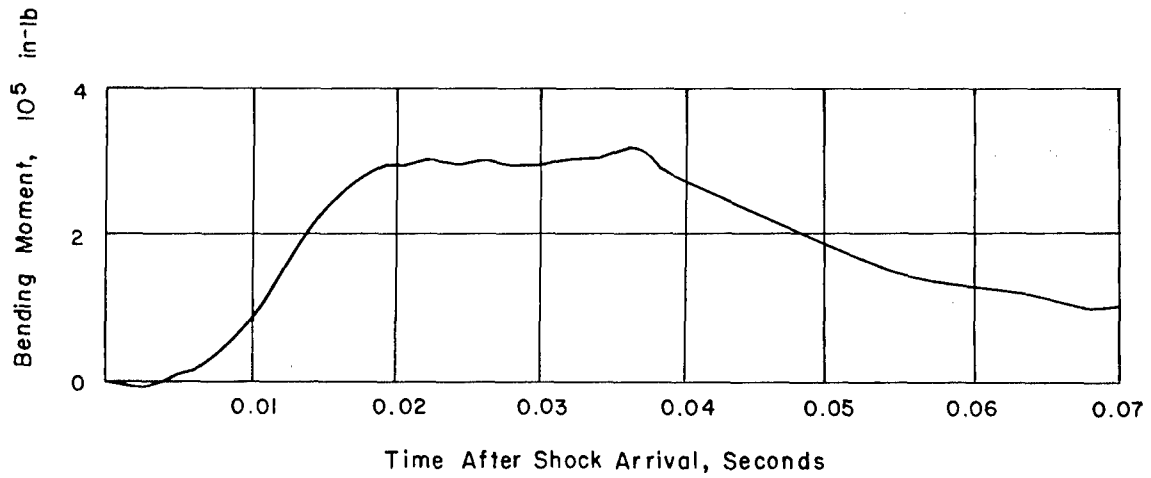


Figure 8.33 Wing bending moment at Station 72 from rosette measurements, Shot Hood.

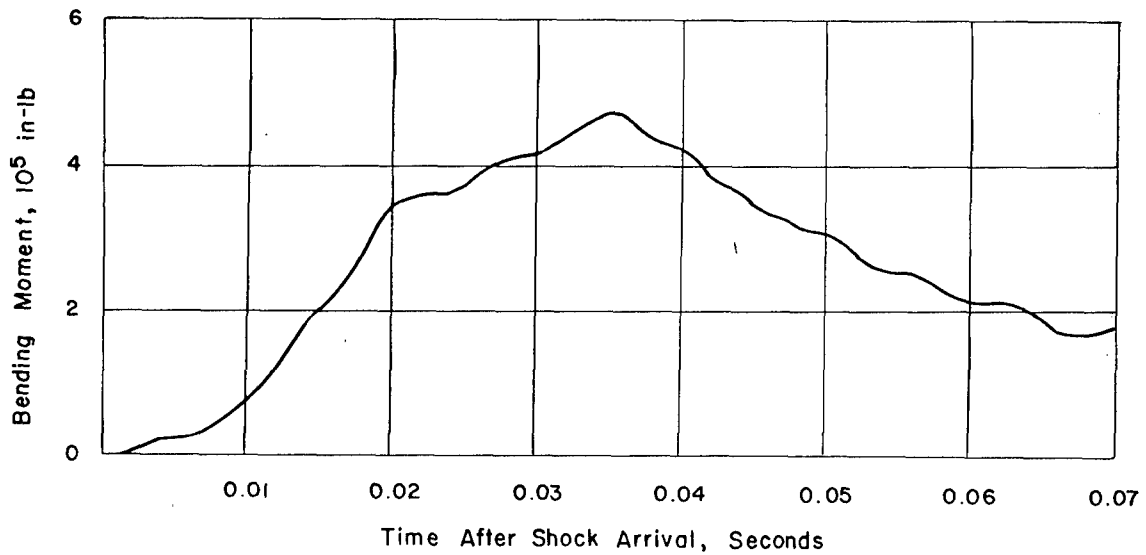


Figure 8.34 Wing bending moment at Station 72 from rosette measurements, Shot Diablo.

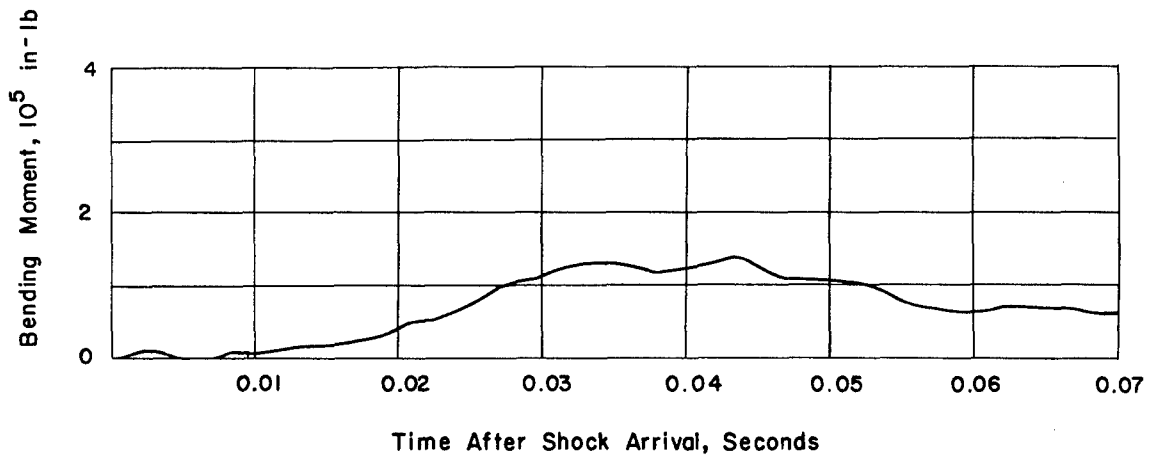


Figure 8.35 Wing bending moment at Station 72 from rosette measurements, Shot Doppler, Airplane No. 827.

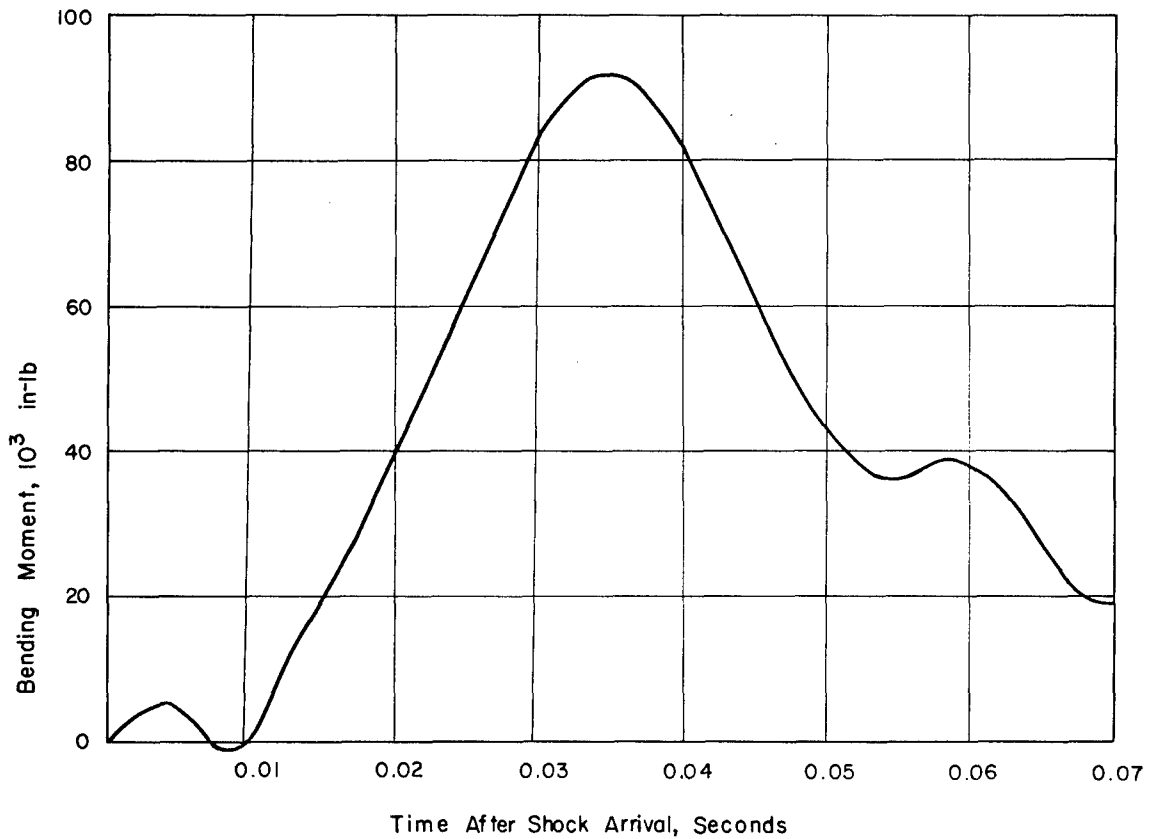


Figure 8.36 Wing bending moment at Station 113 from rosette measurements, Shot Boltzmann.

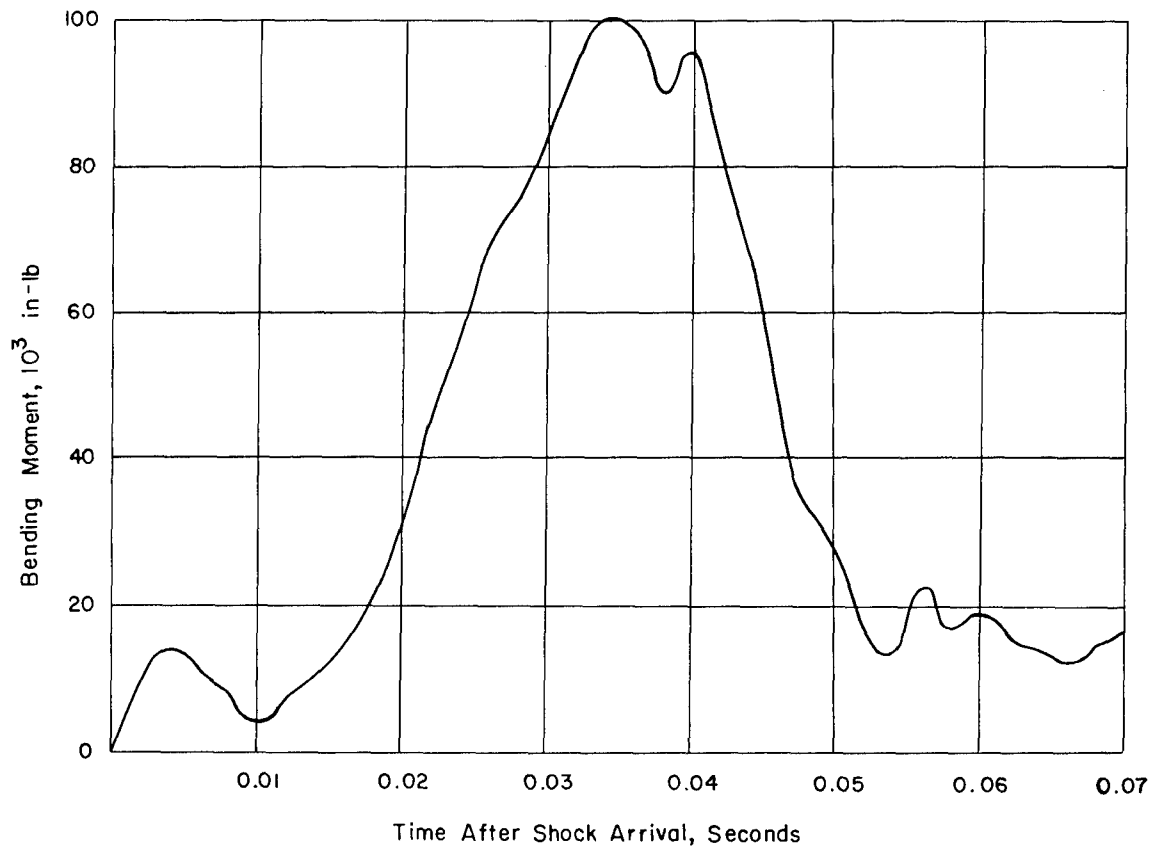


Figure 8.37 Wing bending moment at Station 113 from rosette measurements, Shot Priscilla.

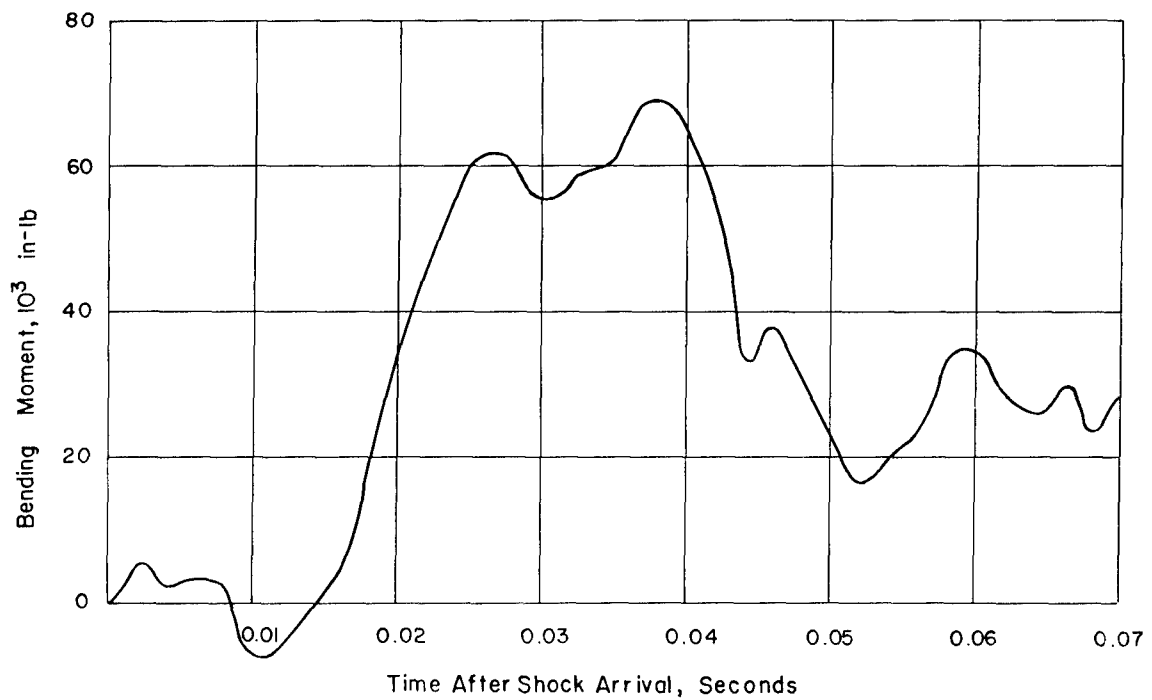


Figure 8.38 Wing bending moment at Station 113 from rosette measurements, Shot Diablo.

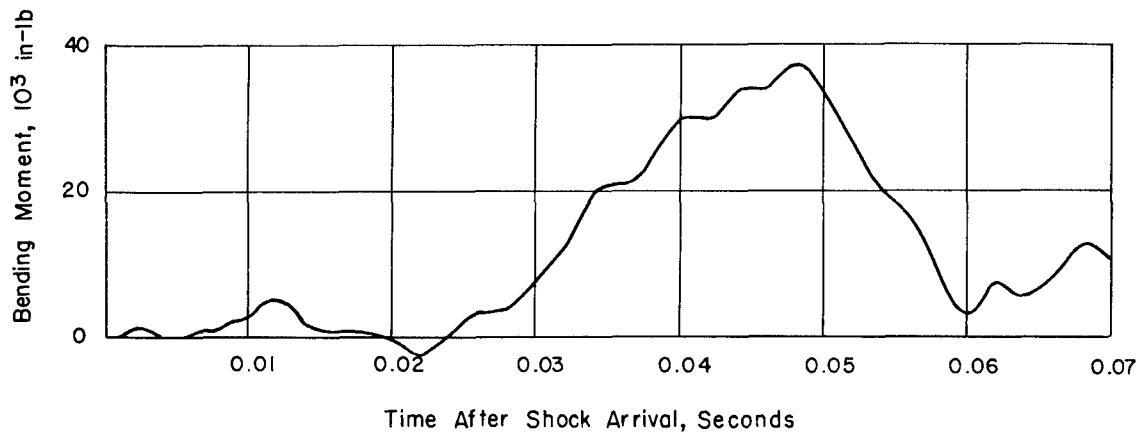


Figure 8.39 Wing bending moment at Station 113 from rosette measurements, Shot Doppler, Airplane No. 827.

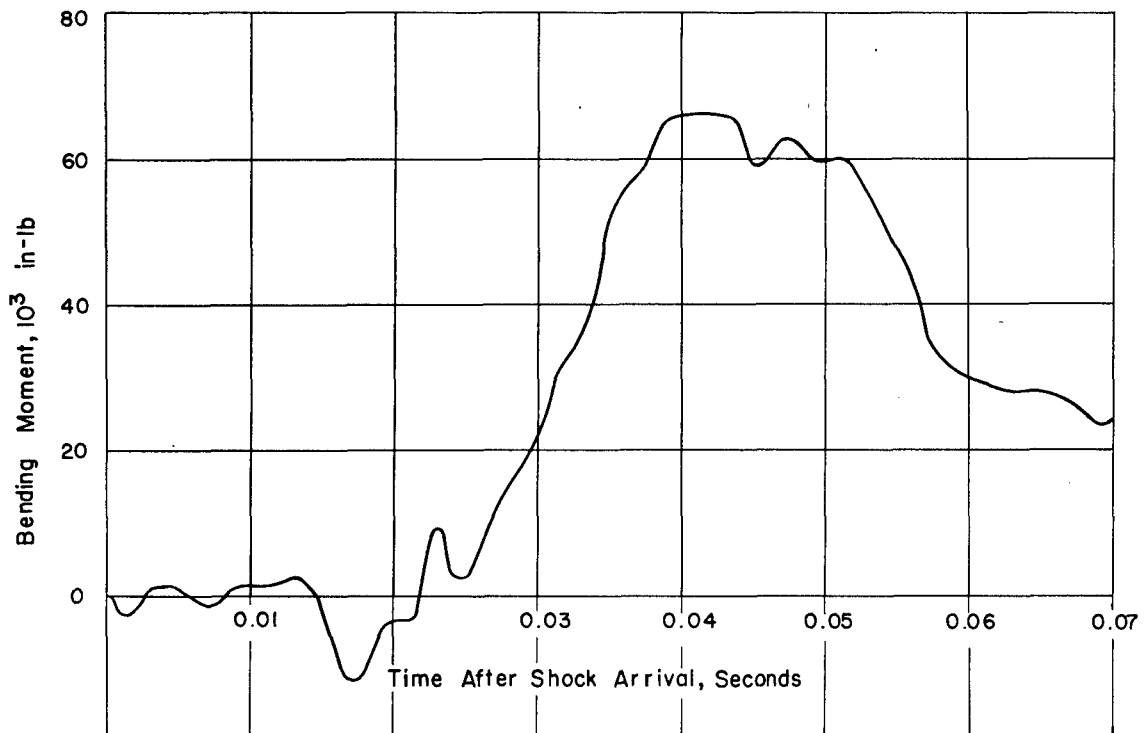


Figure 8.40 Wing bending moment at Station 113 from rosette measurements, Shot Smoky.

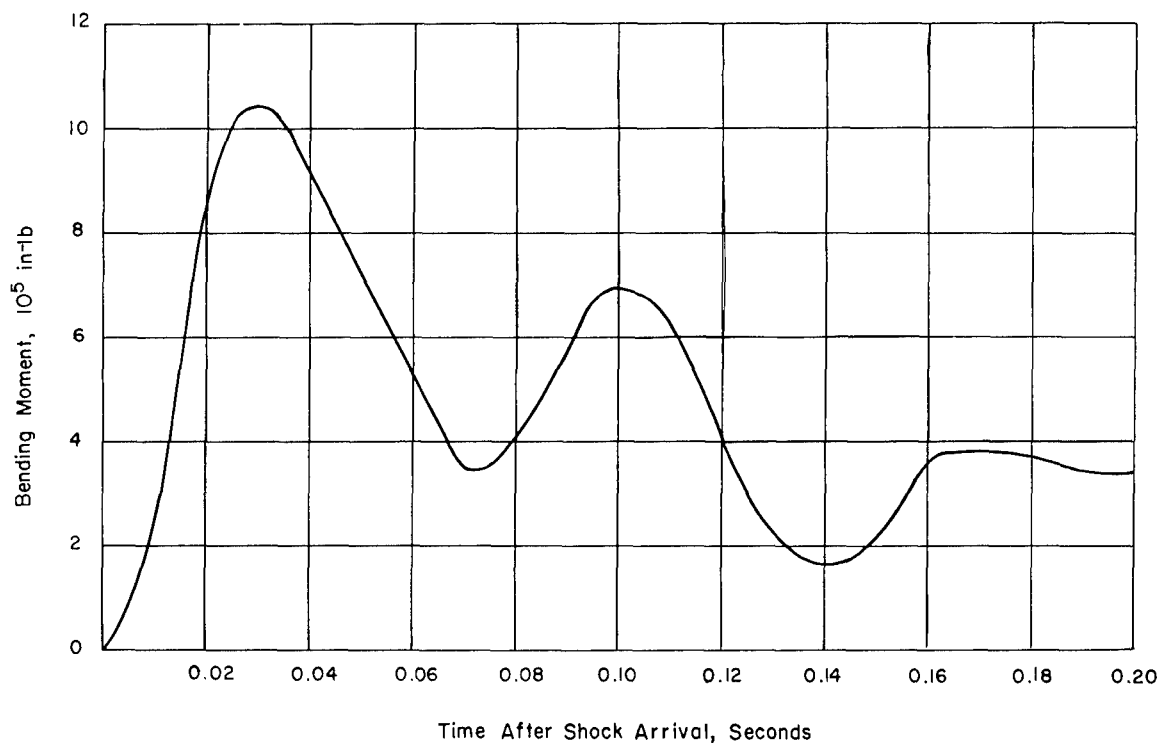


Figure 8.41 Wing bending moment at Station 36.5, matrix measurement, extended time plot, Shot Diablo.

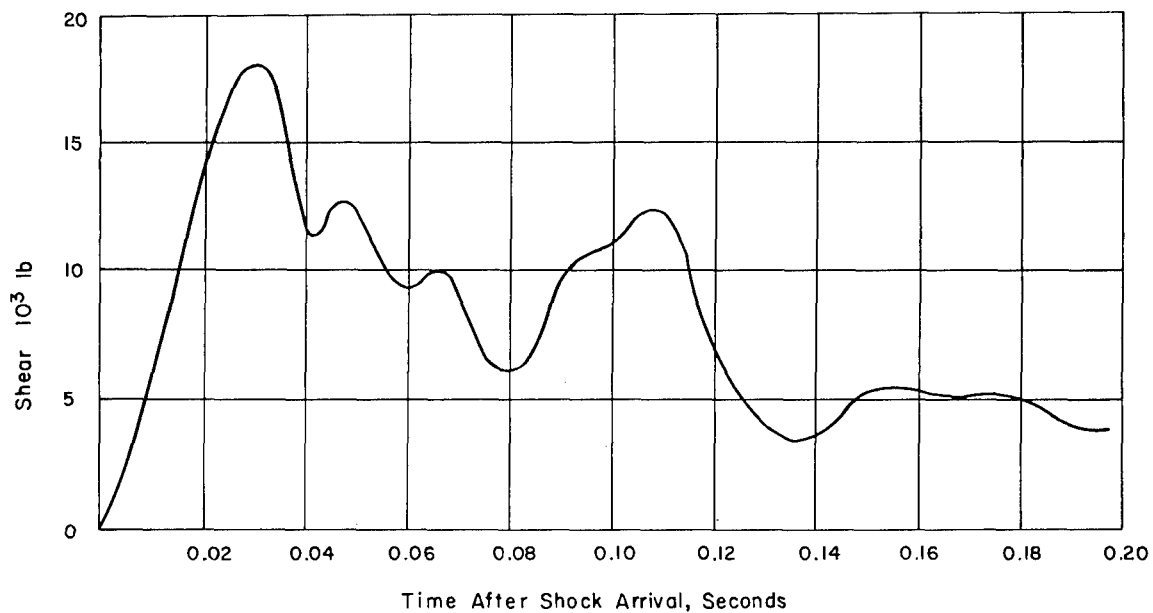


Figure 8.42 Wing shear at Station 36.5, matrix measurement, extended time plot, Shot Diablo.

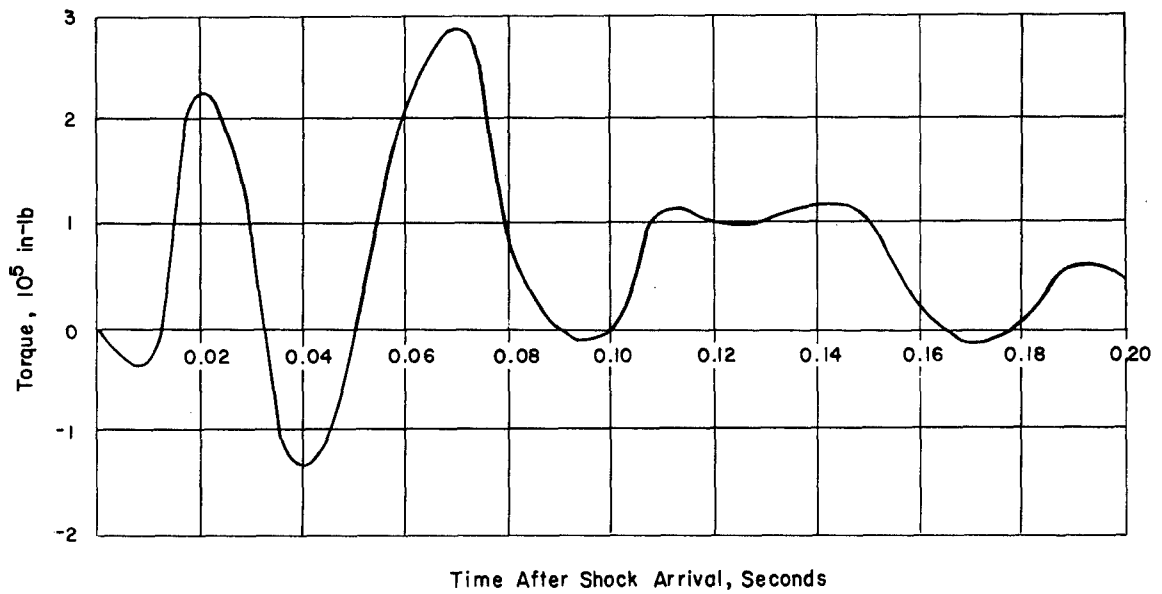


Figure 8.43 Wing torque about fuselage Station 283, matrix measurement, at Station 36.5, extended time plot, Shot Diablo.

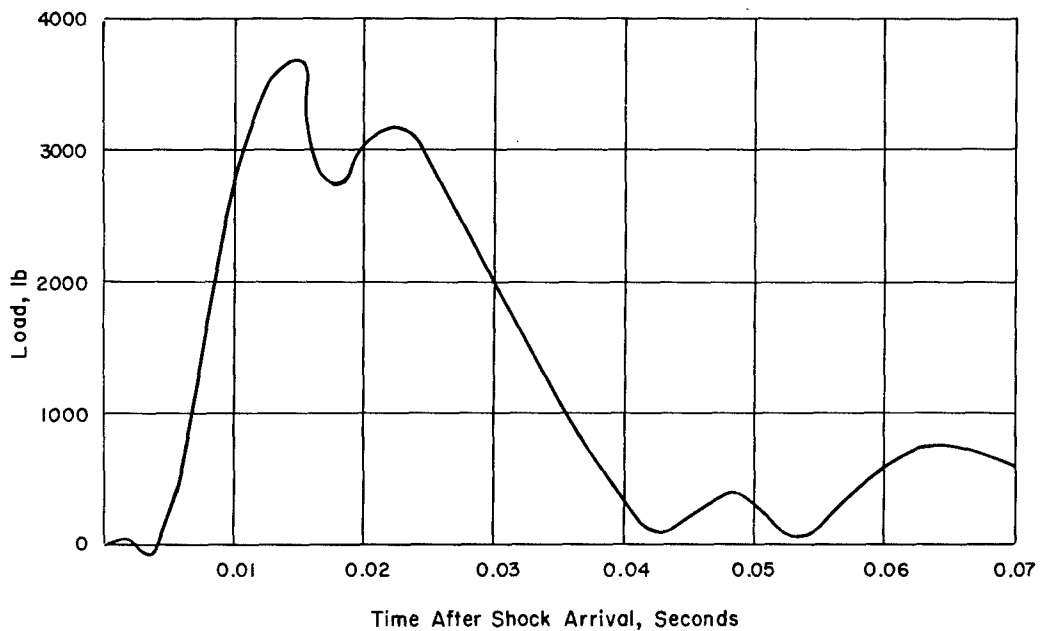


Figure 8.44 Horizontal stabilizer load, matrix method, Shot Diablo.

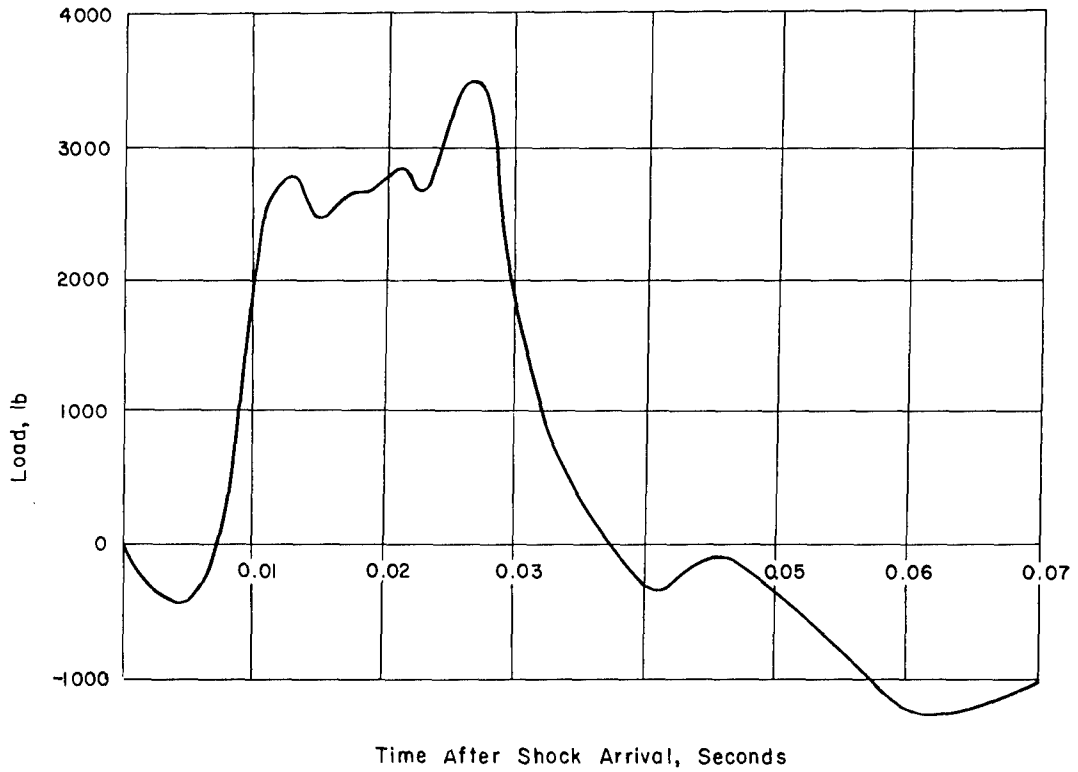


Figure 8.45 Horizontal stabilizer load computed from actuator and lug reactions, Shot Shasta.

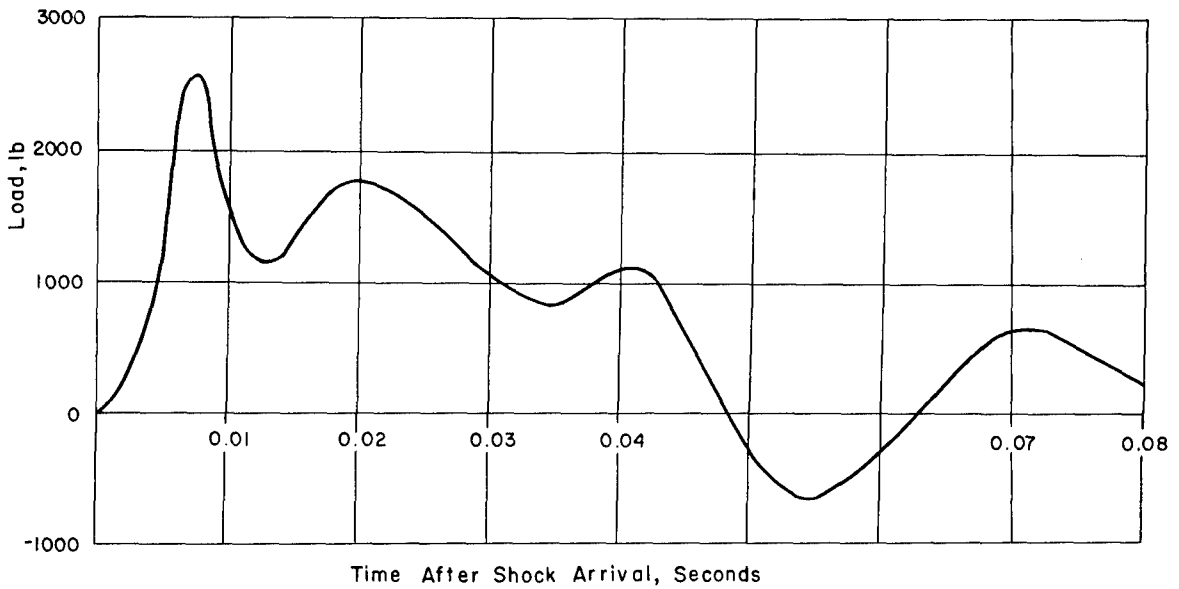


Figure 8.46 Horizontal stabilizer load, matrix method, Shot Doppler, Airplane No. 827.

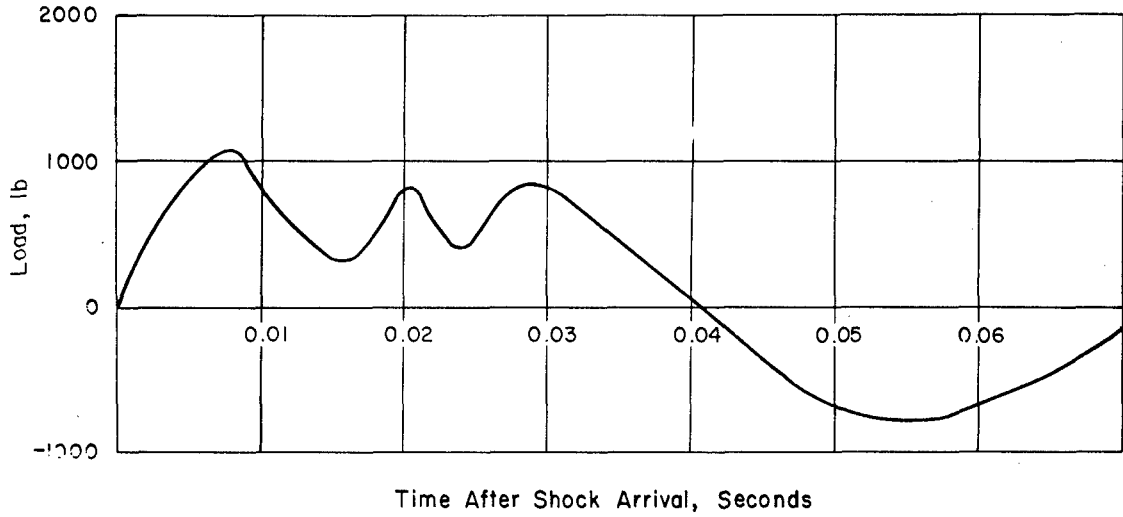


Figure 8.47 Horizontal stabilizer load computed from actuator and lug reactions, Shot Doppler, Airplane No. 831.

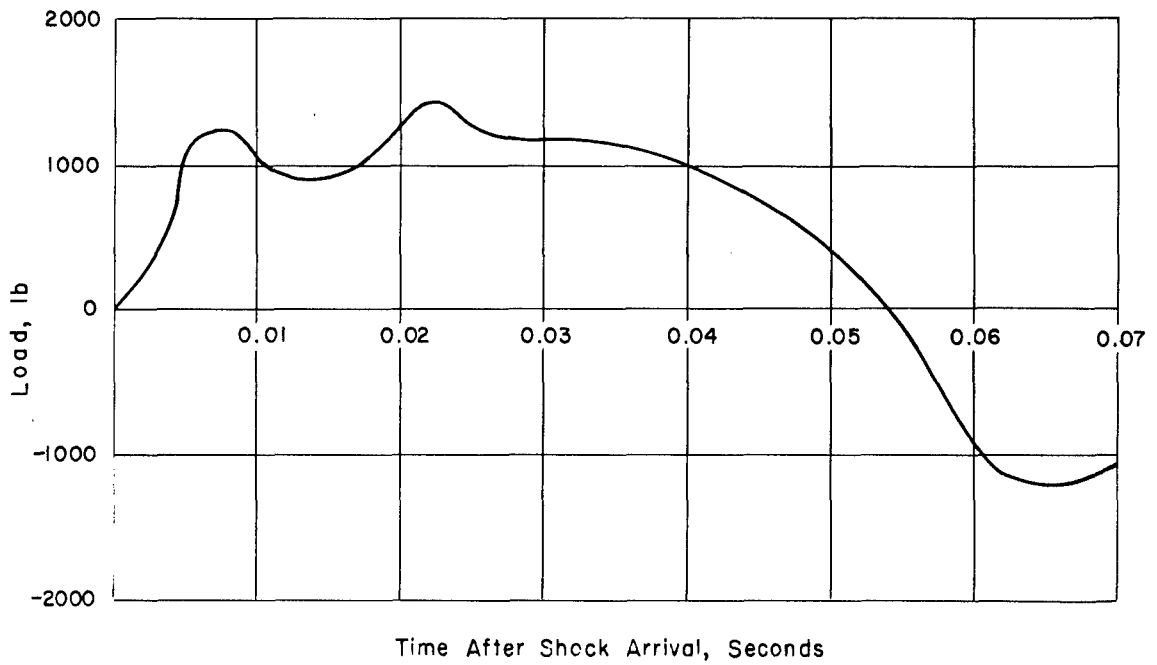


Figure 8.48 Horizontal stabilizer load computed from actuator and lug reactions, Shot Smoky.

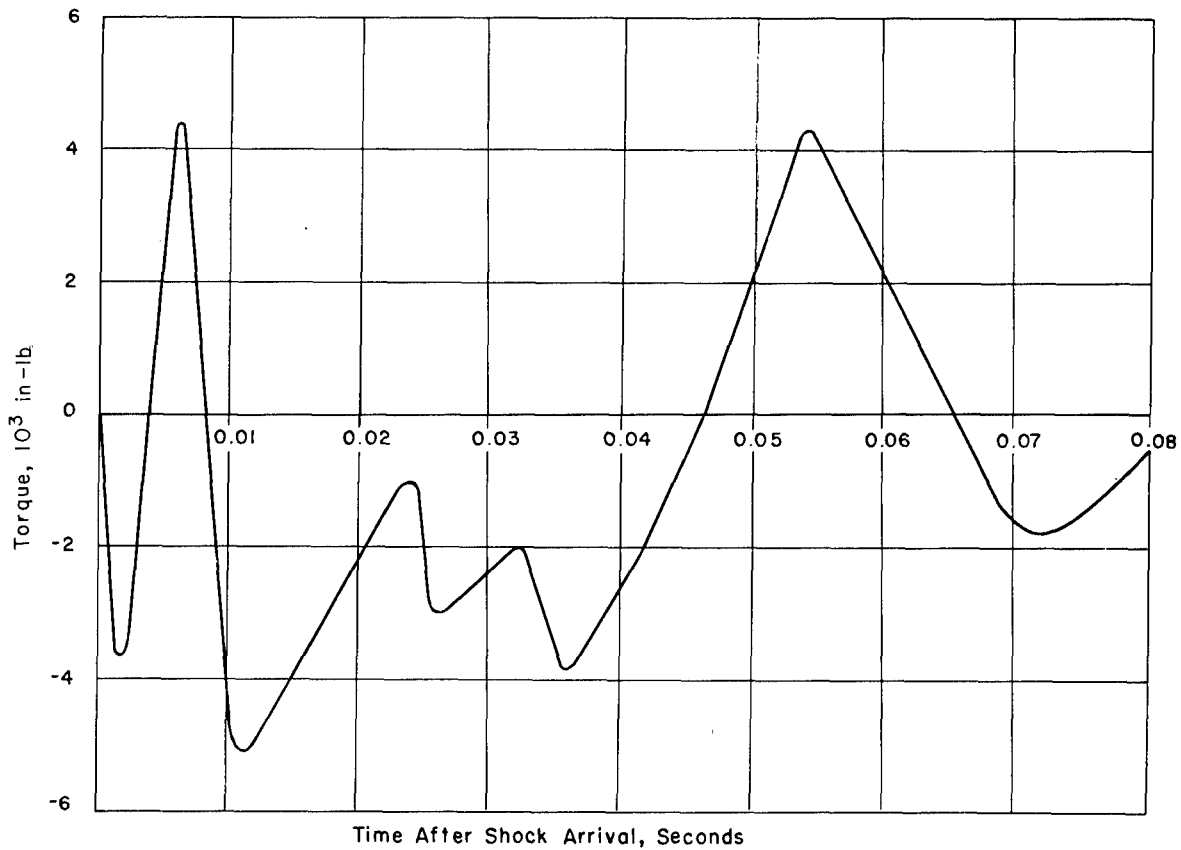


Figure 8.49 Horizontal stabilizer torque about fuselage Station 437.6, matrix method, Shot Diablo.

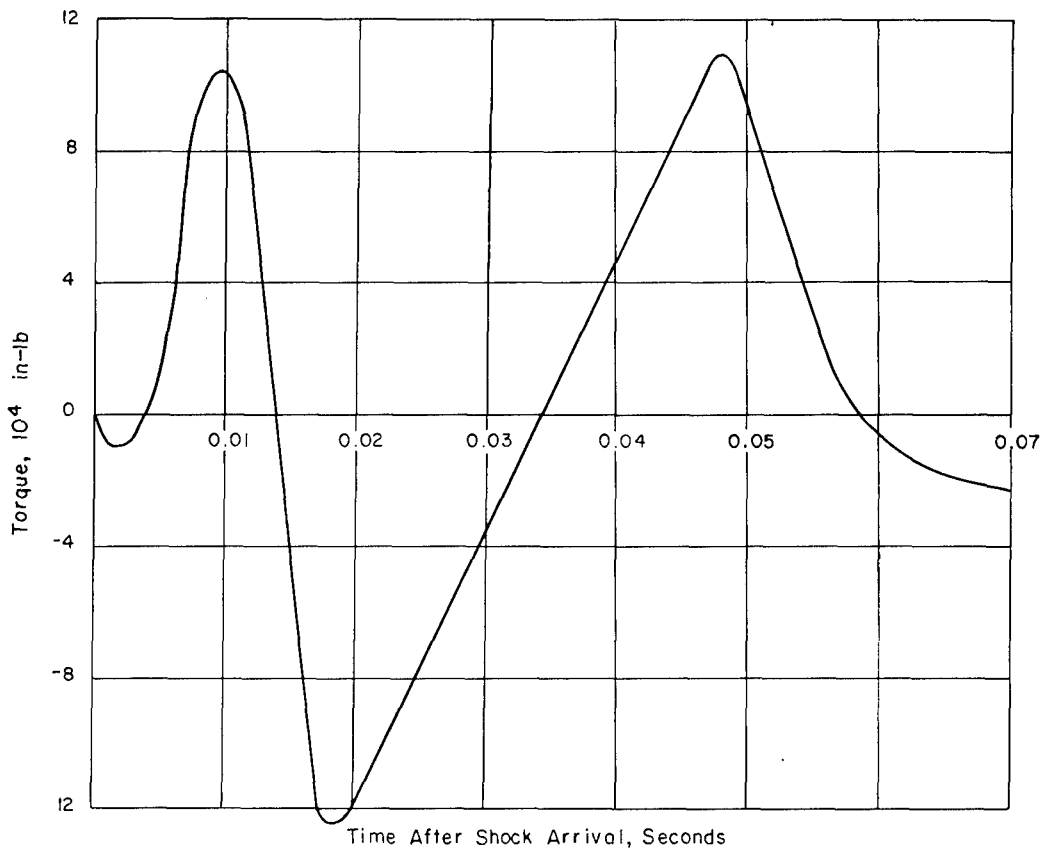


Figure 8.50 Horizontal stabilizer torque about fuselage Station 437.6, matrix method, Shot Doppler, Airplane No. 827.

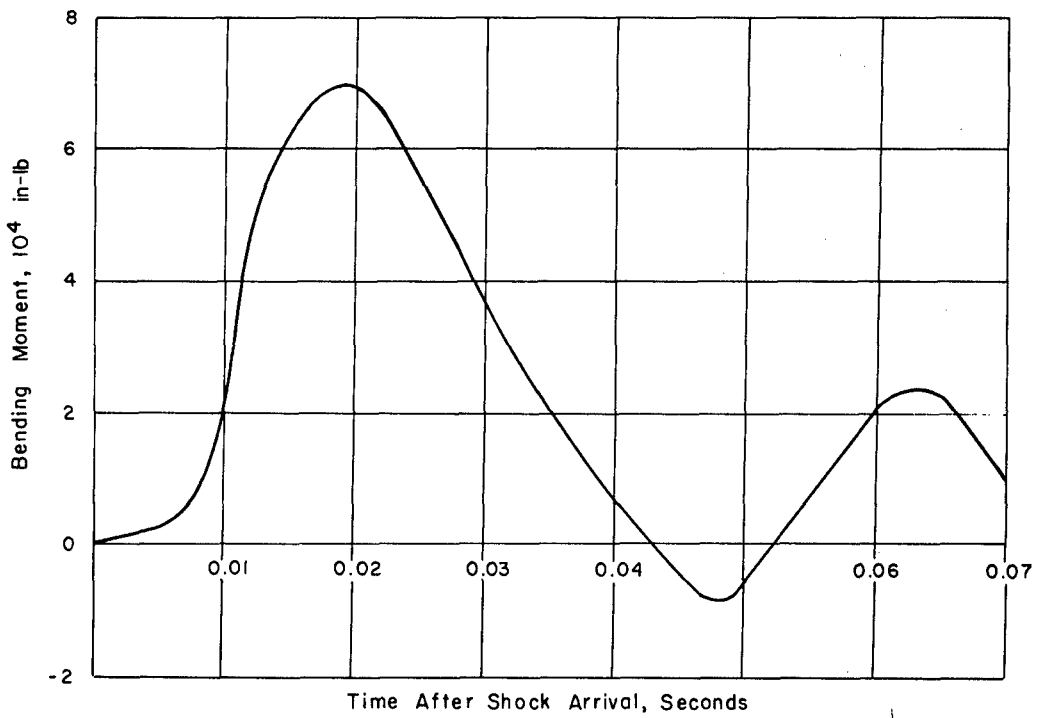


Figure 8.51 Horizontal stabilizer bending moments, matrix method, Shot Diablo.

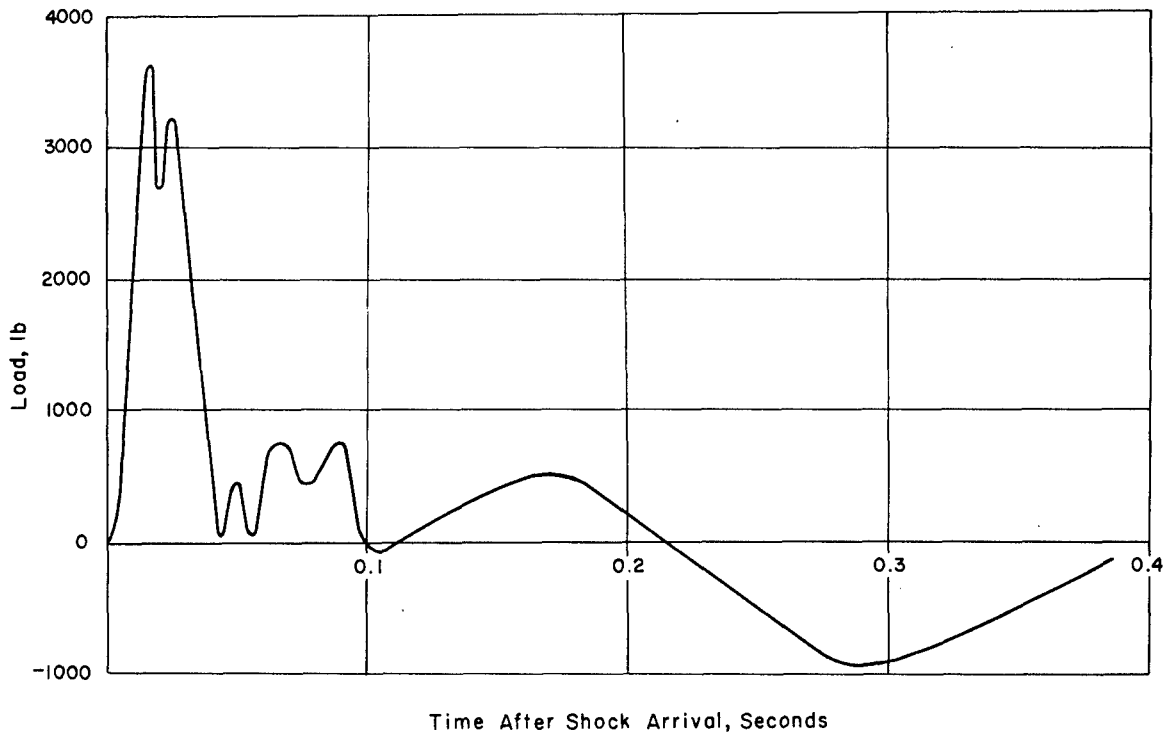


Figure 8.52 Horizontal stabilizer load, matrix method, extended time plot, Shot Diablo.

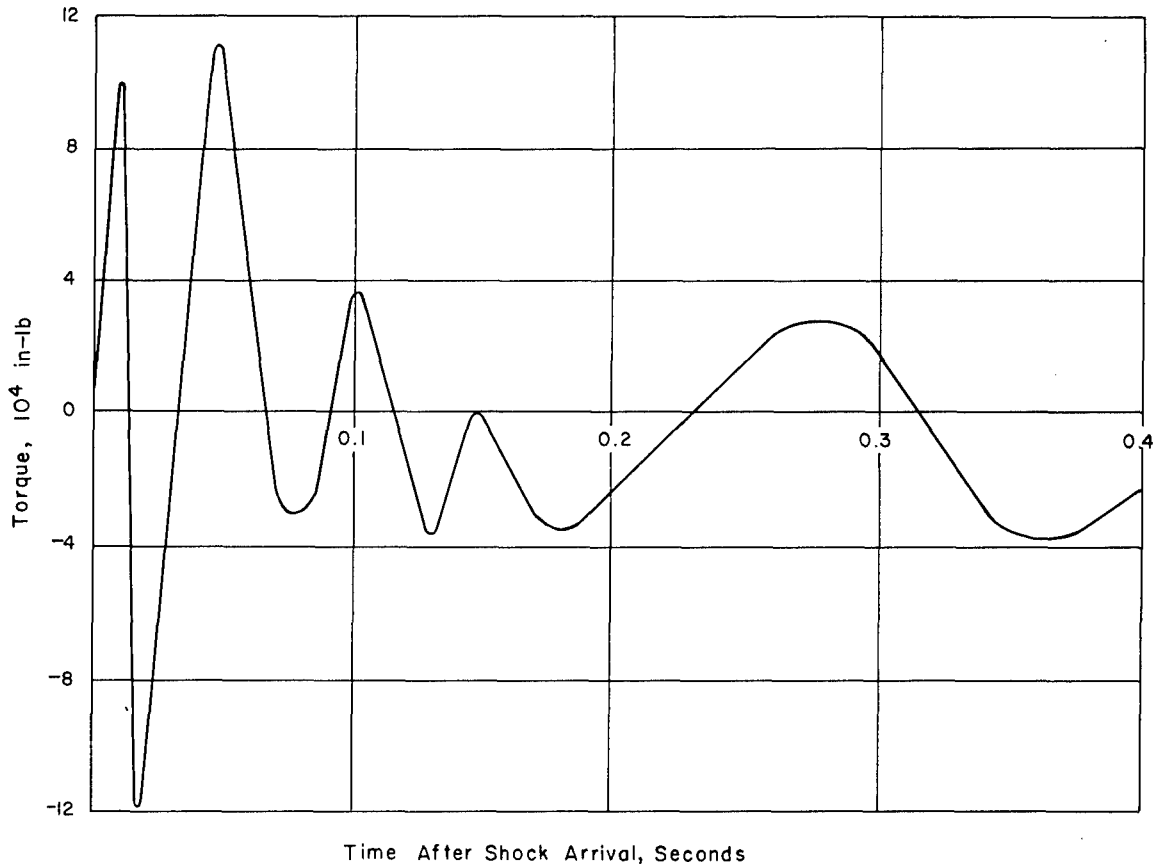


Figure 8.53 Horizontal stabilizer torque about fuselage Station 437.6, matrix method, extended time plot, Shot Diablo.

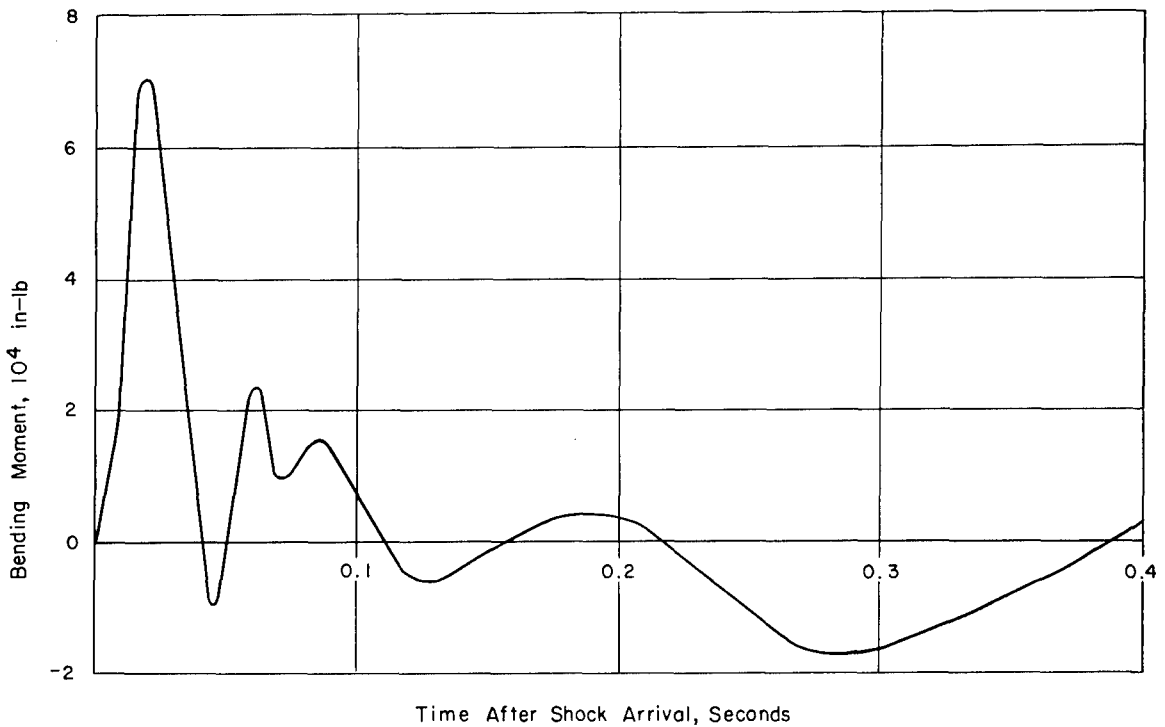


Figure 8.54 Horizontal stabilizer bending moment, matrix method, extended time plot, Shot Diablo.

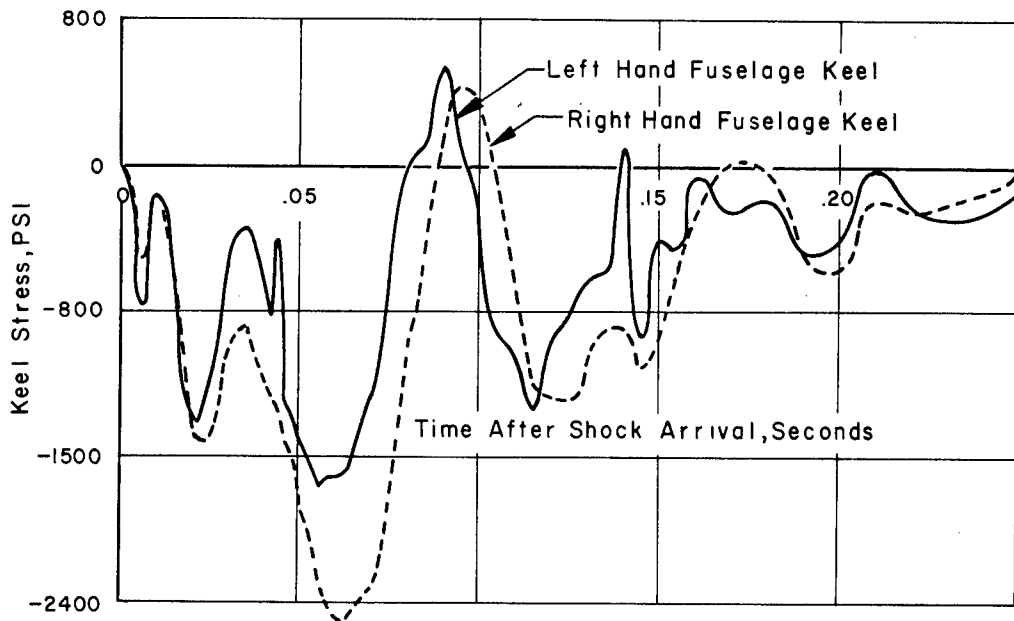


Figure 8.55 Fuselage keel stresses, Shot Shasta.

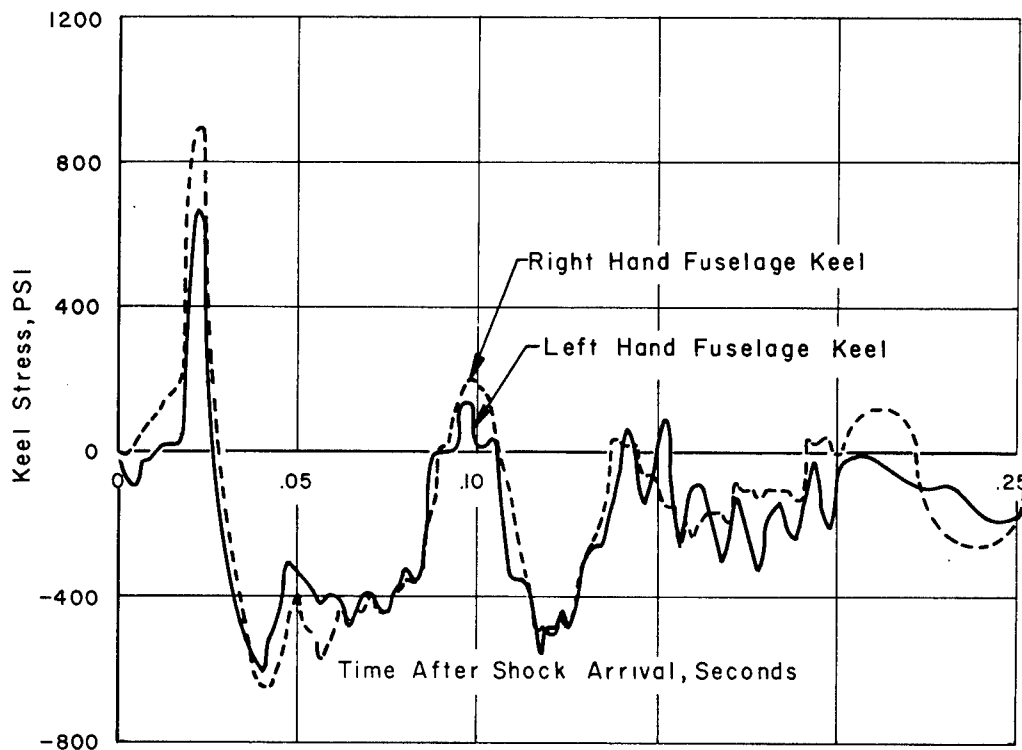


Figure 8.56 Fuselage keel stresses, Shot Doppler, Airplane No. 137831.

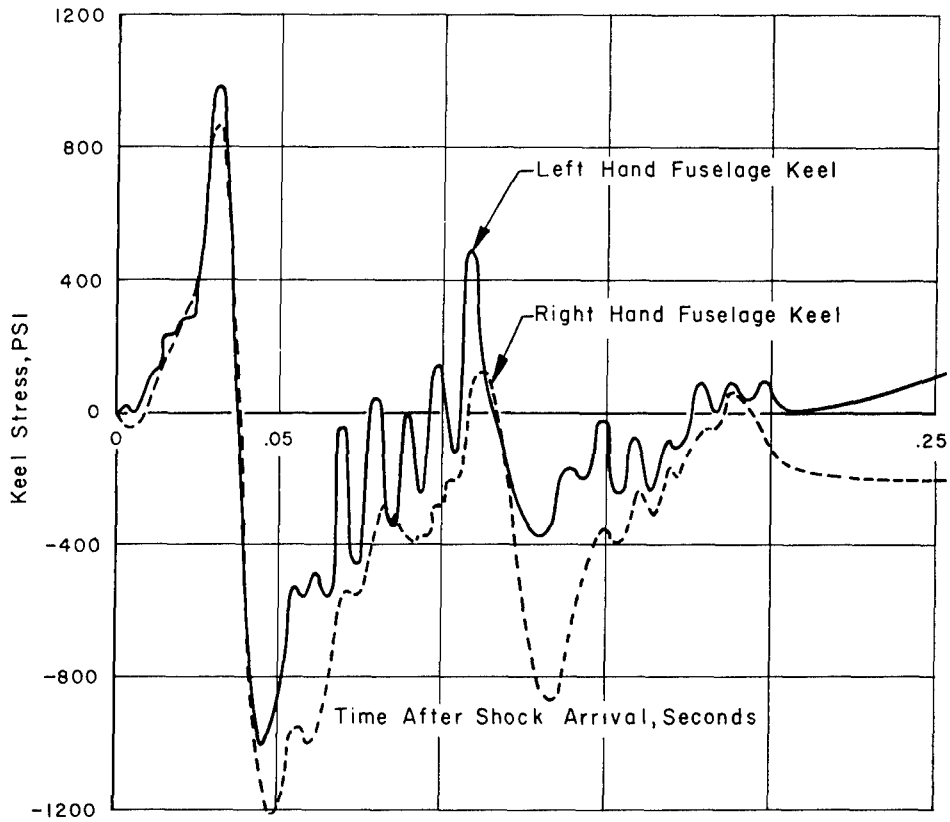


Figure 8.57 Fuselage keel stresses, Shot Smoky.

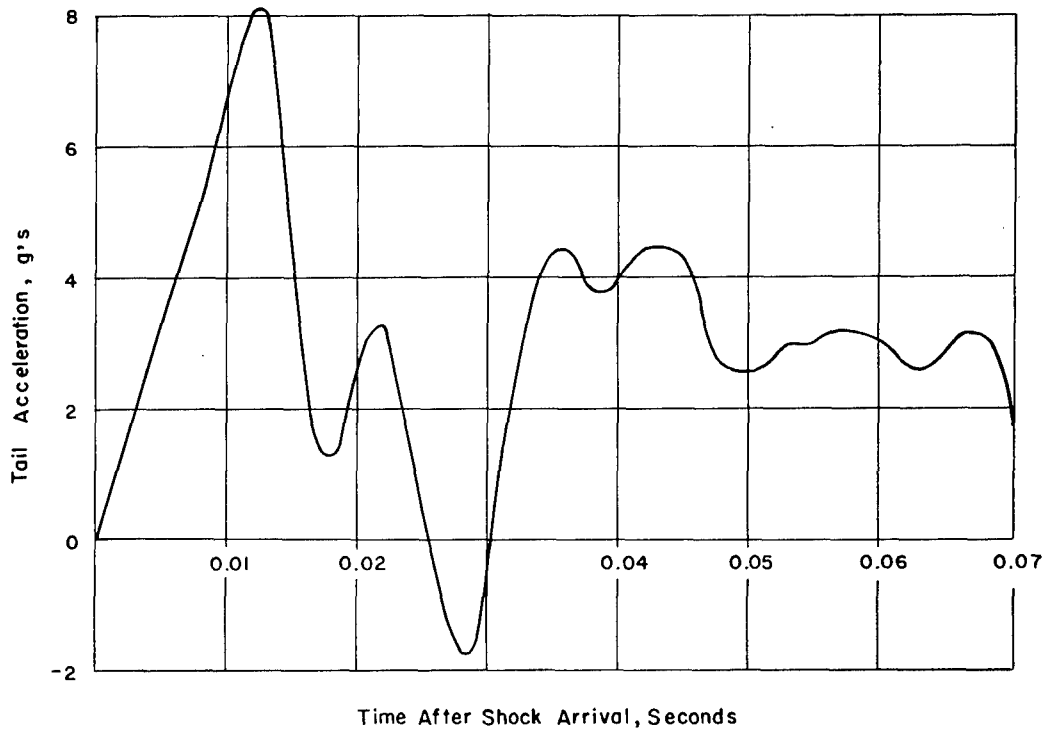


Figure 8.58 Measured tail acceleration versus time, Shot Boltzmann.

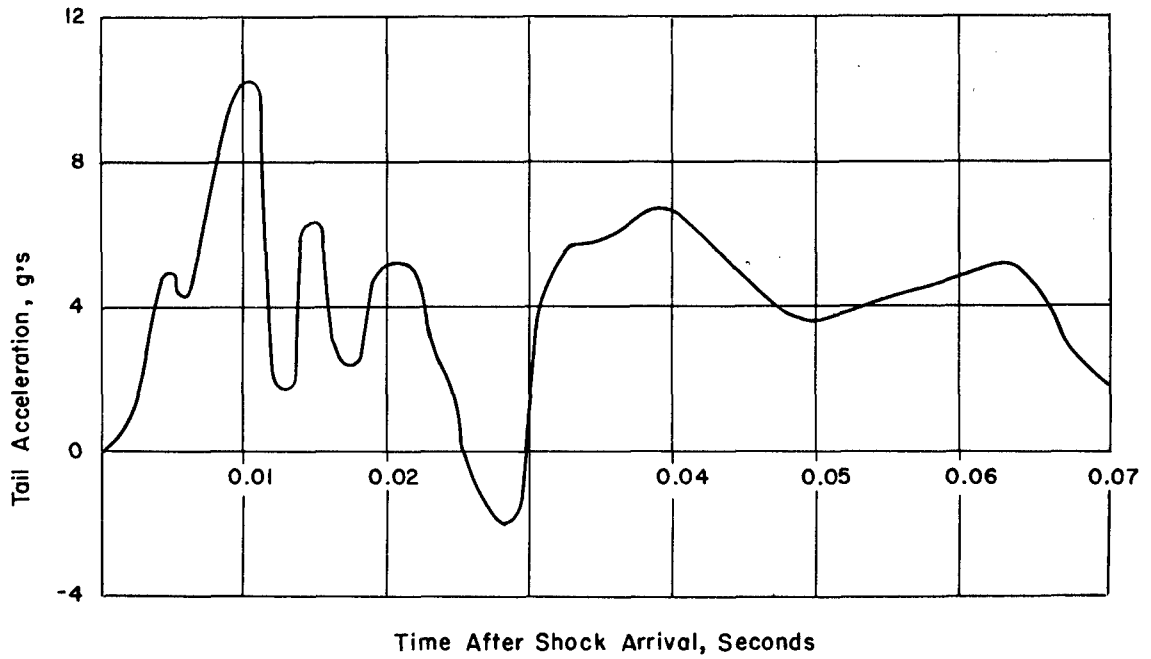


Figure 8.59 Measured tail acceleration versus time, Shot Priscilla.

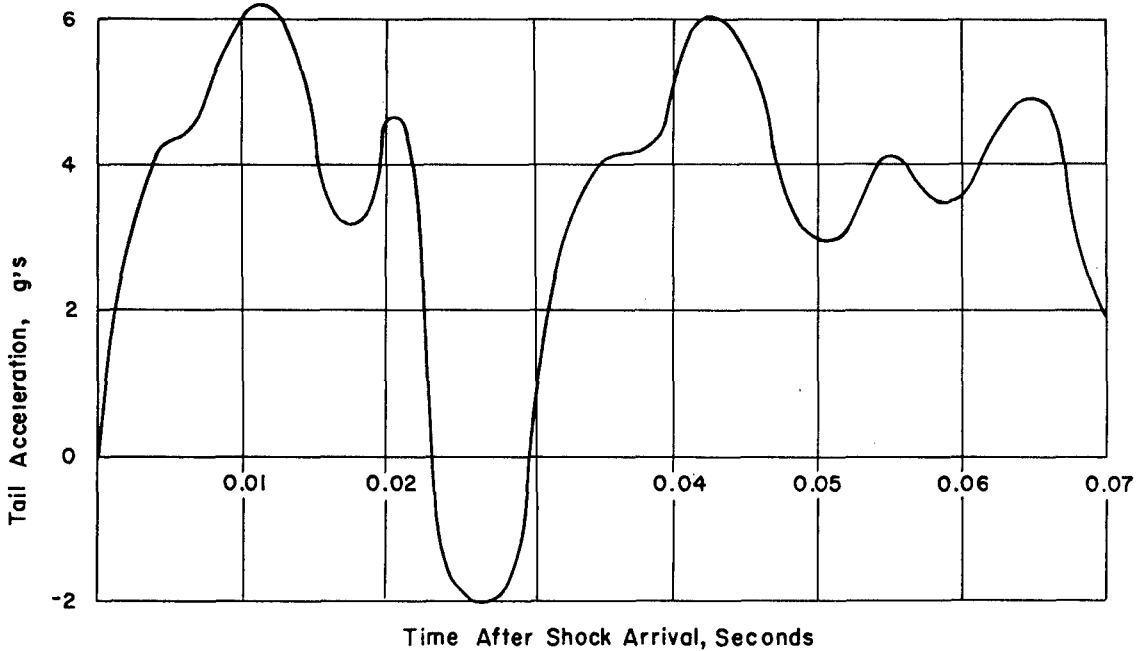


Figure 8.60 Measured tail acceleration versus time, Shot Hood.

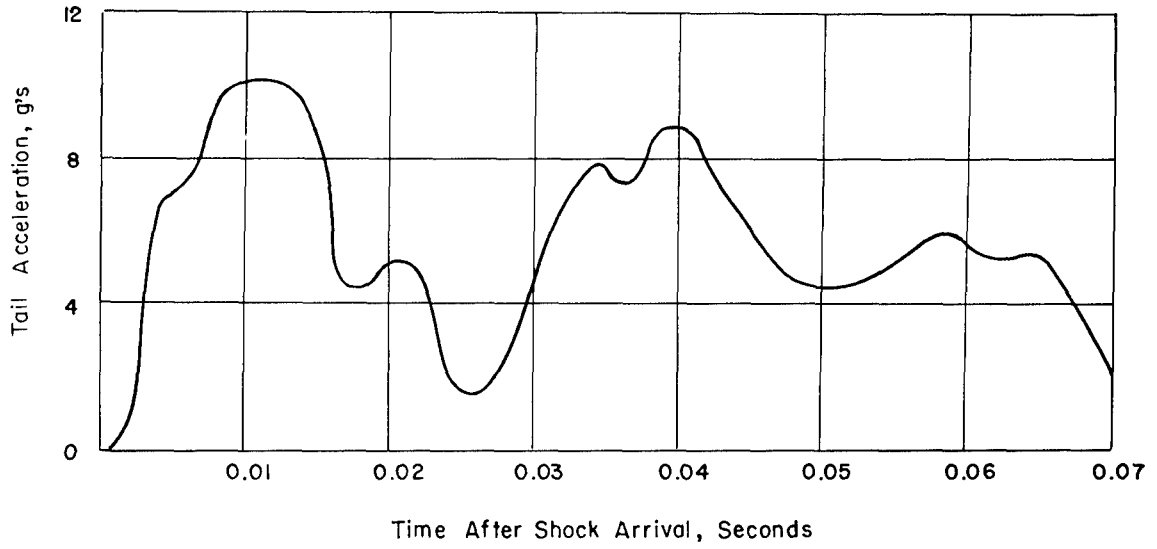


Figure 8.61 Measured tail acceleration versus time, Shot Diablo.

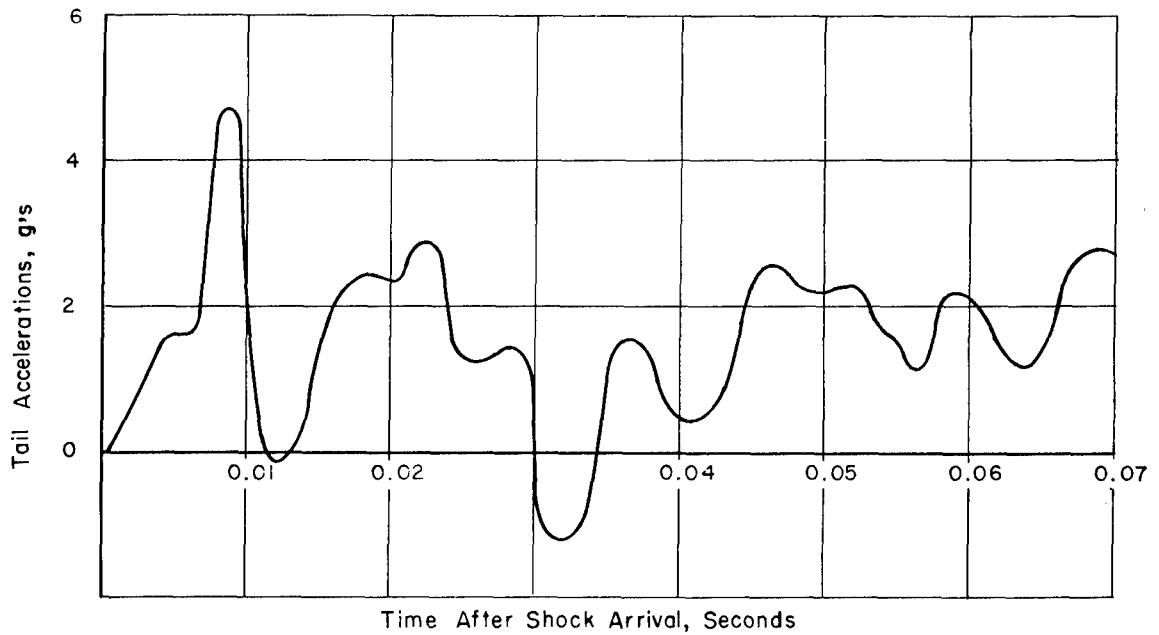


Figure 8.62 Measured tail acceleration versus time, Shot Doppler, Airplane No. 827.

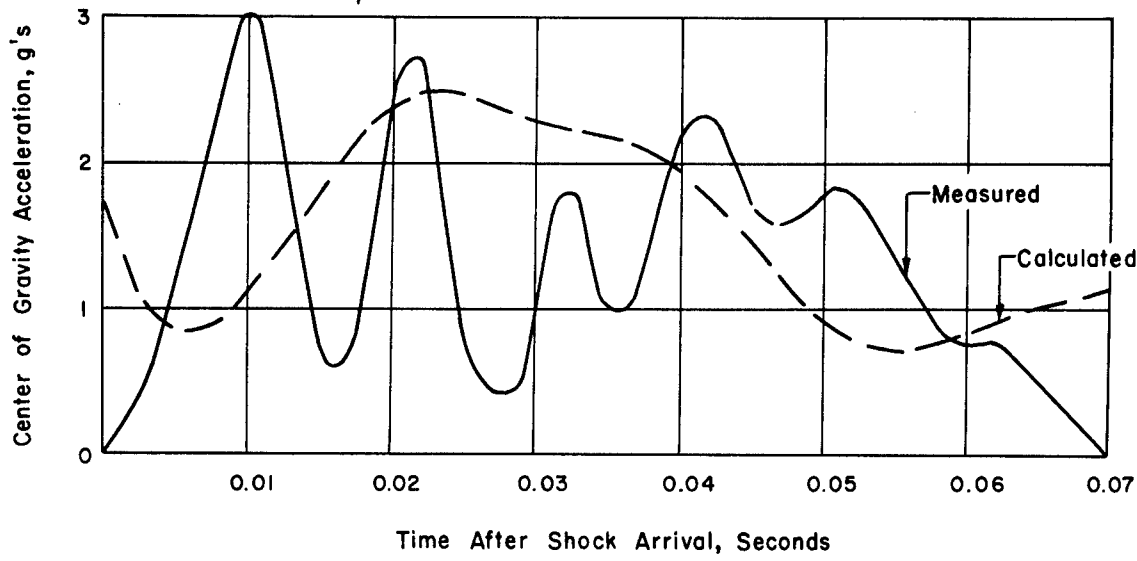


Figure 8.63 Comparison of measured and calculated center of gravity acceleration, Shot Boltzmann.

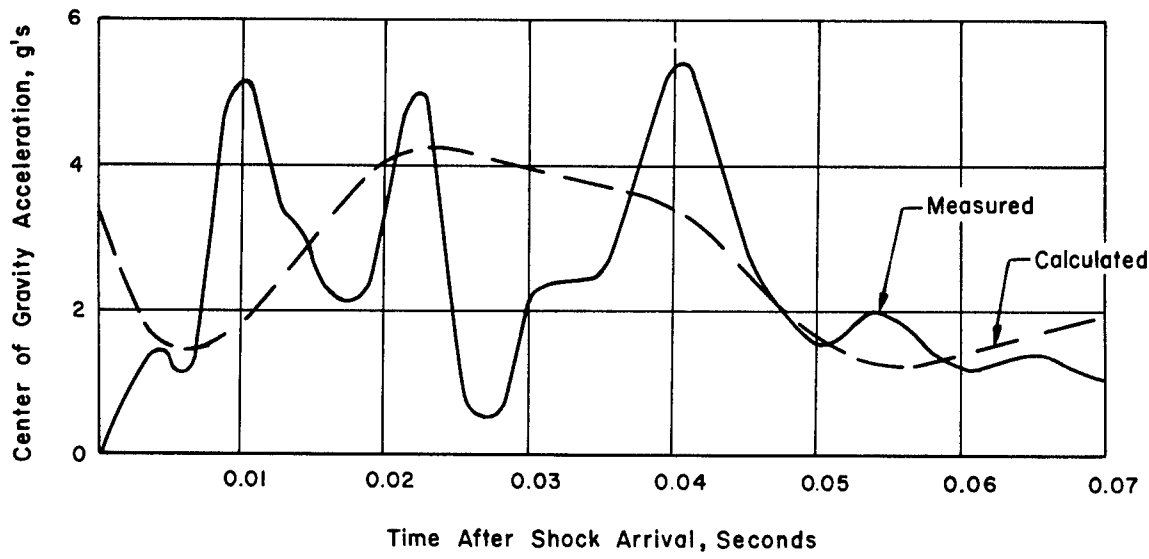


Figure 8.64 Comparison of measured and calculated center of gravity acceleration, Shot Priscilla.

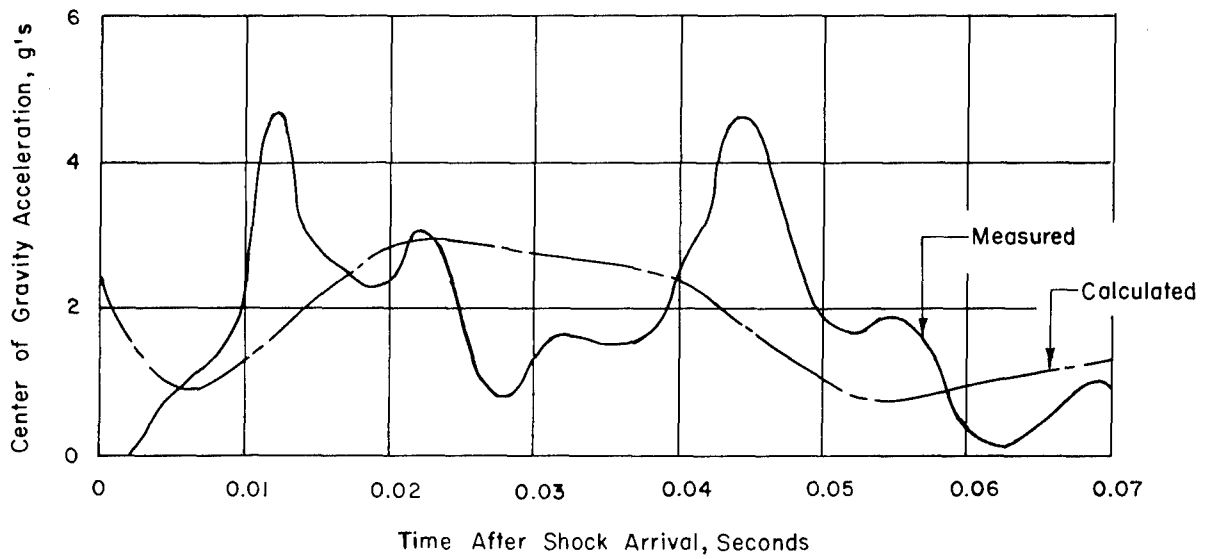


Figure 8.65 Comparison of measured and calculated center of gravity acceleration, Shot Hood

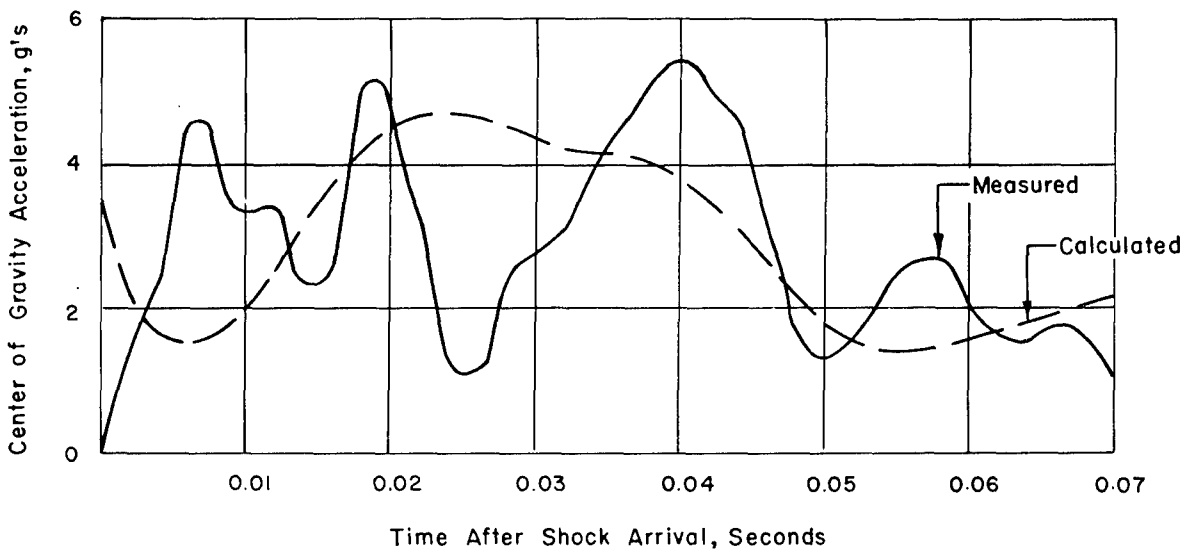


Figure 8.66 Comparison of measured and calculated center of gravity acceleration, Shot Diablo.

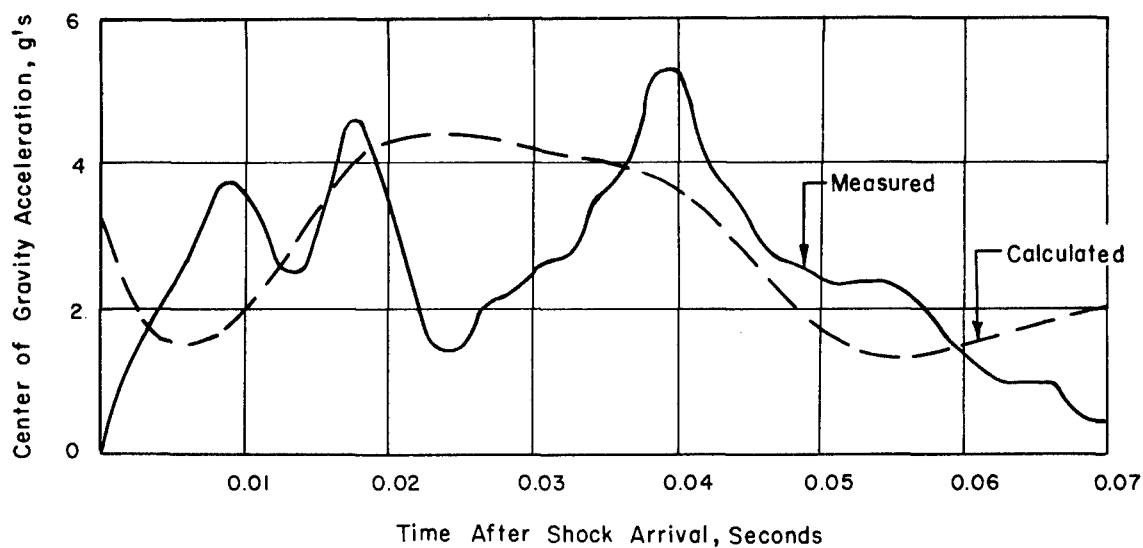


Figure 8.67 Comparison of measured and calculated center of gravity acceleration, Shot Shasta.

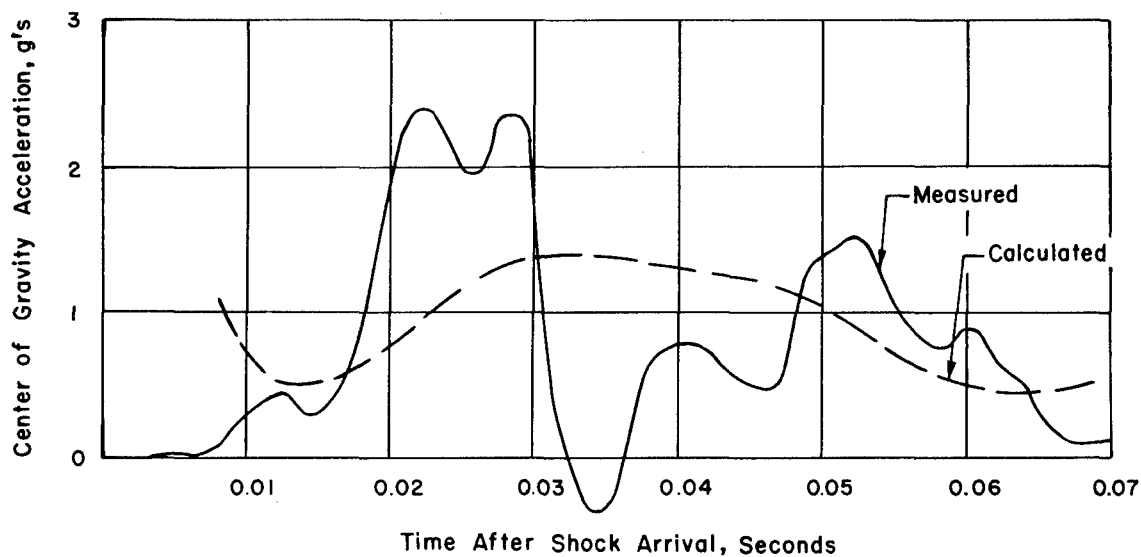


Figure 8.68 Comparison of measured and calculated center of gravity acceleration, Shot Doppler, Airplane No. 827.

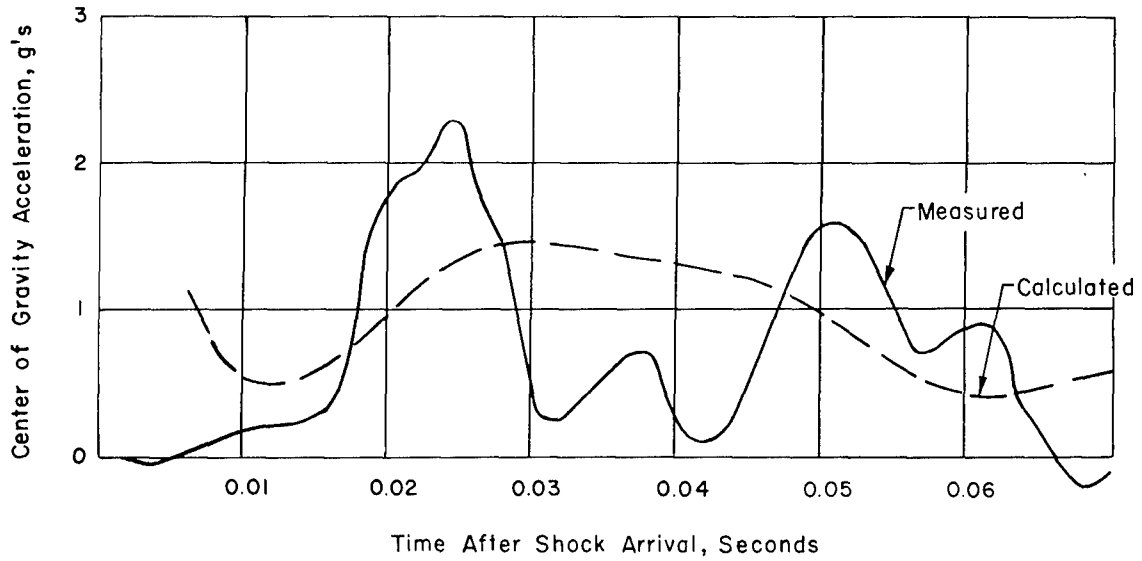


Figure 8.69 Comparison of measured and calculated center of gravity acceleration, Shot Doppler, Airplane No. 831.

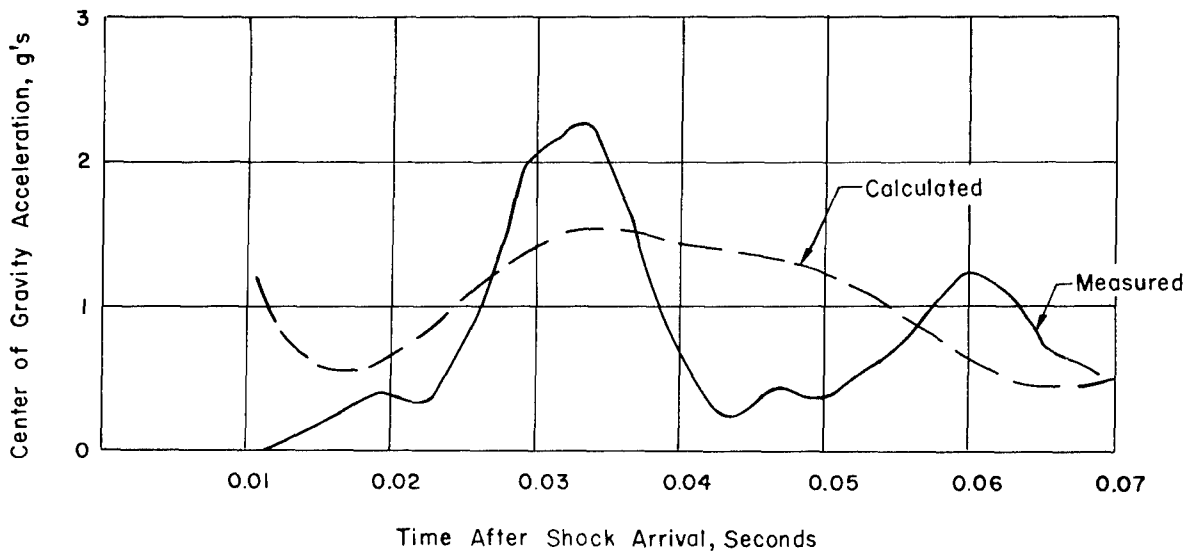


Figure 8.70 Comparison of measured and calculated center of gravity acceleration, Shot Smoky.

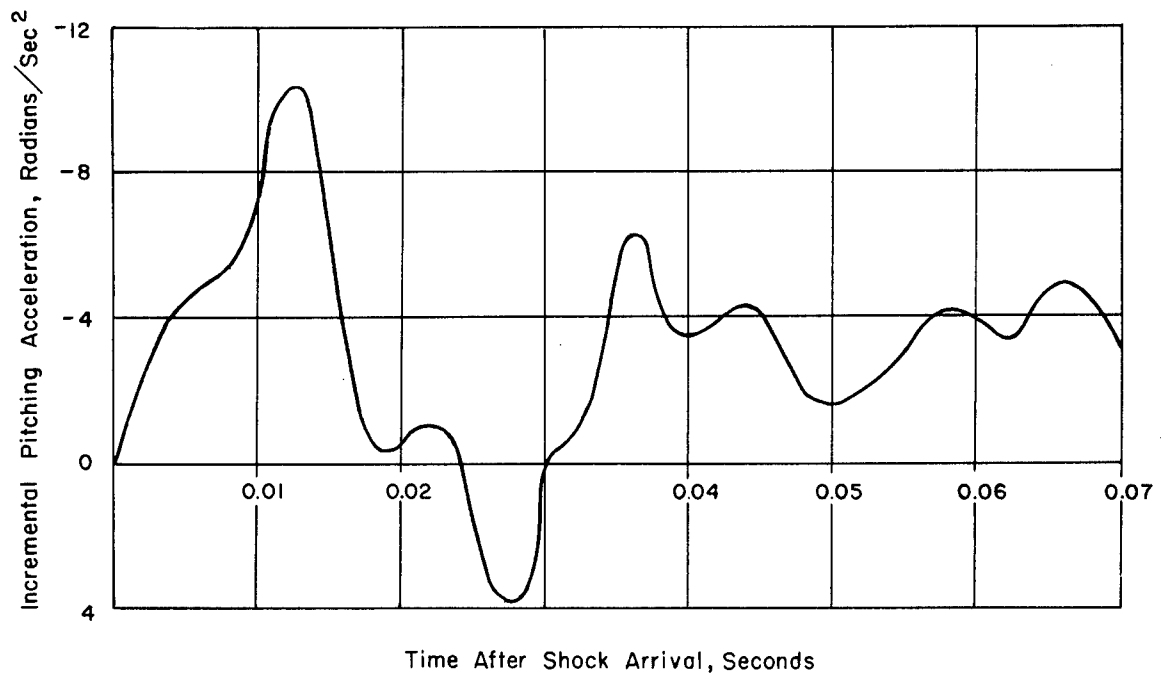


Figure 8.71 Incremental pitching acceleration versus time, Shot Boltzmann.

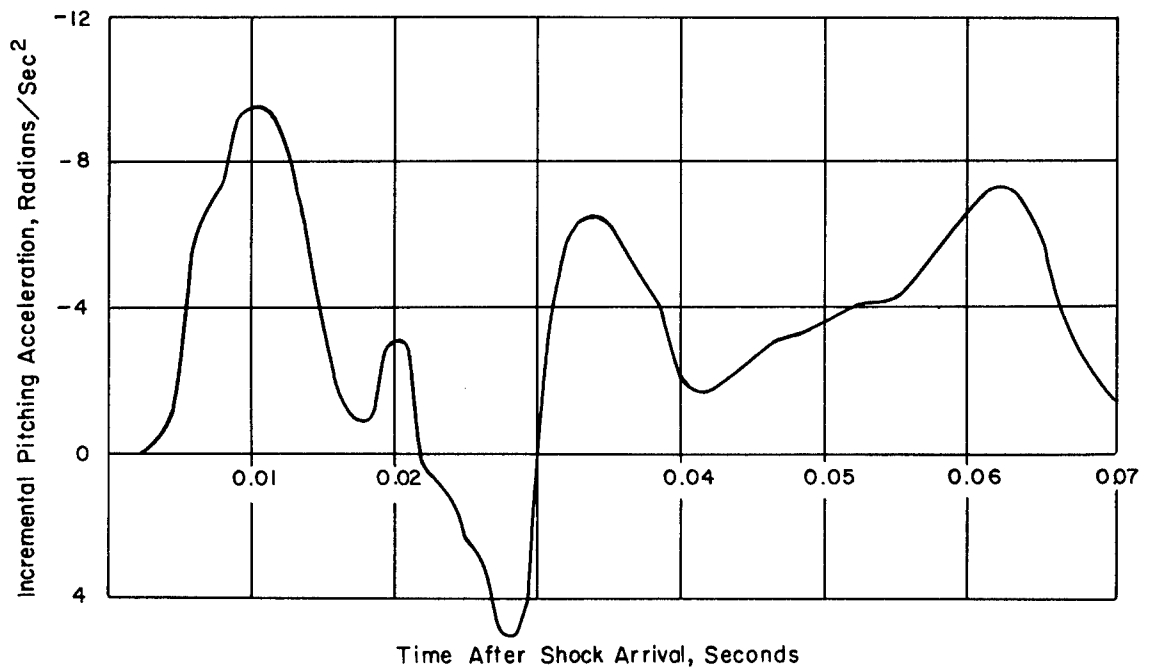


Figure 8.72 Incremental pitching acceleration versus time, Shot Priscilla.

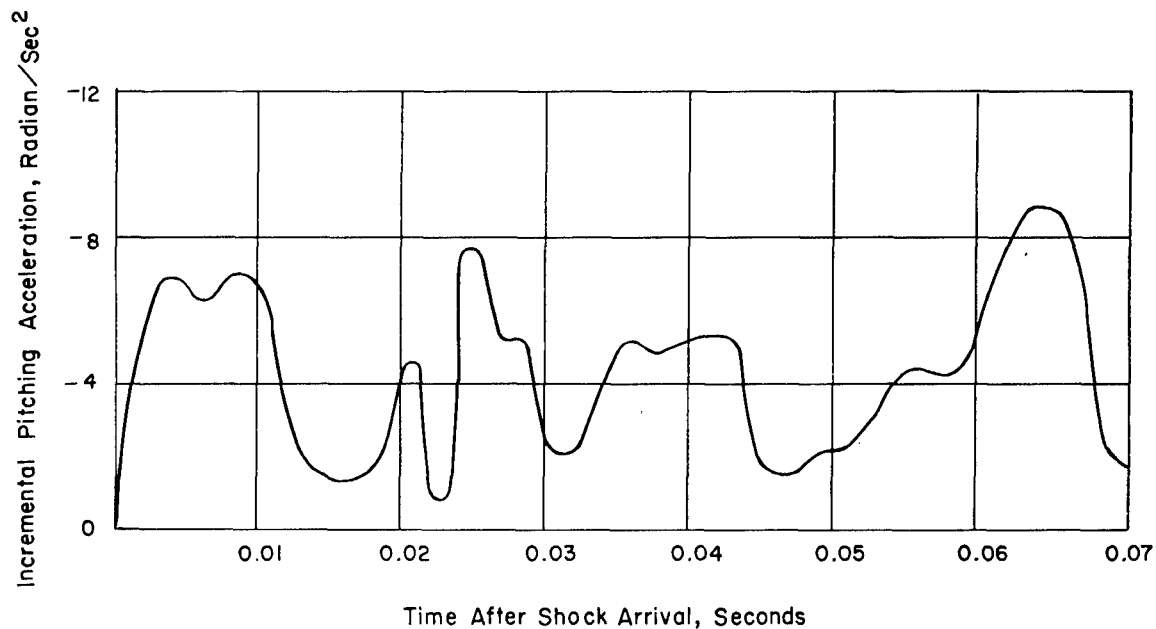


Figure 8.73 Incremental pitching acceleration versus time, Shot Hood.

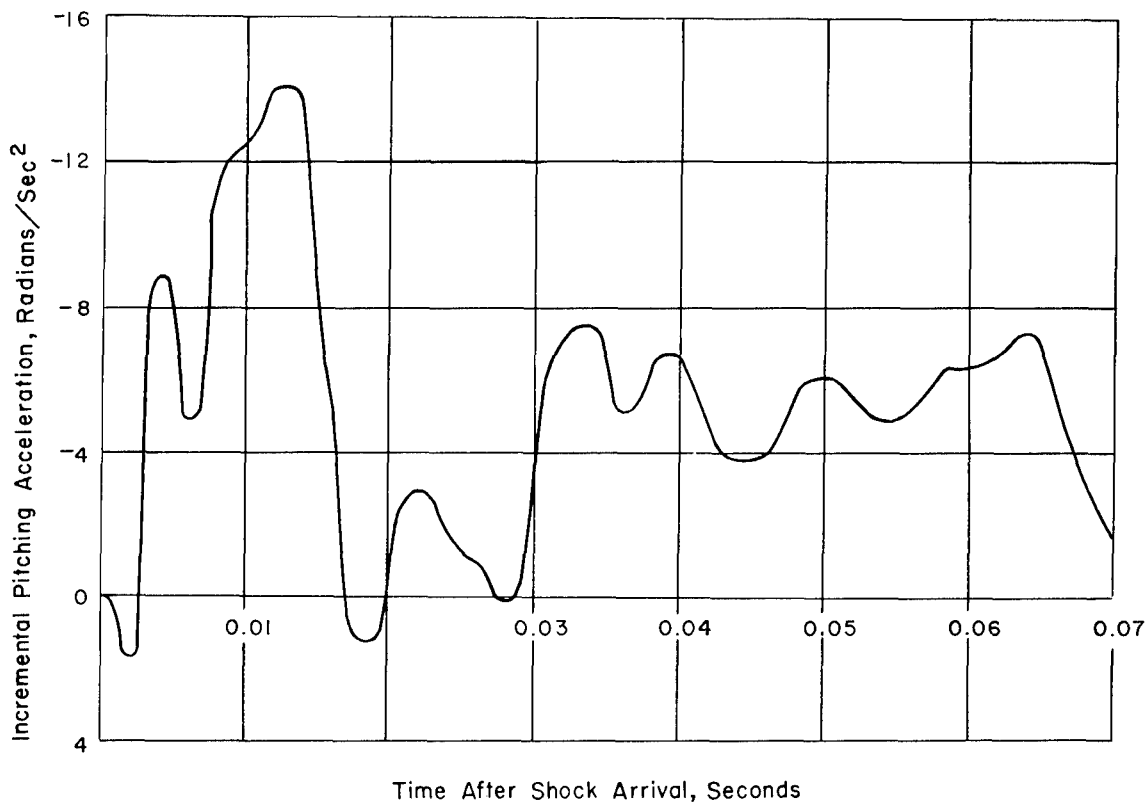


Figure 8.74 Incremental pitching acceleration versus time, Shot Diablo.

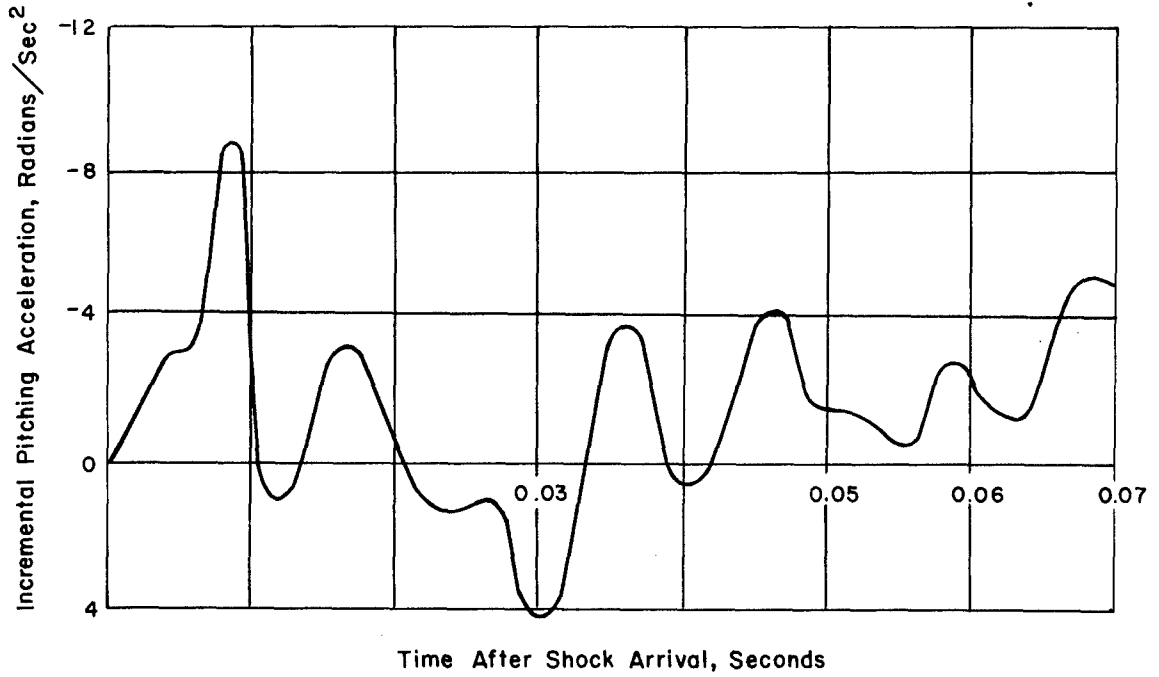


Figure 8.75 Incremental pitching acceleration versus time, Shot Doppler, Airplane No. 137827.

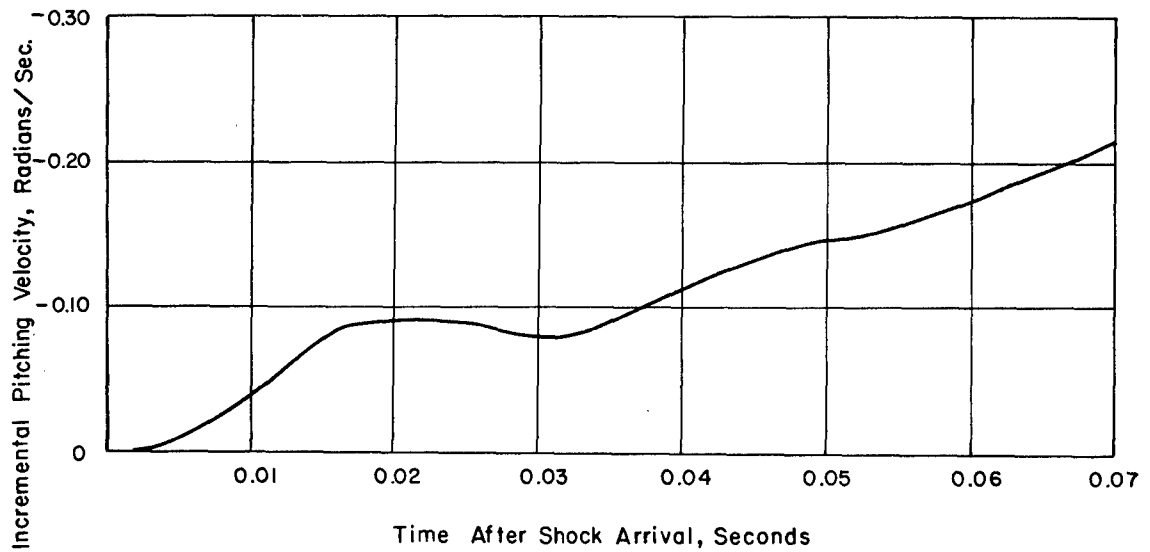


Figure 8.76 Incremental pitching velocity versus time, Shot Boltzmann.

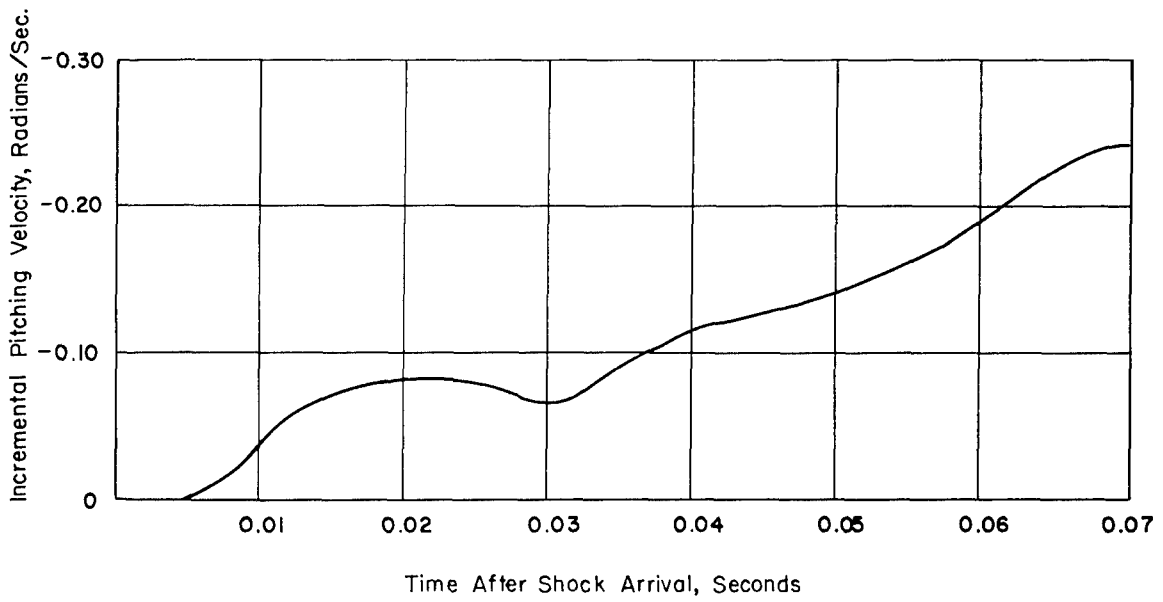


Figure 8.77 Incremental pitching velocity versus time, Shot Priscilla.

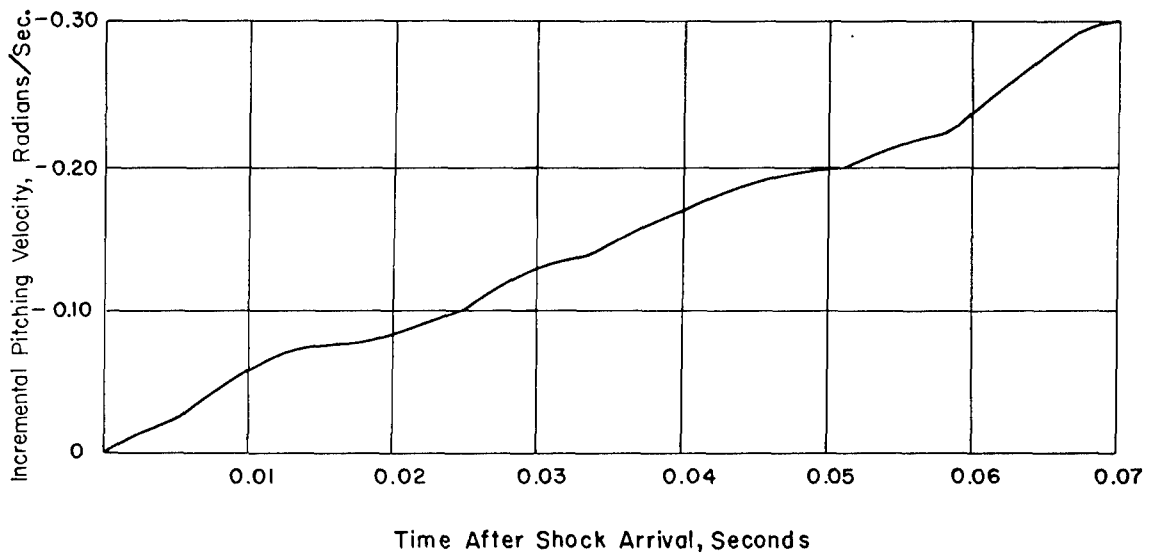


Figure 8.78 Incremental pitching velocity versus time, Shot Hood.

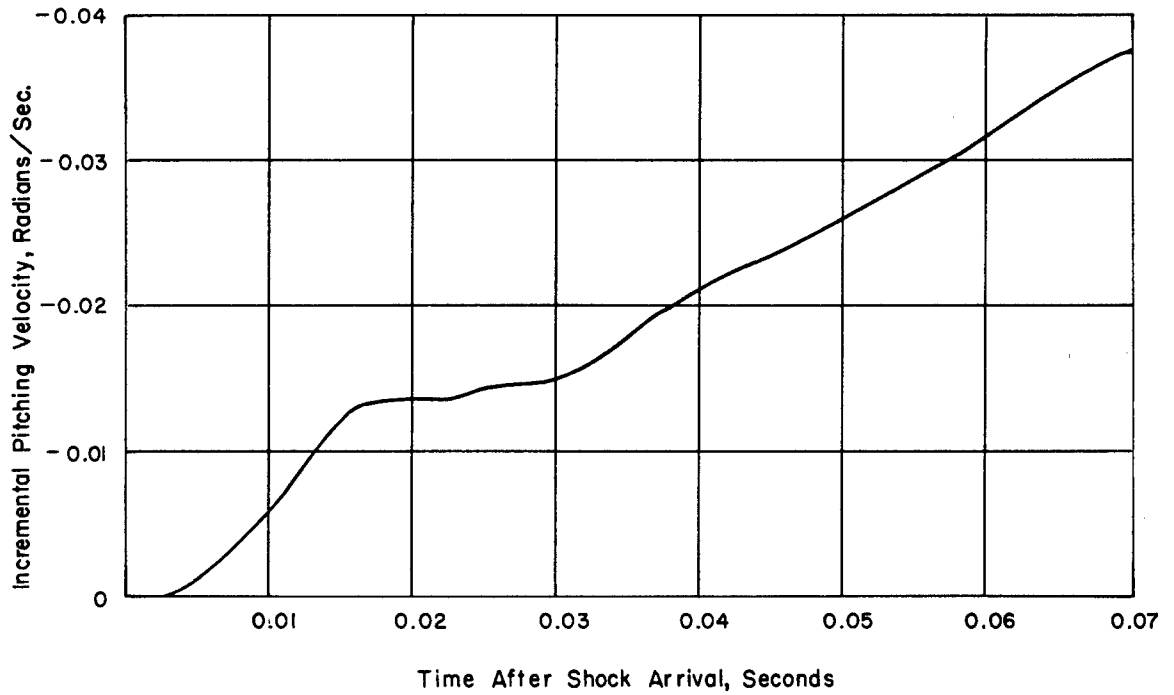


Figure 8.79 Incremental pitching velocity versus time, Shot Diablo.

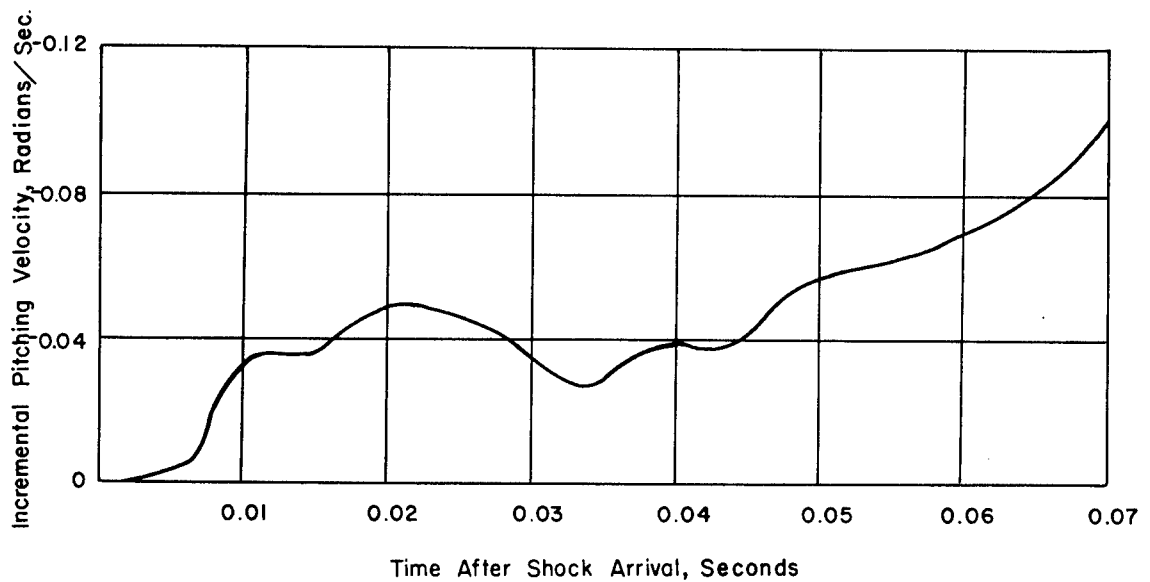


Figure 8.80 Incremental pitching velocity versus time, Shot Doppler, Airplane No. 137827.

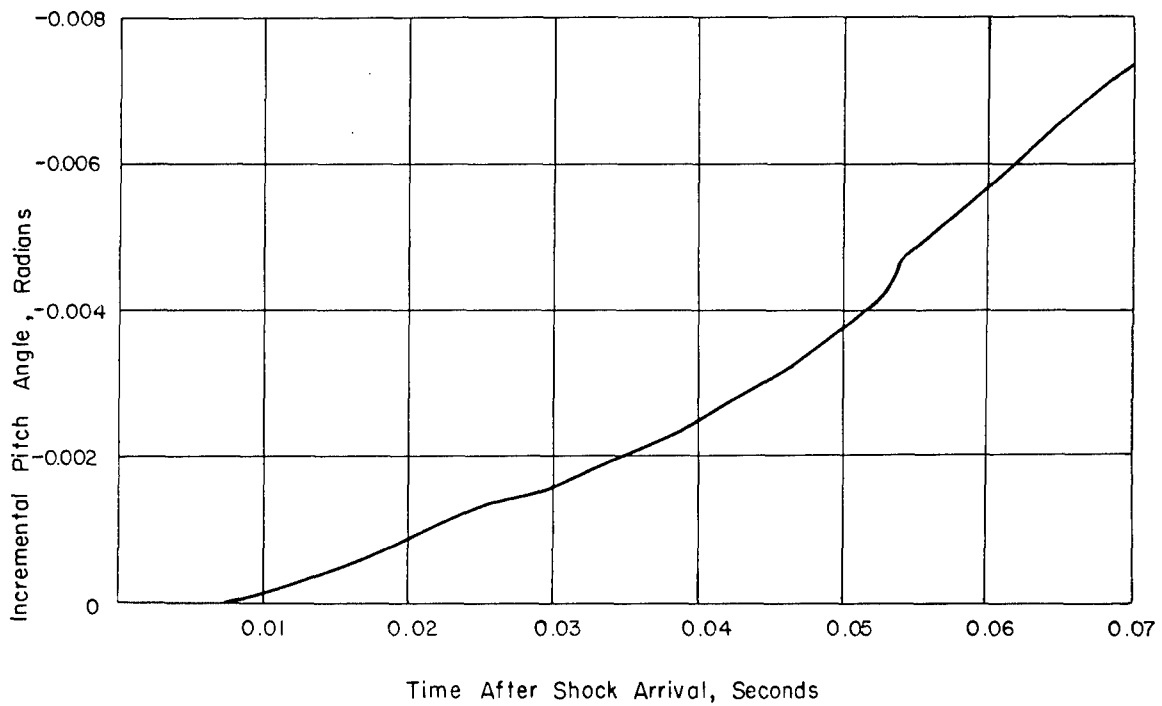


Figure 8.81 Incremental pitch angle versus time, Shot Boltzmann.

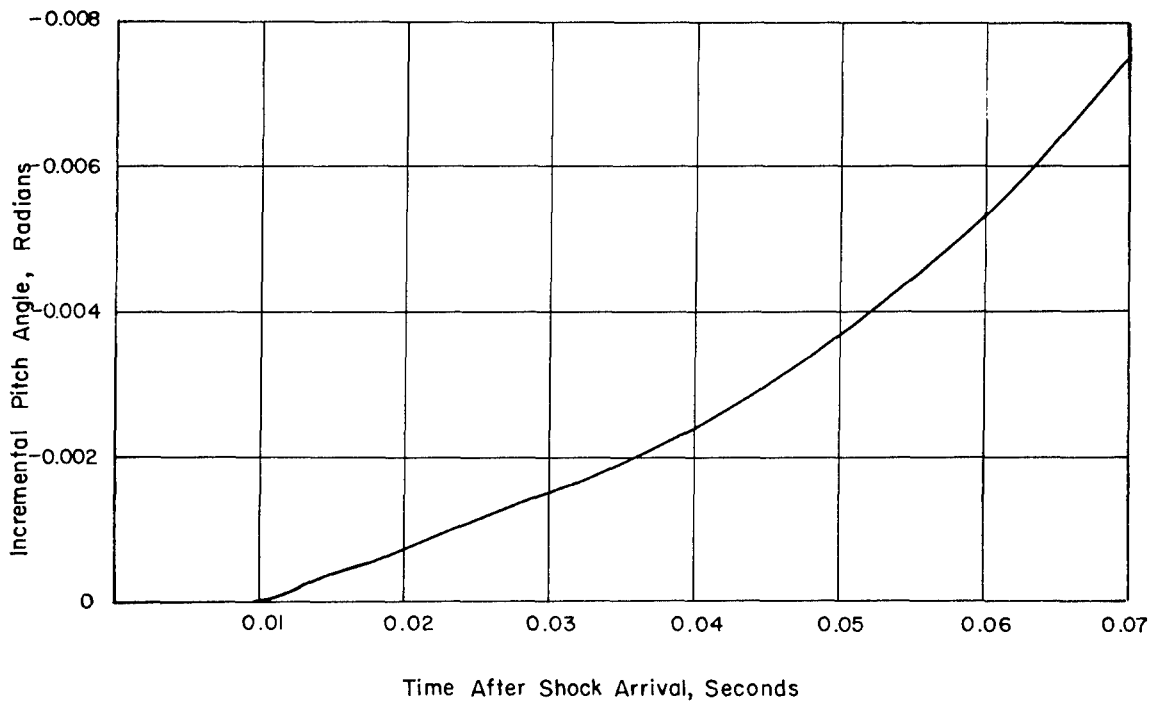


Figure 8.82 Incremental pitch angle versus time, Shot Priscilla.

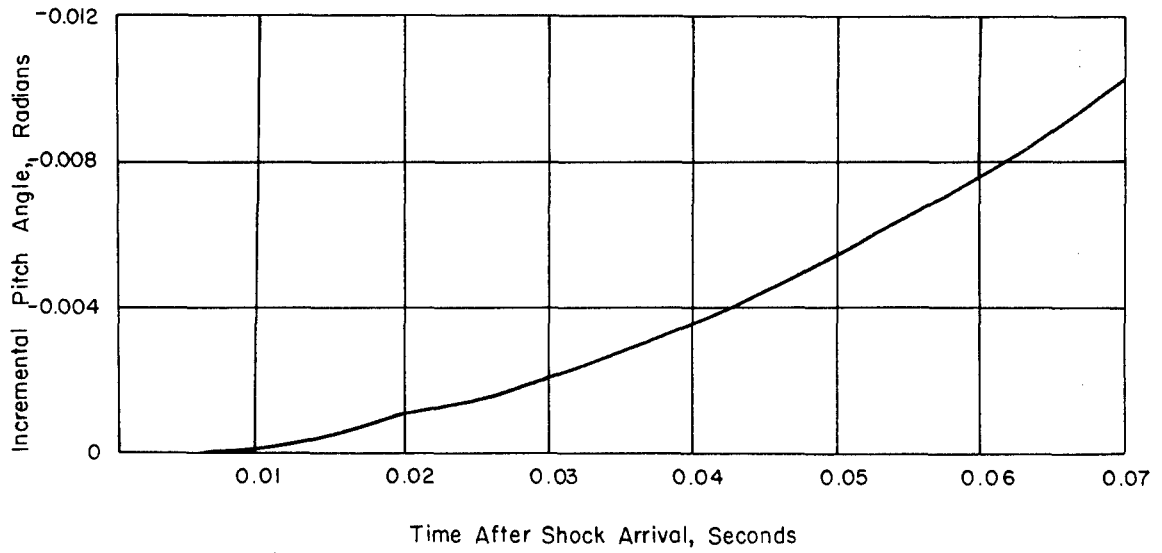


Figure 8.83 Incremental pitch angle versus time, Shot Hood.

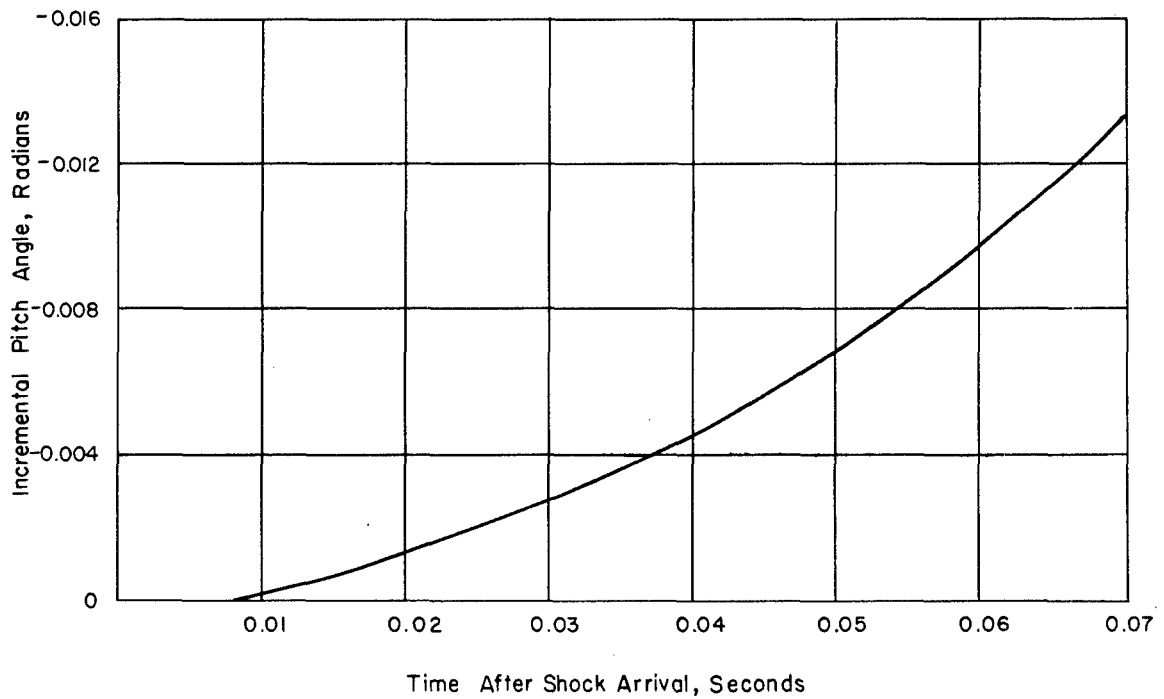


Figure 8.84 Incremental pitch angle versus time, Shot Diablo.

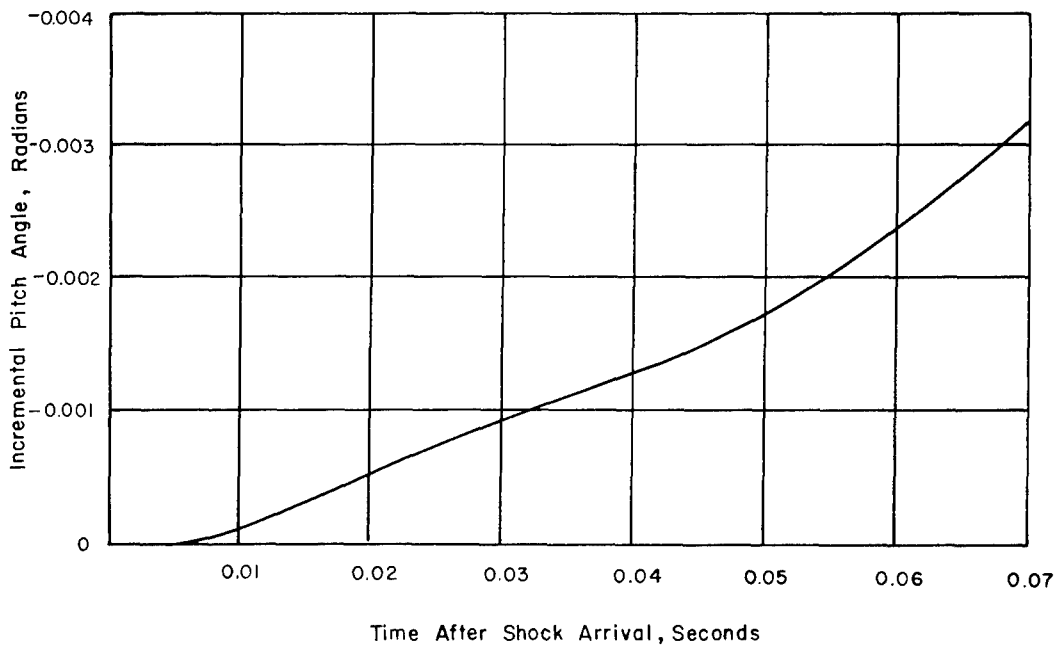


Figure 8.85 Incremental pitch angle versus time, Shot Doppler, Airplane No. 137827.

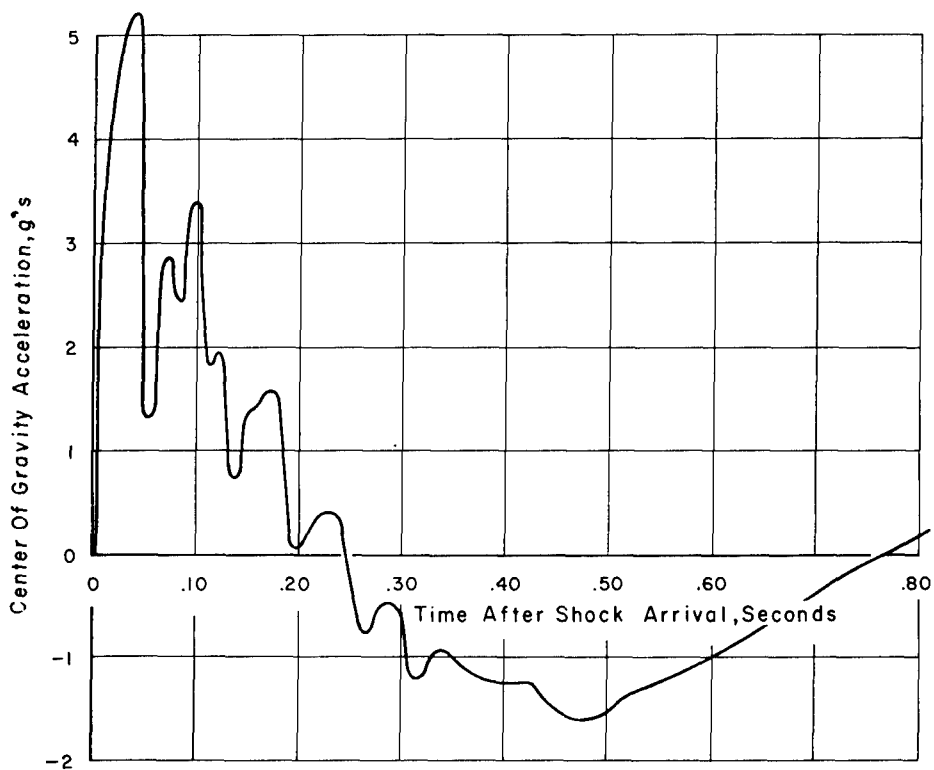


Figure 8.86 Center of gravity acceleration versus time, extended time plot, Shot Diablo.

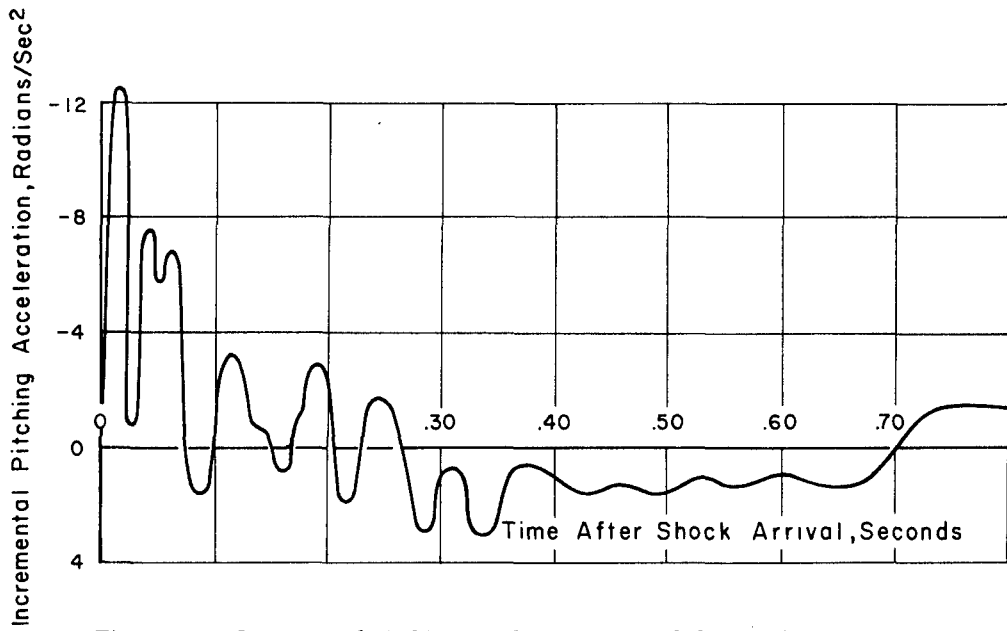


Figure 8.87 Incremental pitching acceleration, extended time plot, Shot Diablo.

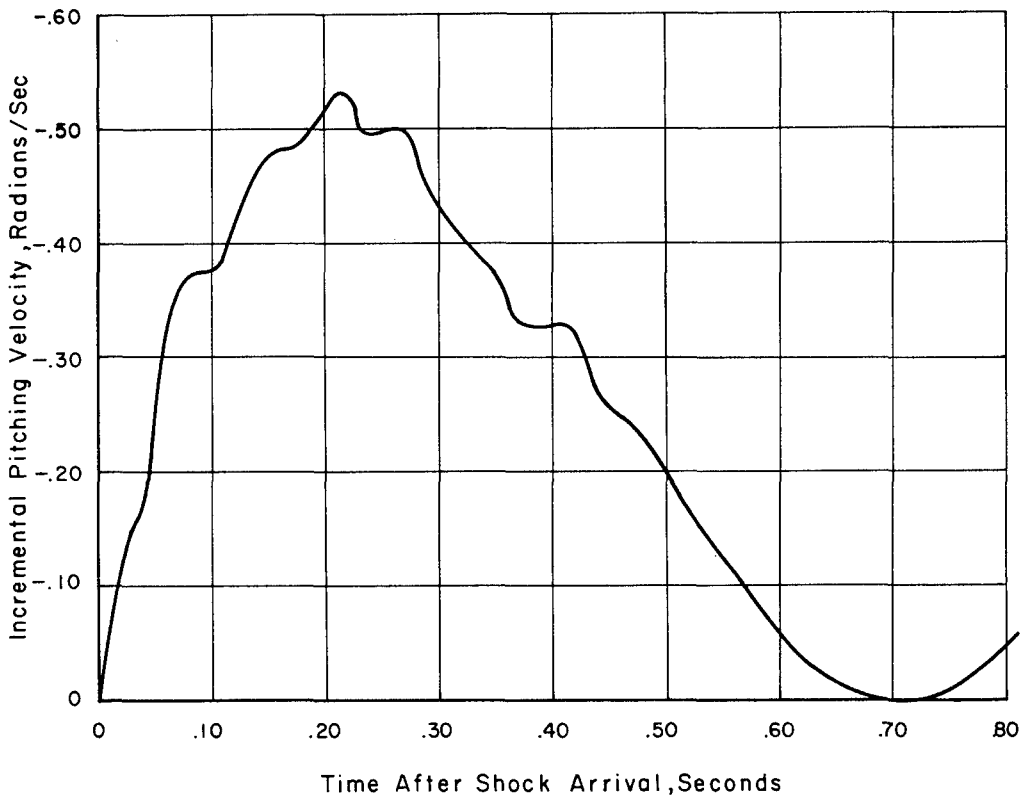


Figure 8.88 Incremental pitching velocity, extended time plot, Shot Diablo.

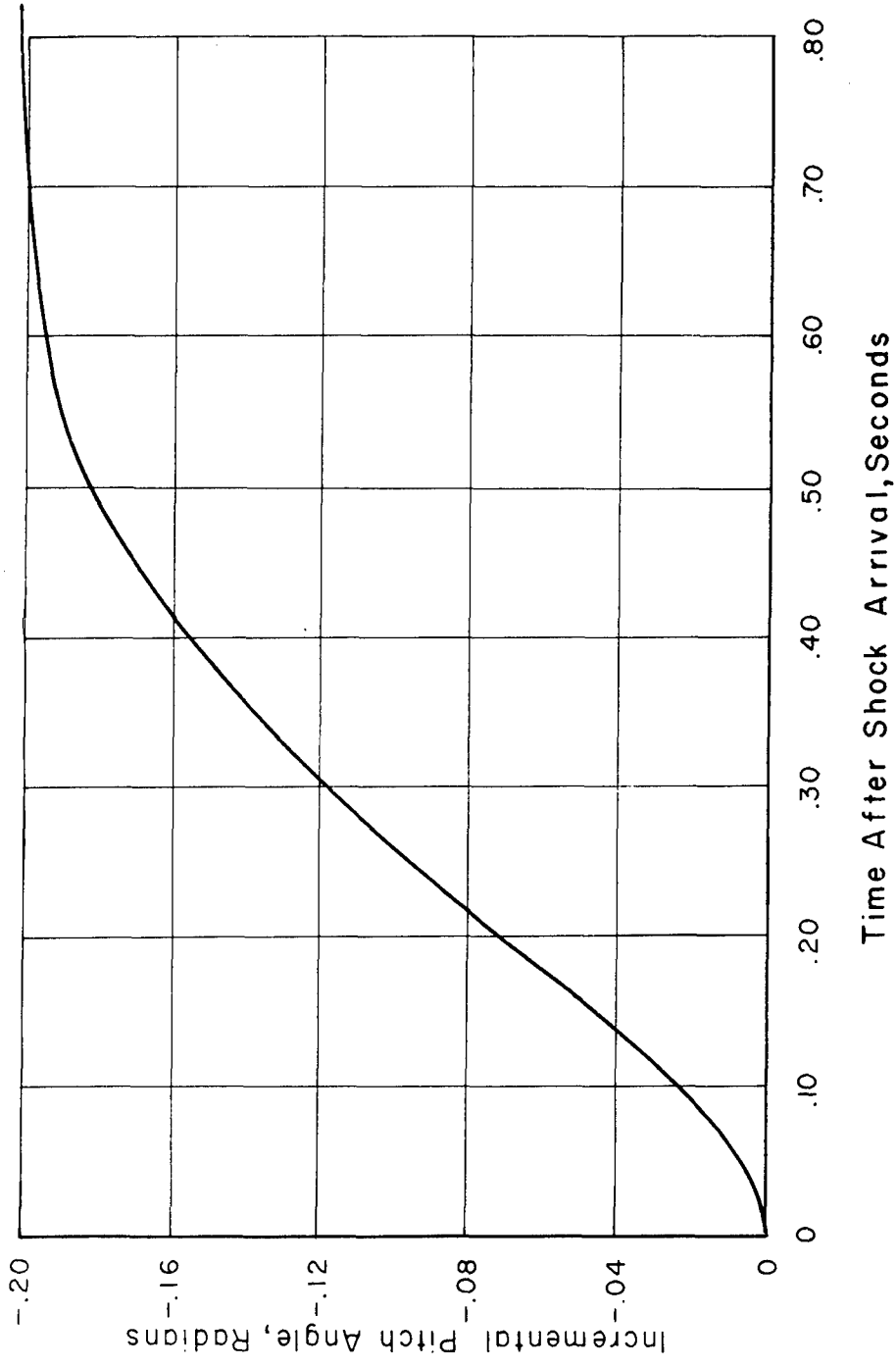


Figure 8.89 Incremental pitch angle, extended time plot, Shot Diablo.

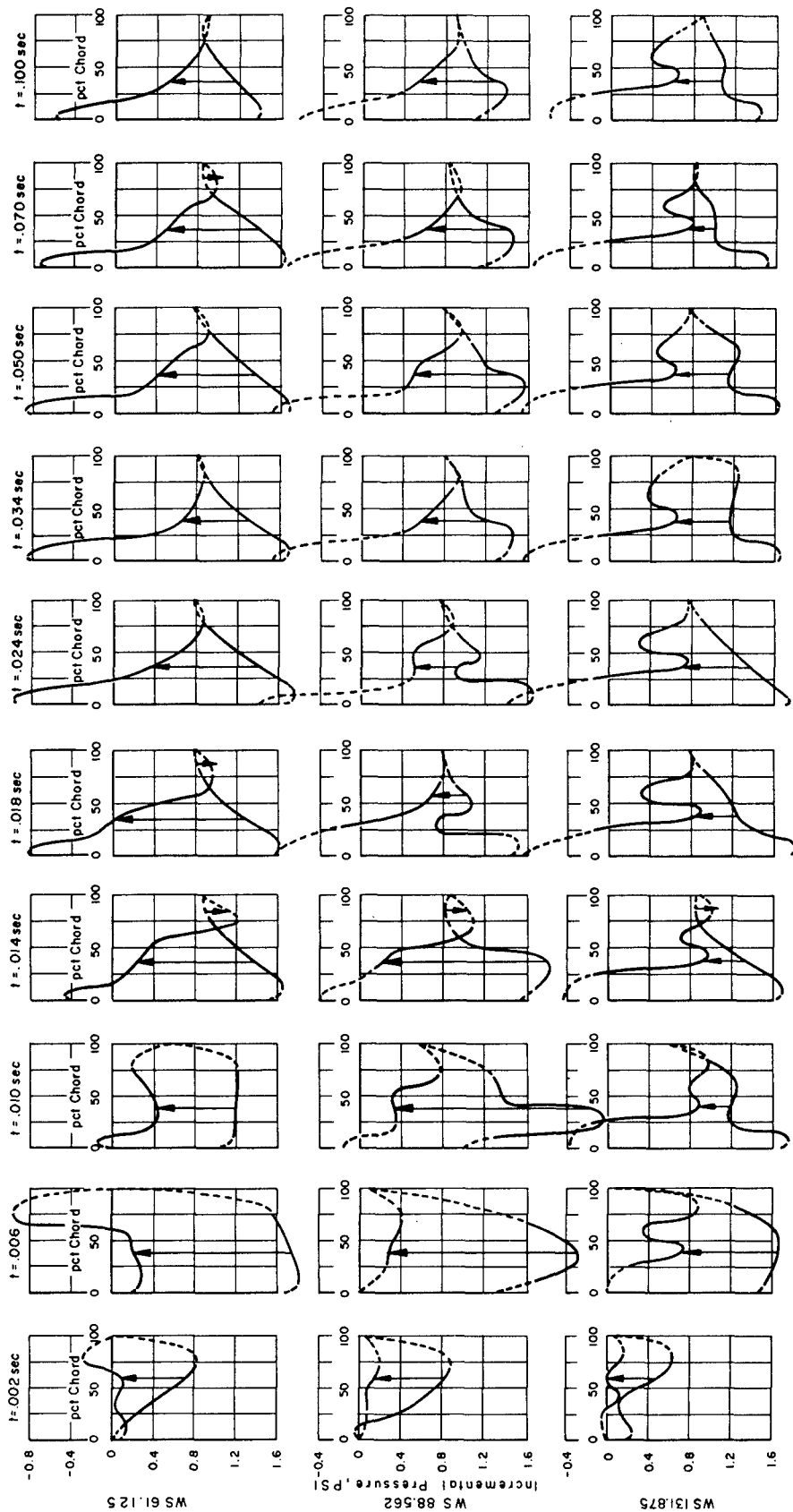


Figure 8.90 Time-wise variation of chord-wise incremental pressure, Shot Priscilla.

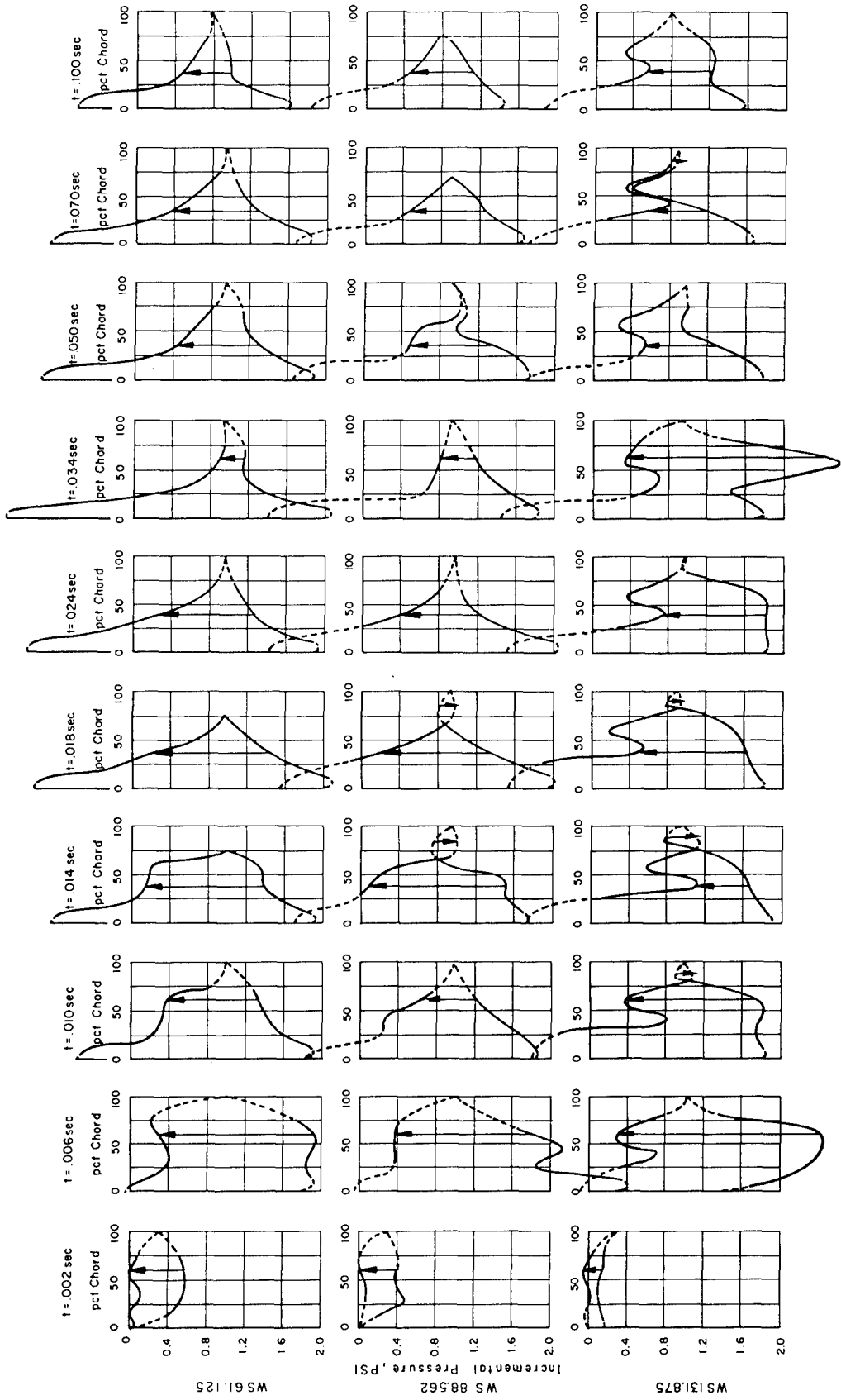


Figure 8.91 Time-wise variation of chord-wise incremental pressure, Shot Diablo.

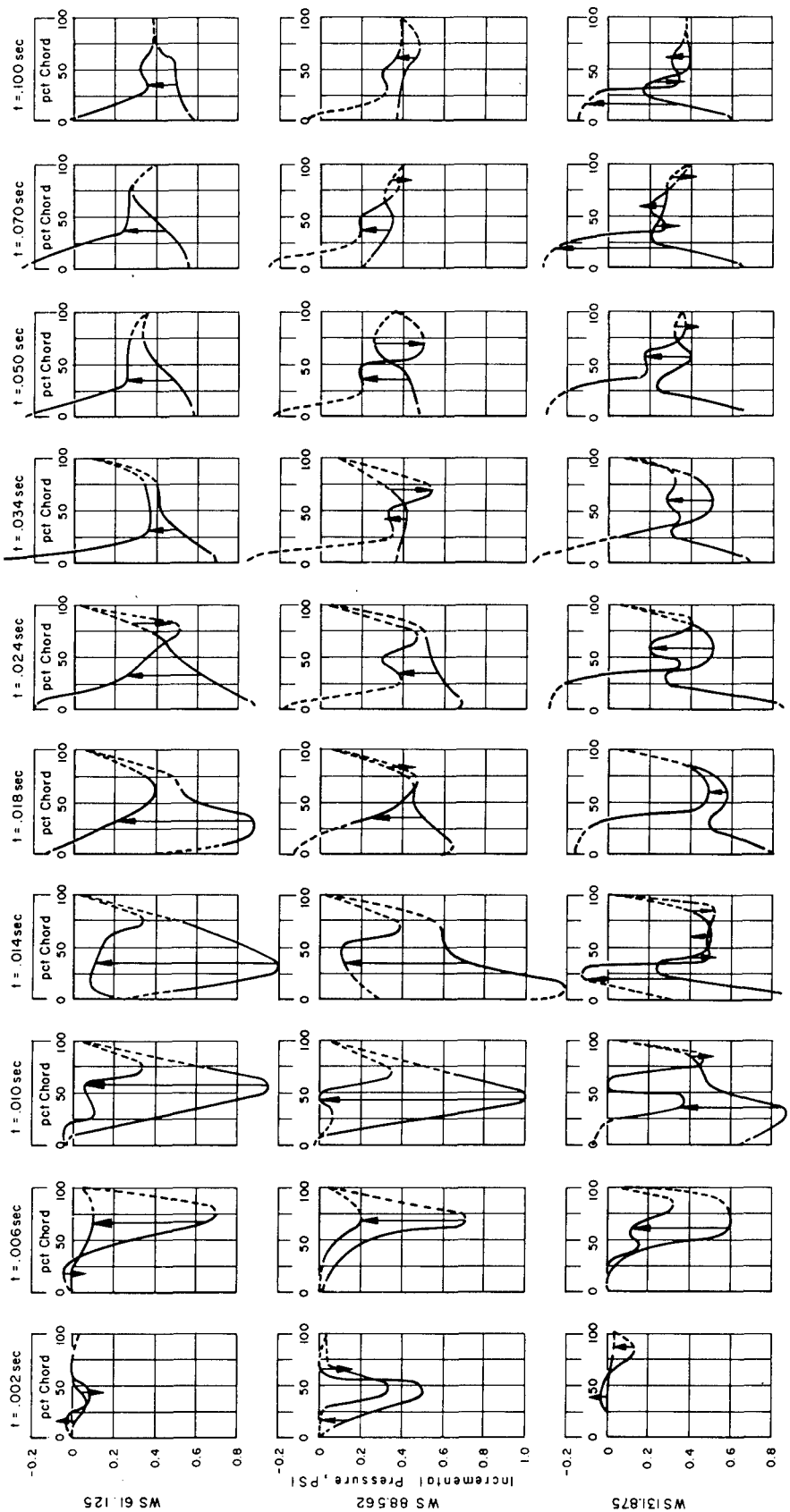


Figure 8.92 Time-wise variation of chord-wise incremental pressure, Shot Doppler, Airplane No. 137827.

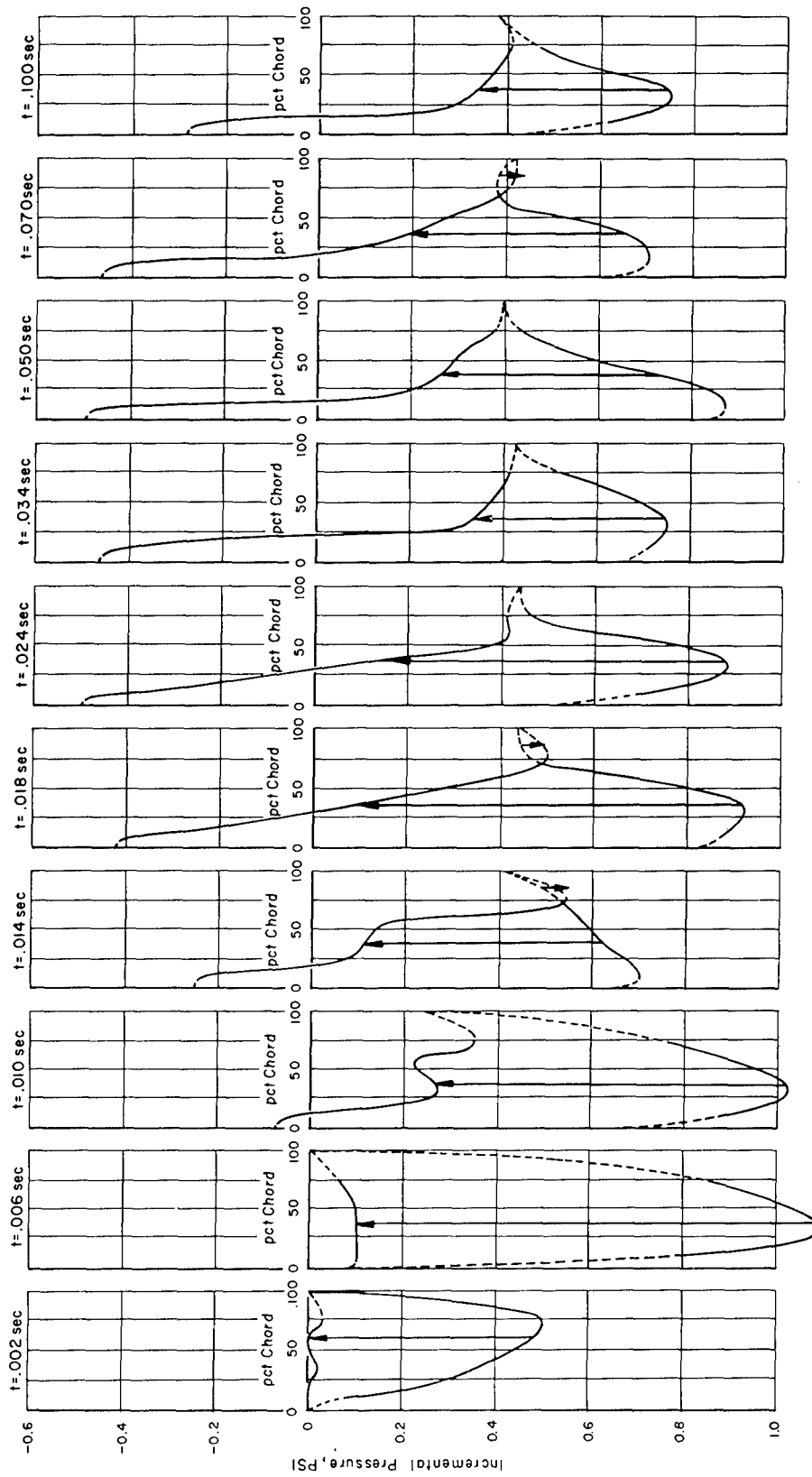


Figure 8.93 Time-wise variation of chord-wise incremental pressure, Shot Boltzmann.

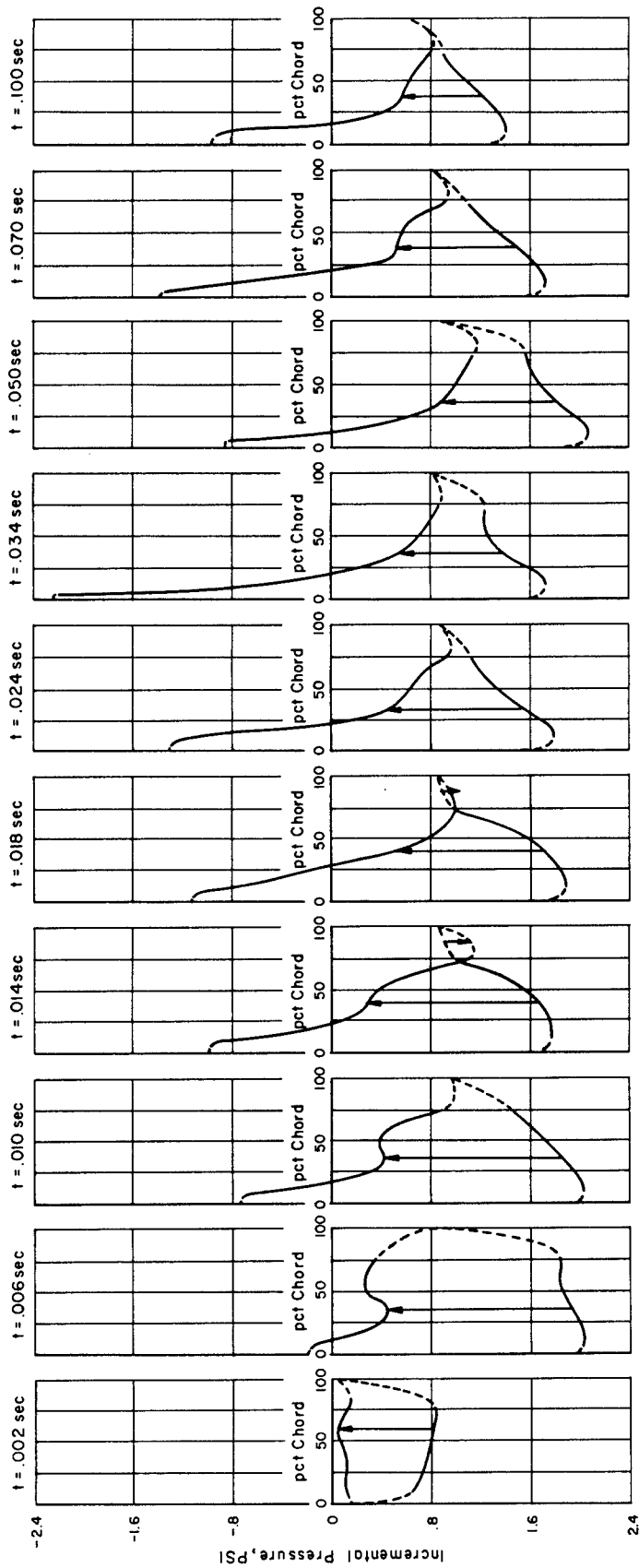


Figure 8.94 Time-wise variation of chord-wise incremental pressure, Shot Shasta.

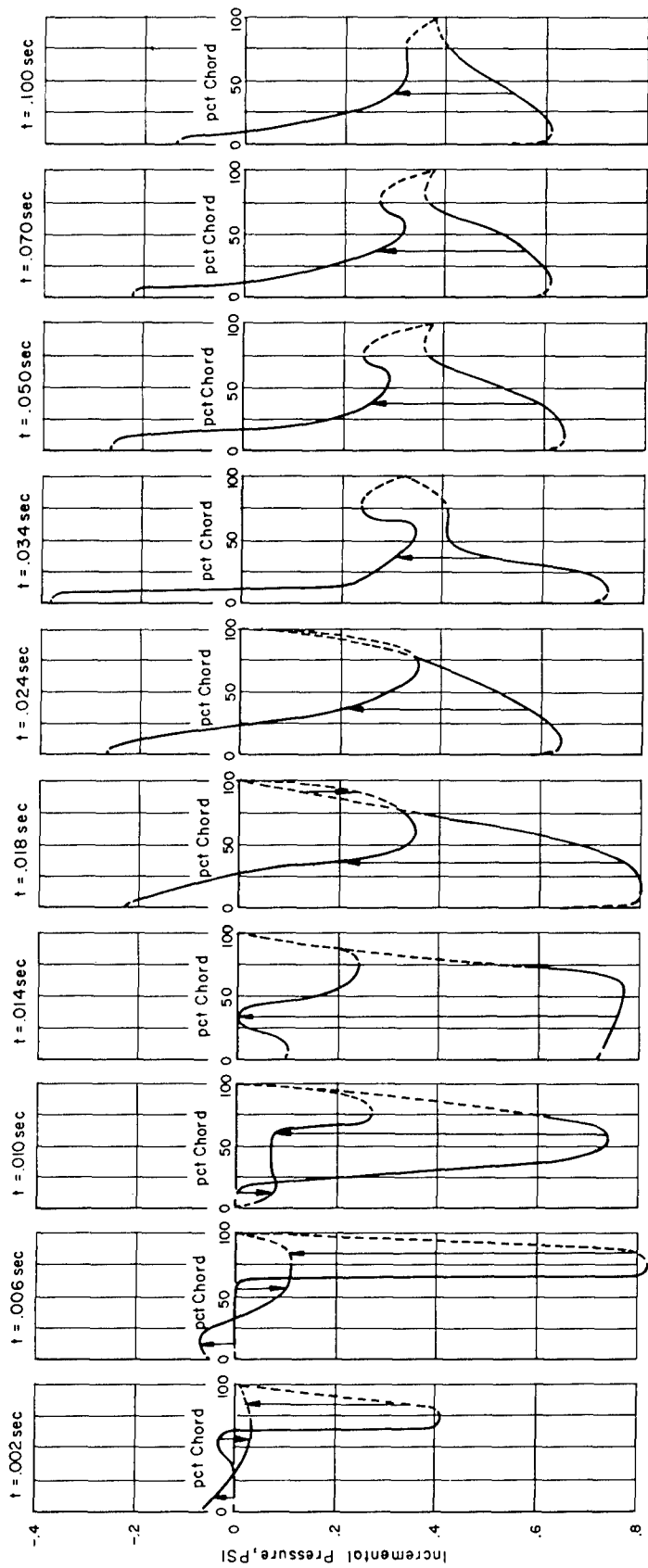


Figure 8.95 Time-wise variation of chord-wise incremental pressure, Shot Doppler, Airplane No. 137831.

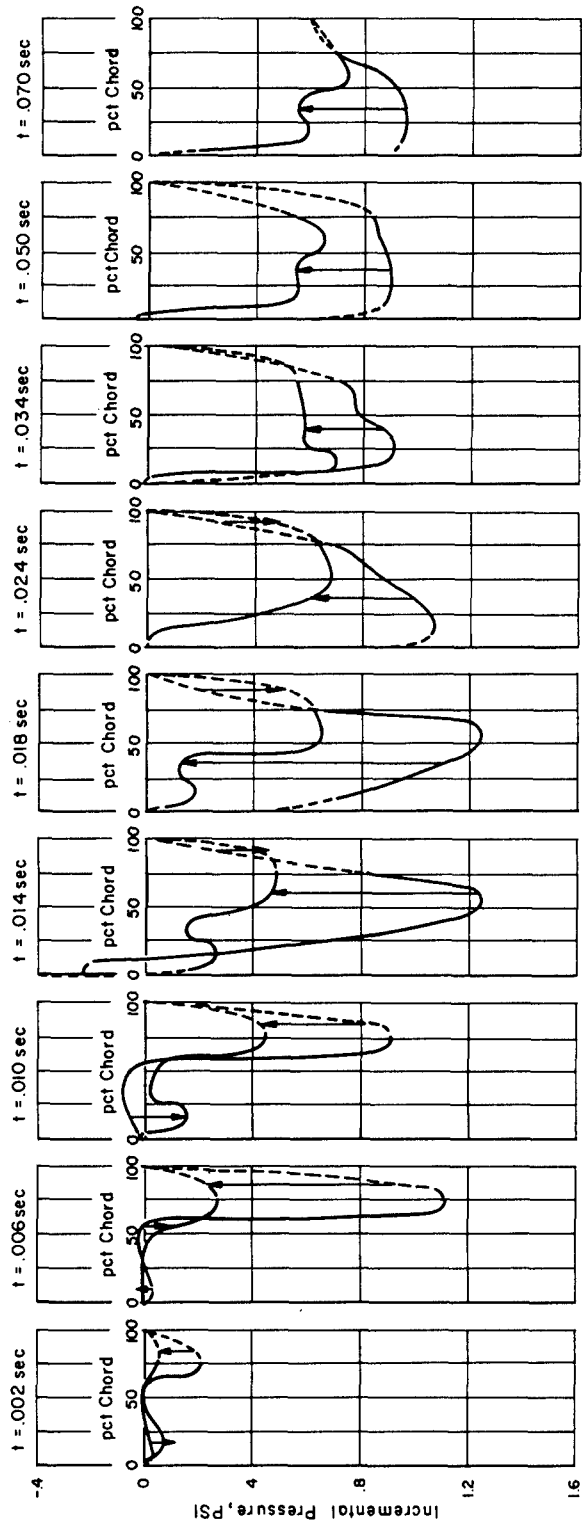


Figure 8.96 Time-wise variation of chord-wise incremental pressure, Shot Smoky.

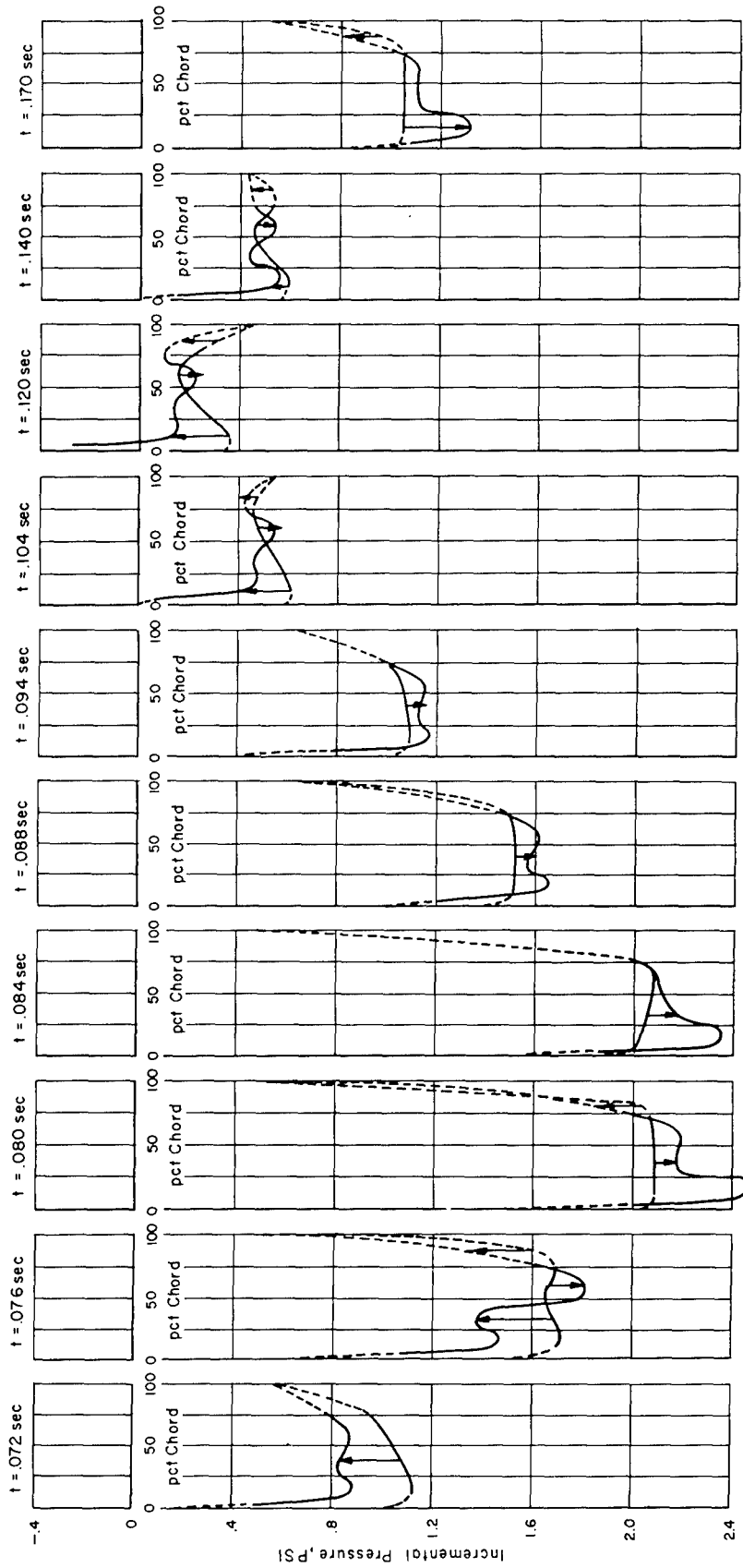


Figure 8.97 Time-wise variation of chord-wise incremental pressure, Shot Smoky.

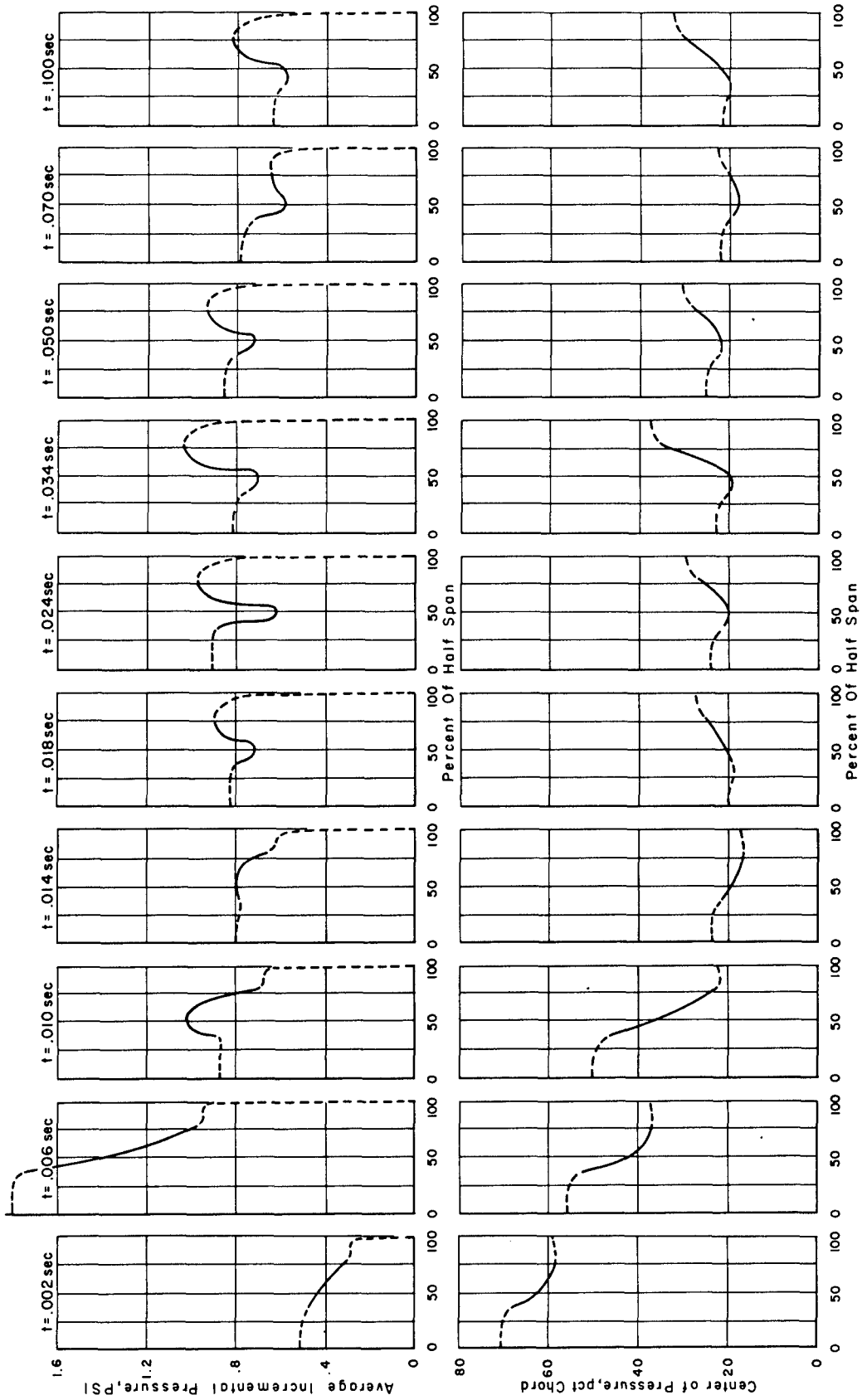


Figure 8.98 Time-wise variation of span-wise incremental pressure and chord-wise center of pressure locations, Shot Priscilla.

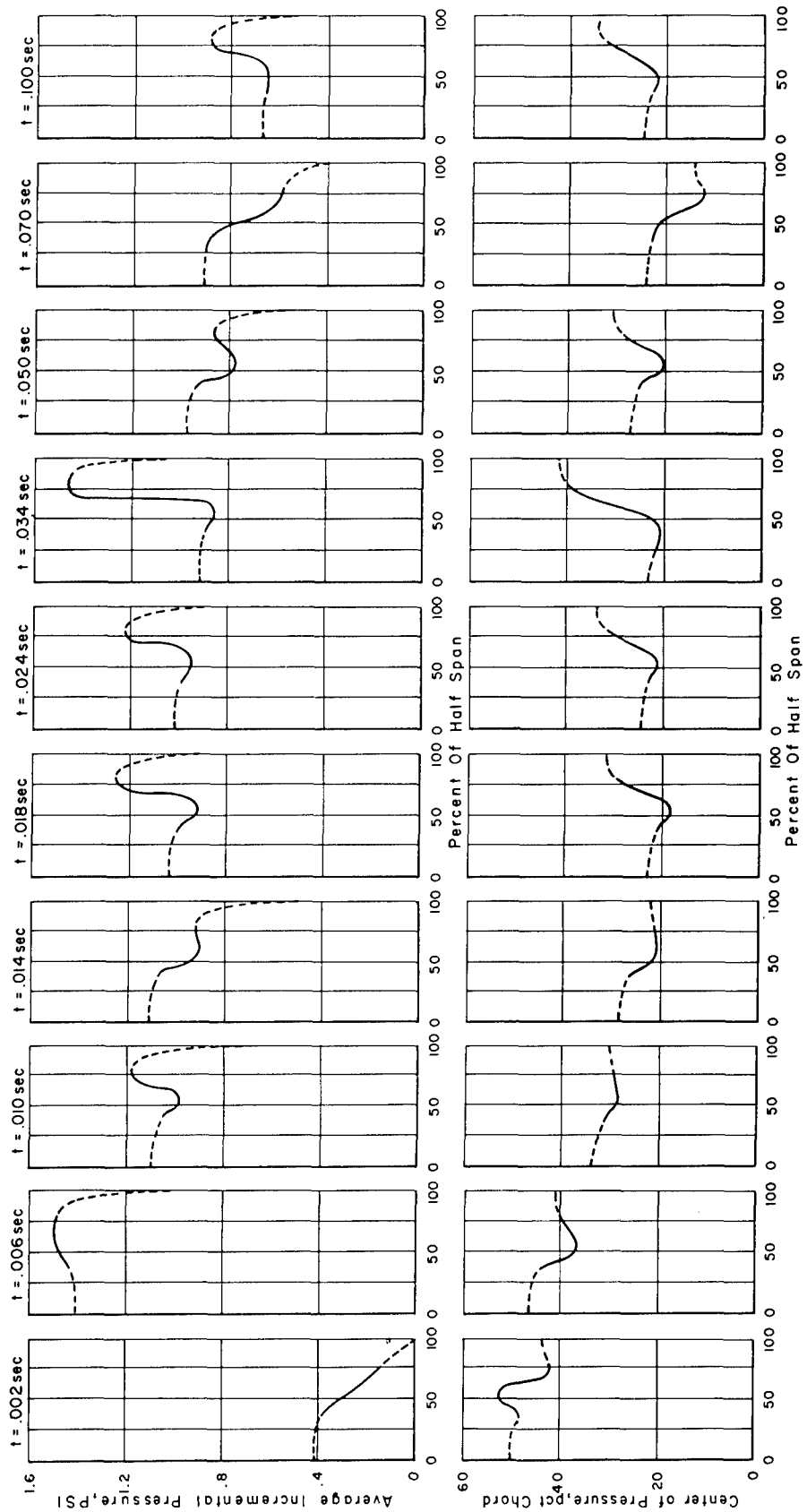


Figure 8.99 Time-wise variation of span-wise incremental pressure and chord-wise center of pressure locations, Shot Diablo.

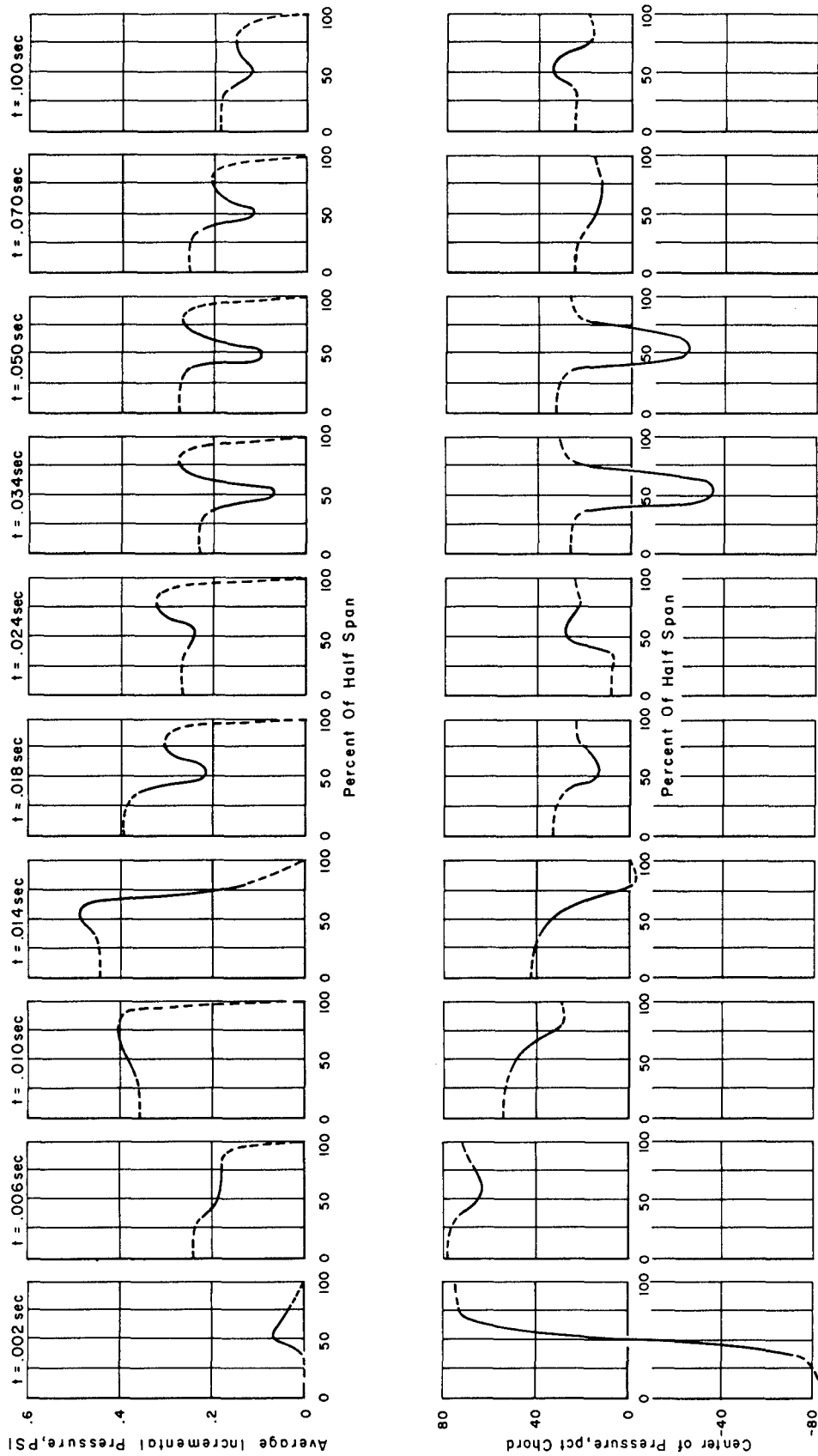


Figure 8.100 Time-wise variation of span-wise incremental pressure and chord-wise center of pressure locations, Shot Doppler, Airplane No. 137827.

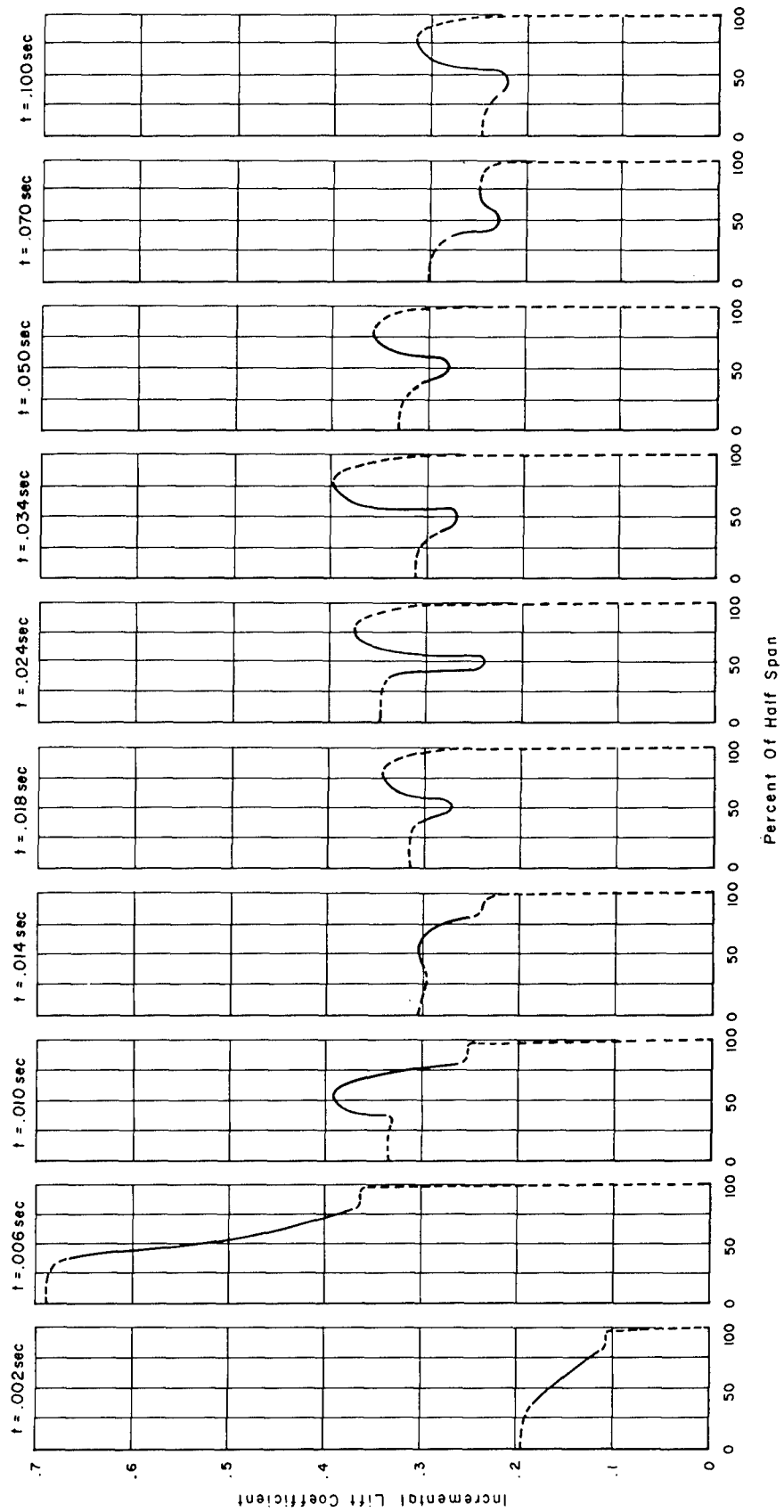


Figure 8.101 Time-wise variation of span-wise section lift coefficients, Shot Priscilla.

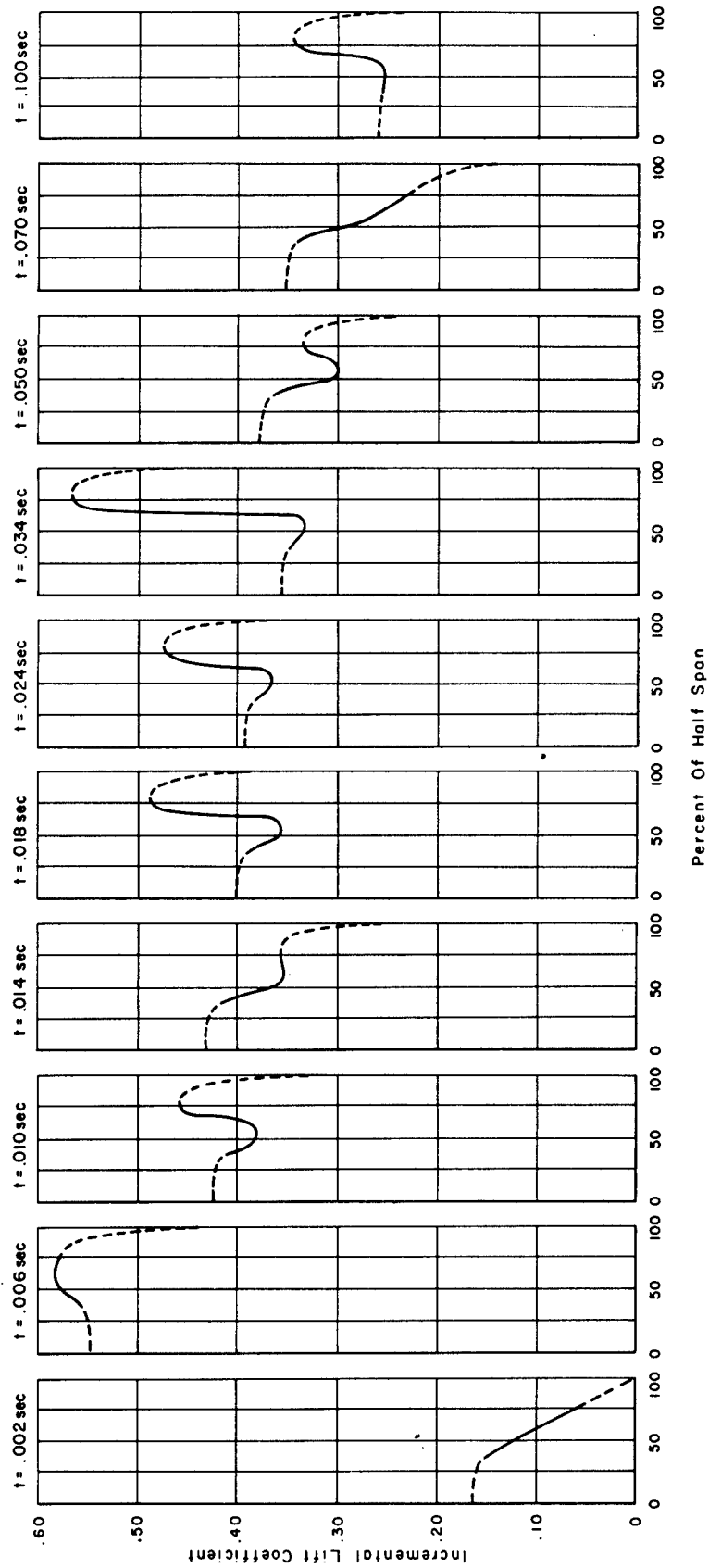


Figure 8.102 Time-wise variation of span-wise section lift coefficients, Shot Diablo.

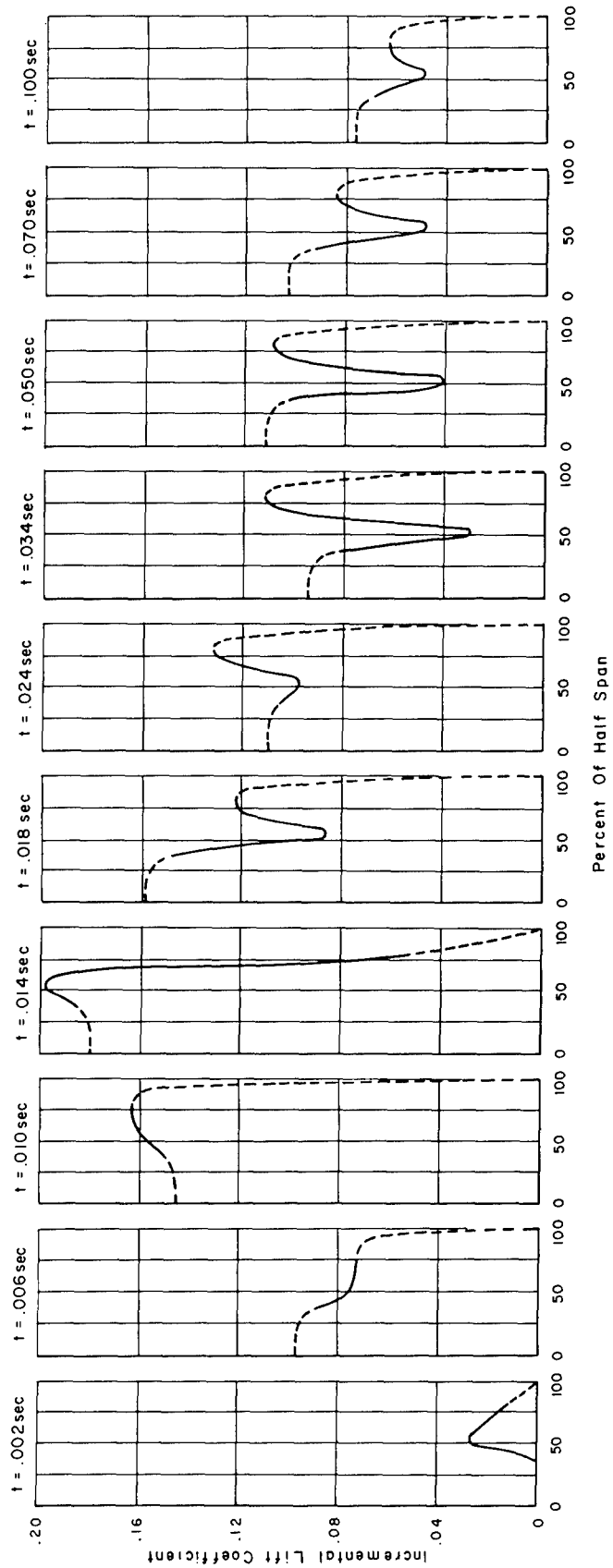


Figure 8.103 Time-wise variation of span-wise section lift coefficients, Shot Doppler, Airplane No. 137827.

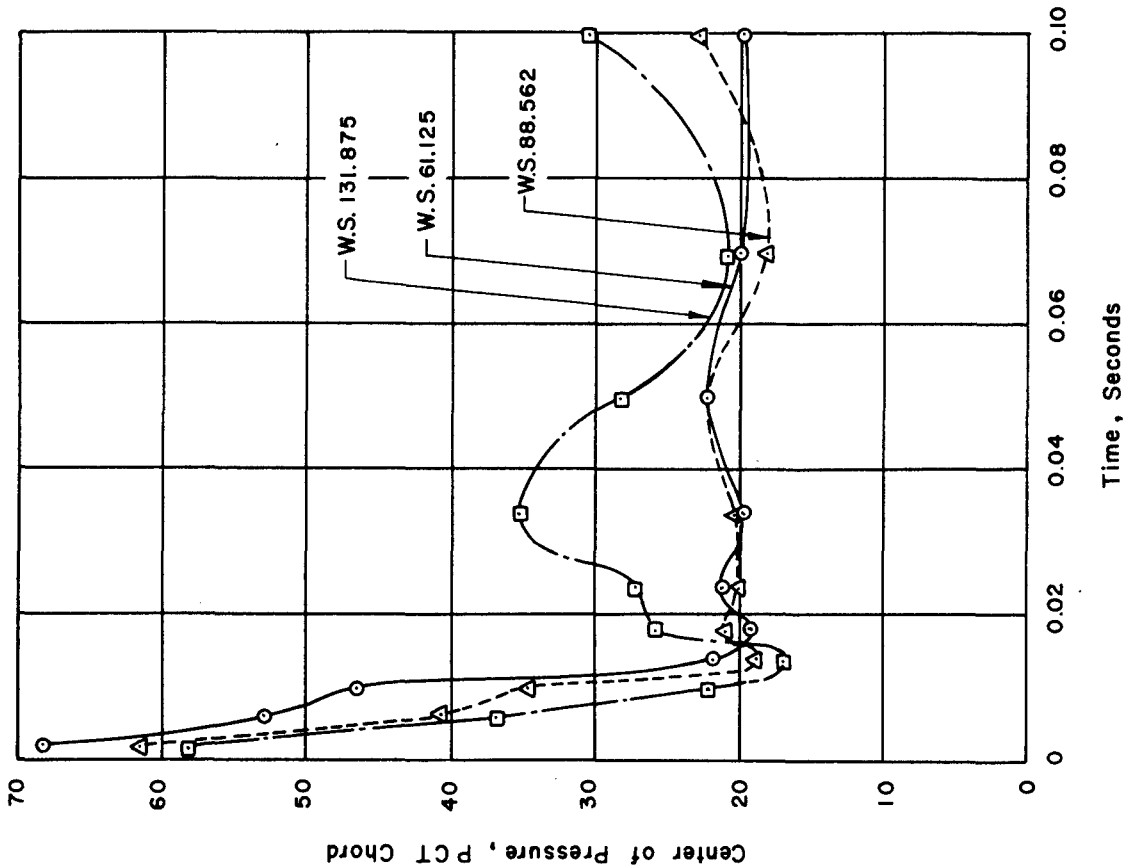


Figure 8.104 Time-wise variation of chord-wise center of pressure locations for three wing stations, Shot Priscilla.

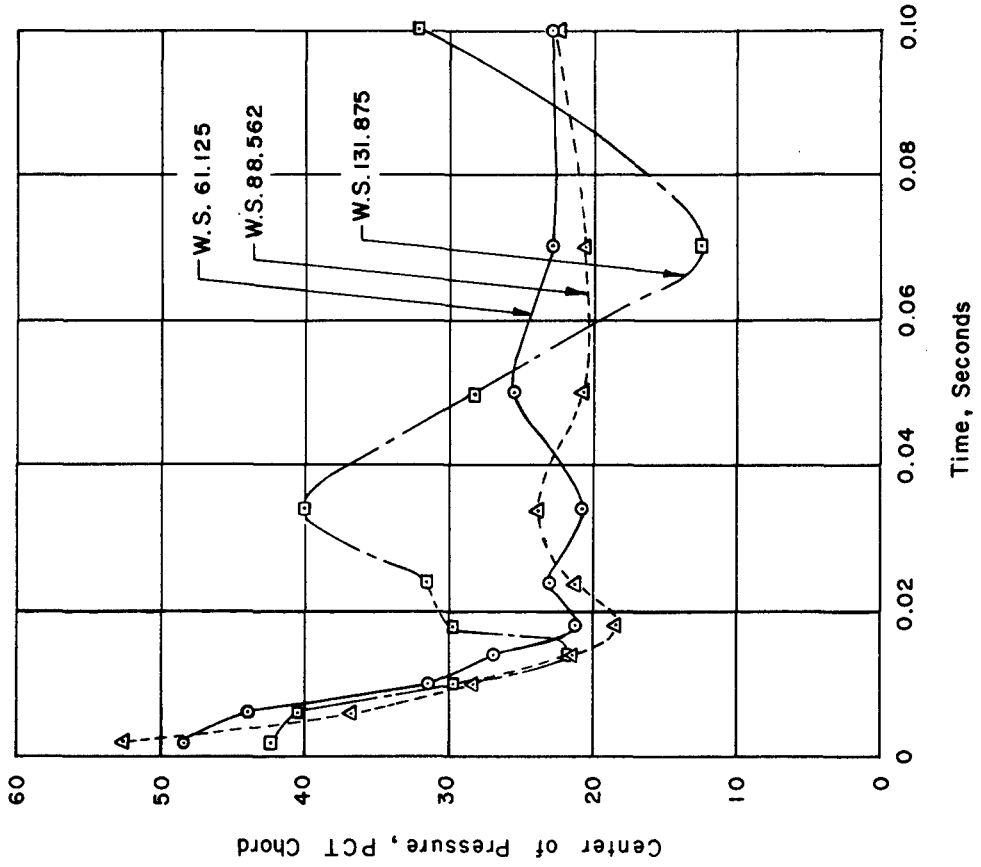


Figure 8.105 Time-wise variation of chord-wise center of pressure locations for three wing stations, Shot Diablo.

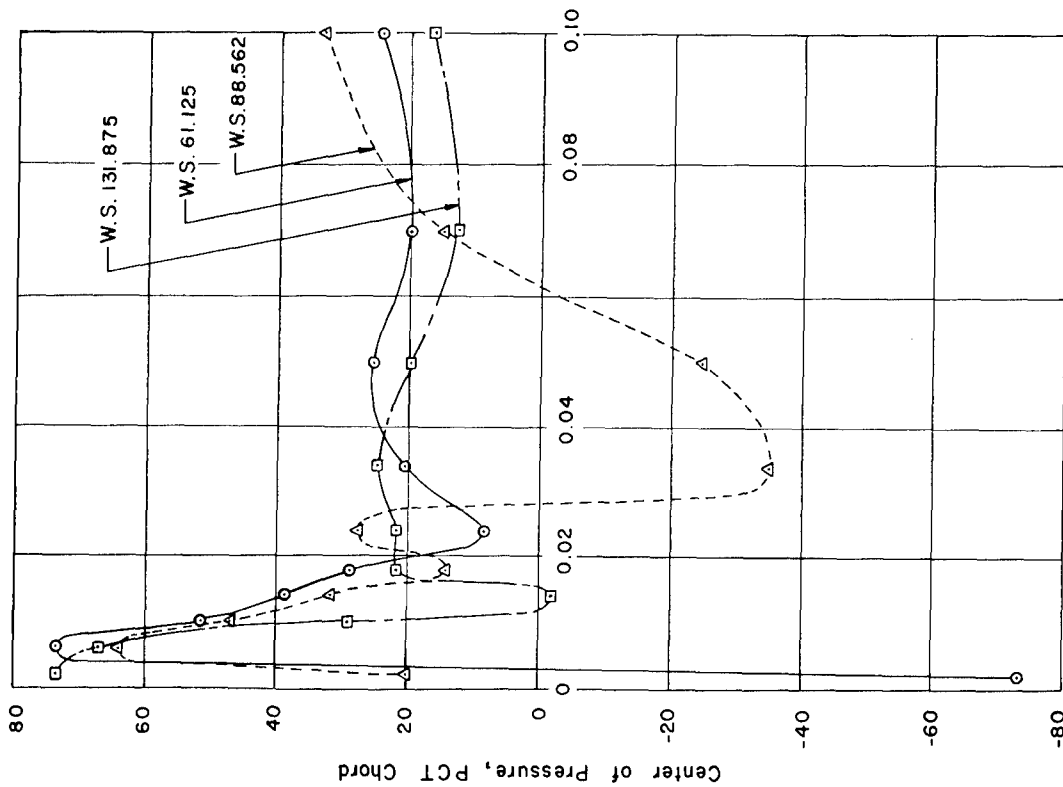


Figure 8.106 Time-wise variation of chord-wise center of pressure locations for three wing stations, Shot Doppler, Airplane No. 137827.

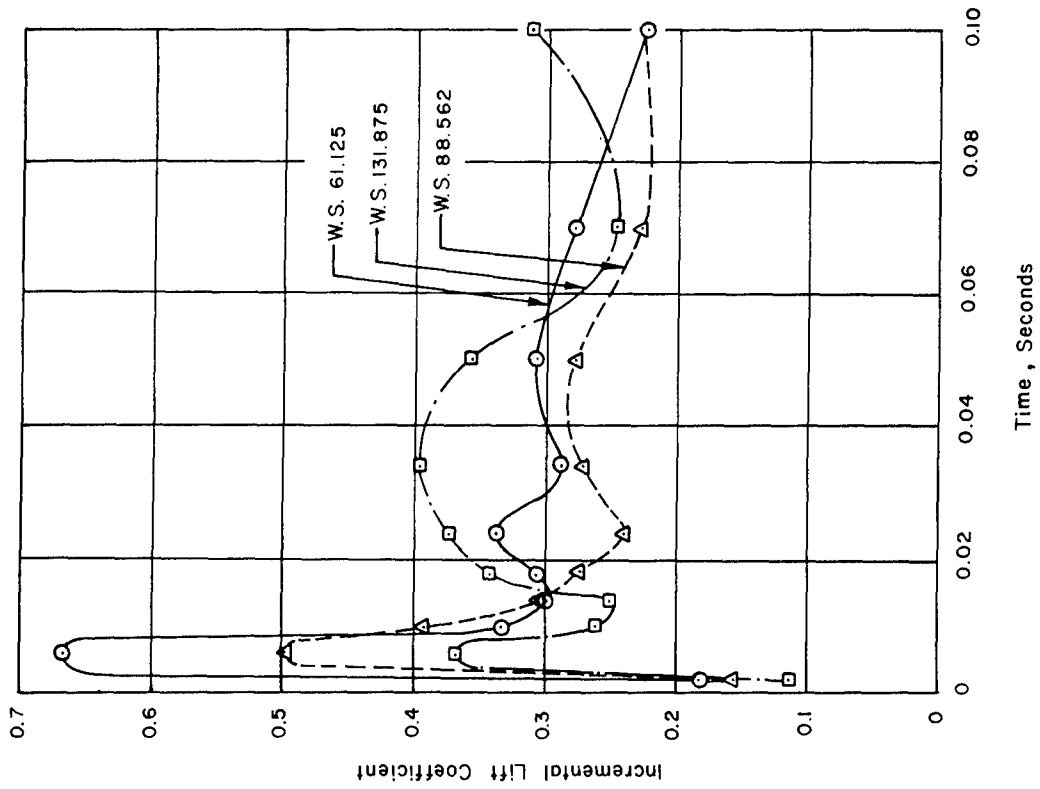


Figure 8.107 Time-wise variation of incremental section lift coefficients for three wing stations, Shot Priscilla.

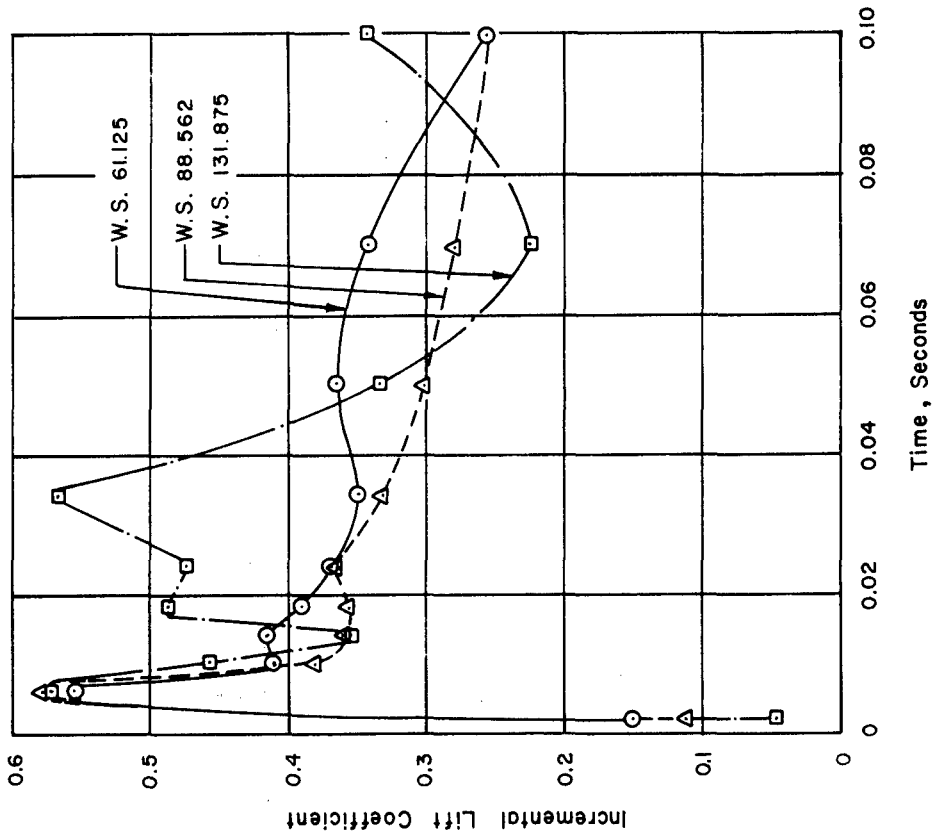


Figure 8.108 Time-wise variation of incremental section lift coefficients for three wing stations, Shot Diablo.

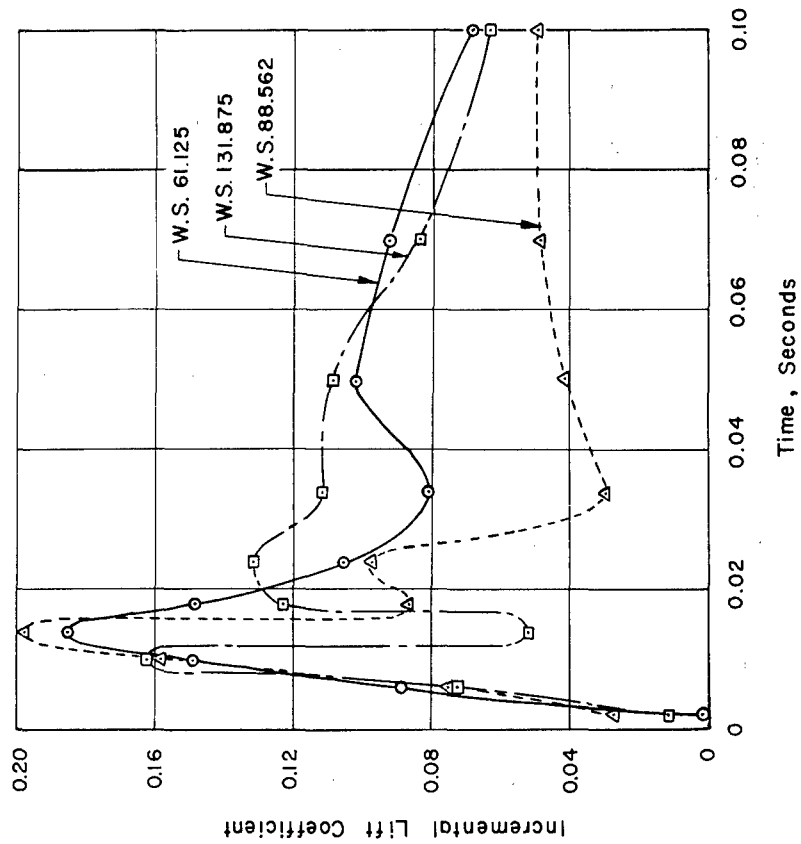


Figure 8.109 Time-wise variation of incremental section lift coefficients for three wing stations, Shot Doppler, Airplane No. 137827.

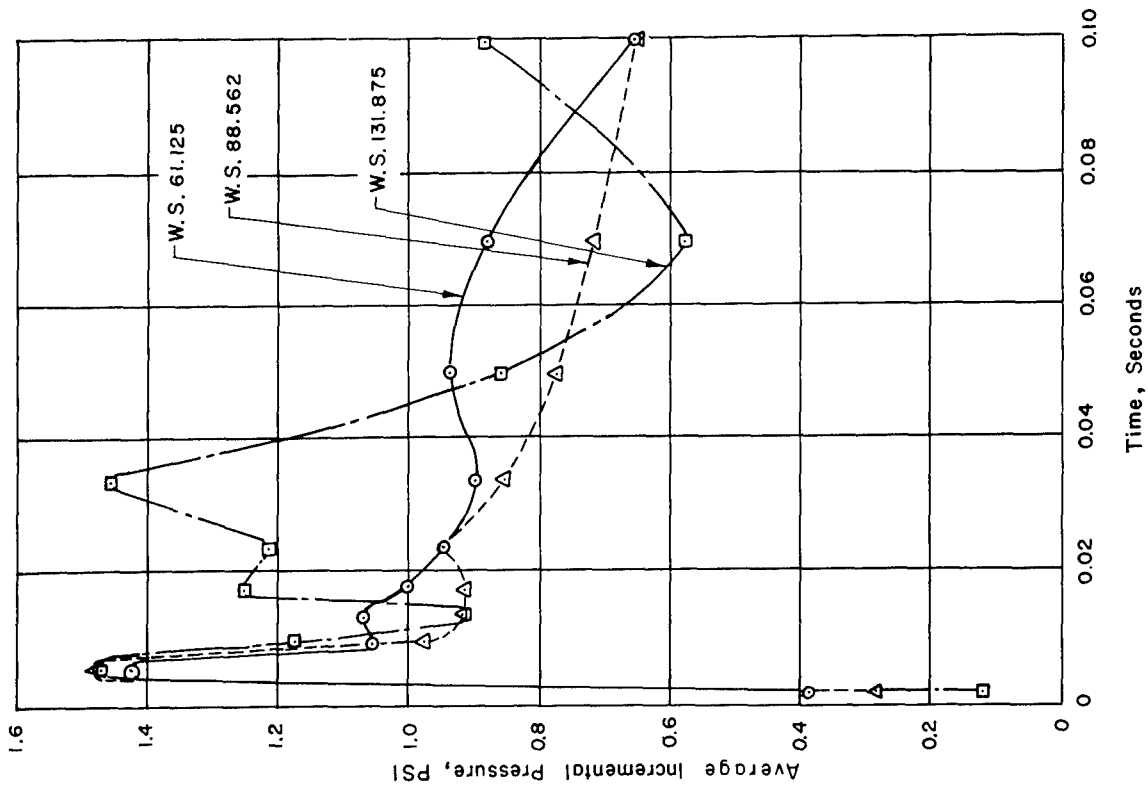


Figure 8.111 Time-wise variation of average incremental pressure for three wing stations, Shot Diablo.

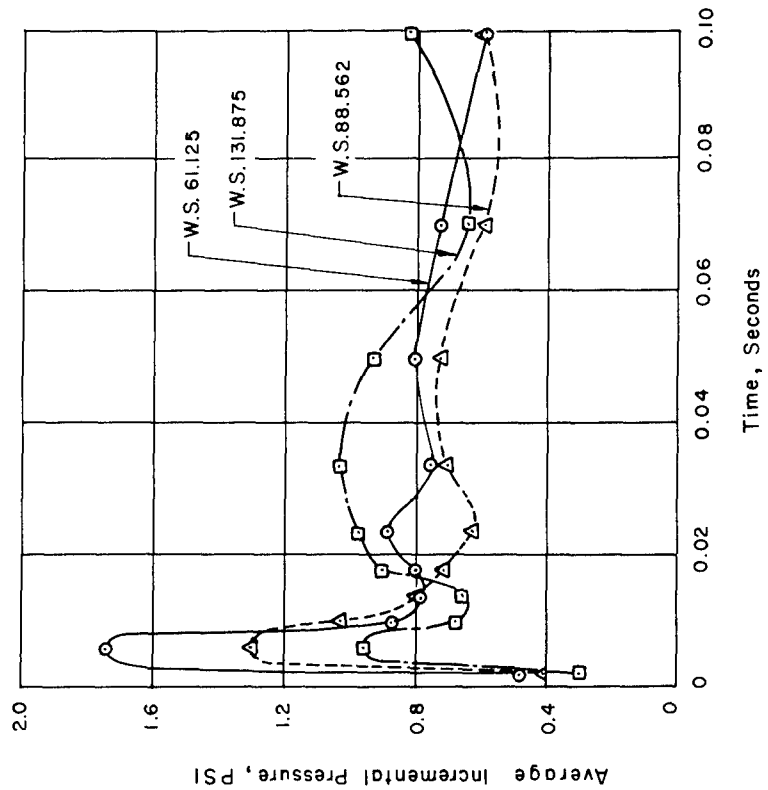


Figure 8.110 Time-wise variation of average incremental pressure for three wing stations, Shot Priscilla.

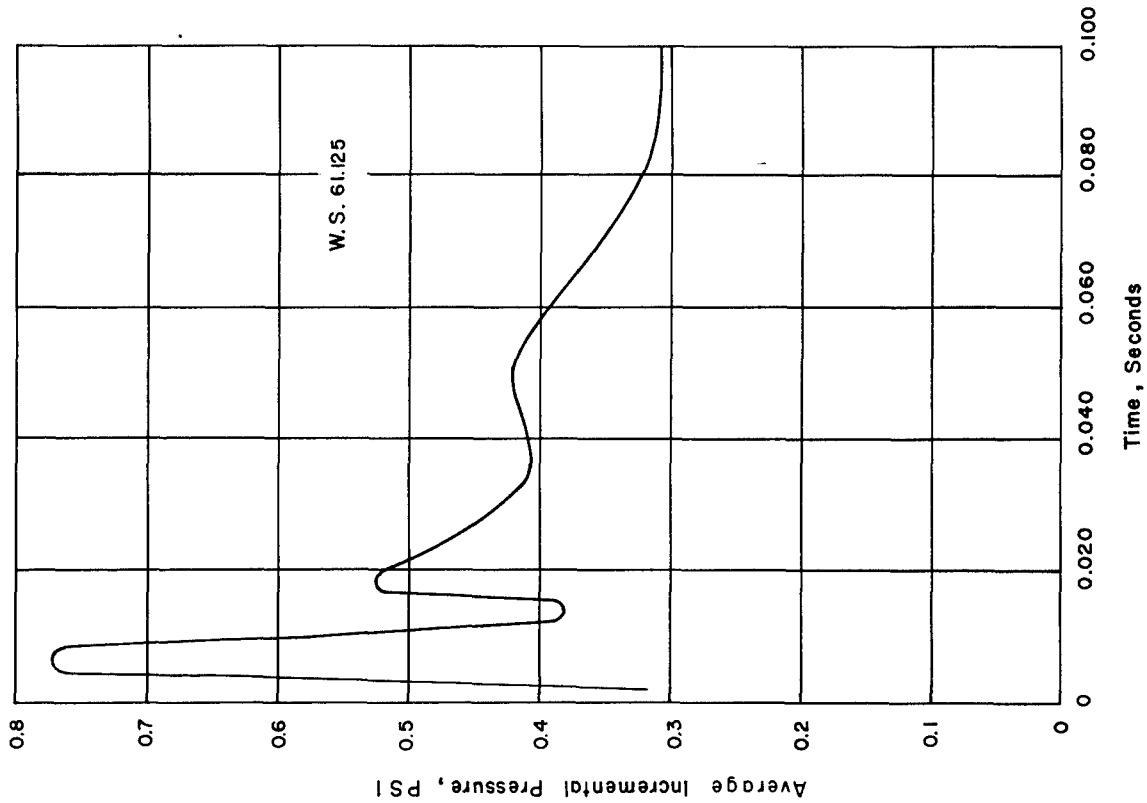


Figure 8.113 Time-wise variation of average incremental pressure, Shot Boltzmann.

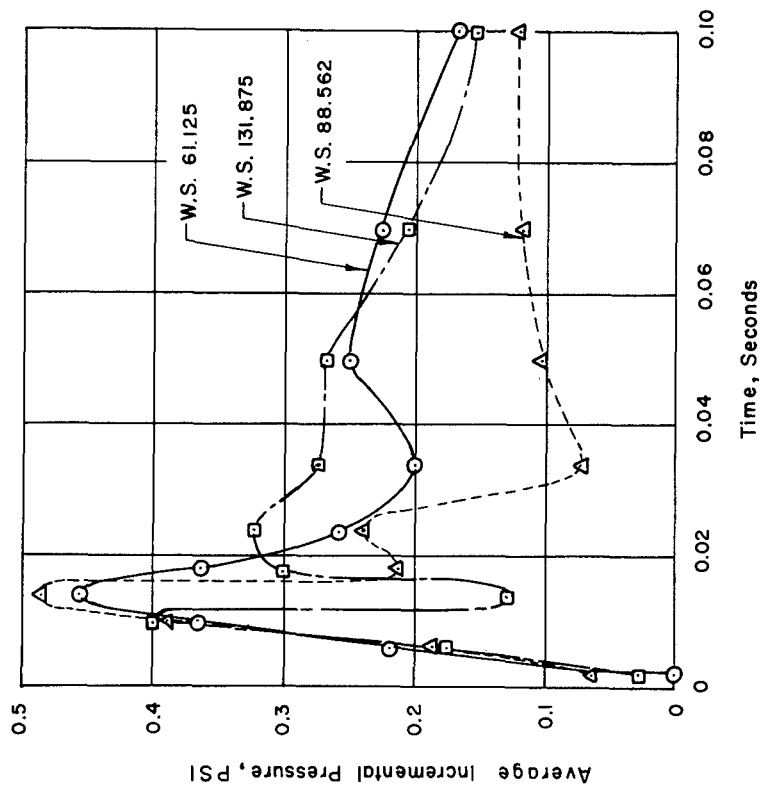


Figure 8.112 Time-wise variation of average incremental pressure for three wing stations, Shot Doppler, Airplane No. 137827.

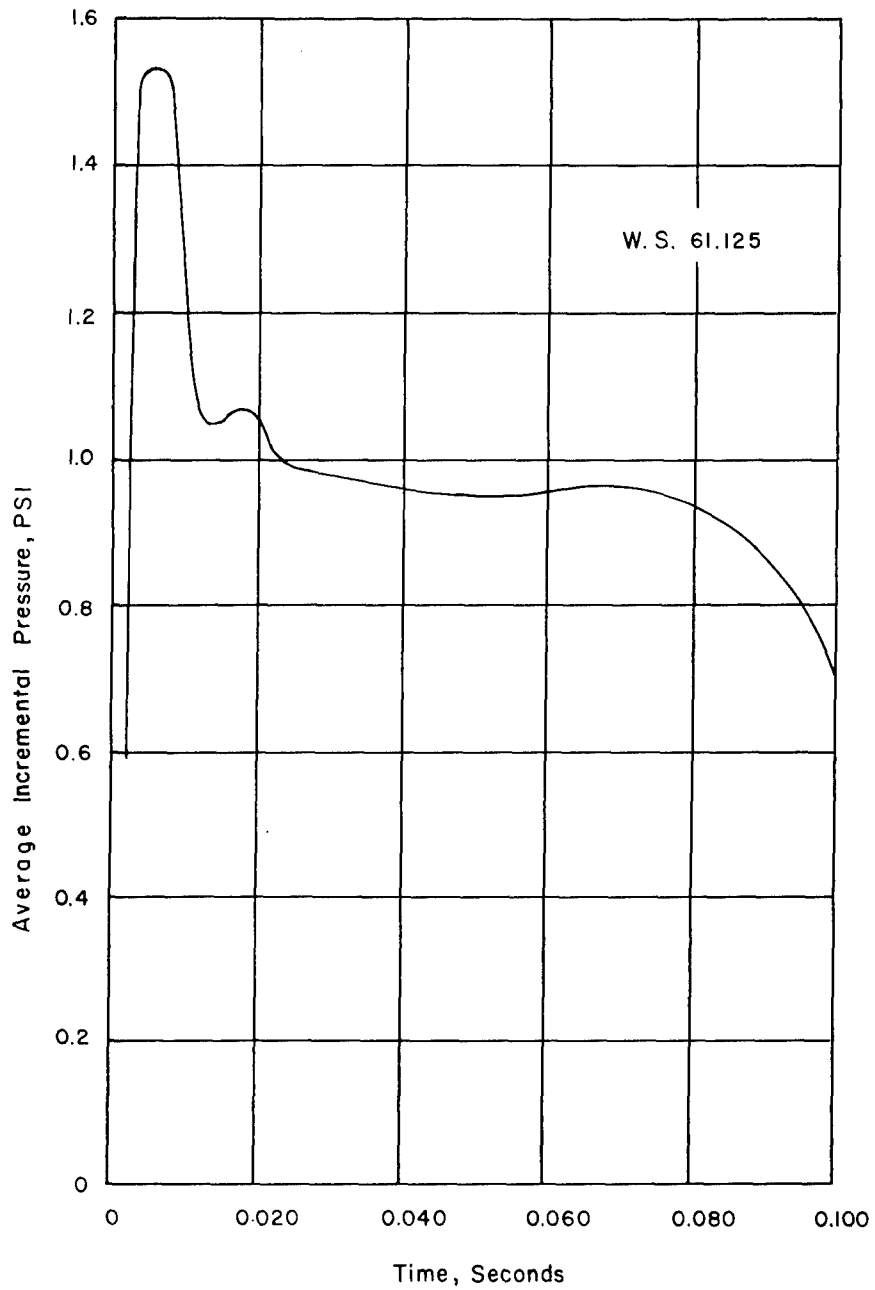


Figure 8.114 Time-wise variation of average incremental pressure, Shot Shasta.

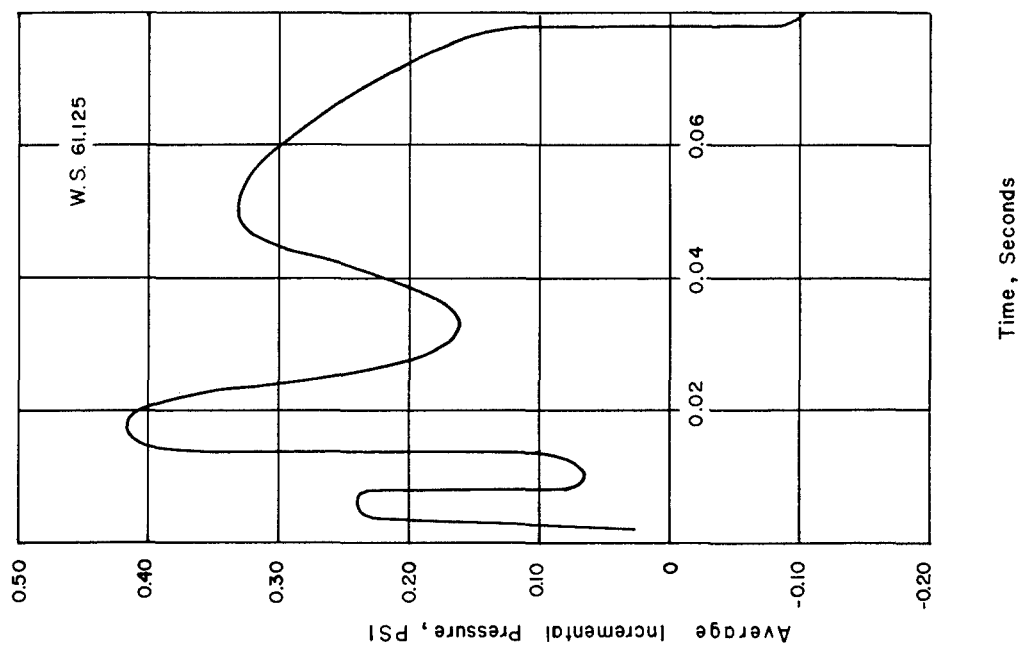


Figure 8.116 Time-wise variation of average incremental pressure, Shot Smoky.

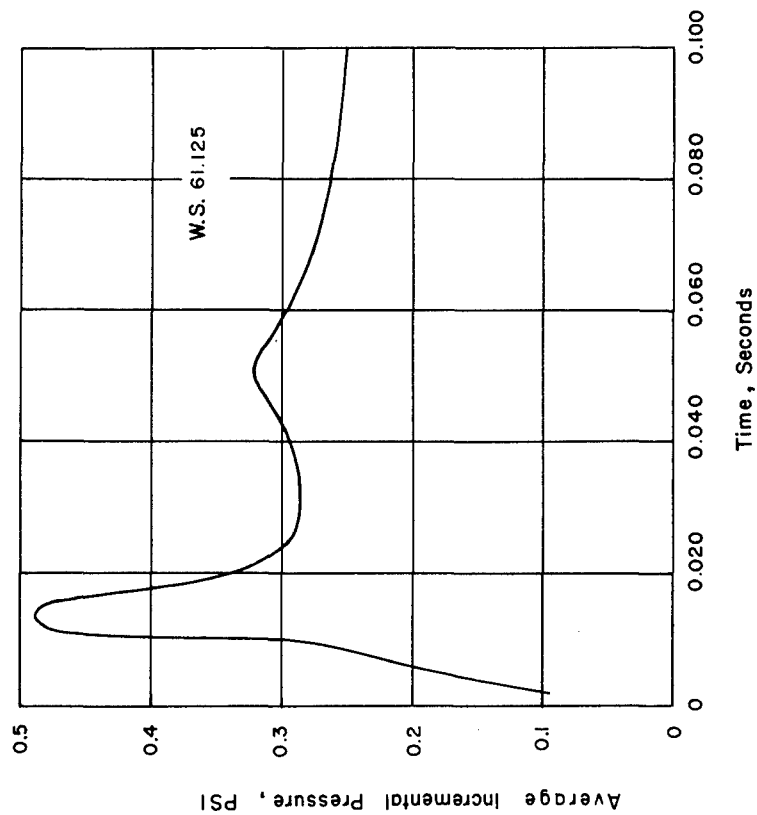


Figure 8.115 Time-wise variation of average incremental pressure, Shot Doppler, Airplane No. 137831.

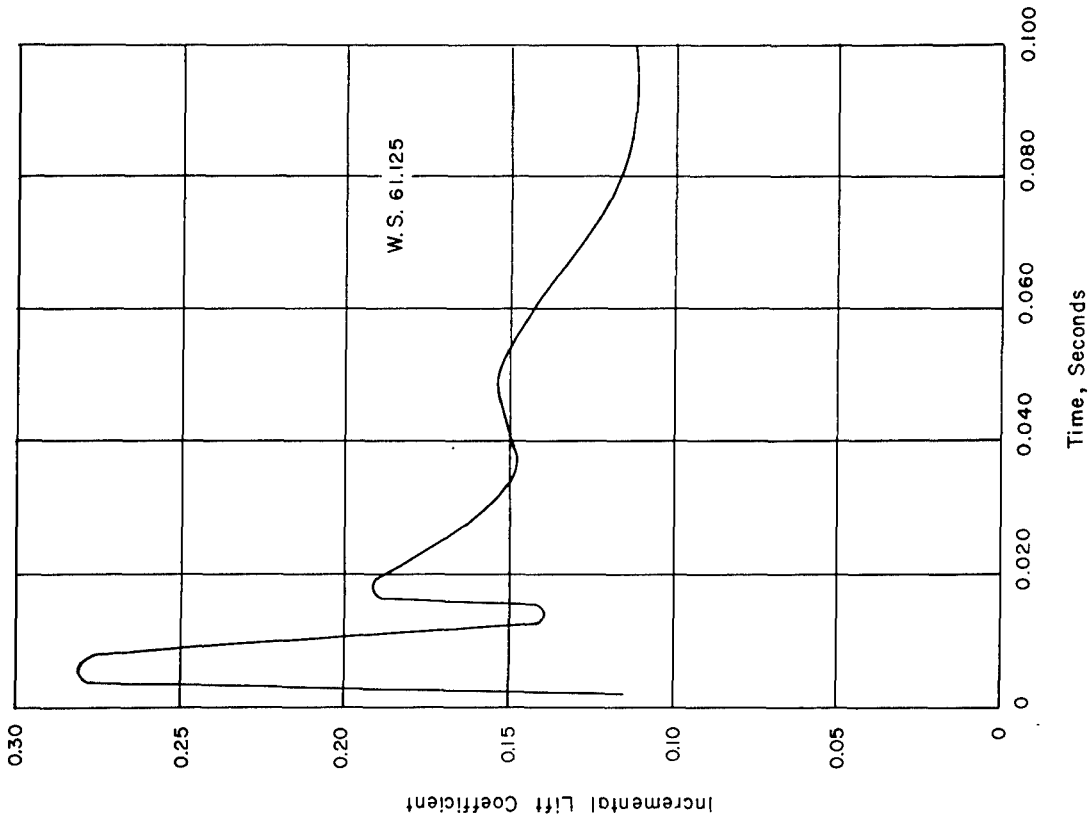


Figure 8.117 Time-wise variation of average incremental pressure, Shot Smoky.

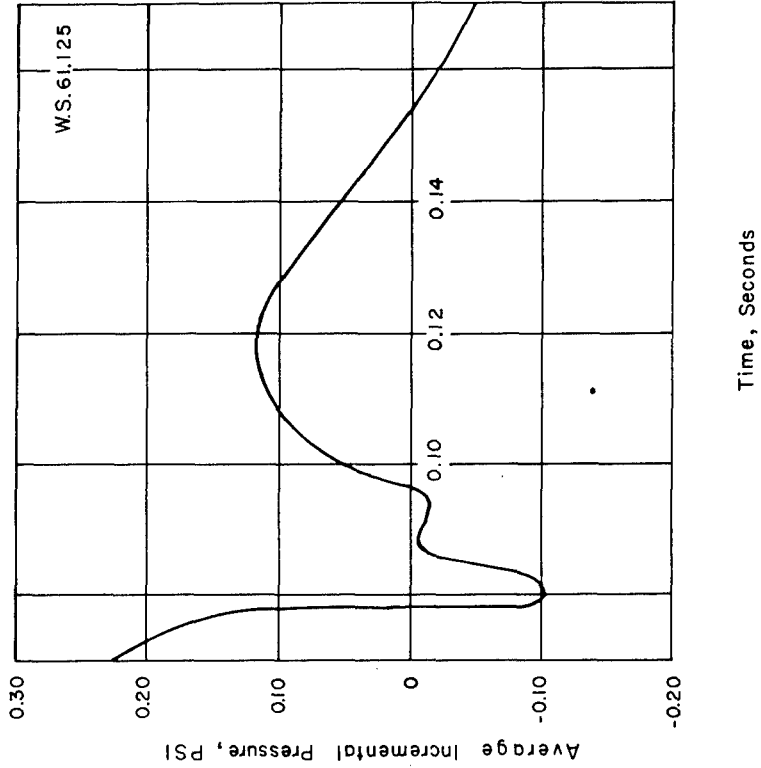


Figure 8.118 Time-wise variation of incremental section lift coefficients, Shot Boltzmann.

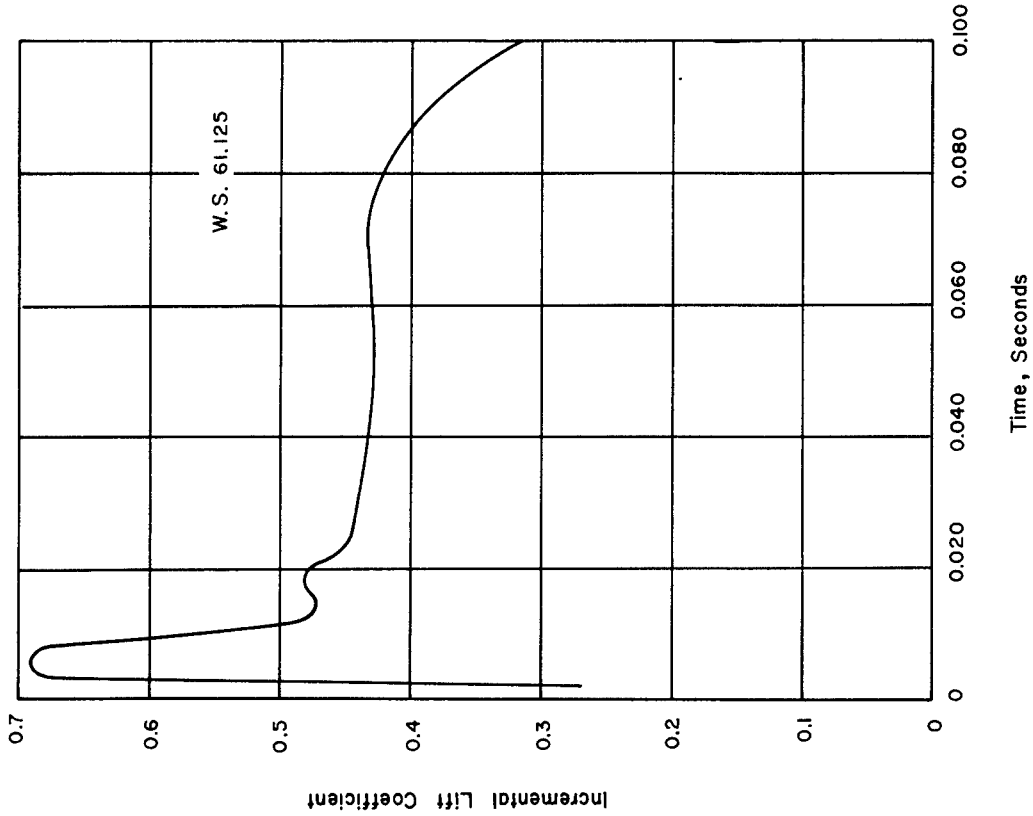


Figure 8.119 Time-wise variation of incremental section lift coefficients, Shot Shasta.

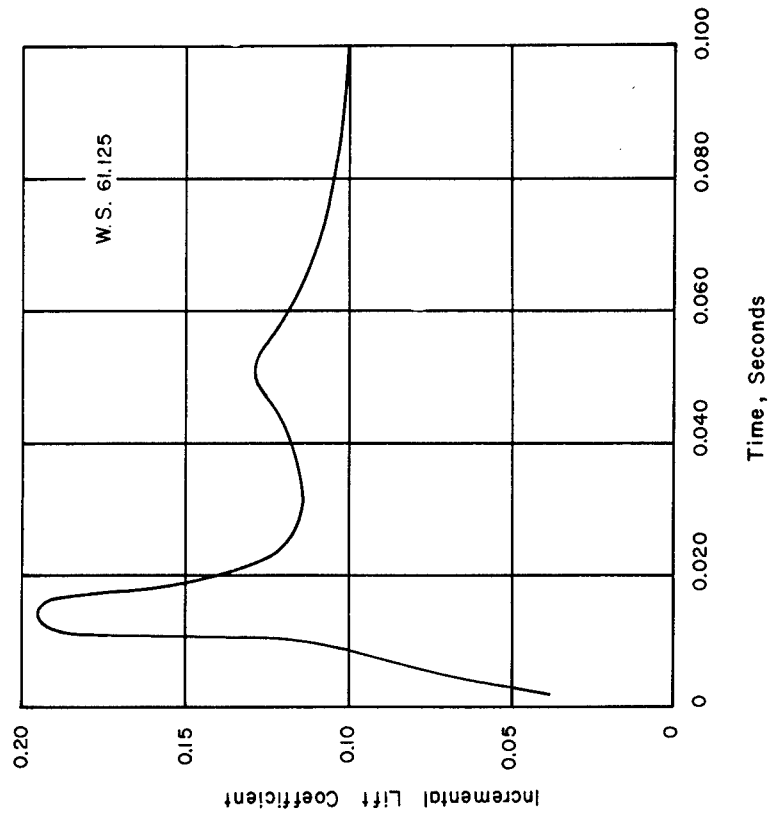


Figure 8.120 Time-wise variation of incremental section lift coefficients, Shot Doppler, Airplane No. 137831.

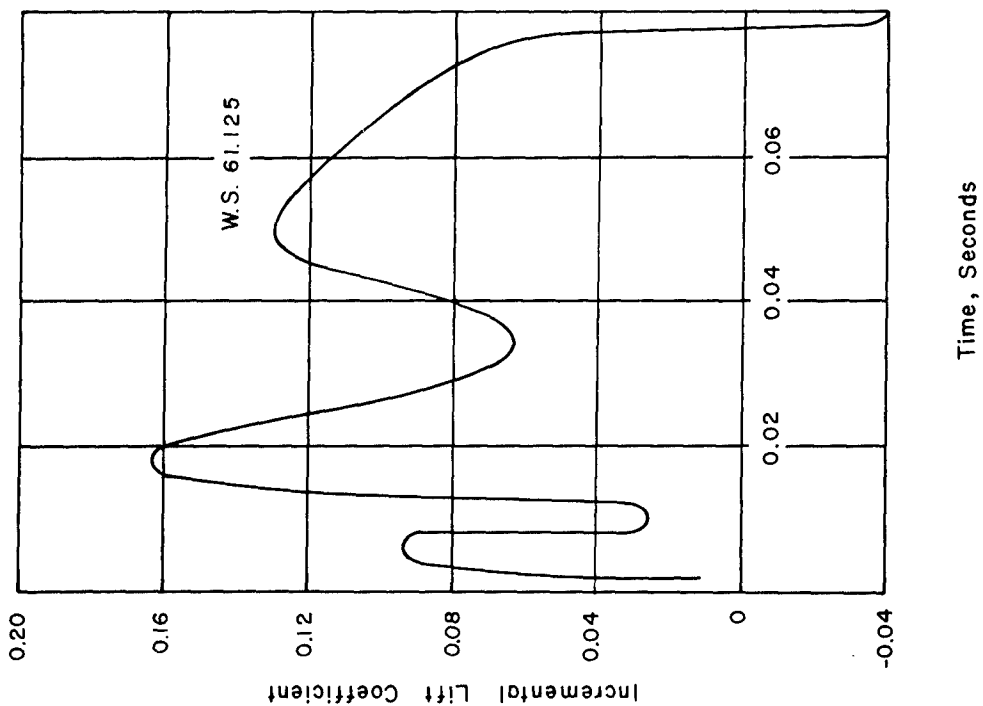


Figure 8.121 Time-wise variation of incremental section lift coefficients, Shot Smoky.

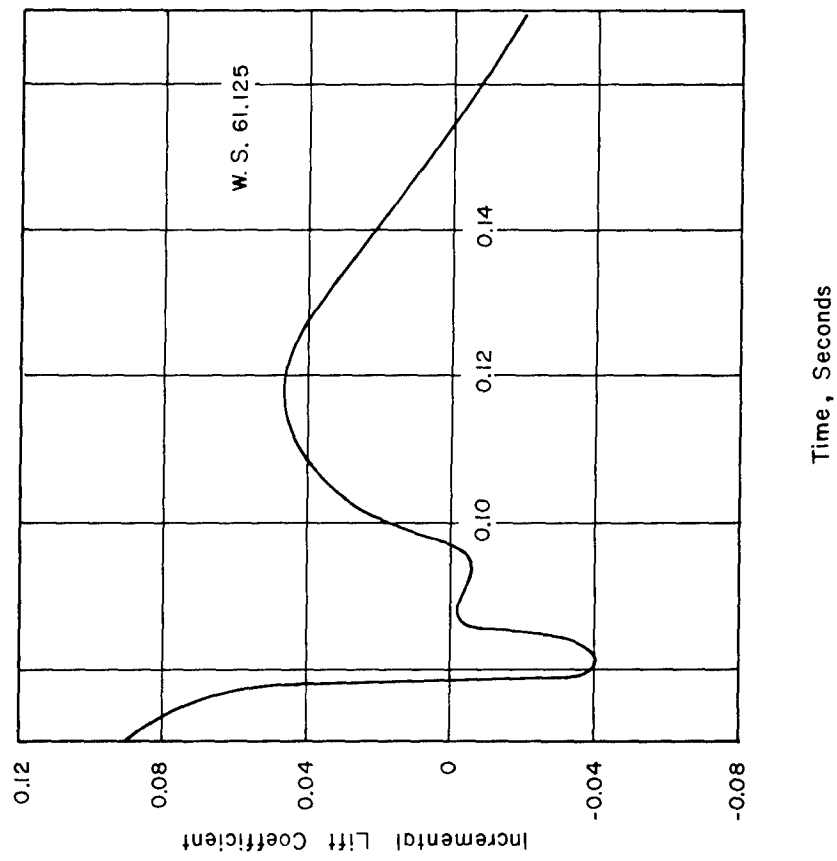


Figure 8.122 Time-wise variation of incremental section lift coefficients, Shot Smoky.

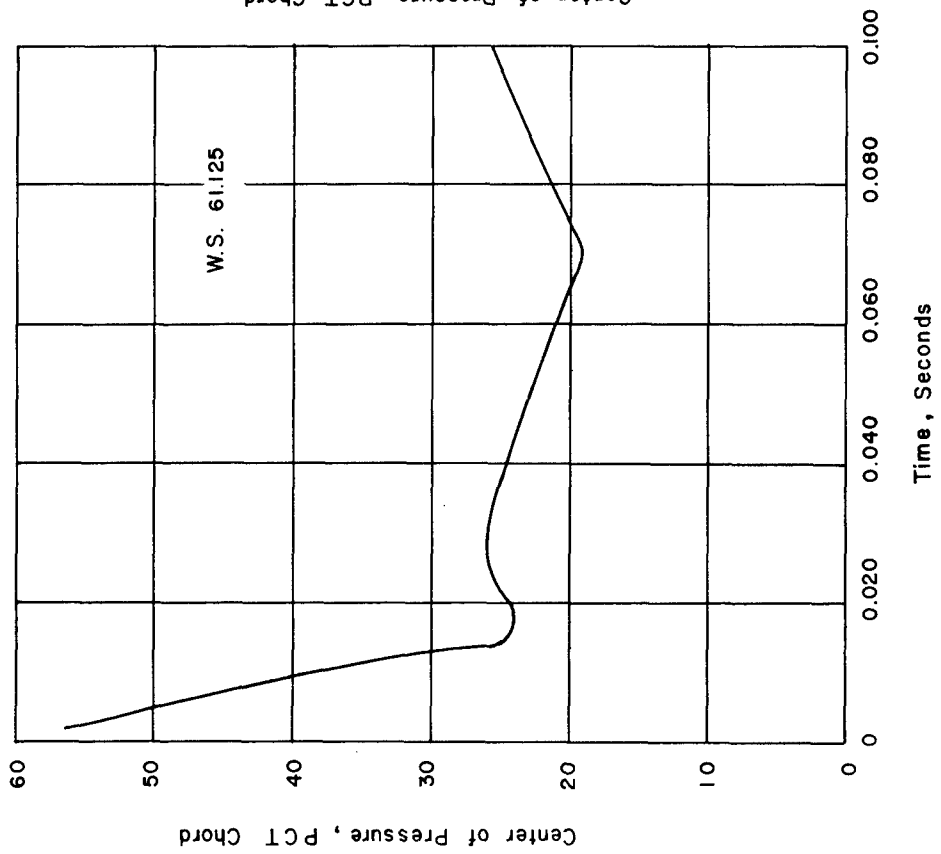


Figure 8.123 Time-wise variation of chord-wise center of pressure location, Shot Boltzmann.

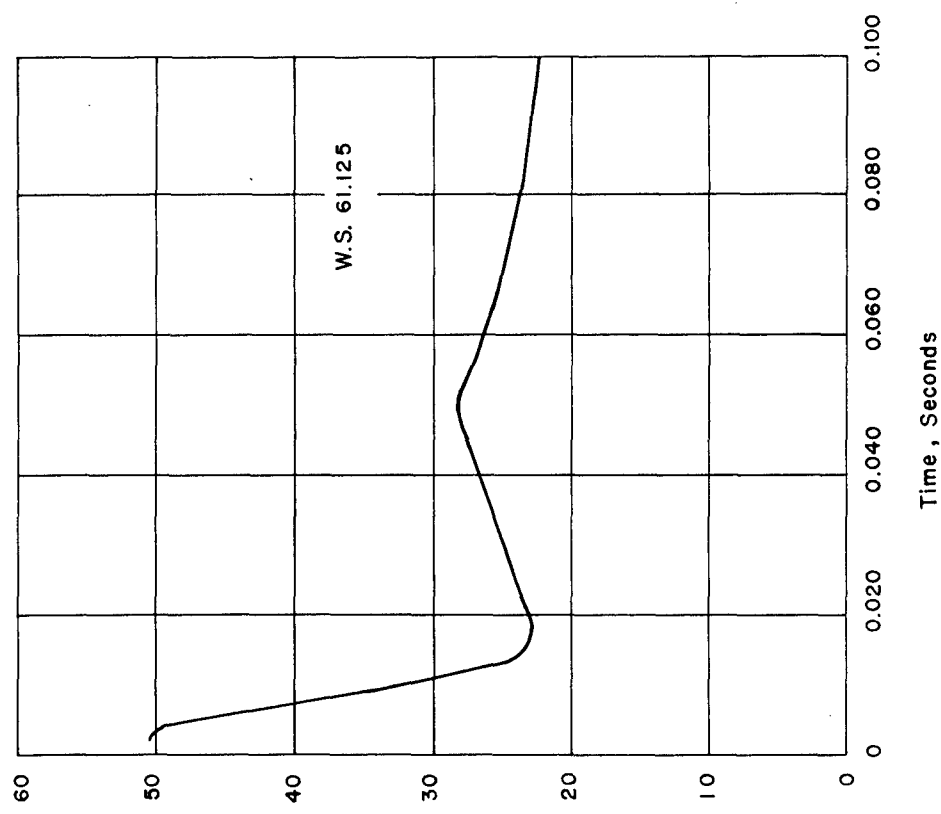


Figure 8.124 Time-wise variation of chord-wise center of pressure location, Shot Shasta.

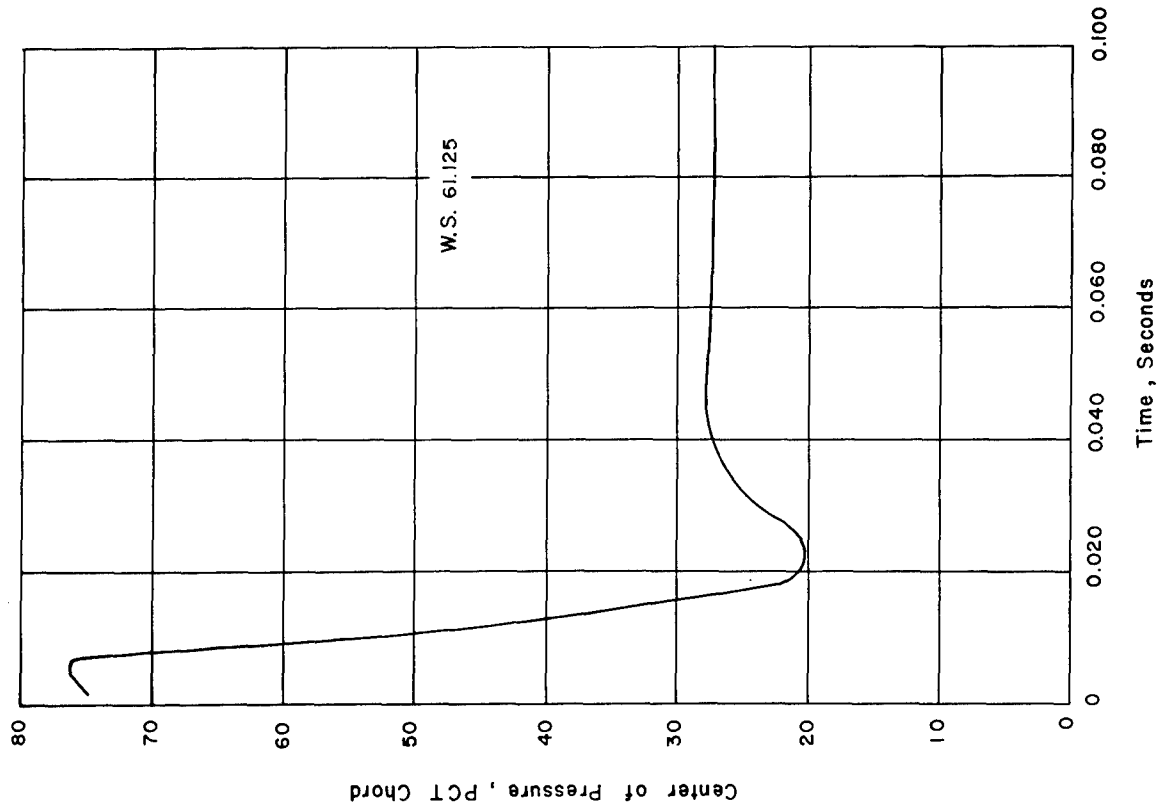


Figure 8.125 Time-wise variation of chord-wise center of pressure location, Shot Doppler, Airplane No. 137831.

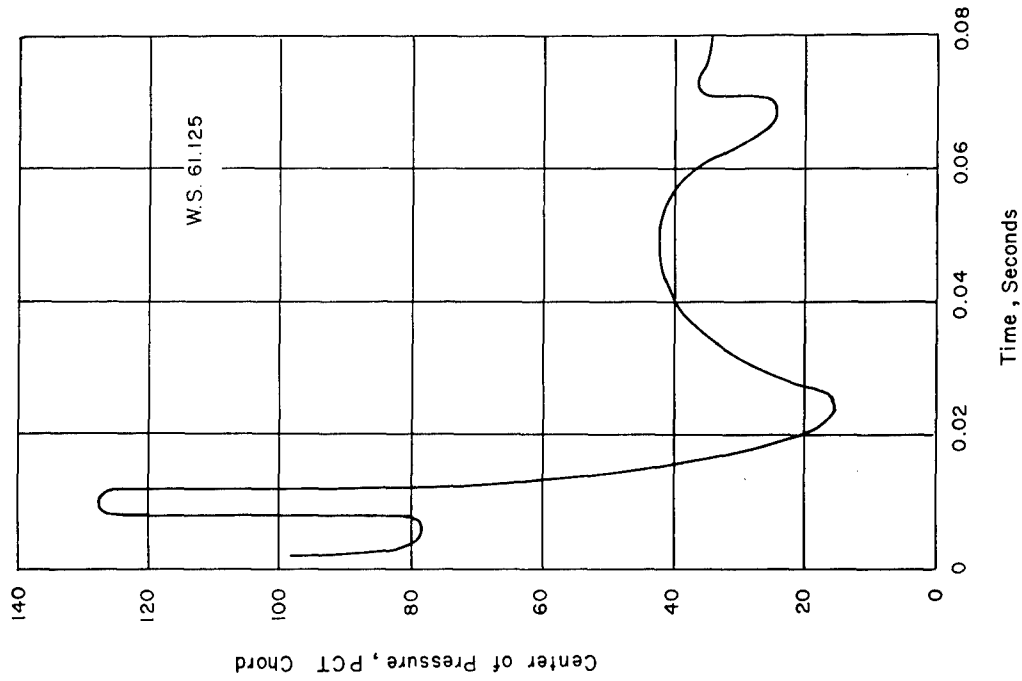


Figure 8.126 Time-wise variation of chord-wise center of pressure location, Shot Smoky.

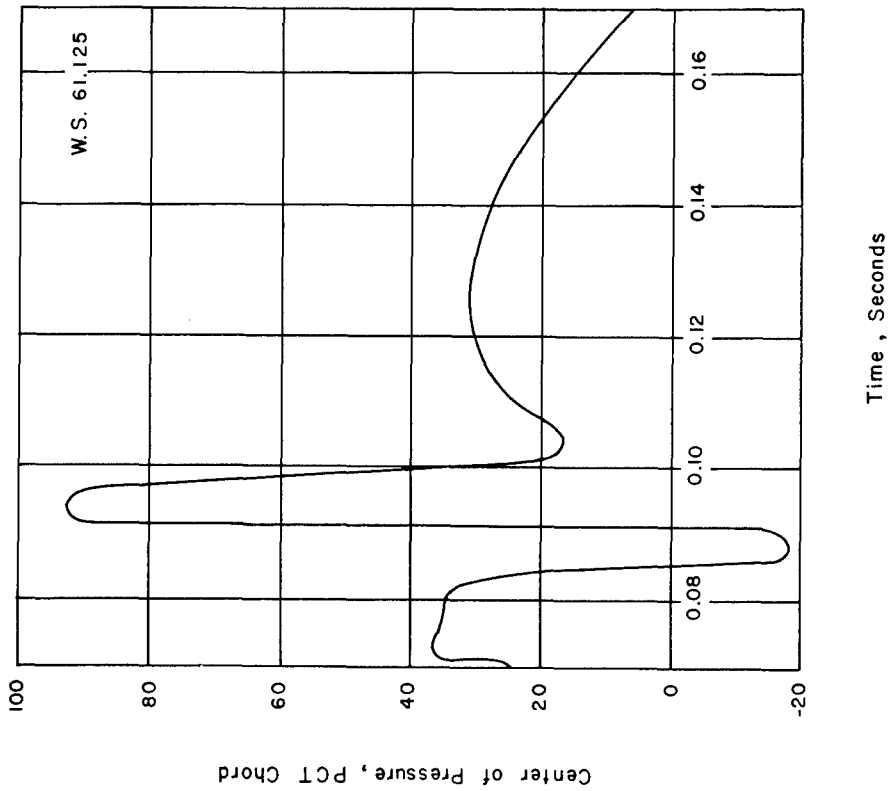


Figure 8.127 Time-wise variation of chord-wise center of pressure location, Shot Smoky.

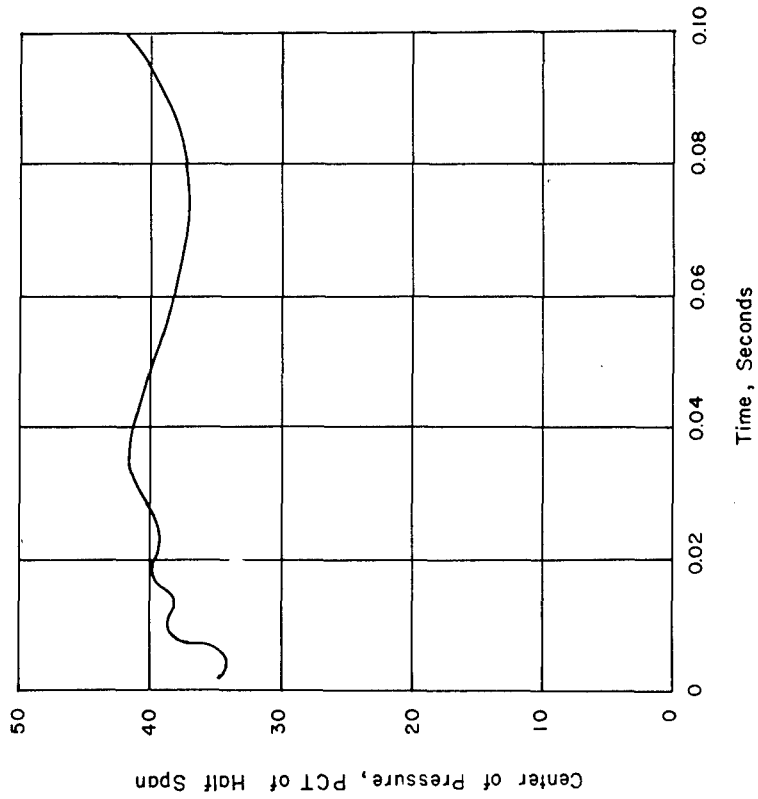


Figure 8.128 Time-wise variation of span-wise center of pressure location, Shot Priscilla.

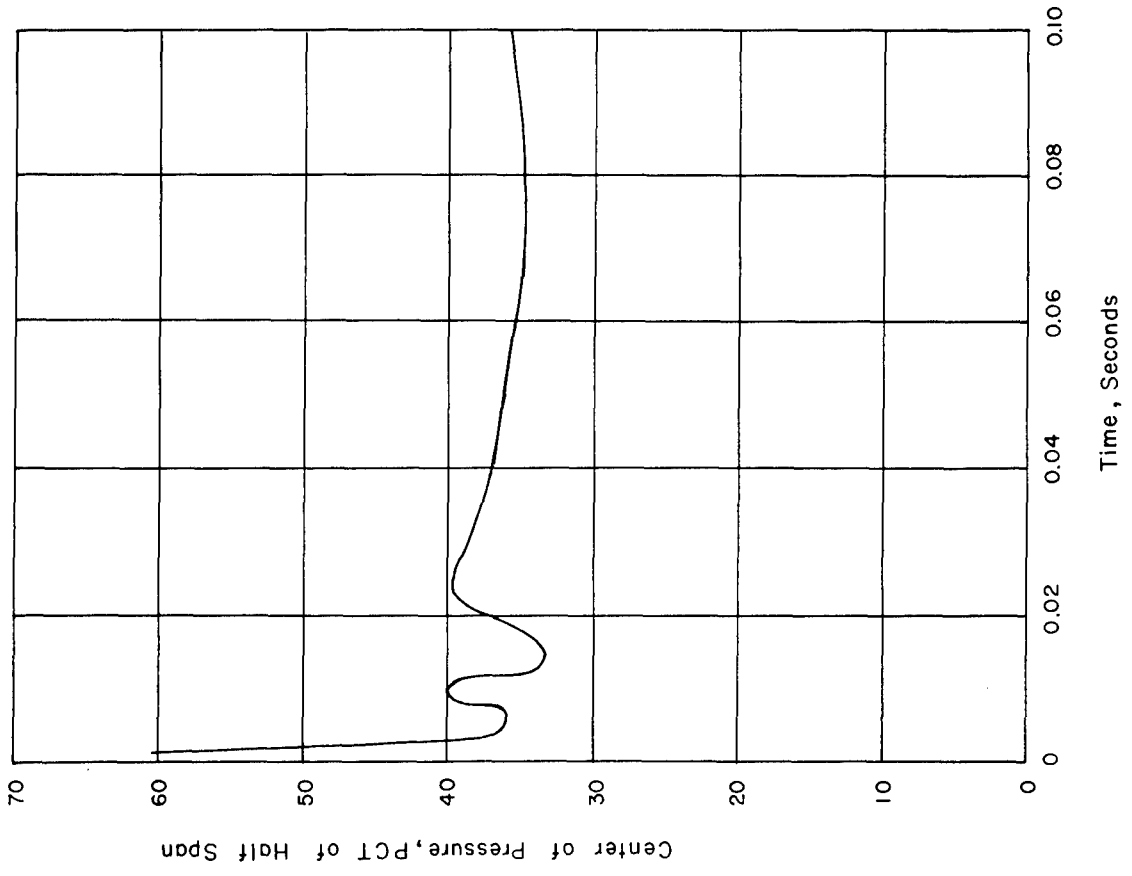


Figure 8.130 Time-wise variation of span-wise center of pressure location, Shot Doppler, Airplane No. 137827.

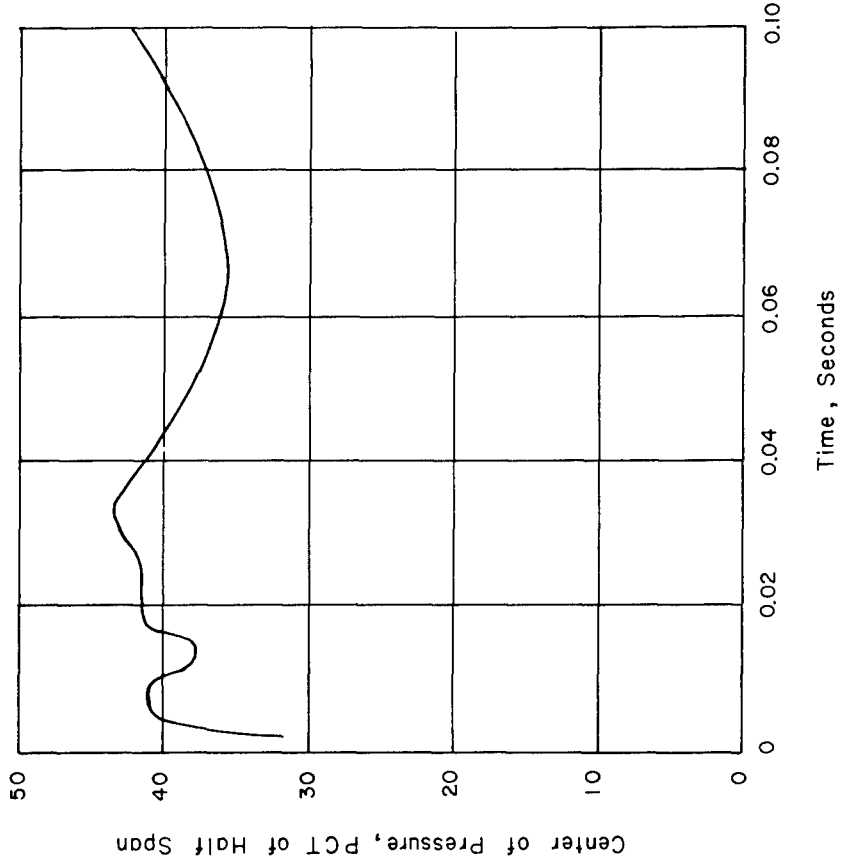


Figure 8.129 Time-wise variation of span-wise center of pressure location, Shot Diablo.

Chapter 9

DELIVERY CAPABILITY OF THE A4D-1 AIRCRAFT

The successful A4D-1 participation in Operation Plumbbob produced data which when combined with the results to be obtained from participation in Operation Hardtack will enable a reliable analysis to be made of the delivery capabilities of the A4D-1 aircraft over a wide range of nuclear weapon yields.

Because of the low level of most of the temperature rises experienced, it was not possible to fully substantiate an absolute upper limit of temperature rise in the aircraft structure.

Chapter 10

CONCLUSIONS

As a result of the tests participated in by Project 5.4 in Operation Plumbbob, the following conclusions can be made:

1. The scattered radiation as measured by the calorimeters in the nose of the aircraft was between 1 and 4 percent of the vertical component of the direct radiation; the instrument directed overhead measured less than 1 percent and the instrument directed to the side measured between 1 and 4 percent. The higher values obtained by the side-directed instrument could be due to reflected energy from the terrain surface. Although the scattered radiation for these tests was negligible, the aircraft were always in clear, cloudless sky, and it cannot be assumed that all atmospheres would produce zero scattering.

2. The methods for calculating the radiant exposure gave values greater than those measured for all shots. Since the scattered radiation was found to be negligible, the omission of this factor from the calculation improved the prediction method although the calculations were still conservative.

3. The measured temperature rise was always less than the calculated value. The main reason for this was the overprediction of the radiant exposure.

4. Maximum temperature rise calculations based on the measured radiant exposure agreed quite well with the measured temperature rise. The agreement was improved further if the mass and thermal capacity of the paint was combined with that of the aluminum skin. All future calculations should take into consideration the paint layer over the skin.

5. An attempt to determine the amount of aerodynamic cooling by comparing the maximum temperature rise of an exposed skin surface to that of an adjacent quartz-covered insulated skin section proved to be of insufficient accuracy. Because of the relatively low temperature rises experienced on most shots, the difference in temperature rise between the two skin sections was not much greater than the experimental accuracy of the data.

6. Overpressure calculations based on the basic 1-kt sea level curve were slightly conservative when compared with the values measured by the boom mounted overpressure pickup.

7. The methods for calculating the time of shock arrival gave excellent agreement with the observed results.

8. The measured nuclear radiation was inconsistent between various recording locations, shots, and calculated values. The inconsistencies were such that no definite conclusions were possible.

9. There were no violent reactions of the engine because of the passage of the shock waves encountered.

10. The dynamic structural analysis method used was adequate for the prediction of peak structural loads but failed to give good time-wise correlation subsequent to the peak load.

11. The choice of gust lift build-up function was extremely important for predicting structural loads on highly rigid airplanes such as the A4D-1 airplanes.

12. A diffraction loading in addition to the gust loading was experienced during the test participations.

13. The reduction of strain gage data by the rosette method was satisfactory for the determination of inflight wing bending moment.

14. The agreement obtained between airplane structural responses which were based upon an analytical method and those which were based upon measured wing pressures indicates that the analytical method satisfactorily accounted for the total forces which acted upon the airplane because of the blast wave.

15. The galvanometers used in the oscillographs for the measurement of wing gust pressures did not provide optimum response for recording this data.

16. The results obtained, when combined with the results to be obtained from participation in Operation Hardtack, will enable a reliable analysis to be made of the A4D-1 nuclear weapon delivery capability.

Chapter 11

RECOMMENDATIONS

1. The structural reponse analysis method should be extended to include more aircraft degrees of freedom, including a third elastic mode.
2. Additional ground vibration tests should be conducted to better define the normal modes of the aircraft.

Appendix A

INSTRUMENTATION

A.1 RECORDING INSTRUMENTATION

The recording instrumentation consisted of one 50-channel oscillograph, one 36-channel oscillograph, one 18-channel oscillograph, and a photo panel recorder. A time of explosion signal was provided by two photocells connected in parallel. Adjustable polaroid filters were installed over the photocells to protect them from excessive energy. The signal generated by the photocells at the time of explosion was recorded on all three oscillographs. Correlation with the photo recorder was obtained by comparing the counter numbers on the photo recorder with those on the oscillographs. The counters on the photo recorder and those on the oscillographs were all controlled by the same timer. In addition, a 50-cycle time trace was recorded on all three oscillographs. Further correlation between recording devices could be obtained by pilot operation of the correlation switch in the cockpit, which actuated the dynamic-reference trace on each oscillograph and flashed a light on the photo recorder.

A.2 INSTRUMENTATION FOR THERMAL MEASUREMENTS

The thin-skin areas on the lower surfaces of the aircraft which were most nearly perpendicular to the direction of thermal radiation experienced the greatest temperature rise, and hence were the most critical from a thermal-effect standpoint. Eighteen thermocouples were located in these regions to measure the thermal response. Thermocouple positions were numbered and located as shown in Figure A.1 and Table A.1.

The general areas instrumented were the thin dural skins of the wing lower leading edge; the lower surfaces of the flap, aileron, and elevator; both sides of the rudder; and the lower surface of the aft fuselage. The thermocouples were located on single thickness skins as far away from stiffeners or other heat absorbing structures as possible.

Two thermocouples, one on the aileron and one on the flap, were protected from convective cooling by quartz covers to measure the magnitude of aerodynamic cooling. Each covered thermocouple was located near an uncovered thermocouple so that direct comparisons could be made between the temperatures of the cooled and uncooled skin surfaces.

Spare thermocouples were installed throughout except for the quartz-covered locations, which were accessible and permitted replacement in the field. To attach a thermocouple, a $\frac{3}{32}$ -inch diameter, 0.005-inch thick brass washer was riveted to the inner surface of the airplane skin with a $\frac{1}{32}$ -inch diameter rivet; the thermocouple leads were then clamped under and soldered to the washer.

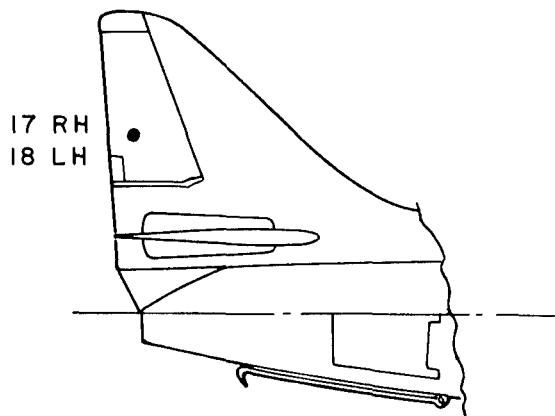
A.3 MEASUREMENT OF THERMAL RADIATION RECEIVED BY THE AIRCRAFT

Calorimeters and radiometers were installed to measure the thermal inputs on the aircraft. Two calorimeters with fields of view of 90 and 160 degrees and a 160-degree radiometer were installed in the after portion of the instrumentation store pointing vertically downward. Two additional 90-degree field of view calorimeters were installed in the aft section of the nose boom to obtain data on scattered radiation; one pointing forward and up, and the other pointing to the side.

The thermal instruments were provided and calibrated by NRDL. The instruments used in each shot, their location and field of view as selected by NRDL are presented in Table A.2. All thermal instruments were equipped with quartz filters.

A.4 CAMERA LOCATIONS

Two GSAP cameras were installed in the forward portion of the instrumentation store to provide a view of the terrain and any cloud cover in the field of view of the vertical thermal instruments.



Thermocouple Number	Skin Gage
1	.025
2, 3	.032
4, 5, 6, 7	.020
8, 9, 10, 11	.032
12, 13	.025
14, 15, 16	.032
17, 18	.020

⊙ Quartz Covered Thermocouple

● Uncovered Thermocouple

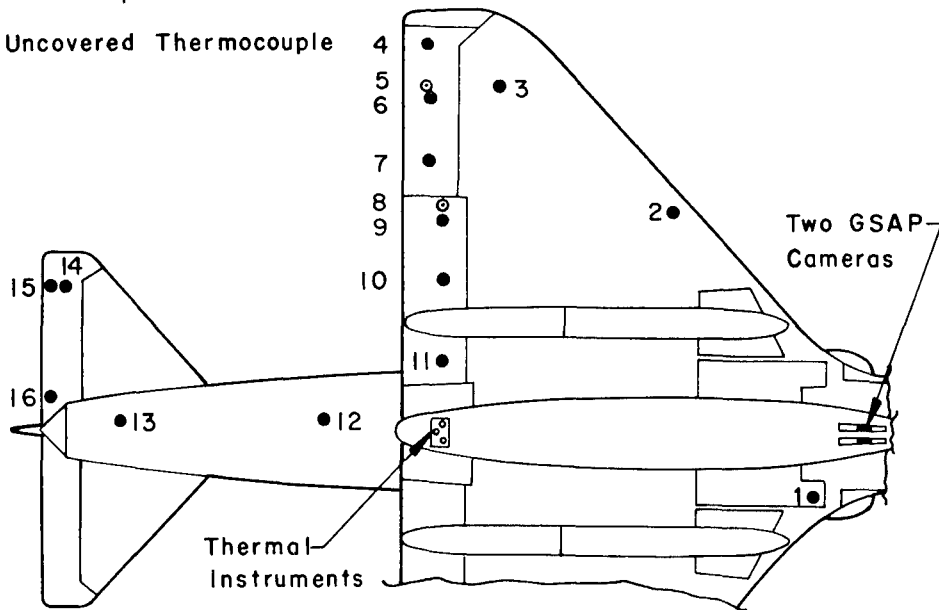


Figure A.1 Thermocouple locations.

The cameras were equipped with 17 mm lenses providing a field of view of 24 degrees 36 minutes longitudinally and 33 degrees 58 minutes laterally. Lens filters were not used for any of the events. Microfile film was used for all events. No shielding from nuclear radiation was installed for these cameras, since a tolerance of 1,000 r for microfile film had been indicated by NRDL.

A.5 OVERPRESSURE MEASUREMENTS

Instrumentation was installed which was capable of recording the time history of the blast overpressure pulse. The primary instrument for this measurement was a pressure transducer located in the nose boom. Two additional transducers were mounted, one on each side of the fuselage just forward of and above the speed brakes (Figure A.2). Statham Model P 131-5D-350 pressure transducers with a differential pressure range of ± 5 psi and a possible ± 7 percent error were used at each location.

The fuselage pickups were added to ensure that overpressure data was obtained in case of failure of the boom mounted system. They also provided a direct measurement of the pressures experienced by the fuselage skin panels. The location of the fuselage pickup points was chosen so that the change in static

pressure because of a change in airplane angle of attack would be minimum.

A.6 WING PRESSURE DISTRIBUTION MEASUREMENTS

The two A4D-1 aircraft were instrumented with pressure transducers to measure the pressure distribution on the upper and lower wing surfaces during the blast gust.

The location of the wing pressure distribution transducers is shown in Figure A.2. Aircraft No. 137831 had one chord-wise row of nine pressure transducers installed along the mean aerodynamic chord of the left-hand wing. The additional time available for instrumentation of Aircraft No. 137827 permitted the installation of pressure transducers at two additional span-wise stations, resulting in three wing stations with a total of 24 pressure pickup points. Table A.3 presents a detailed listing of the span-wise and chord-wise locations of the wing mounted pressure transducers. Because of the leading edge slats, pressure transducers could not be located as close to the leading edge on the upper surface at the two outboard stations as to the inboard station.

All the wing pressure distribution transducers

TABLE A.1 DETAILED THERMOCOUPLE LOCATIONS

Thermocouple Number	Thermocouple Location	Stream-wise Distance from Local Leading Edge	Skin Thickness
		inches	inches
1	LH gun access door	40	0.025
2	RH wing lower skin	9	0.032
3	RH wing lower skin	33	0.032
4	RH aileron lower skin	47	0.020
5	RH aileron lower skin	63	0.020
6	RH aileron lower skin	65	0.020
7	RH aileron lower skin	87	0.020
8	RH flap lower skin	95	0.032
9	RH flap lower skin	101	0.032
10	RH flap lower skin	121	0.032
11	RH flap lower skin	150	0.032
12	Aft fuselage lower skin	343	0.025
13	Aft fuselage lower skin	420	0.025
14	RH elevator lower skin	24	0.032
15	RH elevator lower skin	29	0.032
16	RH elevator lower skin	66	0.032
17	RH rudder	66	0.020
18	LH rudder	66	0.020

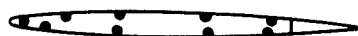
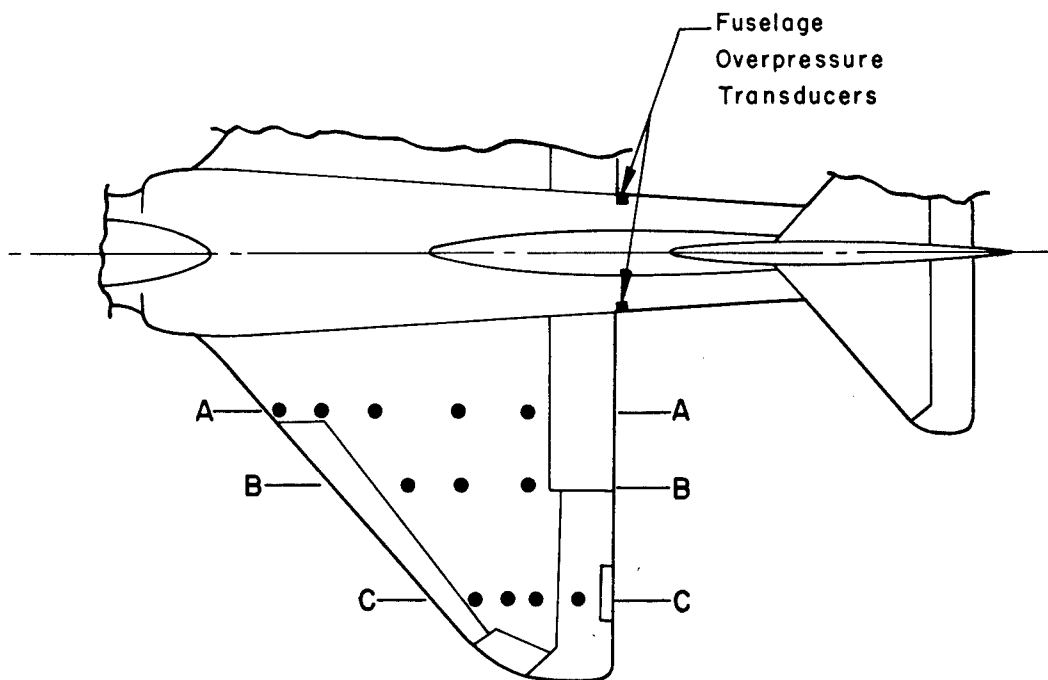
TABLE A.2 THERMAL INSTRUMENTS

Instruments*	NRDL Serial Number	Location†	Field of View	
			Direction‡	Degrees
Boltzmann	137827			
C	Br 69	Store	D	160
C	Br 408	Store	D	90
R	RF10-211	Store	D	160
C	XX-20	Nose	U	90
C	XX-21	Nose	S	90
Priscilla	137827			
C	Bk 237	Store	D	160
C	Wh 402	Store	D	90
R	RF50-203	Store	D	160
C	XX-20	Nose	U	90
C	XX-21	Nose	S	90
Hood	137827			
C	Bk 237	Store	D	160
C	Wh 402	Store	D	90
R	RF50-203	Store	D	160
C	XX-20	Nose	U	90
C	XX-21	Nose	S	90
Diablo	137827			
C	Br 69	Store	D	160
C	Br 408	Store	D	90
R	RF10-211	Store	D	160
C	XX-20	Nose	U	90
C	XX-21	Nose	S	90
Shasta	137831			
C	Br 67	Store	D	160
C	Br 189	Store	D	90
R	RF10-212	Store	D	160
C	XX-22	Nose	U	90
C	XX-23	Nose	S	90
Doppler	137827			
C	Br 69	Store	D	160
C	Wh 402	Store	D	90
R	RF10-210	Store	D	160
Doppler	137831			
C	Br 67	Store	D	160
C	Wh 403	Store	D	90
R	RF10-212	Store	D	160
C	XX-22	Nose	U	90
C	XX-23	Nose	S	90
Smoky	137831			
C	Bk 246	Store	D	160
C	Wh 401	Store	D	90
R	RF50-202	Store	D	160
C	XX-22	Nose	U	90
C	XX-23	Nose	S	90

*C, calorimeter; R, radiometer.

†Store, external instrumentation store; Nose, forward nose compartment.

‡D, vertically down; U, up and forward; S, side.



Sect. A-A

BuNo. 137831 & BuNo. 137827



Sect. B-B

BuNo 137827 Only



Sect. C-C

BuNo 137827 Only

Figure A.2 Wing and fuselage pressure transducer locations.

TABLE A.3 DETAILED WING PRESSURE TRANSDUCER LOCATIONS

Aircraft Number		Left-hand Wing Station	Surface	Chord Location
137827	137831			
		inches		pct
x	x	61	Upper	3.51
x	x	61	Upper	15.95
x	x	61	Upper	32.15
x	x	61	Upper	56.28
x	x	61	Upper	75.50
x	x	61	Lower	9.49
x	x	61	Lower	32.18
x	x	61	Lower	56.76
x	x	61	Lower	74.10
x		89	Upper	28.26
x		89	Upper	46.65
x		89	Upper	70.10
x		89	Lower	10.57
x		89	Lower	29.19
x		89	Lower	47.23
x		89	Lower	68.40
x		132	Upper	25.17
x		132	Upper	41.75
x		132	Upper	58.08
x		132	Upper	82.19
x		132	Lower	6.22
x		132	Lower	30.22
x		132	Lower	58.21
x		133	Lower	82.94

were Statham P 130-15A-350 instruments with a 15 psia range and a natural frequency of 8,500 cps. The oscillograph galvanometers were Consolidated Engineering 7-315 instruments with a frequency range of 0 to 60 cps when damped to 64 percent of critical. The galvanometers in all circuits were nominally damped to 64 percent of critical.

A.7 STRUCTURAL RESPONSE INSTRUMENTATION

Aircraft structural response to the blast gust was measured by means of electrical strain gages located on the wing, the horizontal stabilizer, and the fuselage. The gage installations were designed to permit measurement of loads and stresses resulting from either symmetrical or side gusts. Since the gusts received were symmetrical in all cases, only the symmetrical system of gages was used and, therefore, no description of the side gust measurement system is presented in this report. The symmetrical system consisted of 49 recording channels composed

of: (1) 48 gages mounted on the right hand wing upper surface and on the spar webs, requiring 40 recording channels; (2) a system of coupled gages mounted on the horizontal stabilizer, its supports and actuator, requiring seven recording channels; and (3) four gages mounted on the forward fuselage keels, requiring two recording channels.

With the exception of the gages on the fuselage keels, strain gage installations were designed as load measuring systems; that is, the results of the various strain gage readings were combined to give total applied loads, while the individual gages on the keel were combined to measure local stress. Structural analysis of the A4D-1 indicated that the critical area for the airplane structure for the loadings anticipated was bending moment at the wing root. Therefore, the strain gages at Wing Station 36.5 were used during the test progress to indicate the percentage of allowable structural loading attained during each event.

The wing strain gage installation was designed to permit the measurement of wing bending moment,

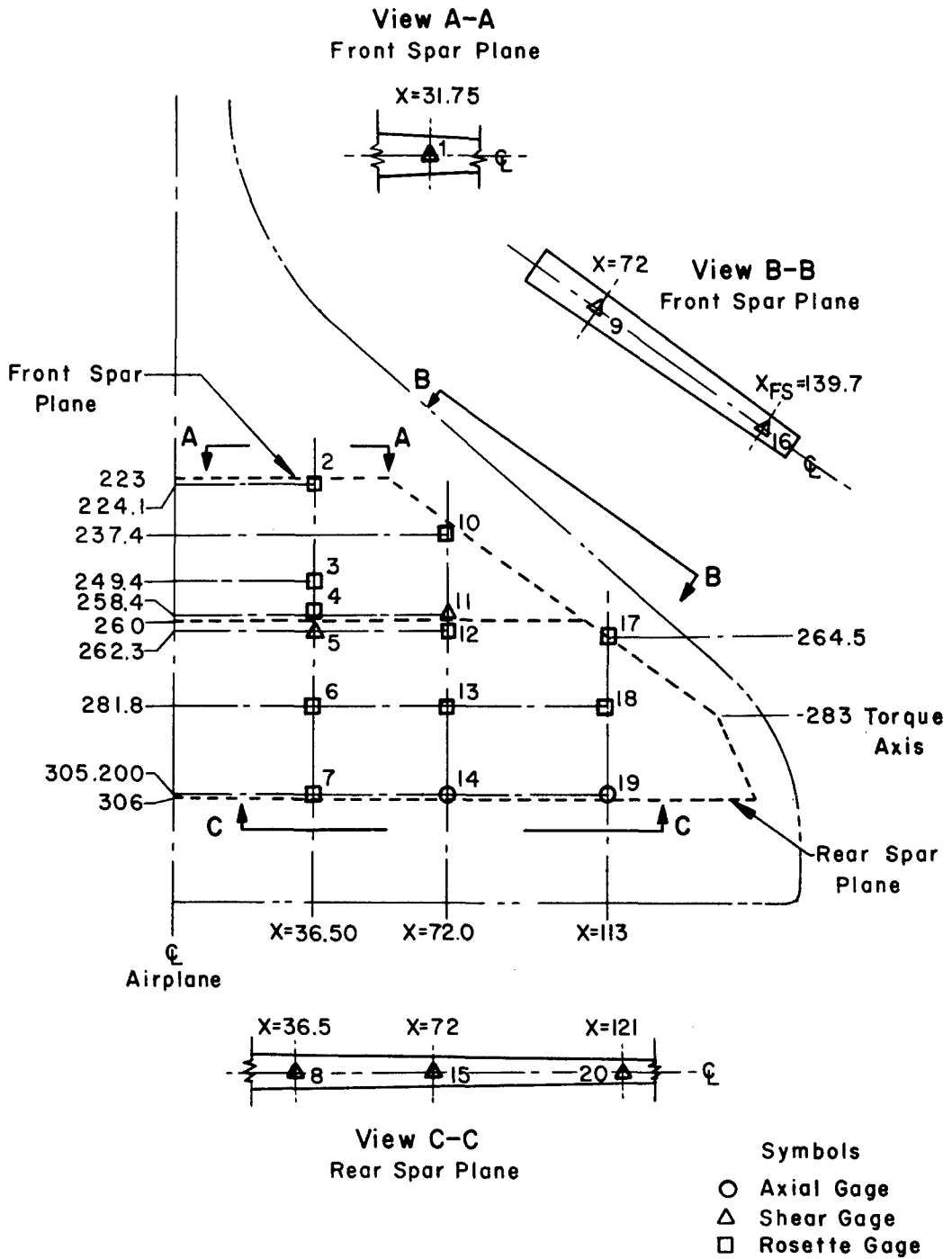


Figure A.3 Strain gage locations.

torque, and shear at three span-wise locations. Laboratory calibration of the wing mounted gages was accomplished subsequent to the test program. The gage installation on the horizontal stabilizer was a system of coupled strain gages calibrated in the laboratory prior to the tests to permit measurement of total horizontal tail load together with span-wise and chord-wise center of pressure.

The general location of wing and fuselage strain gages is shown in Figure A.3. The location of the coupled gage system for the horizontal stabilizer is not shown as the system is complex and the location of each gage has no individual significance.

Other instruments installed for measurement of response to the blast gust were: (1) normal accelerometer at center of gravity, (2) normal accelerometer in tail, (3) aircraft-attitude gyro, (4) pitch-rate gyro, and (5) fuel-quantity gages for determining airplane weight and center of gravity.

A.8 ENGINE INSTRUMENTATION

Although theoretical analysis and the results of previous nuclear weapon tests indicated that no detrimental engine effects would be experienced during the Operation Plumbbob shot participations, a limited amount of instrumentation was installed on the engine.

Instrumentation was installed on the engine to measure and record the following:

p_{t2} compressor inlet total pressure
 p_{s2} compressor inlet static pressure
 p_{s3} compressor discharge static pressure
 p_{t6} turbine discharge total pressure
 T_{t5} turbine discharge total temperature
 p_{fm} fuel distribution manifold pressure
N engine rpm

Engine rpm was recorded on the photo recorder

and all other engine data was recorded on the oscillographs.

Measurements of T_{t5} and p_{t6} indicated the outlet conditions of the engine; p_{t2} , p_{s2} , and outside air temperature indicated inlet conditions. Effects of engine inlet and exhaust changes on the fuel control system were indicated by p_{fm} .

The above data measured the conditions which could contribute to compressor stall and/or flame-out.

A.9 FLIGHT ENVIRONMENTAL AND SPECIAL INSTRUMENTATION

A time of explosion signal was provided by photo-cells and recorded on each oscillograph and the photo recorder.

Position indicators were provided to show the angle of the stabilizer, elevator, rudder, and ailerons.

The following additional environmental data was recorded:

Time (clock)
Outside Air Temperature
Airspeed
Altitude
Heading (compass)
Attitude (pitch)
Pitch Rate
Reference Static Pressure for Overpressure Transducers
Fuel Quantity (wing and fuselage)

Nuclear radiation was measured by Landsverk dosimeters and by film badges. Four film badges were located in the bottom portion of the nose section, and six in the cockpit map case. Dosimeters with various ranges were located in the nose-wheel door and in the leg pocket of the pilot's flight suit.

Appendix B

METHOD OF SCALING SHOCK WAVE EFFECTS

The data in Reference 6 for a 1-kt burst at sea level and the scaling equations of Reference 7 were used to predict the burst effects for the test conditions. For convenience, the scaling relationships are summarized below. In all cases sea level conditions are for the NACA standard atmosphere.

Slant range

$$R' = R_1 (E)^{1/3} \left(\frac{P_0}{P_a} \right)^{1/2} \quad (\text{B.1})$$

Overpressure

$$\Delta P' = \Delta P_1 \left(\frac{P_a}{P_0} \right) \quad (\text{B.2})$$

The overpressure curve for a 1-kt burst in homogeneous sea level atmosphere from BuAer Confidential letter, Aer-AD-41 (015652), dated 10-15-57, was used instead of the overpressure curve of Reference 6.

Time of shock arrival

$$t' = t_1 \left(\frac{C_0}{C_a} \right) (E)^{1/3} \left(\frac{P_0}{P_a} \right)^{1/2} \quad (\text{B.3})$$

Density of air behind shock front

$$\rho' = \rho_1 \left(\frac{\rho_a}{\rho_0} \right) \quad (\text{B.4})$$

Particle velocity behind shock front (gust velocity)

$$U' = U_1 \left(\frac{C_a}{C_0} \right) \quad (\text{B.5})$$

Duration of positive phase

$$t'_+ = t_{+1} \left(\frac{C_0}{C_a} \right) (E)^{1/3} \left(\frac{P_0}{P_a} \right)^{1/2} \quad (\text{B.6})$$

where

R = Slant range, (feet)

E = Total radiochemical yield, (kt)

ΔP = Overpressure, (psi)

P = Ambient atmospheric pressure, (psi)

t = Time of shock arrival, (sec)

ρ = Density, (slug/ft³)

U = Particle velocity behind shock front, (ft/sec)

C = Speed of sound, (ft/sec)

t₊ = Duration of positive pressure phase, (sec)

Superscripts ' = Desired yield and altitude conditions

Subscripts 1 = Values for 1 kt at sea level (Reference 6)

0 = Ambient conditions at sea level NACA Standard atmosphere

a = Ambient conditions at desired altitude

All ambient conditions at altitude refer to receiver altitude.

Appendix C

DYNAMIC STRUCTURAL ANALYSIS

C.1 INTRODUCTION

This appendix contains an outline of the methods used to calculate the aircraft structural response for comparison with the measured response obtained in Operation Plumbbob.

C.2 METHOD OF ANALYSIS

The method of analysis is described below under the headings of Assumptions, Equations of Motion, Solution of the Equations of Motion, and Scaling the Solutions.

C.2.1 Assumptions. The analysis method presented here is dependent upon the validity of certain assumptions. For subsequent discussion these assumptions are divided into three categories: structure, aerodynamic loading, and inertia.

Structure. The analytical structural model consisted of a flexible wing attached to a rigid fuselage and tail. The structural displacements of the model were represented by the displacements of its first three normal modes (rigid body translation, first wing bending, and first wing torsion). Rigid body pitching displacements were ignored.

Aerodynamic Loading. In the analysis, two sources of aerodynamic loading were considered: the gust and the overpressure. The wing lift caused by gust penetration was assumed to reach its peak value at the instant of its application (step function). The overpressure loading was derived from consideration of the diffraction model illustrated in Figure C.1. This diffraction model was selected from several which were considered because it came the closest to accounting for the difference between response measurements and the response calculations based upon gust input alone. Briefly, the diffraction phenomenon was considered to consist of: (1) the striking of the wing lower surface by a blast wave which propagates in a direction normal to the wing surface at velocity U ; (2) the reflection of the blast wave

from the wing lower surface leaving a region of doubled blast wave overpressure (Δp) in the wake of the reflected wave; (3) formation of expansion (rarefaction) waves at the leading and trailing edges of the wing and the subsequent propagation at velocity U of these waves into the region of doubled overpressure, thus cancelling the doubling effect; and (4) the envelopment of the wing upper surface by the separated portions of the blast wave with closure velocity U .

The analysis of the above model was conducted using a value of 1,000 fps for the blast wave propagation speed (U) and a value of unity for the overpressure. The forcing functions shown in Figures C.2, C.3, and C.4 were obtained from analysis of this model. It was assumed that these forcing functions could be modified to account for arbitrary overpressure (Δp) and blast wave inclination (θ) by multiplying their amplitudes by the factor $\Delta p \sin \theta$. The angle θ is defined as the angle between a normal to the wing reference plane and the blast wave.

It was further assumed that the effects of aerodynamic damping (lift due to aircraft motion) were directly proportional to the local wing velocities. This amounts to replacing the two-dimensionally correct Wagner function, customarily used to represent lift growth due to wing motion, with a step function. This assumption is consistent with the use of a step function for lift growth due to gust penetration and has some theoretical justification for delta wing planforms, c.f. Reference 14.

Inertia. The aircraft normal modes mentioned under structure above were determined from ground vibration tests of the aircraft without fuel. The effect of the average fuel weight at the time of shock arrival in Operation Plumbbob was added to the analysis model. It was assumed that the mass coupling thus introduced into the equations of motion adequately represented the dynamic effects of wing fuel.

C.2.2 Equations of Motion. The equations of motion for the response of the aircraft to gust and overpressure loads are given by:

$$M_{ij}\ddot{Q}_i + M_{ij}\omega_i^2 Q_i = F_i \quad (C.1) \quad f_2 = 0.005261 \frac{\rho}{2} C_{L\alpha} V S u_{eq} \quad (C.7)$$

where M_{ij} = a third order square matrix of generalized masses corresponding to the three normal modes together with the mass-coupling elements introduced through the addition of fuel

Q_i = a column matrix whose elements are the three generalized coordinates corresponding to displacement in the three normal modes

ω_i = the frequency of vibration of the i^{th} mode, radians per second, $\omega_0 = 0$

F_i = a column matrix whose elements consist of the generalized forces corresponding to each normal mode including the effects of aerodynamic damping

where S = wing area, ft^2

u_{eq} = equivalent vertical gust velocity, ft/sec
 $= \frac{\rho_1 u}{\rho} \left[1 - \frac{u}{V} \cos \theta \right] \sin \theta$

u = air material velocity behind the blast wave, ft/sec

ρ_1 = air density behind the blast wave, slugs/ft^3

θ = angle between the vector direction of u and the horizontal, degrees

and other symbols are as previously defined.

For the overpressure input the functions f_0 , f_1 , and f_2 were taken from Figures C.2, C.3, and C.4 which give the generalized overpressure inputs for a unit overpressure.

Dots appearing above a term indicate successive differentiations with respect to time.

When the numerical values of the generalized terms are inserted and the matrix multiplication is carried out, Equation C.1 becomes a system of three second order differential equations, namely:

$$\ddot{q}_0 = f_0 - d(0.6732\dot{q}_0 + 0.2543\dot{q}_1 - 0.6491\dot{q}_2) - s(0.02518q_1 - 0.2284q_2) \quad (C.2)$$

$$\ddot{q}_1 = f_1 - 1.9\dot{q}_2 - 10.350q_1 - d(8.396\dot{q}_0 + 7.668\dot{q}_1 - 20.765\dot{q}_2) - s(0.7703q_1 - 7.622q_2) \quad (C.3)$$

$$\ddot{q}_2 = f_2 - 0.1295\dot{q}_1 - 61.600q_2 - d(0.6871\dot{q}_0 + 0.3704\dot{q}_1 + 0.8861\dot{q}_2) - s(0.02907q_1 - 0.3484q_2) \quad (C.4)$$

where d = damping function = $(\rho/2) C_{L\alpha} V$

s = spring rate function = $(\rho/2) C_{L\alpha} V^2$

ρ = free stream ambient density, slugs/ft^3

$C_{L\alpha}$ = lift curve slope (taken from steady state wind tunnel measurements), C_L/radian

V = aircraft forward speed prior to shock arrival, ft/sec

q = generalized coordinate corresponding to displacement in the normal mode indicated by the subscript

f = forcing function corresponding to the normal mode indicated by the subscript
subscripts ()₀ = the rigid body translation normal mode

()₁ = the first wing bending normal mode

()₂ = the first wing torsion normal mode

Forcing functions f_0 , f_1 , and f_2 were used to introduce either the gust input or the overpressure input. For the gust input these were:

$$f_0 = 0.00515 \frac{\rho}{2} C_{L\alpha} V S u_{eq} \quad (C.5)$$

$$f_1 = 0.06429 \frac{\rho}{2} C_{L\alpha} V S u_{eq} \quad (C.6)$$

C.2.3 Solution of the Equations of Motion. The solution of Equations C.2, C.3, and C.4 poses no particular mathematical difficulty. When each of the terms entering into the equations has been determined, the solution may be obtained in a routine but, unfortunately, somewhat tedious and time consuming manner. Thus, it was considered desirable to obtain solutions which were of sufficient generality to permit the scaling of single solutions to represent a variety of aircraft positions and blast inputs.

It was first noted that the spring rate and damping terms, s and d , appearing in the equations varied only slightly for the range of conditions pertinent to Operation Plumbbob. Hence, typical values for the spring rate and damping terms were selected and assumed constant. This procedure was later justified by examining solutions which contained the extreme upper and lower limits for the damping and spring rate terms. It was found that the variations in the final solutions were small and well within the accuracy limits for this type of dynamic analysis.

With the damping and spring rate terms fixed, the equations of motion gave solutions which were linear functions of the forcing terms f_0 , f_1 , and f_2 . In section C.2.1 it was assumed that the overpressure input forcing functions are proportional to the quantity $\Delta p \sin \theta$ which may be represented as Δp_{eq} . Similarly, the gust input forcing functions are proportional to the quantity $\frac{\rho}{2} C_{L\alpha} V S u_{eq}$. In paragraph C.2.4 it will be shown that

$$\frac{\rho}{2} C_{L\alpha} V S u_{eq} = 32 \Delta p_{eq} V_{eq} \quad (C.8)$$

where V_{eq} is defined by Equation C.19.

Thus, utilizing the linearity of the equations of motion, fixing the values of the spring rate and damping terms, and noting the proportionality of the forcing functions to the quantities Δp_{eq} and V_{eq} it was possible to obtain unit solutions to the equations of motion. Since the forcing functions for the gust

and overpressure vary differently with time it was necessary to obtain separate unit solutions for each of the two forcing functions. The unit solutions consisted of time histories of the generalized coordinates and their derivatives.

Time histories of the wing bending moment and the aircraft center of gravity acceleration were then obtained from the formulas:

$$\Delta M_{22} = 5,946d(1 - \dot{q}_0) - 1,963\ddot{q}_0 - 583\dot{q}_1 - 1,810\ddot{q}_2 - 2,630d\dot{q}_1 - 6,143d\dot{q}_2 - 450sq_1 + 4,164sq_2 \quad (C.9)$$

$$\Delta M_{36} = 4,555(1 - \dot{q}_0) - 1,346\ddot{q}_0 - 480\dot{q}_1 - 1,429\ddot{q}_2 - 2,237d\dot{q}_1 - 5,014d\dot{q}_2 - 381sq_1 + 3,544sq_2 \quad (C.10)$$

$$\Delta n_{cg} = \frac{1}{32.2} [\ddot{q}_0 - 0.0552\ddot{q}_1 - 0.195\ddot{q}_2] \quad (C.11)$$

where ΔM_{22} = incremental wing bending moment at Station 22.0, in-lb

ΔM_{36} = incremental wing bending moment at Station 36.5, in-lb

Δn_{cg} = incremental center of gravity acceleration, g

and other symbols are as previously defined.

Since these time histories were based upon unit values of the terms Δp_{eq} and V_{eq} , it was necessary to develop a scaling technique to produce results for specific values corresponding to the A4D-1 aircraft positions in Operation Plumbbob.

C.2.4 Scaling the Solutions. From Equations C.2, C.3, and C.4 it can be seen that for given values of the damping and spring rate terms d and s , the aircraft response is a linear function of the input terms f_0 , f_1 , and f_2 .

By assumption, the overpressure inputs were proportional to the term $\Delta p \sin \theta$. Thus the unit overpressure solutions were scaled by multiplying computed responses by this factor.

It will now be shown that a simple scale factor can be derived for scaling unit gust solutions to solutions valid for arbitrary blast wave strengths and aircraft orientations.

From Equations C.5, C.6, and C.7 it is apparent that the gust inputs are proportional to the equivalent gust velocity, u_{eq} , or more specifically to the term

$$\frac{\rho}{2} C_{L\alpha} V S u_{eq}$$

$$\text{Since } u_{eq} = \frac{\rho_1 u}{\rho} \left[1 - \frac{u}{V} \cos \theta \right] \sin \theta \quad (C.12)$$

$$\frac{\rho}{2} C_{L\alpha} V S u_{eq} = \frac{\rho_1 C_{L\alpha} V S}{2} \left[1 - \frac{u}{V} \cos \theta \right] \sin \theta \quad (C.13)$$

The material velocity (u) and density (ρ_1) are given by the Rankine-Hugoniot equations (c.f. Reference 15) as:

$$u = \frac{5}{7} C \frac{\Delta p}{p} \frac{1}{\left[1 + \frac{6 \Delta p}{7 p} \right]^{1/2}} \quad (C.14)$$

$$\rho_1 = \frac{\left[7 + \frac{6 \Delta p}{p} \right]}{\left[7 + \frac{\Delta p}{p} \right]} \rho \quad (C.15)$$

where u = material velocity behind the blast wave, ft/sec

C = ambient speed of sound, ft/sec

ρ = ambient density, slugs/ft³

ρ_1 = density behind the blast wave, slugs/ft³

Δp = blast wave overpressure, psf

p = ambient pressure, psf

Forming the product $\rho_1 u$, expanding by the binomial formula, and neglecting terms containing powers of $\frac{\Delta p}{p}$ higher than the first, one obtains:

$$\rho_1 u = \frac{5}{7} \frac{\Delta p}{p} C \rho \quad (C.16)$$

Inserting the Operation Plumbbob average value of 0.186 for $\frac{C \rho}{p}$ there results:

$$\rho_1 u = .133 \Delta p \quad (C.17)$$

Substituting into Equation C.12, with $C_{L\alpha} = 3.67$, and $S = 130.6$ square feet:

$$\frac{\rho}{2} C_{L\alpha} V S u_{eq} = 32 \left[1 - \frac{u}{V} \cos \theta \right] V \Delta p \sin \theta \quad (C.18)$$

Letting

$$V_{eq} = V \left[1 - \frac{u}{V} \cos \theta \right] \quad (C.19)$$

$$\Delta p_{eq} = \Delta p \sin \theta \quad (C.20)$$

$$\text{gives } \frac{\rho}{2} C_{L\alpha} V S u_{eq} = 32 V_{eq} \Delta p_{eq} \quad (C.21)$$

Substituting Equation C.21 into the equations of motion C.2, C.3, and C.4 gives a set of equations which are linear in the product $\Delta p_{eq} V_{eq}$. Thus, it was possible to solve these equations using unit values for Δp_{eq} and V_{eq} and to scale the results to represent arbitrary aircraft positions and gust inputs by multiplying the unit solutions by appropriate values of Δp_{eq} and V_{eq} .

It should be noted that the only important assumption made in the derivation of Equation C.21 was that the ratio $\frac{\Delta p}{p}$ was small in comparison with unity.

This condition was fulfilled for all the positions of Operation Plumbbob.

C.3 DETERMINATION OF CRITICAL WING RESPONSE

The wing bending moments given by Equations C.9 and C.10 are incremental bending moments, that is, they represent changes from steady state. It was thus necessary to add steady state bending moments to the computed values to make comparisons with the structural allowable moments. The steady state bending moments used for wing Stations 22.0 and 36.5 are 330,000 and 262,000 in-lb respectively. These values are based upon unaccelerated level flight calculations for an A4D-1 aircraft with a gross weight of 12,500 pounds, with a forward center of gravity, and at an altitude of 10,000 feet. This was sufficiently

close to the preshock arrival condition of the A4D-1 aircraft in Operation Plumbbob that no corrections to the above values were made.

Critical wing response was predicted to occur at Wing Station 22.0. Space restrictions, however, did not permit the installation of strain gages at this station. Consequently strain gages were installed at the closest practical wing station, namely 36.5. The bending moment readings obtained from Station 36.5 were then compared with a fictitious allowable bending moment representing the moment at 36.5 which would be experienced when the Critical Station 22.0, was subjected to its design limit load. On this basis the design limit loads for Stations 22.0 and 36.5 were 2.9×10^6 and 2.19×10^6 in-lb respectively.

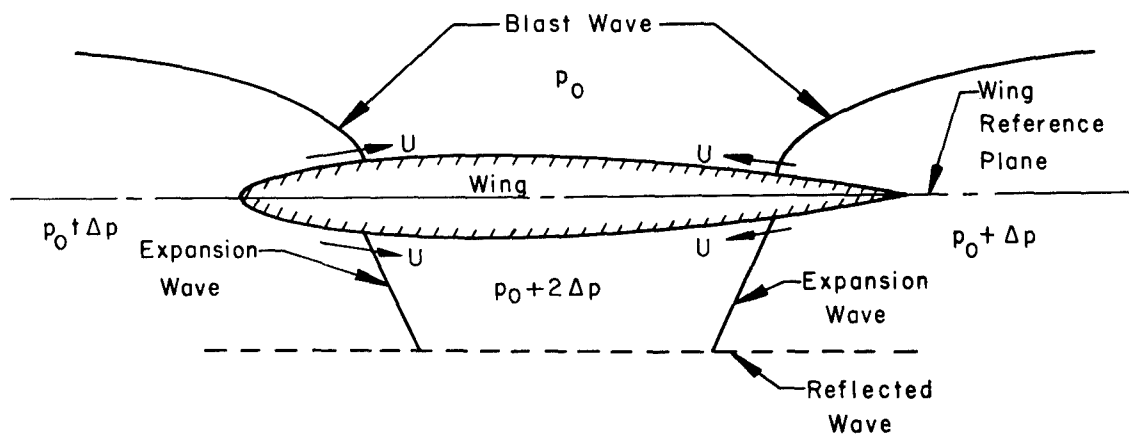


Figure C.1 Assumed diffraction model shown shortly after the blast wave has begun enveloping the wing.

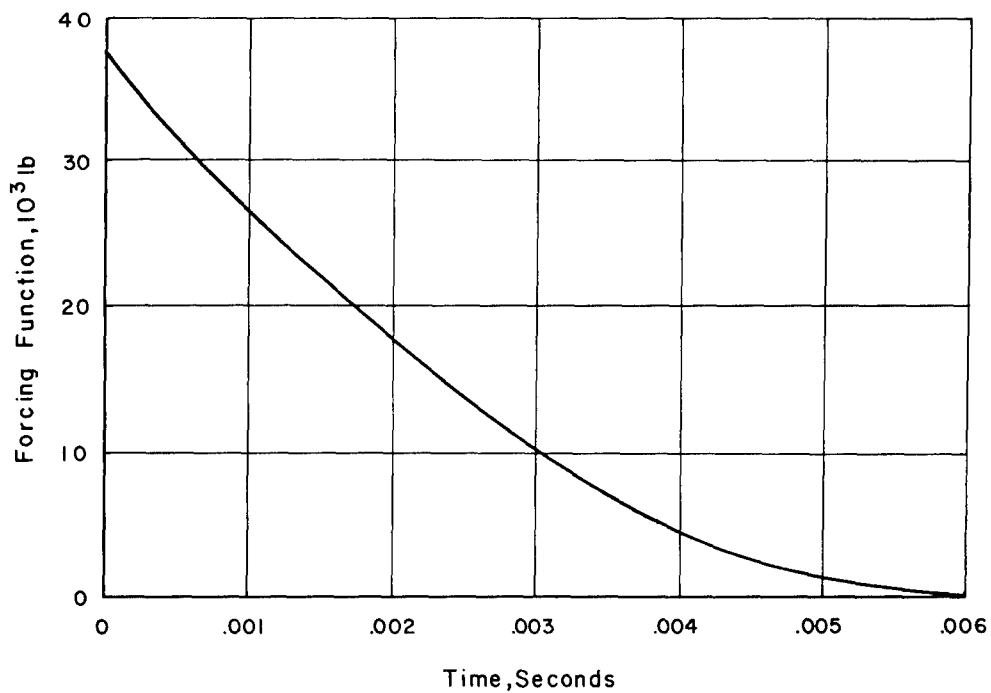


Figure C.2 Unit overpressure forcing function, f_0 , rigid body translation.

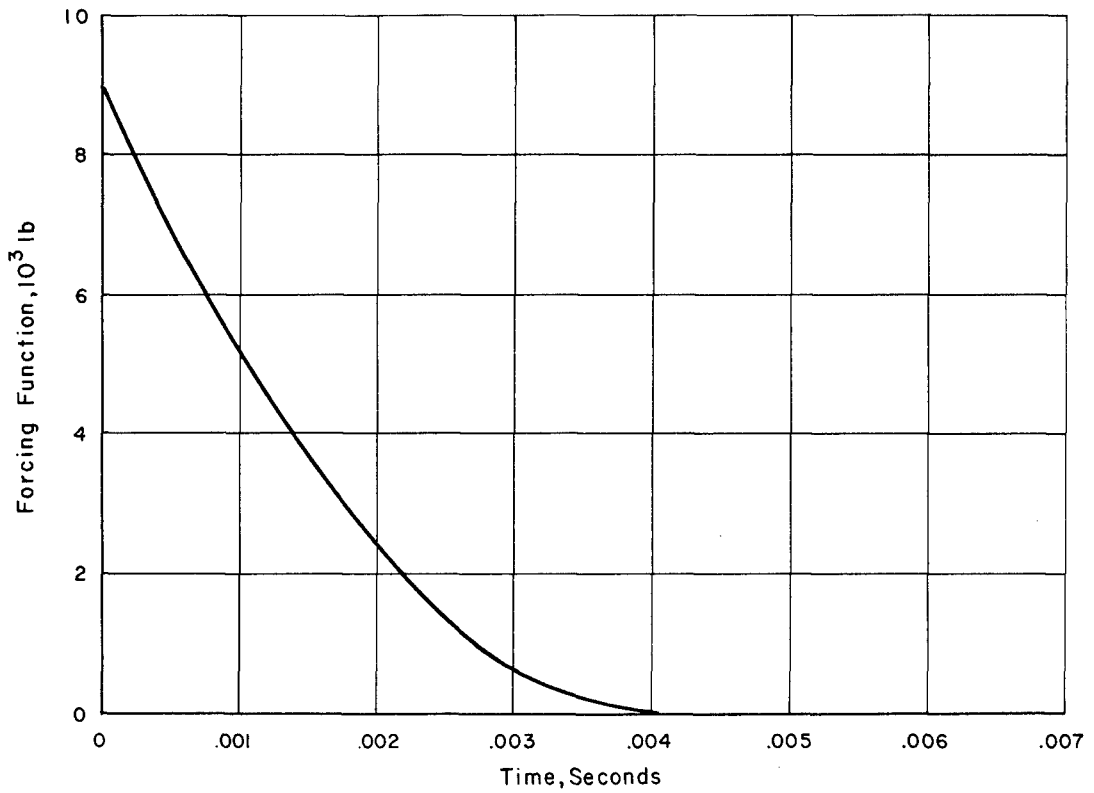


Figure C.3 Unit overpressure forcing function, f_1 , first bending mode.

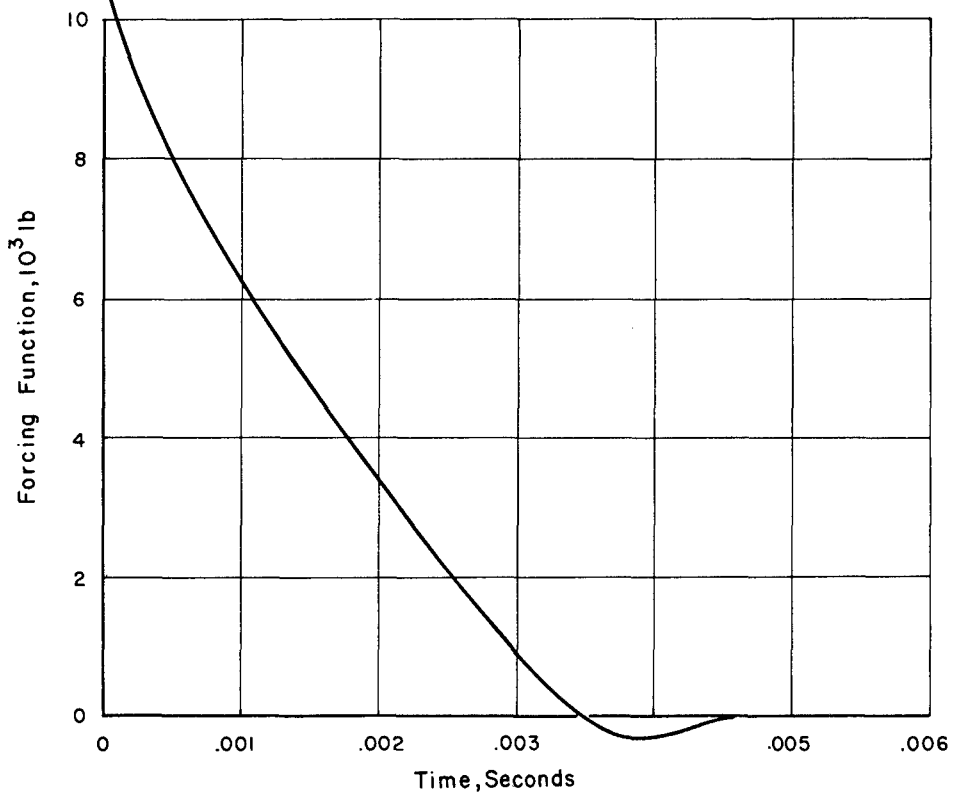


Figure C.4 Unit overpressure forcing function, f_2 , first torsion mode.

Appendix D

THE ROSETTE METHOD

The rosette method of strain gage data reduction was a system for the conversion of elastic strain to wing bending moment. To accomplish the conversion it was necessary to have a knowledge of the wing geometry and the distribution of the wing structural material. On the basis of this knowledge it was possible to determine coefficients by which the bending moment at a given wing station could be determined from the formula

$$M = \sum K_n \sigma \varphi_n \quad (D.1)$$

where M = bending moment, in-lb

K_n = bending moment coefficient for the nth strain gage location (n refers to the gage location numbers given in Figure A.3), in³

$\sigma \varphi_n$ = component of wing normal stress in a direction perpendicular to the aircraft center line, psi

Prior to participation in Operation Plumbbob, basic coefficients were calculated for each gage location. These basic coefficients are listed in Table D.1.

The stress $\sigma \varphi_n$ was found from the strain gage readings at each location by conventional rosette data reduction techniques except for Gages 14 and 19. Gages 14 and 19 were axial gages oriented in a direction perpendicular to the aircraft center line; therefore, the bending stress, $\sigma \varphi_n$, was taken as the direct stress obtained from the gage reading.

During test participation two types of strain gage malfunction were encountered which required modification of the basic system of coefficients.

A rosette gage is composed of three strain gages. For the purpose of this report, the individual gages of a rosette are defined according to their orientation. The principal leg of a strain rosette refers to the gage whose orientation is closest to that of the compressive principal stress. The auxiliary gages are the remaining two gages of the rosette.

In certain of the tests, auxiliary legs of strain rosettes failed. This difficulty was remedied by deter-

mining the bending stress, $\sigma \varphi$, as the stress given by the principal gage multiplied by a correction factor. This correction factor was determined from other test participations in which all the gages of the rosette in question were operative.

The other type of strain gage malfunction which necessitated correction occurred when the principal leg of a rosette failed. In this instance the entire rosette reading was replaced with the reading for a neighboring rosette multiplied by a correction factor which was determined from the ratio of wing beam depths at the rosette stations in question. A list of the correction factors is presented in Table D.2.

TABLE D.1 BASIC COEFFICIENTS

Wing Station	Gage Number*	K_n
36.5	1	0
	2	29.92
	3	25.34
	4	28.90
	5	0
	6	23.56
	7	10.54
	8	0
72.0	9	0
	10	23.64
	11	0
	12	27.40
	13	18.02
	14	9.42
	15	0
113.0	16	0
	17	9.58
	18	13.98
	19	9.11
	20	0

*See Figure A.3

TABLE D.2 CORRECTION FACTORS FOR BASIC COEFFICIENTS

Wing Station	Shot	Gage Number*	Correction Factor	Type of Correction†
36.5	Hood	4	1.120	A
36.5	Doppler (137827)	4	1.120	A
		2	1.076	B (Replace Rosette 2 with Rosette 3)
36.5	Doppler (137831)	3	0.930	B (Replace Rosette 3 with Rosette 2)
		2	1.000	A
		6	1.150	A
		7	1.470	A
36.5	Smoky	2	1.076	B (Replace Rosette 2 with Rosette 3)
72.0	Boltzmann	13	0.867	B (Replace Rosette 13 with Rosette 12)
72.0	Doppler (137827)	10	1.050	A
113.0	Smoky	17	1.000	A
		18	0.920	B (Replace Rosette 18 with Rosette 17)

*See Figure A.3.

† Type A correction consists of using the principal gage of the rosette for determining $\sigma\phi$; type B correction consists of replacing an entire rosette with an adjacent one for determining $\sigma\phi$.

Appendix E

WING PRESSURE TIME HISTORIES

Figures E.1 through E.17 are time histories of measured wing pressure for Shot Diablo. It should be noted that the quantity plotted is the total pressure recorded for each pressure tap. Incremental pressures can be obtained by subtracting the reading at the time of shock arrival (t_{s_a}) from all subsequent readings. The traces are labeled with the coordinates of the pressure tap. These are given in terms of wing station (WS), percent of the local wing chord (%), and upper or lower wing surface (US or LS). The time scale is measured from time zero.

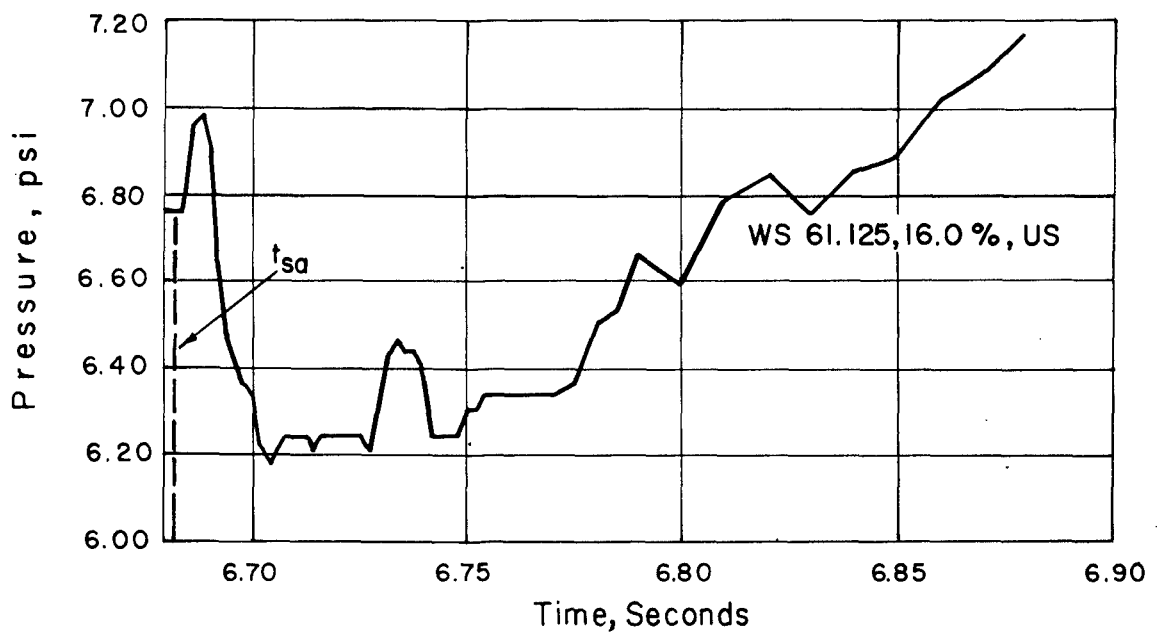
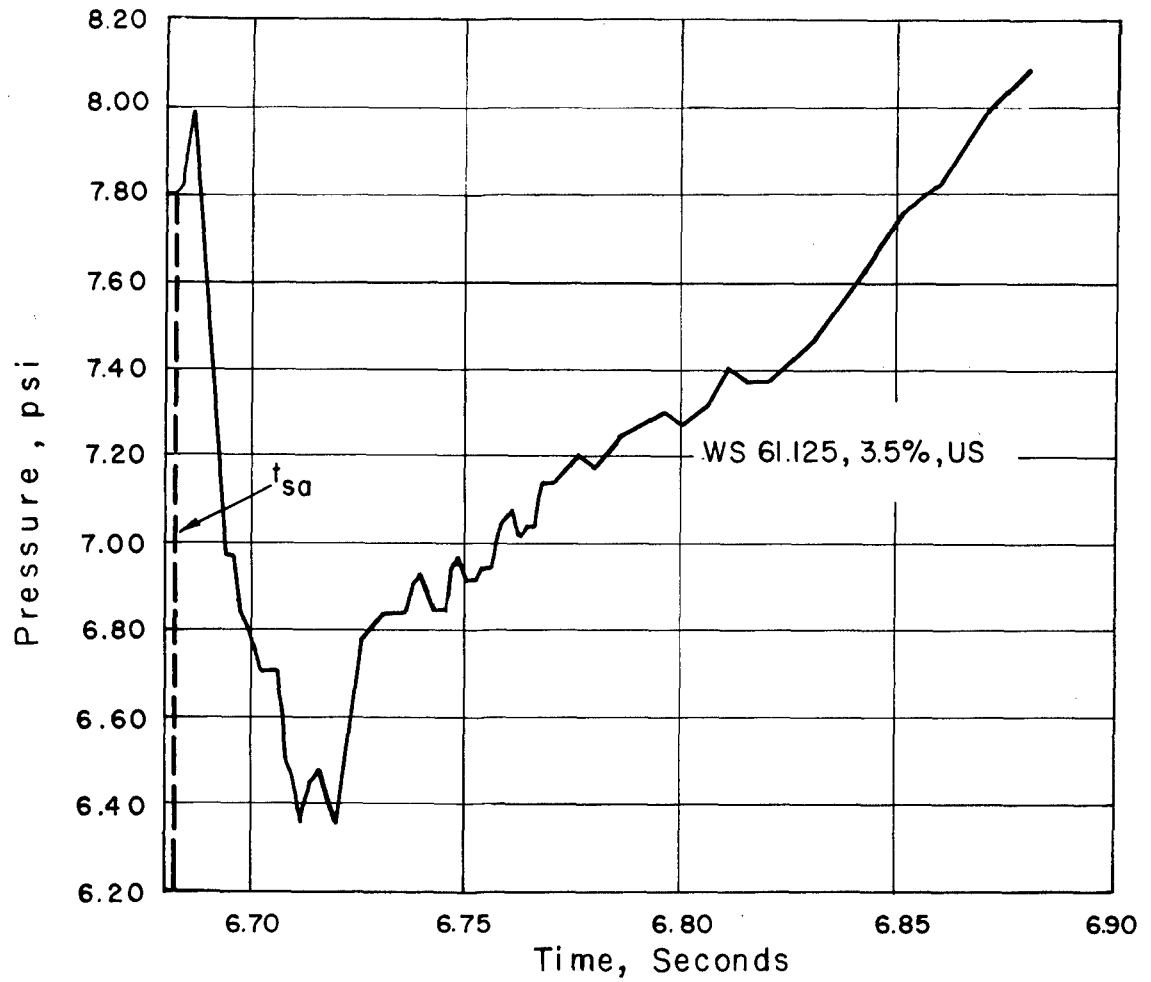


Figure E.1 Local wing pressure time histories, Shot Diablo.

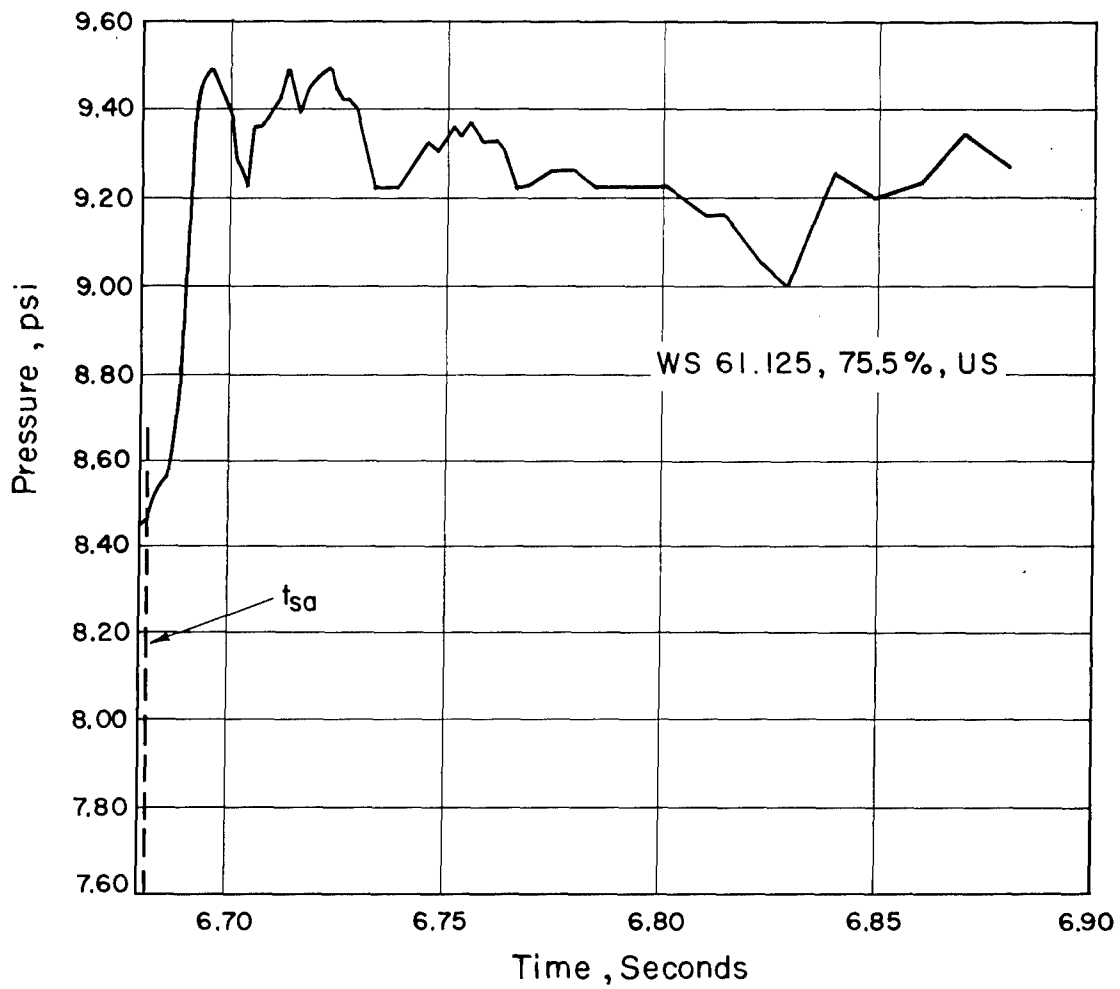


Figure E.2 Local wing pressure time history, Shot Diablo.

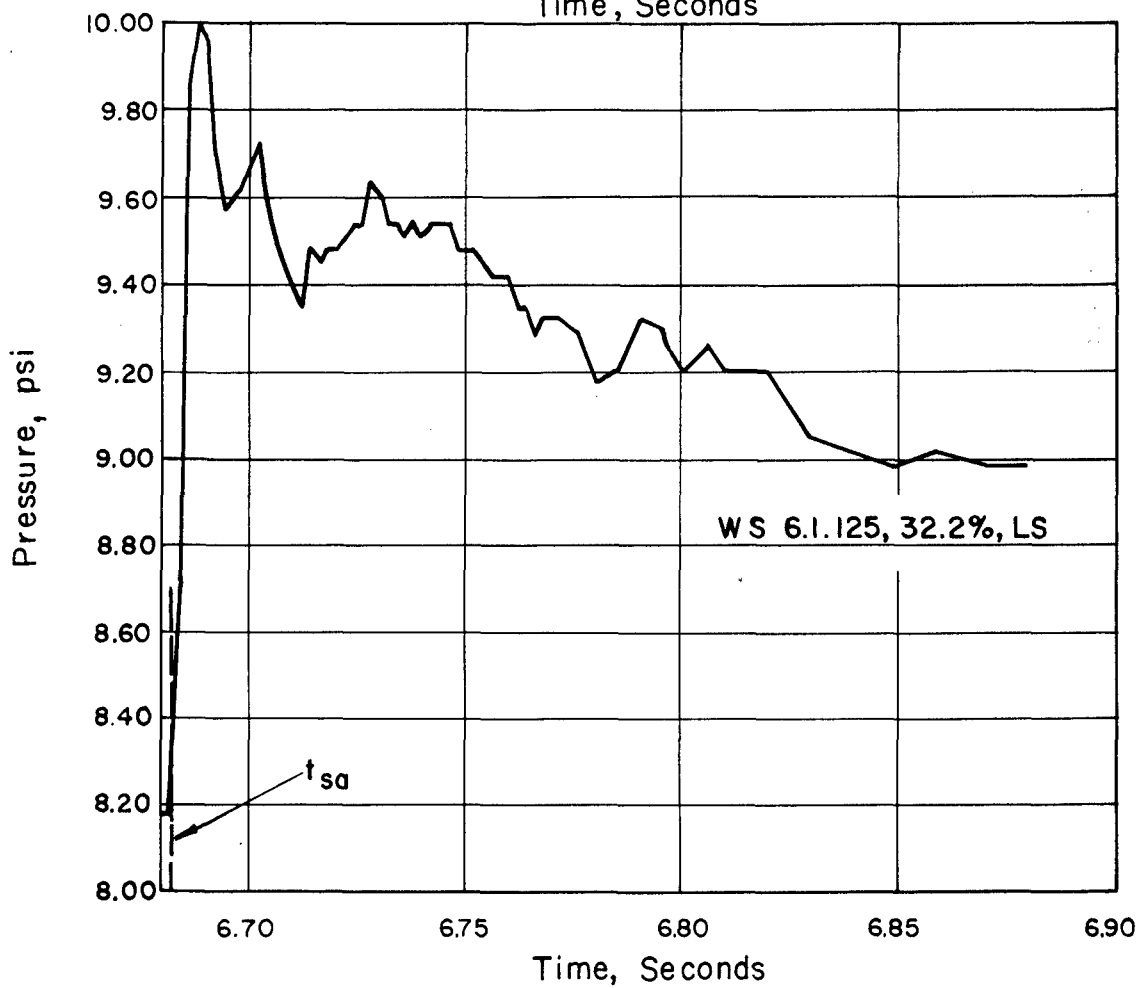
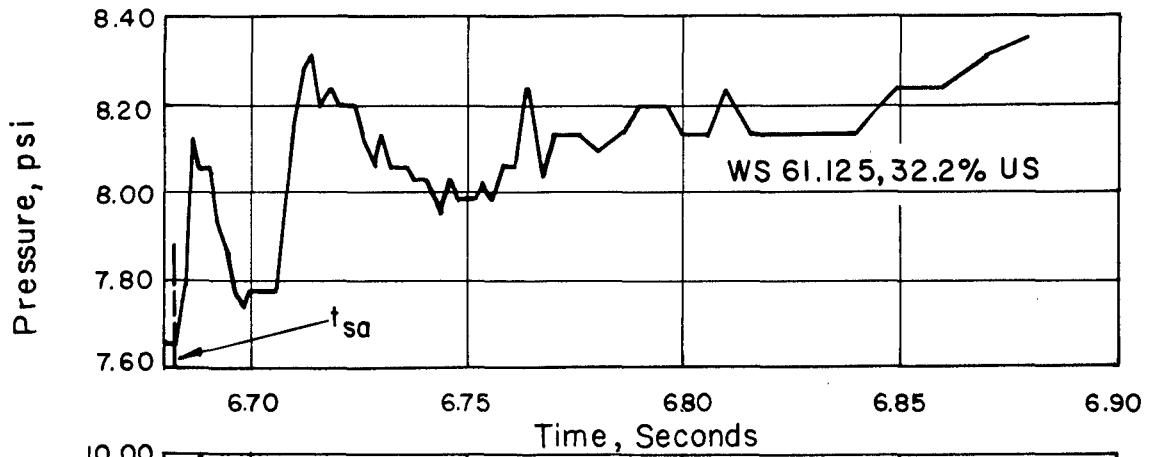


Figure E.3 Local wing pressure time histories, Shot Diablo.

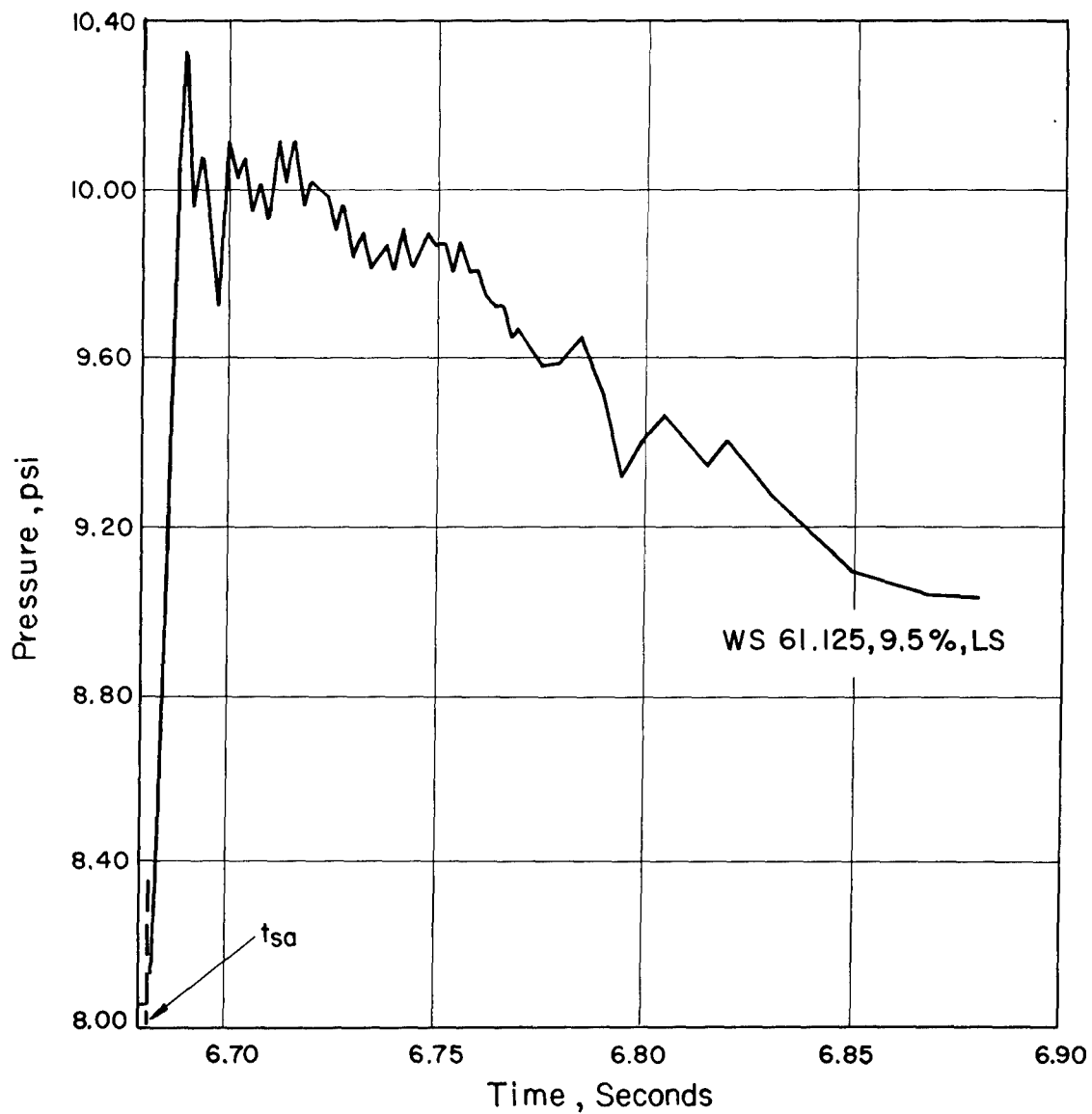


Figure E.4 Local wing pressure time history, Shot Diablo.

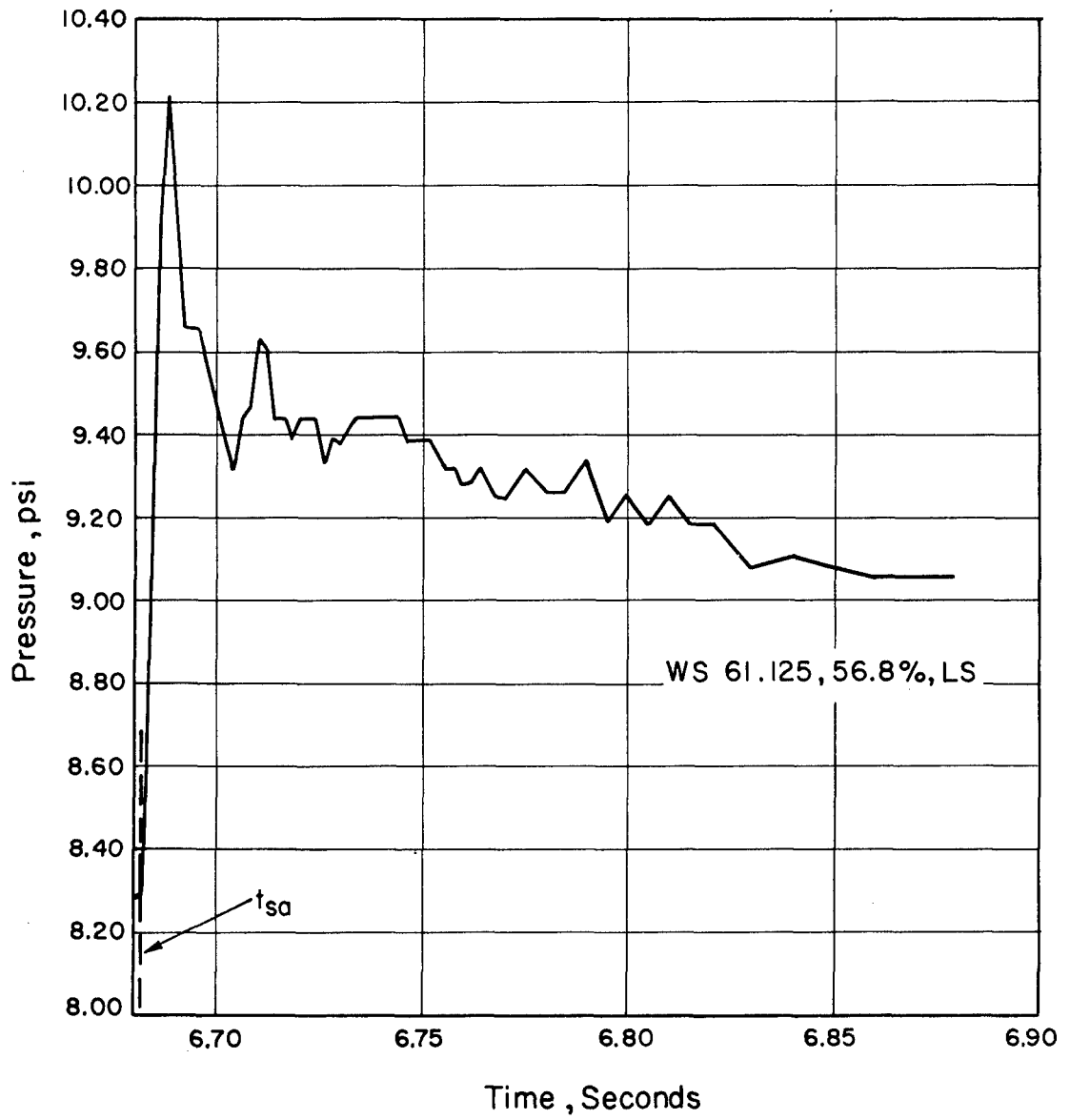


Figure E.5 Local wing pressure time history, Shot Diablo.

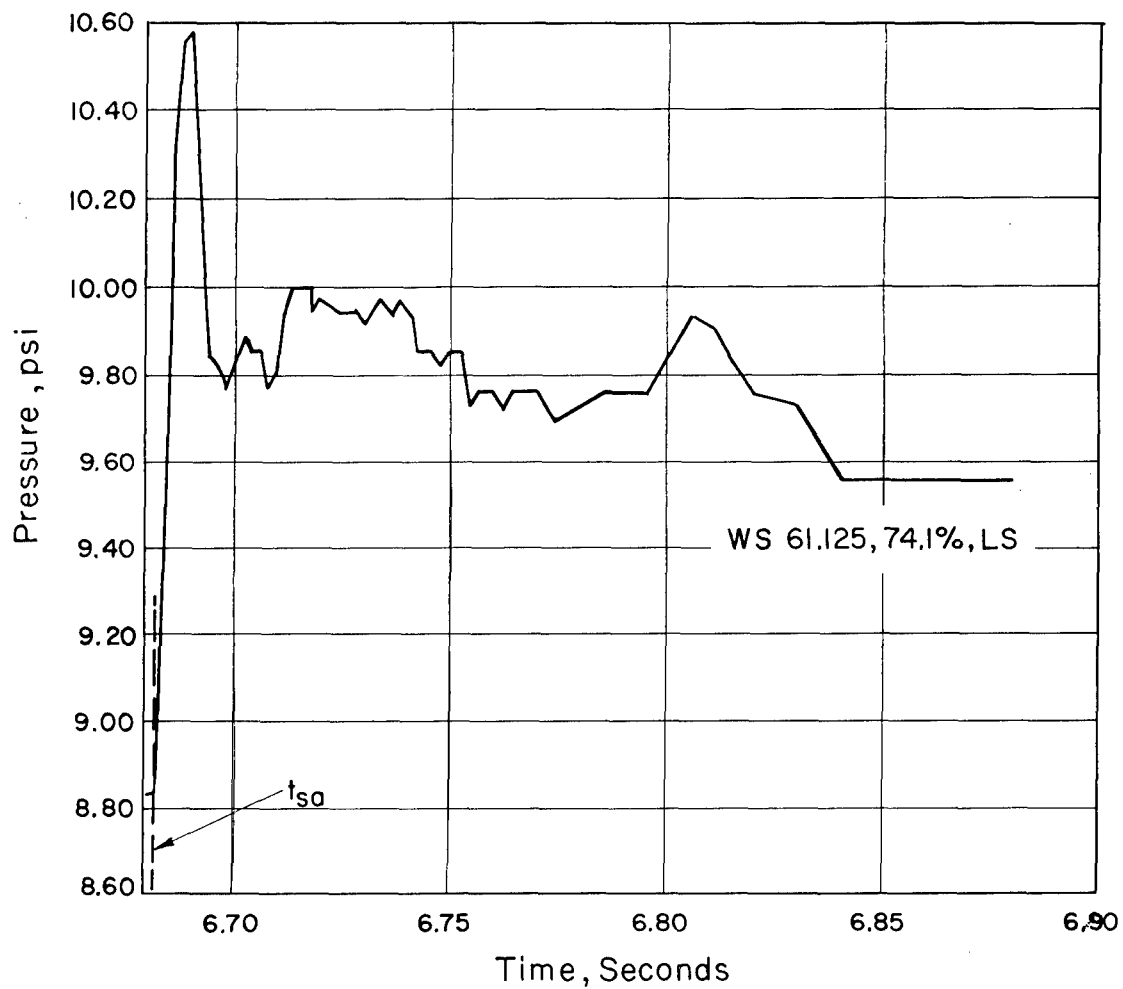


Figure E.6 Local wing pressure time history, Shot Diablo.

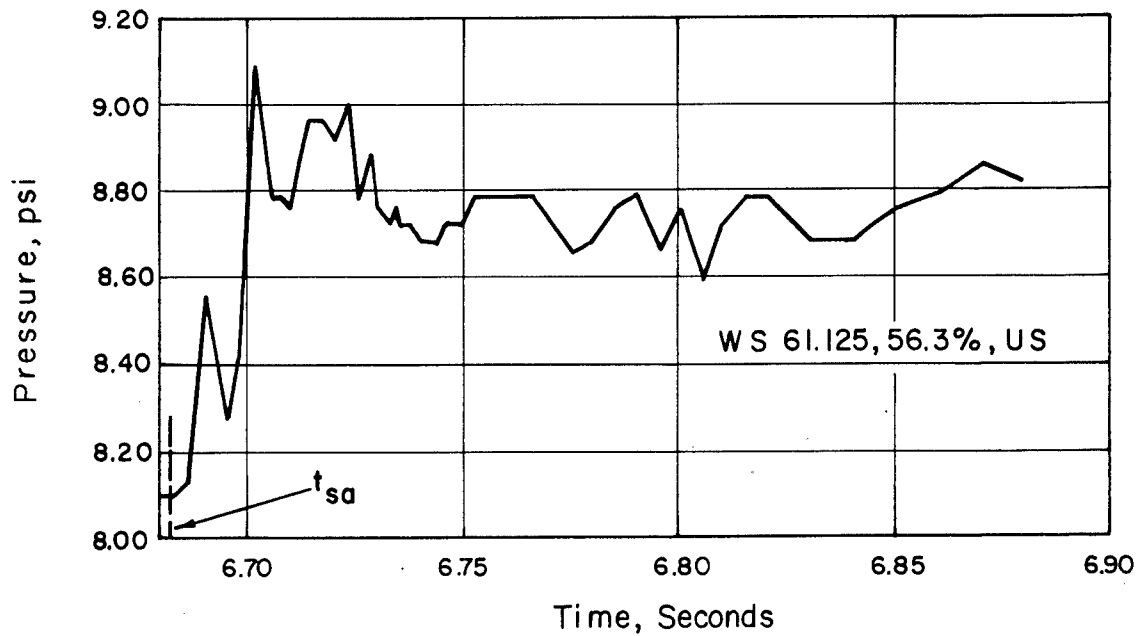
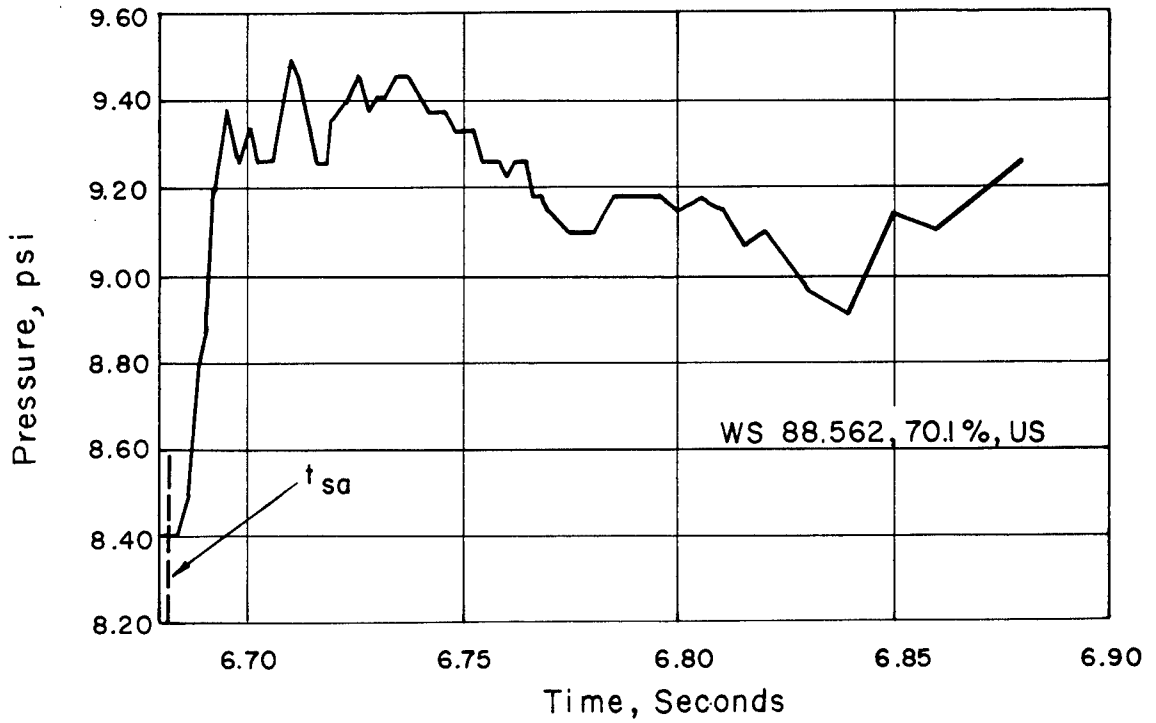


Figure E.7 Local wing pressure time histories, Shot Diablo.

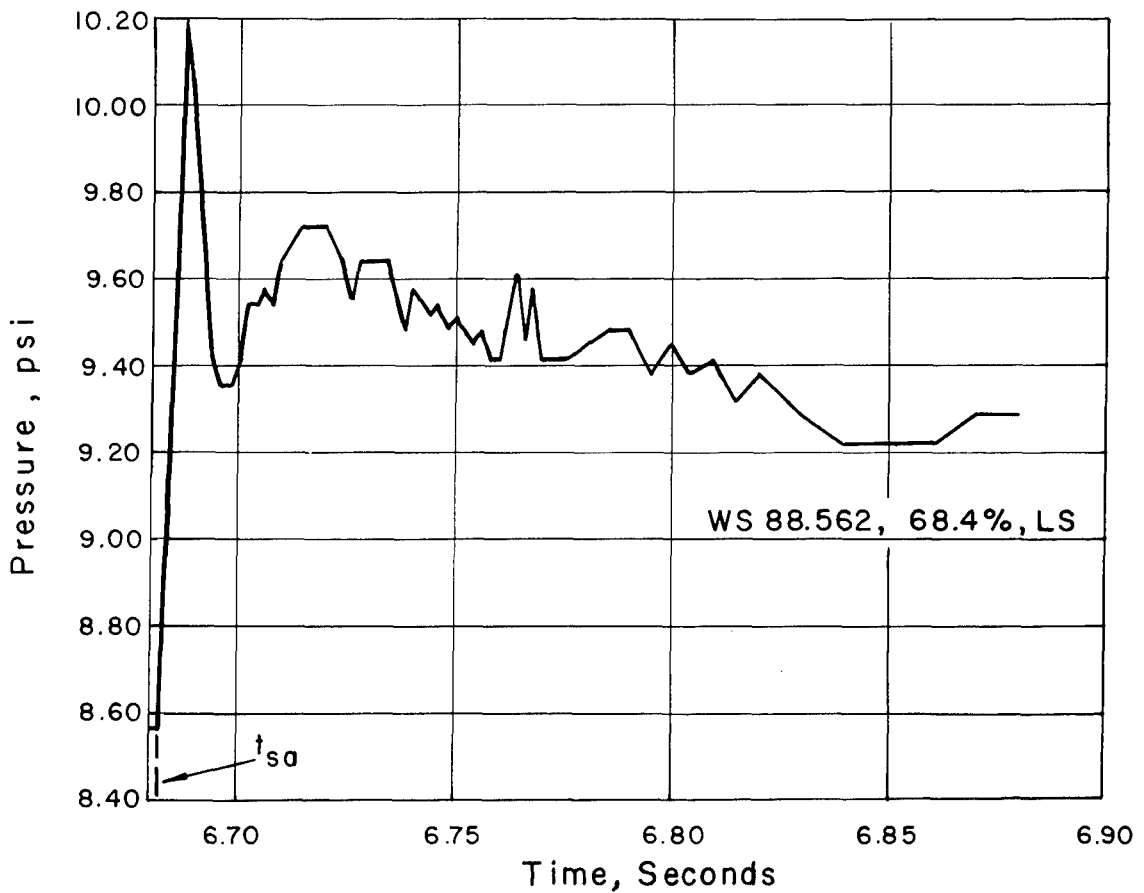
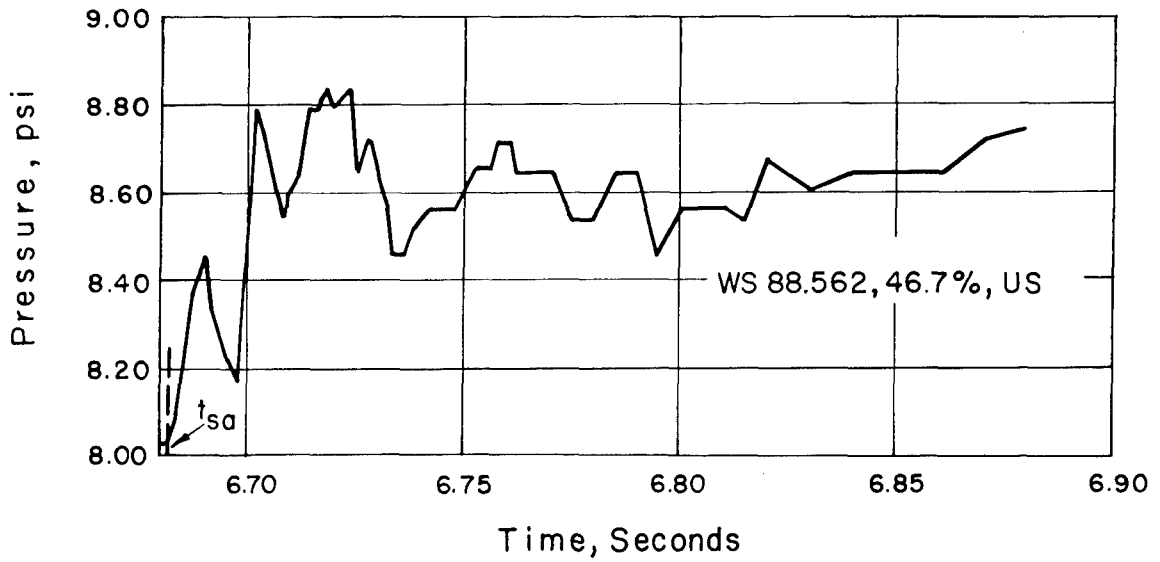


Figure E.8 Local wing pressure time histories, Shot Diablo.

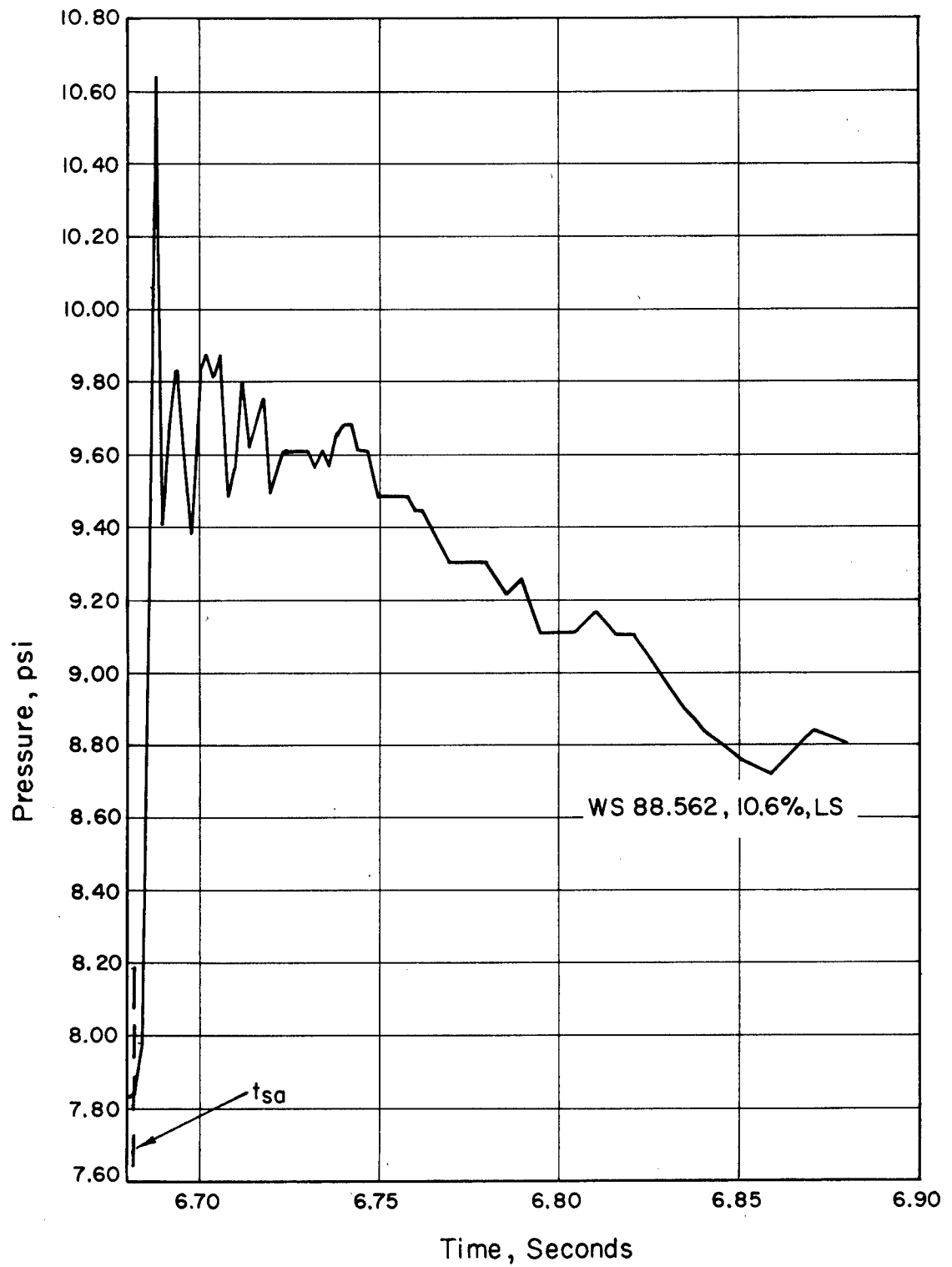


Figure E.9 Local wing pressure time history, Shot Diablo.

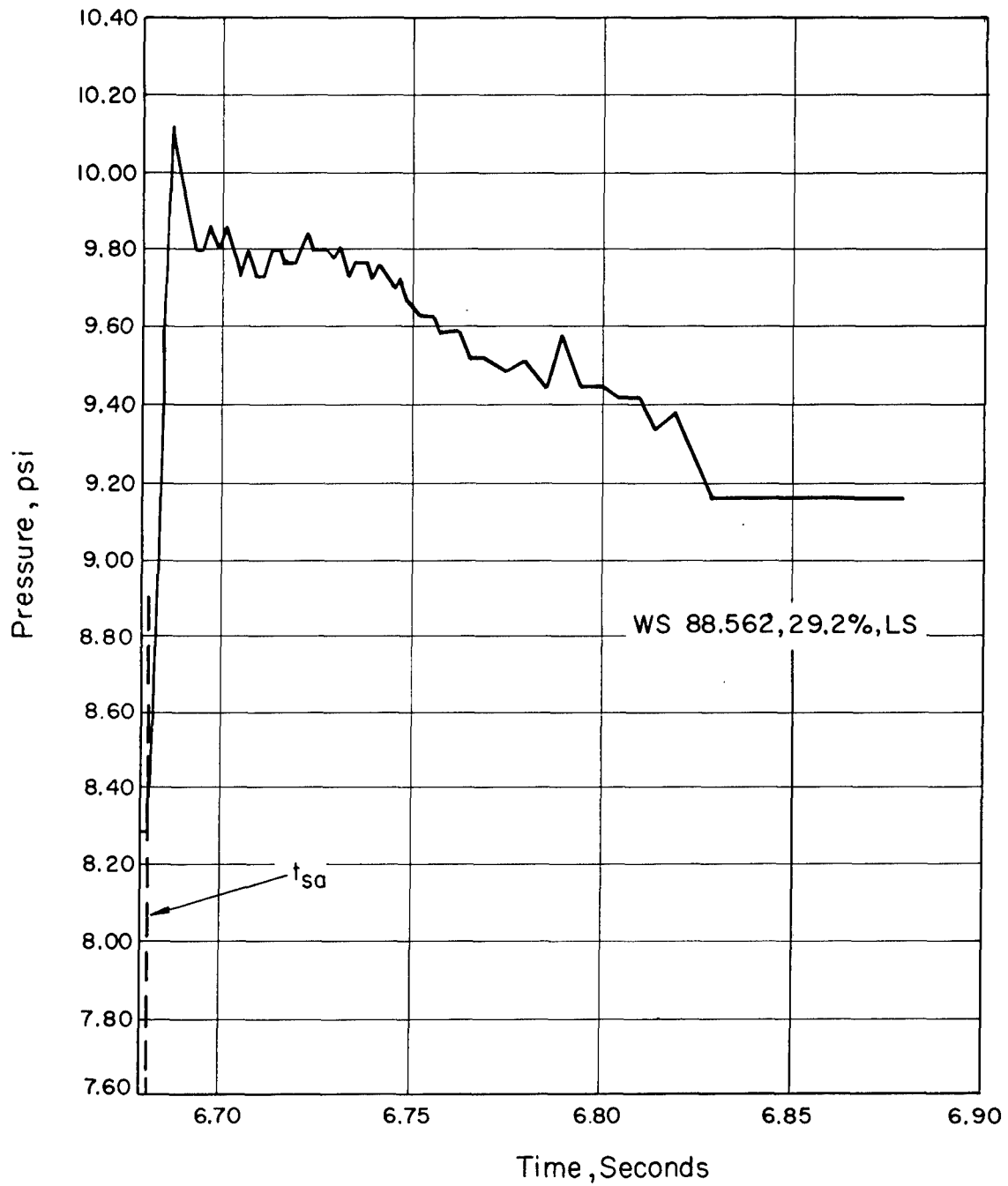


Figure E.10 Local wing pressure time history, Shot Diablo.

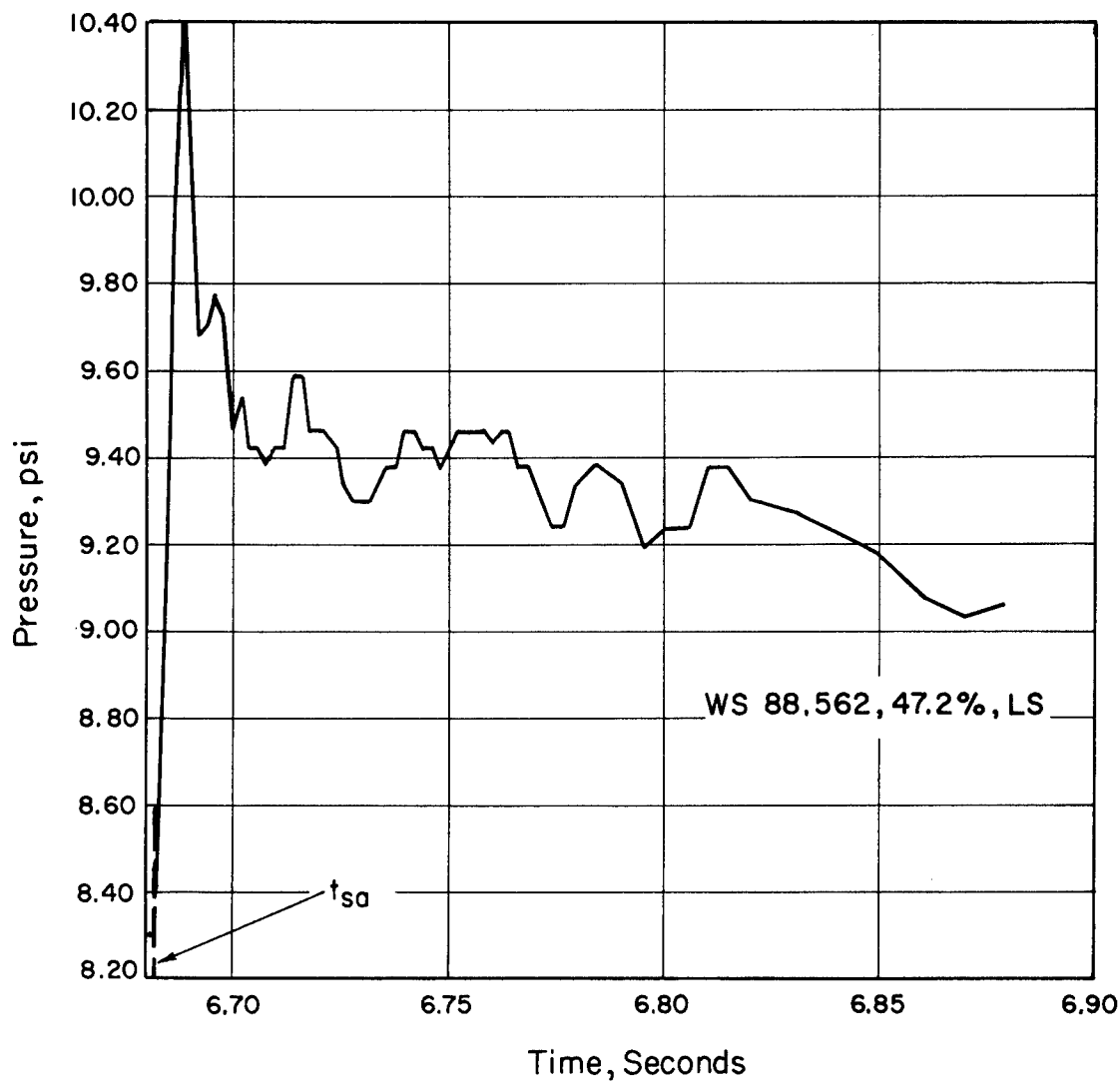


Figure E.11 Local wing pressure time history, Shot Diablo.

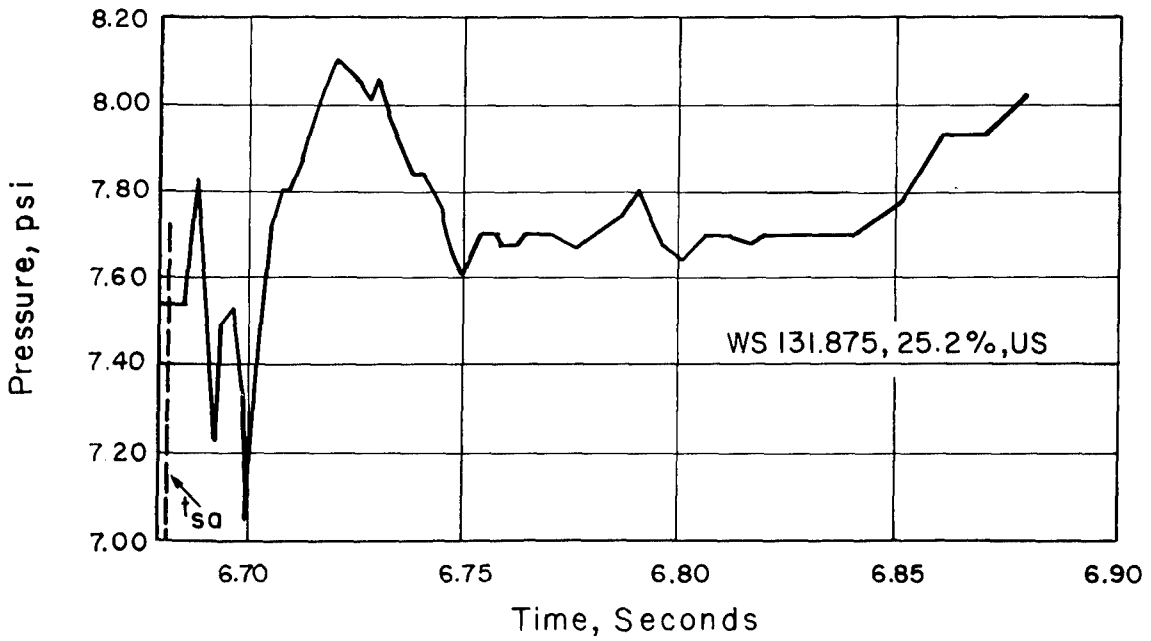
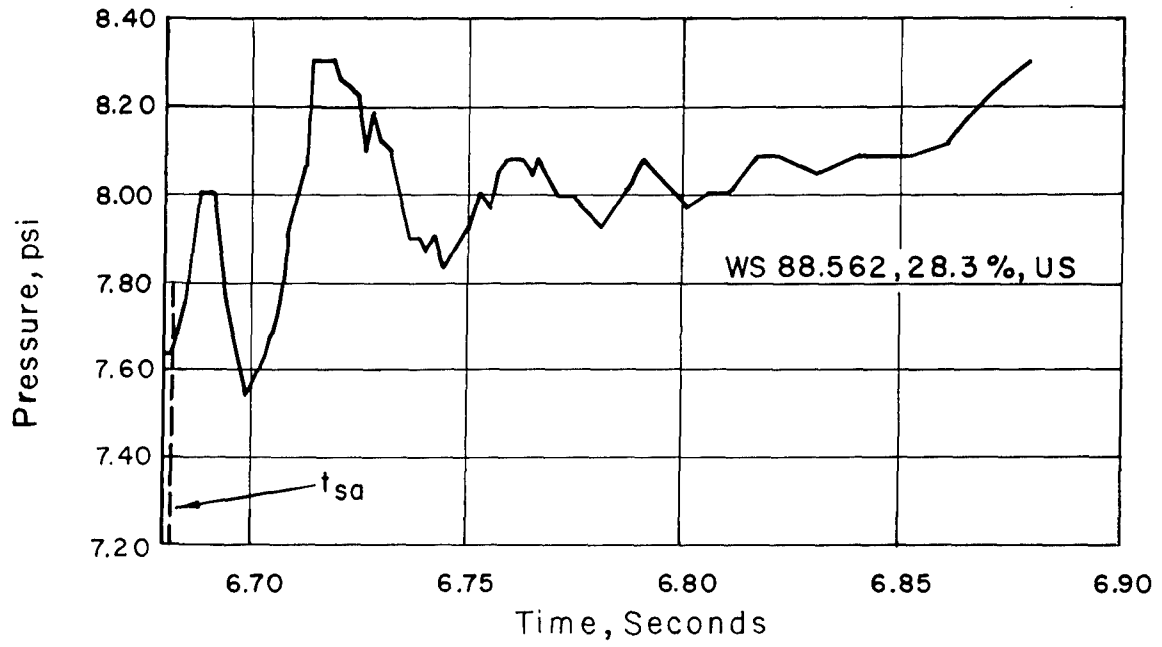


Figure E.12 Local wing pressure time histories, Shot Diablo.

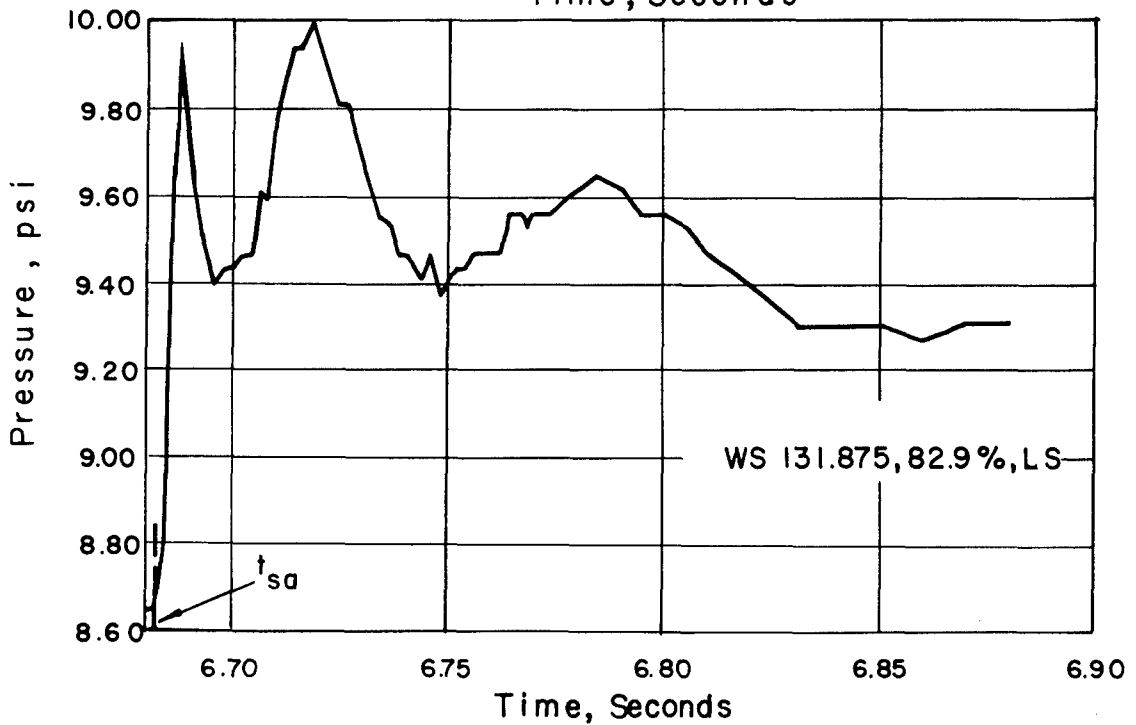
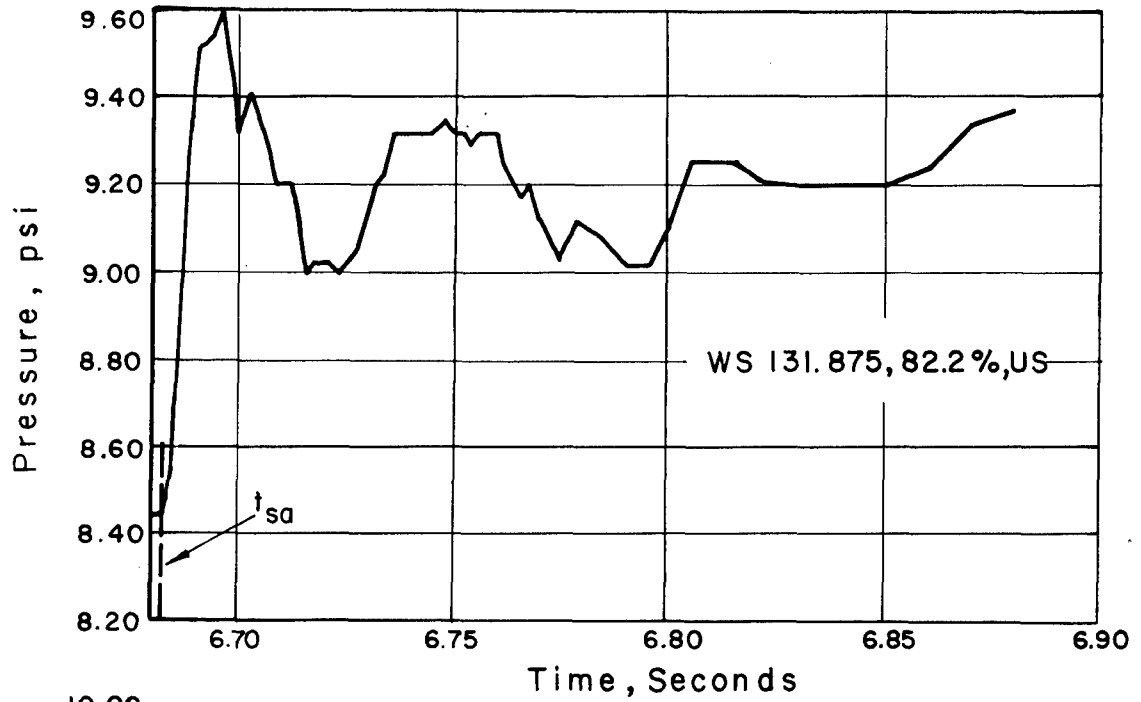


Figure E.13 Local wing pressure time histories, Shot Diablo.

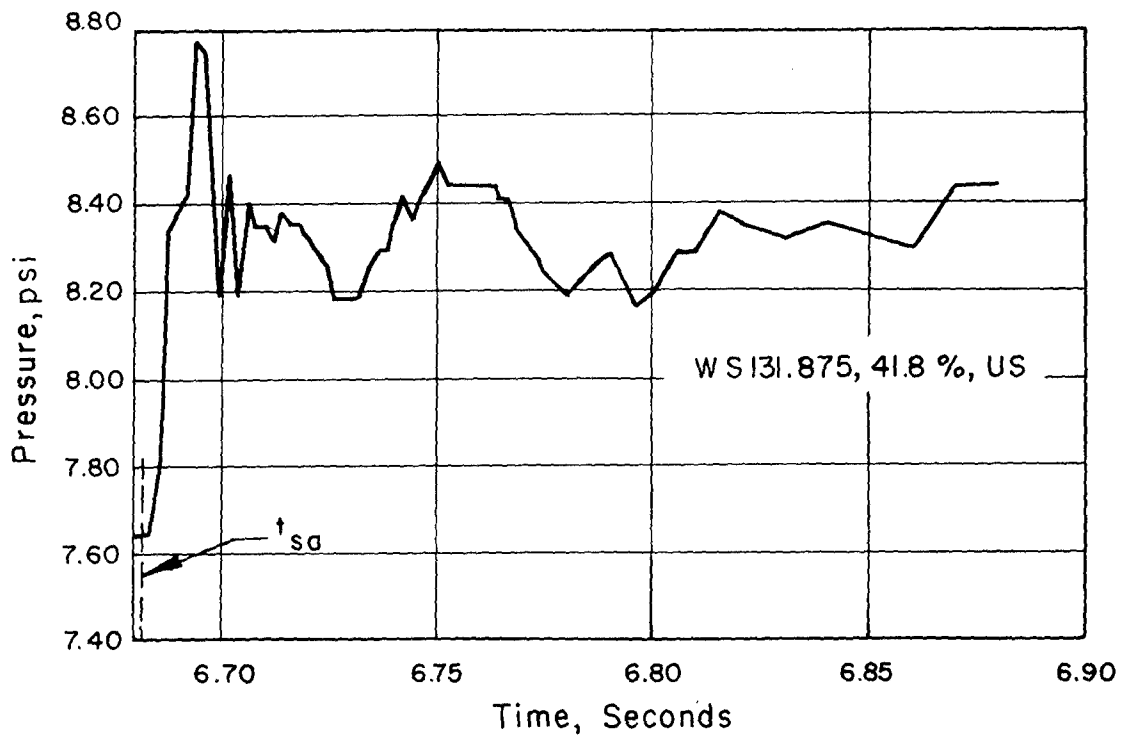
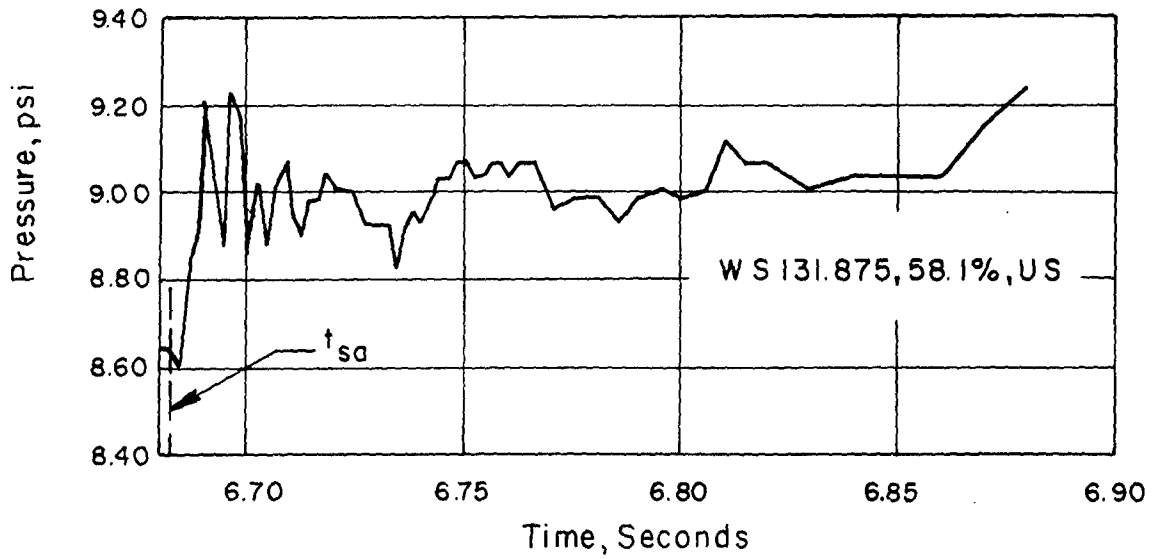


Figure E.14 Local wing pressure time histories, Shot Diablo.

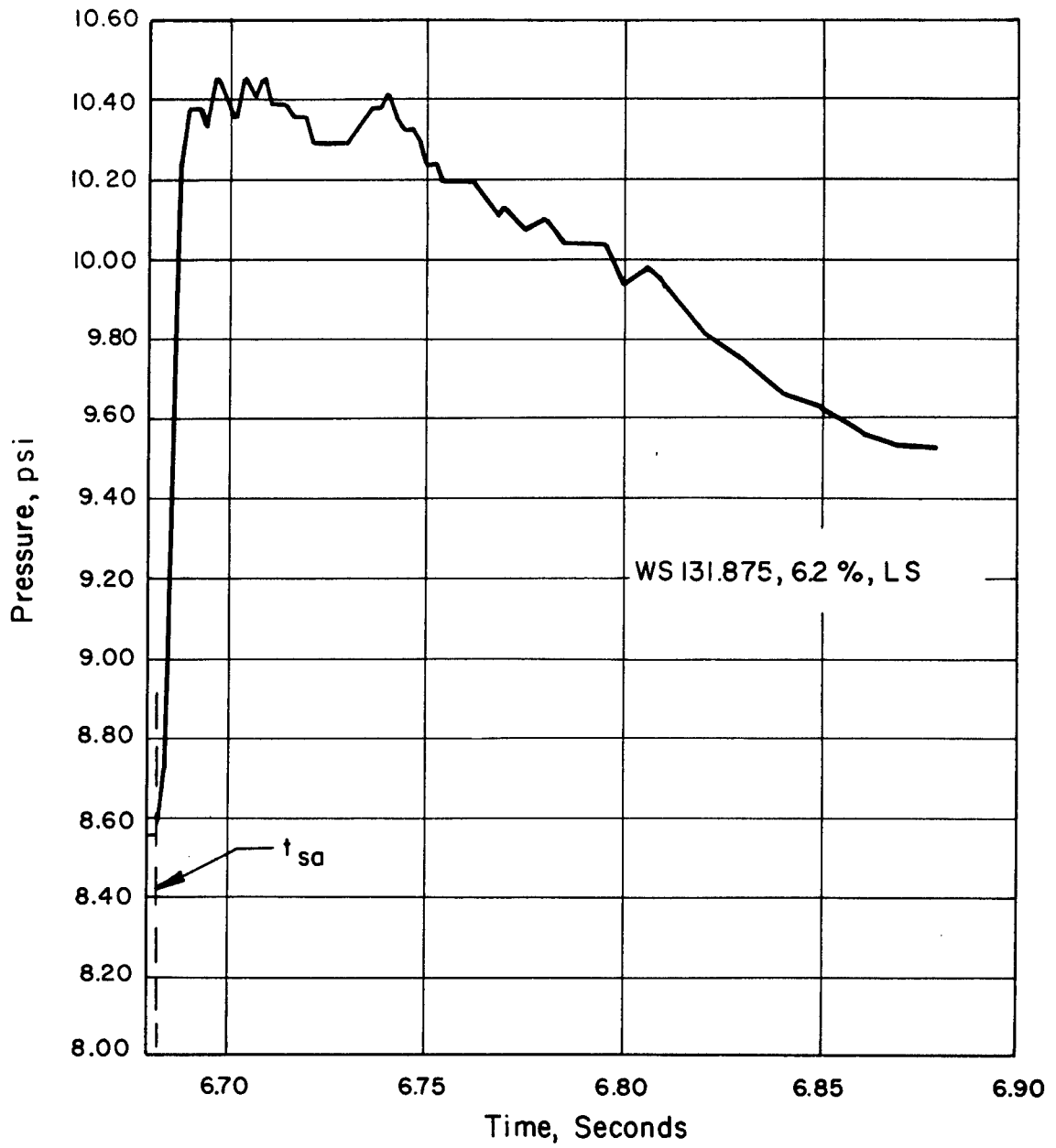


Figure E.15 Local wing pressure time history, Shot Diablo.

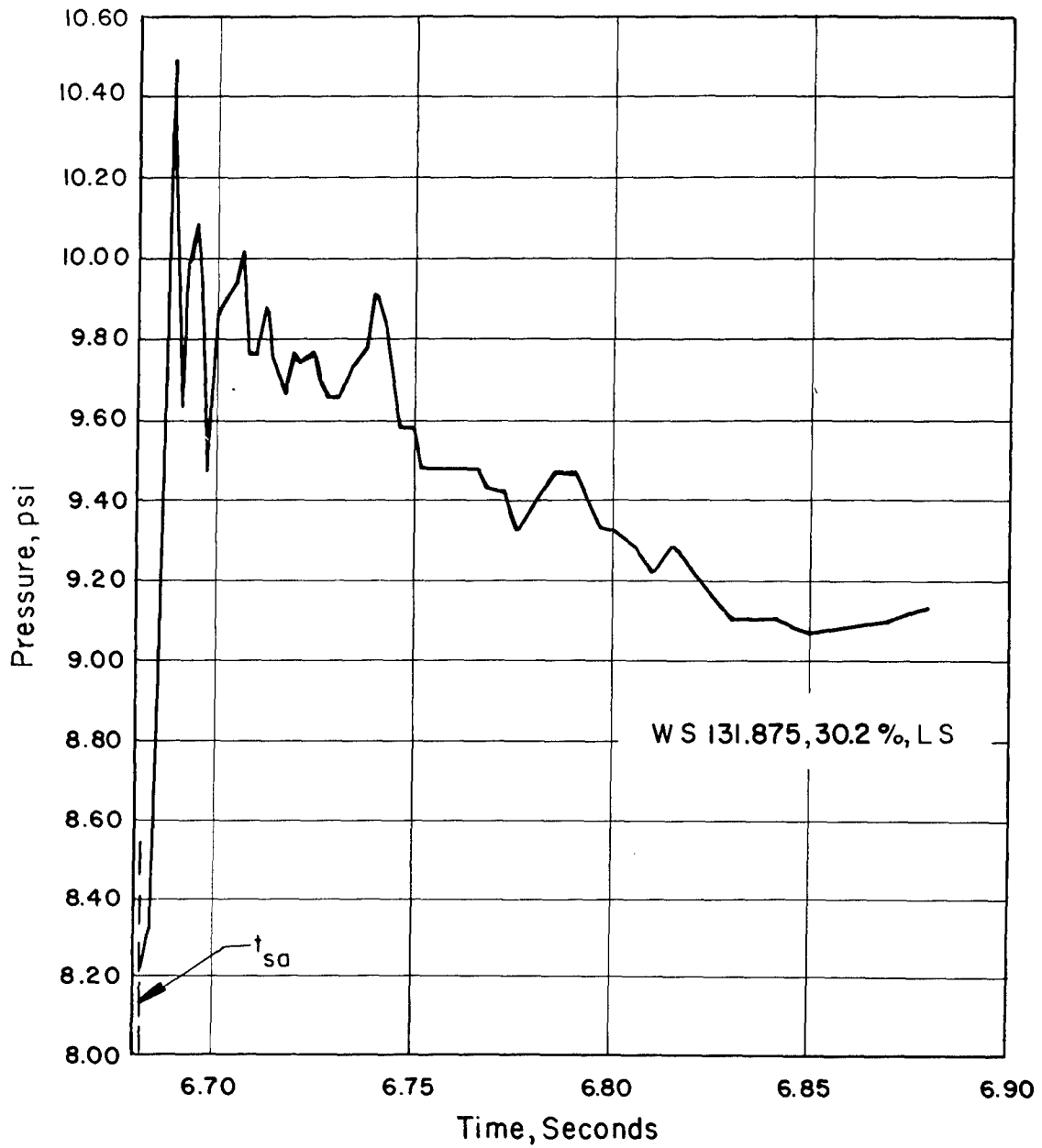


Figure E.16 Local wing pressure time history, Shot Diablo.

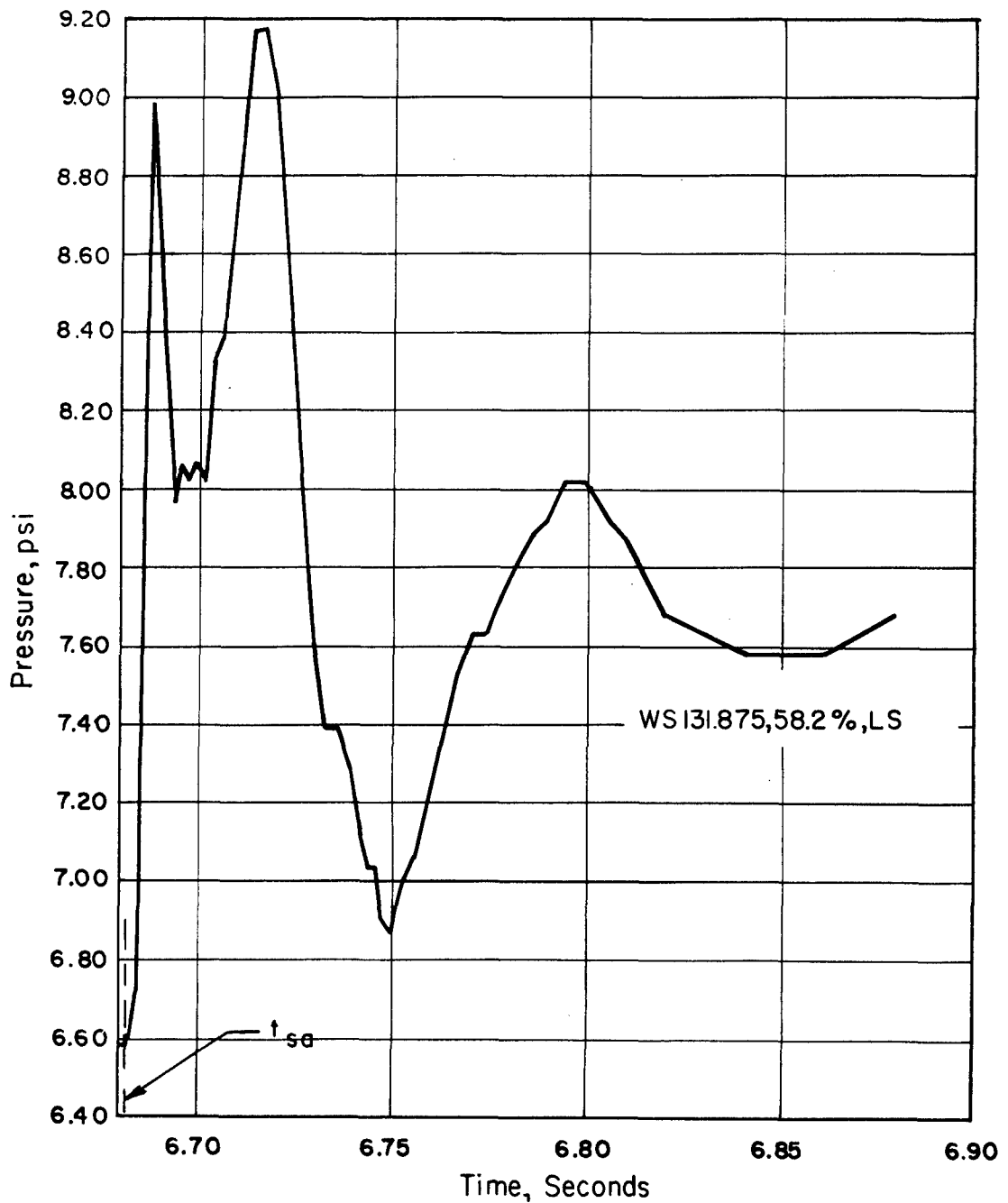


Figure E.17 Local wing pressure time history, Shot Diablo.

REFERENCES

1. "Model A4D-1 Airplane Preliminary Analysis of Special Weapons Delivery Capability"; ES 26245; 16 April 1956; Douglas Aircraft Company, Inc., El Segundo, California; Secret Restricted Data.
2. "Flight Paths and Positions for Model A4D-1 Airplanes in Operation Plumbbob"; ES 26559; 31 January 1957; Revised 30 April 1957; Douglas Aircraft Company, Inc., El Segundo, California; Secret Restricted Data.
3. Arthur Grossman, Edward I. Gray, and Claude W. Brenner; "Handbook for the Prediction of the Thermal Radiation Energy Received by an Aircraft Surface in Space from a Nuclear Detonation," Technical Note Nr. 55-172; August 1955; Wright Air Development Center, Wright-Patterson Air Force Base, Ohio; Secret Restricted Data.
4. L. M. Barker; "Diffusion Reflection of Radiation from Spherical and Hemispherical Sources to an Inclined Receiver," SC-3827 (TR); 4 April 1956; Sandia Corporation, Albuquerque, New Mexico, Secret.
5. Louis E. Bothell; 1261; "The Dependent Effects of Flyaway and Convective Cooling on the Expected Temperature Rise of Aircraft Delivering Nuclear Weapons"; SC-3846(TR); 8 June 1956; Sandia Corporation, Albuquerque, New Mexico; Secret.
6. "Capabilities of Atomic Weapons (U)"; OPNAV Instruction 003400.1A; Revised Edition, 1 June 1955; Armed Forces Special Weapons Project; Secret Restricted Data.
7. Cooke and Broyles; "Curves of Atomic Weapon Effects for Various Burst Altitudes (S. L. to 100,000 ft.)"; SC-3282(TR); 9 March 1954; Sandia Corporation, Albuquerque, New Mexico; Secret Restricted Data.
8. BuAer Secret Restricted Data Letter Aer-AD-41, Serial 001865, dated 21 November 1956; "Mach Stem Propagation Information."
9. J. A. Drischler and F. W. Diedrich; "Lift and Moment Responses To Penetration of Sharp Edged Traveling Gusts With Application To Penetration of Weak Blast Waves"; NACA TN 3956; May 1957; Langley Aeronautical Laboratory, Langley Field, Virginia; Unclassified.
10. R. L. Bisplinghoff, H. Ashley, and R. L. Halfman; "Aeroelasticity"; 1955; Addison-Wesley Publishing Co., Inc.; Unclassified.
11. "Wing and Horizontal Stabilizer Calibration, Model A4D-1 Airplane"; February 1958; Douglas Aircraft Company, Inc., El Segundo, California; Confidential, Modified Handling.
12. "Estimated Airplane Weight Distribution, Model A4D-1"; ES 16196A; 5 January 1953; revised November 1957; Douglas Aircraft Company, Inc., El Segundo, California; Confidential, Modified Handling.
13. "Summary of Recorded Wing Pressure Time Histories and Free Stream Overpressures Obtained During A4D-1 Airplane Participation In Operation Plumbbob"; ES 29041; Douglas Aircraft Company, Inc., El Segundo, California; Confidential, Modified Handling.
14. J. A. Drischler; "Approximate Indicial Lift Functions For Several Wings of Finite Span in Incompressible Flow As Obtained From Oscillatory Lift Coefficients"; NACA TN 3639; May 1956; Langley Aeronautical Laboratory, Langley Field; Virginia; Unclassified.
15. H. W. Liepmann and A. Roshko; "Elements of Gasdynamics"; 1957; John Wiley and Sons; Unclassified.
16. "The Radiation Field of a Source Located Above an Indefinite Diffuse Plane"; ES 17782; 22 March 1956; Douglas Aircraft Company, Inc., El Segundo, California; Confidential.
17. W. E. Schorr; "Outline For Obtaining Deliverable Yield"; SC 1283-2, Unpublished; Sandia Corporation, Albuquerque, New Mexico; Secret Restricted Data.
18. "Thermal Diffusivity of Aircraft Exterior Finishes"; Materials and Process Engineering Laboratory Report, MP 12,998; 14 January 1958; Douglas Aircraft Company, Inc., Santa Monica, California; Unclassified.

DISTRIBUTION

Military Distribution Category 52

- ARMY ACTIVITIES
- 1 Deputy Chief of Staff for Military Operations, D/A, Washington 25, D.C. ATTN: Dir. of SM&R
- 2 Chief of Research and Development, D/A, Washington 25, D.C. ATTN: Atomic Div.
- 3 Assistant Chief of Staff, Intelligence, D/A, Washington 25, D.C.
- 4 Chief of Engineers, D/A, Washington 25, D.C. ATTN: ENGTB
- 5- 6 Office, Chief of Ordnance, D/A, Washington 25, D.C. ATTN: ORDTN
- 7 Chief of Transportation, D/A, Office of Planning and Int., Washington 25, D.C.
- 8- 10 Commanding General, U.S. Continental Army Command, Ft. Monroe, Va.
- 11 Director of Special Weapons Development Office, Headquarters CONARC, Ft. Bliss, Tex. ATTN: Capt. Chester I. Peterson
- 12 President, U.S. Army Artillery Board, Ft. Sill, Okla.
- 13 President, U.S. Army Air Defense Board, Ft. Bliss, Tex.
- 14 President, U.S. Army Aviation Board, Ft. Rucker, Ala. ATTN: ATBG-DG
- 15 Commandant, U.S. Army Command & General Staff College, Ft. Leavenworth, Kansas. ATTN: ARCHIVES
- 16 Commandant, U.S. Army Air Defense School, Ft. Bliss, Tex. ATTN: Command & Staff Dept.
- 17 Commandant, U.S. Army Artillery and Missile School, Ft. Sill, Okla. ATTN: Combat Development Department
- 18 Commandant, U.S. Army Aviation School, Ft. Rucker, Ala.
- 19 Commandant, U.S. Army Ordnance School, Aberdeen Proving Ground, Md.
- 20 Commandant, U.S. Army Ordnance and Guided Missile School, Redstone Arsenal, Ala.
- 21 Commanding General, U.S. Army Chemical Corps, Research and Development Comd., Washington 25, D.C.
- 22- 23 Commanding Officer, Chemical Warfare Lab., Army Chemical Center, Md. ATTN: Tech. Library
- 24 Commanding Officer, Diamond Ord. Fuze Labs., Washington 25, D.C. ATTN: Chief, Nuclear Vulnerability Br. (230)
- 25- 26 Commanding General, Aberdeen Proving Grounds, Md. ATTN: Director, Ballistics Research Laboratory
- 27- 28 Commanding General, U.S. Army Ord. Missile Command, Redstone Arsenal, Ala.
- 29 Commander, Army Rocket and Guided Missile Agency, Redstone Arsenal, Ala. ATTN: Tech Library
- 30 Commanding General, White Sands Proving Ground, Las Cruces, N. Mex. ATTN: ORDES-OM
- 31 Commander, Army Ballistic Missile Agency, Redstone Arsenal, Ala. ATTN: ORDAB-HT
- 32 Commanding General, Ordnance Ammunition Command, Joliet, Ill.
- 33 Commanding Officer, USA Transportation Research Command, Ft. Eustis, Va. ATTN: Chief, Tech. Info. Div.
- 34 Commanding Officer, USA Transportation Combat Development Group, Ft. Eustis, Va.
- 35 Director, Operations Research Office, Johns Hopkins University, 6935 Arlington Rd., Bethesda 14, Md.
- 36 Commander-in-Chief, U.S. Army Europe, APO 403, New York, N.Y. ATTN: Opot. Div., Weapons Br.
- NAVY ACTIVITIES
- 37 Chief of Naval Operations, D/N, Washington 25, D.C. ATTN: OP-03EG
- 38 Chief of Naval Operations, D/N, Washington 25, D.C. ATTN: OP-75
- 39 Chief of Naval Operations, D/N, Washington 25, D.C. ATTN: OP-922G1
- 40- 41 Chief of Naval Research, D/N, Washington 25, D.C. ATTN: Code 811
- 42- 43 Chief, Bureau of Aeronautics, D/N, Washington 25, D.C.
- 44- 47 Chief, Bureau of Aeronautics, D/N, Washington 25, D.C. ATTN: AER-AD-41/20
- 48 Chief, Bureau of Ordnance, D/N, Washington 25, D.C.
- 49 Chief, Bureau of Ordnance, D/N, Washington 25, D.C. ATTN: S.P.
- 50 Director, U.S. Naval Research Laboratory, Washington 25, D.C. ATTN: Mrs. Katherine H. Cass
- 51- 52 Commander, U.S. Naval Ordnance Laboratory, White Oak, Silver Spring 19, Md.
- 53 Director, Material Lab. (Code 900), New York Naval Shipyard, Brooklyn 1, N.Y.
- 54 Commanding Officer, U.S. Naval Mine Defense Lab., Panama City, Fla.
- 55- 56 Commanding Officer, U.S. Naval Radiological Defense Laboratory, San Francisco, Calif. ATTN: Tech. Info. Div.
- 57 Commanding Officer, U.S. Naval Schools Command, U.S. Naval Station, Treasure Island, San Francisco, Calif.
- 58 Superintendent, U.S. Naval Postgraduate School, Monterey, Calif.
- 59 Commanding Officer, Nuclear Weapons Training Center, Atlantic, U.S. Naval Base, Norfolk 11, Va. ATTN: Nuclear Warfare Dept.
- 60 Commanding Officer, Nuclear Weapons Training Center, Pacific, Naval Station, San Diego, Calif.
- 61 Commanding Officer, U.S. Naval Damage Control Tng. Center, Naval Base, Philadelphia 12, Pa. ATTN: ABC Defense Course
- 62 Commanding Officer, Air Development Squadron 5, VX-5, China Lake, Calif.
- 63 Director, Naval Air Experiment Station, Air Material Center, U.S. Naval Base, Philadelphia, Pa.
- 64 Commander, Officer U.S. Naval Air Development Center, Johnsville, Pa. ATTN: NAS, Librarian
- 65 Commanding Officer, Naval Air Sp. Wpns. Facility, Kirtland AFB, Albuquerque, N. Mex.
- 66 Commander, U.S. Naval Ordnance Test Station, China Lake, Calif.
- 67 Commandant, U.S. Marine Corps, Washington 25, D.C. ATTN: Code AO3H
- 68 Director, Marine Corps Landing Force, Development Center, MCS, Quantico, Va.
- 69 Commanding Officer, U.S. Naval CIC School, U.S. Naval Air Station, Glynco, Brunswick, Ga.
- AIR FORCE ACTIVITIES
- 70 Assistant for Atomic Energy, HQ, USAF, Washington 25, D.C. ATTN: DCS/O
- 71 Hq. USAF, ATTN: Operations Analysis Office, Office, Vice Chief of Staff, Washington 25, D. C.
- 72- 73 Air Force Intelligence Center, HQ, USAF, ACS/I (AFCIN-3V1) Washington 25, D.C.
- 74 Director of Research and Development, DCS/D, HQ, USAF, Washington 25, D.C. ATTN: Guidance and Weapons Div.
- 75 The Surgeon General, HQ, USAF, Washington 25, D.C. ATTN: Bio.-Def. Pre. Med. Division
- 76 Commander, Tactical Air Command, Langley AFB, Va. ATTN: Doc. Security Branch
- 77 Commander, Air Defense Command, Ent AFB, Colorado. ATTN: Assistant for Atomic Energy, ADLDC-A
- 78 Commander, Hq. Air Research and Development Command, Andrews AFB, Washington 25, D.C. ATTN: RDRWA
- 79 Commander, Air Force Ballistic Missile Div. Hq. ARDC, Air Force Unit Post Office, Los Angeles 45, Calif. ATTN: WDSOT
- 80- 81 Commander, AF Cambridge Research Center, L. G. Hanscom Field, Bedford, Mass. ATTN: CR&ST-2
- 82- 86 Commander, Air Force Special Weapons Center, Kirtland AFB, Albuquerque, N. Mex. ATTN: Tech. Info. & Intel. Div.

CONFIDENTIAL

- 87- 88 Director, Air University Library, Maxwell AFB, Ala.
89 Commander, Lowry Technical Training Center (TW),
Lowry AFB, Denver, Colorado.
- 90 Commandant, School of Aviation Medicine, USAF, Randolph
AFB, Tex. ATTN: Research Secretariat
- 91 Commander, 1009th Sp. Wpns. Squadron, HQ. USAF, Washington
25, D.C.
- 92- 94 Commander, Wright Air Development Center, Wright-Patterson
AFB, Dayton, Ohio. ATTN: WCOSI
- 95- 96 Director, USAF Project RAND, VIA: USAF Liaison Office,
The RAND Corp., 1700 Main St., Santa Monica, Calif.
- 97 Commander, Air Defense Systems Integration Div., L. G.
Hanscom Field, Bedford, Mass. ATTN: SIDE-S
- 98 Chief, Ballistic Missile Early Warning Project Office,
220 Church St., New York 13, N.Y. ATTN: Col. Leo V.
Skinner, USAF
- 99 Commander, Air Technical Intelligence Center, USAF,
Wright-Patterson AFB, Ohio. ATTN: AFCIN-4Bla, Library
- 100 Assistant Chief of Staff, Intelligence, HQ. USAF, APO
633, New York, N.Y. ATTN: Directorate of Air Targets
- 101 Commander-in-Chief, Pacific Air Forces, APO 953, San
Francisco, Calif. ATTN: PFCIE-MB, Base Recovery
- OTHER DEPARTMENT OF DEFENSE ACTIVITIES
- 102 Director of Defense Research and Engineering, Washington 25,
D.C. ATTN: Tech. Library
- 103 Chairman, Armed Services Explosives Safety Board, DOD,
Building T-7, Gravelly Point, Washington 25, D.C.
- 104 Director, Weapons Systems Evaluation Group, Room LE880,
The Pentagon, Washington 25, D.C.
- 105-108 Chief, Defense Atomic Support Agency, Washington 25, D.C.
ATTN: Document Library
- 109 Commander, Field Command, DASA, Sandia Base, Albuquerque,
N. Mex.
- 110 Commander, Field Command, DASA, Sandia Base, Albuquerque,
N. Mex. ATTN: FCTG
- 111-115 Commander, Field Command, DASA, Sandia Base, Albuquerque,
N. Mex. ATTN: FCWT
- 116 Administrator, National Aeronautics and Space Adminis-
tration, 1520 "H" St., N.W., Washington 25, D.C. ATTN:
Mr. R. V. Rhode
- 117 Commander-in-Chief, Strategic Air Command, Offutt AFB,
Neb. ATTN: OAWS
- 118 Commander-in-Chief, EUCOM, APO 128, New York, N.Y.
- ATOMIC ENERGY COMMISSION ACTIVITIES
- 119-121 U.S. Atomic Energy Commission, Technical Library, Washing-
ton 25, D.C. ATTN: For DMA
- 122-123 Los Alamos Scientific Laboratory, Report Library, P.O.
Box 1663, Los Alamos, N. Mex. ATTN: Helen Redman
- 124-128 Sandia Corporation, Classified Document Division, Sandia
Base, Albuquerque, N. Mex. ATTN: H. J. Smyth, Jr.
- 129-131 University of California Lawrence Radiation Laboratory,
P.O. Box 808, Livermore, Calif. ATTN: Clovis G. Craig
- 132 Essential Operating Records, Division of Information Serv-
ices for Storage at ERC-H. ATTN: John E. Hans, Chief,
Headquarters Records and Mail Service Branch, U.S. AEC,
Washington 25, D.C.
- 133 Weapon Data Section, Technical Information Service
Extension, Oak Ridge, Tenn.
- 134-165 Technical Information Service Extension, Oak Ridge,
Tenn. (Surplus)